Explaining recent heterogeneous glacier change in the Annapurna Conservation Area, central Himalayas

Arminel Mary Lovell

Thesis submitted for the degree of Doctor of Philosophy

School of Geography, Politics and Sociology,
Newcastle University

December, 2019

Abstract

Since the 1970s, Himalayan glaciers have been shrinking in area, losing mass and decelerating in conjunction with warming air temperatures. This has serious implications for regional water resources. However, recent glacier change has been spatially heterogeneous and significant uncertainty remains about the sources (e.g. supraglacial debris, glacial hypsometry, avalanche-contributing area) of this local variability in the Himalayan glacier response to climate change. This thesis aims to characterise recent glacier changes in the Annapurna Conservation Area (ACA) in central Nepal and identify the extent and sources of local variability in the glacier change signal across a range of spatial (regional-, glacier- and sub-glacier-scale) and temporal (decadal to hourly) scales. Results show widespread glacier area loss (8.5% between 2000 and 2014/15) and mass loss (-0.28 ± 0.24 m w.e. a^{-1} between 2000 and 2013/16) in the ACA. However, glacier changes were spatially variable, with distinct glacier responses observed between sub-regions in the ACA. Individual glacier change was also modulated by supraglacial debris and glacier hypsometry. However, glacier elevation and avalanche-contributing area only influenced glacier change in the northern part of the study region, indicating that the strength of local controls was not spatially uniform. This thesis also identified another source of glacier response variability in the ACA, of potentially very localised importance, through the documentation of the first surge-type glacier in the central Himalayas. Sabche glacier had a very short surge cycle (~10 years), which is hypothesised to be modulated by subglacial topography, a mechanism that is rarely documented in published literature. Lastly, field data from Annapurna South glacier showed that the temperature and thermal properties of supraglacial debris varied both seasonally and between debris profiles of different thickness, which in turn had an important influence on the timing and magnitude of ablation. Overall, this thesis demonstrates the scale of local glacier change variability in the ACA and shows that the sources of this variability are complex and far from uniform. This work helps to put bounds on the level of noise occurring in the Himalayan glacier change signal and what can be considered a ‘normal’ range of variability. This heterogeneity should be taken into consideration when predicting how Himalayan glaciers will respond to climate change, and the impact of these glacier changes on local communities.

Acknowledgements

I would like to thank the following. My PhD supervisors Rachel Carr, Chris Stokes and Ann Rowan for their support and guidance throughout the project. IAPETUS NERC Doctoral Training Partnership (Grant code: NE/LOO2590/1) for funding the PhD and providing a supportive cohort of PhD students and training opportunities.

Fieldwork: The Quaternary Research Association and the Mount Everest Foundation for additional financial fieldwork support. Emily Hill for being a great PhD twin and field assistant. Alex Cumming, Jack Oxtoby and James Linighan for banter and company on fieldwork. Dhananjay Regmi and Ramraj Rijal at Himalayan Research Expeditions for their logistic and fieldwork support. Laxmi for being a fantastic guide and keeping me alive and safe on two field trips. The rest of the guide and porter team: Jas Raj, Arjun, Pramish, Smith, Aditya, Thile, Binay and Bibbin. Northumbria University and Cambridge University for lending us spare Kovacs drill heads. Alex Densmore for identifying the geology of rocks from the field site. Devin Harrison for help building the radiation shields.

Remote sensing: George Kania and Brian Claydon for setting up the GIS labs in the Newcastle Geography department. The European Space Agency for providing funding for the Pléiades and SPOT stereo satellite images. The US Geological Survey for providing Landsat, ASTER, SRTM and ASTER GDEM v2 data. The National Snow and Ice Data Center for providing the HMA DEMs. The Japan Aerospace Exploration Agency for providing the ALOS Global DEM. Marco Bagnardi for help processing Pleiades DEMs in *Erdas Imagine*. Robert Hattersley for assistance with DEM co-registration. Everyone else who helped me along the way. The editors and anonymous reviewers for constructive comments on the published chapters.

Other: Newcastle Geography Department staff. WWF UK Climate Change team. Francesca Falcini and Lauren Knight: my Svalbard mates and informal PhD support network. Newcastle Geography office crew and Durham Geography pub crew. My family for keeping me grounded. Haz for encouraging me to do a PhD in glaciology. And obviously Will for agreeing to a few more years of long distance and sticking through it all with me.

Cheers.

Declaration

This thesis is the result of my own work conducted between September 2015 and December 2019 under the supervision of J. R. Carr, C. R. Stokes and A. V. Rowan. It has not been previously submitted for a degree or other qualification in this or any other university. Chapters 3 and 4 are based on published chapters in which J. R. Carr and C. R. Stokes are co-authors. For the published chapters, I conducted the data collection and analysis, led the development of the paper, wrote the text and designed the figures. All authors provided editorial input and guidance on the development of the research. A full description of the author contributions for the published chapters are detailed at the beginning of the chapters.

Contents

List of Tables

List of Figures

1. Chapter 1: Introduction

1.1 Background and motivation

High Mountain Asia (HMA), which includes the Himalayas, Karakoram, Hindu Kush Pamirs and Tibetan Plateau (Figure 1.1), contains the largest area of snow and ice (40,800 km^2) outside of the polar regions (Bolch *et al.*, 2012). Since the 1970s, glaciers across most of HMA, with the exception of some parts of the Karakoram, eastern Pamir and western Kunlun regions, have lost mass (Brun *et al.*, 2017; Maurer *et al.*, 2019), retreated (Zemp *et al.*, 2015), and their flow has decelerated (Dehecq *et al.*, 2018), coinciding with warming regional air temperatures (Shekhar *et al.*, 2010; Kattel and Yao, 2013; Krishnan *et al.*, 2019). These trends in mass loss are particularly pronounced in the western, central and eastern Himalayas (Brun *et al.*, 2017), and mass loss in these regions has accelerated since ca. 2000 (Maurer *et al.*, 2019). Himalayan glaciers feed into the Brahmaputra, Ganges and Indus river basins that provide water resources for approximately 800 million people (Immerzeel *et al.*, 2010). Therefore, shrinkage of glaciers in their upper catchments have major implications for regional water resources, as glacial melt provides a base level of flow during dry seasons (Pritchard, 2019). Enhanced meltwater production from glacier mass loss also potentially increases the risk of cryospheric hazards such as glacial lake outburst floods (Bajracharya and Mool, 2010; Veh *et al.*, 2019), which can have catastrophic consequences for local communities and infrastructure (Yamada and Sharma, 1993; Rounce *et al.*, 2017).

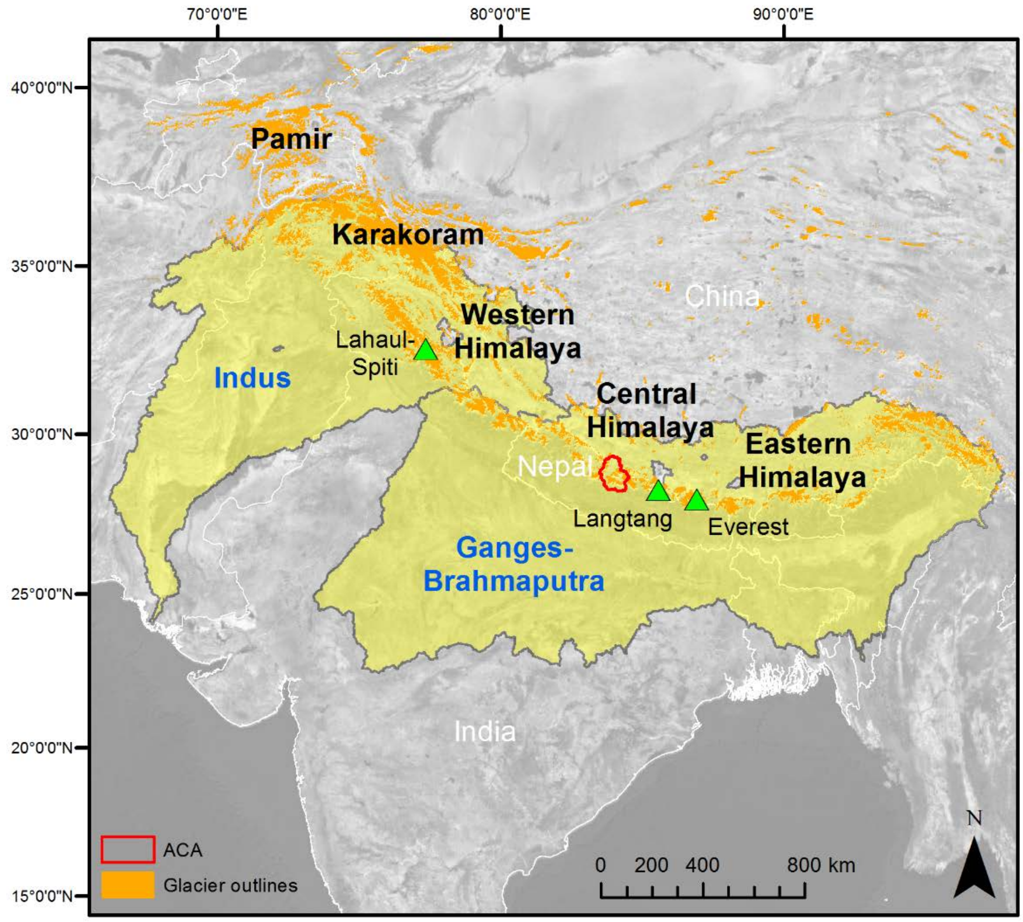

Figure 1.1: Location map of High Mountain Asia showing the glacierised area, the Indus and Ganges-Brahmaputra river basins (outlines provided by HydroSHEDS, courtesy of World Wildlife Fund) and the location of the Annapurna Conservation Area (ACA).

Within the overall trends in mass loss, Himalayan glacier change has been spatially variable at the local scale (Brun *et al.*, 2019). This heterogeneity is thought to be driven by factors specific to individual glaciers, such as supraglacial debris, geometry and hypsometry (e.g. Ragettli *et al.*, 2016; King *et al.*, 2017; Robson *et al.*, 2018). However, there are still gaps in our understanding about the scale of this variability, what a ‘normal’ range of variability, or noise, in the glacier change signal looks like, and how it should be considered when attempting to forecast future glacier response to climate change. While studies investigating the influence of local controls on small numbers of glaciers (<30 glaciers) have been able to identify relatively strong relationships between local controls and glacier change variability (Pellicciotti *et al.*, 2015; Ragettli *et al.*, 2016; Salerno *et al.*, 2017), the glacier change signal tends to be noisier, and the drivers of local glacier change variability are less clear, when studying glacier changes at much larger spatial scales (Brun *et al.*, 2019). Recent research investigating spatially variable glacier change across HMA has suggested that the influence of local controls on glacier behaviour is spatially variable and stronger in some parts of HMA than others (Brun *et al.*, 2019). For example, mean glacier elevation contributed to explaining variability in glacier mass balance in 10 of 12 regions in HMA but did not influence mass balance in Lahaul-Spiti or Pamir Alai (Brun *et al.*, 2019). The study also found that the local controls investigated only explained a small fraction of the glacier mass balance variability and that much of the noise in the glacier change signal was unaccounted for (Brun *et al.*, 2019). This glacier change variability is a challenge when attempting to project how these glaciers will respond to future climate change and how they might affect regional and local water resources.

Considering the potential impacts of Himalayan glacier change on water resources and hazards, it is crucial to improve our understanding of the extent of local variability in the glacier change signal. Therefore, one of the primary motivations for this project is to investigate recent Himalayan glacier change characteristics and identify the scale and sources of local variability in the glacier change signal to gain a better understanding of what constitutes a 'normal' amount of noise in the glacier change dataset. This will be addressed by assessing glacier changes in the Annapurna Conservation Area (ACA), Nepal (Figure 1.2), a region that has not been documented in much detail and where there are large variations in the characteristics of the glaciers.

As part of the drive to characterise the potential sources of variability in the Himalayan glacier change signal, this work also investigates surge-type glacier behaviour in the central Himalayas and its role in driving spatially variable glacier change. This stems from initial exploratory work of glacier changes in the region that identified a strong candidate for a surge-type glacier that had not previously been documented. Investigating the controls on a newly identified surge-type glacier can provide useful insight into how internal dynamics contribute to variability in the glacier change signal in this area and the potential implications of this variability for local water resources and hazards.

This work was also motivated by the limited availability of field data on small-scale interactions between supraglacial debris, a key source of variability in the Himalayan glacier change signal (Benn *et al.*, 2012), and ice melt in the Himalayas. In particular, there are very few studies that have investigated the influence of the thermal regime of supraglacial debris on sub-debris ice melt beyond the length of an ablation season and these studies have been focused on a small number of glaciers in the Himalayas (Nicholson and Benn, 2013; Chand and Kayastha, 2018). Surface energy-balance models, which are used to calculate sub-debris melt rates and predict glacier responses to climate change, are based on assumptions derived from field observations (Nicholson and Benn, 2006; Reid and Brock, 2010). Therefore, it is important to expand the available field dataset to explore whether these assumptions are applicable in other parts of the Himalayas.

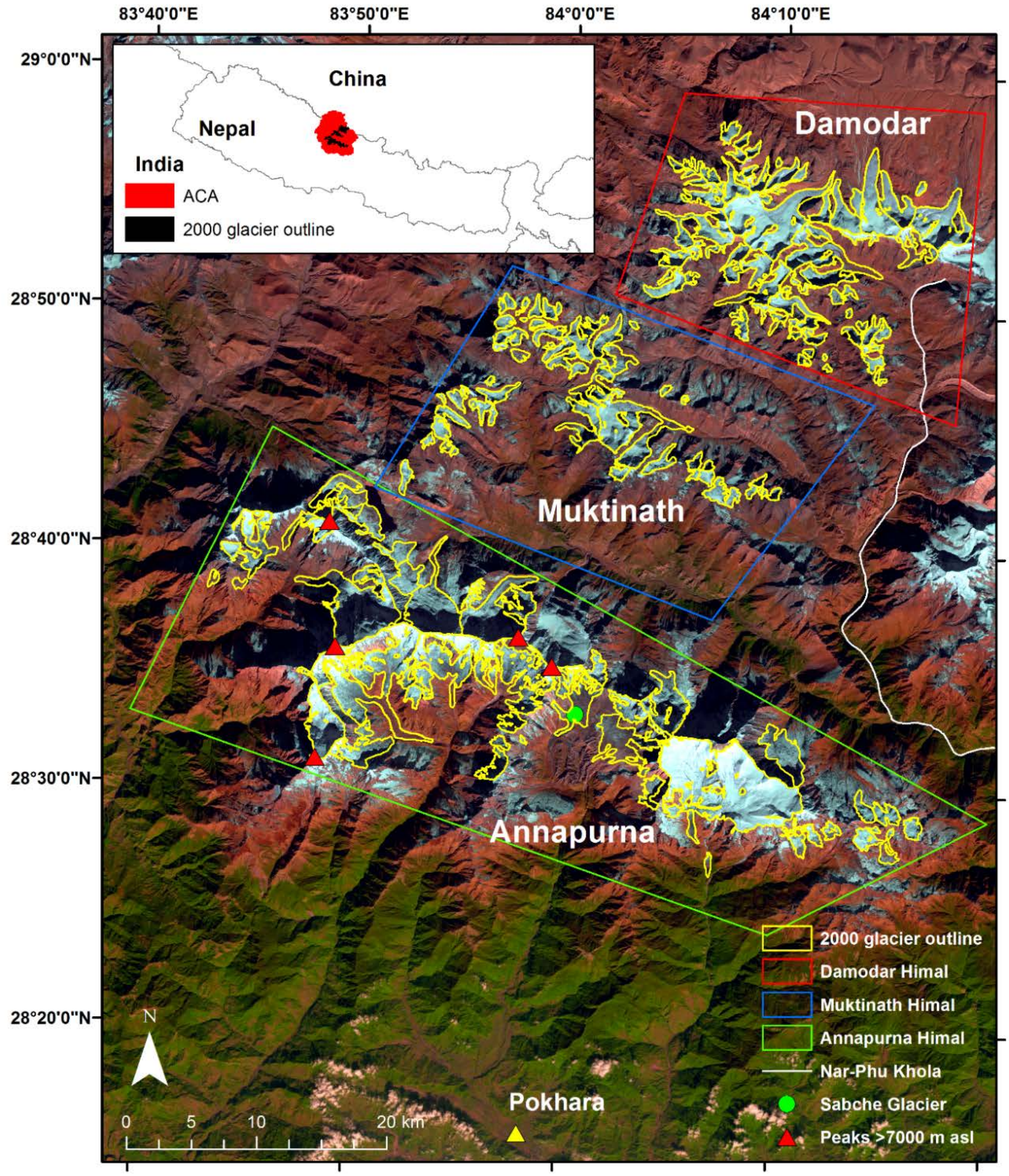

Figure 1.2: Map of the Annapurna Conservation Area (ACA) study area including glacier outlines mapped in 2000, the Damodar Himal, the Muktinath Himal and the Annapurna Himal sub-regions and the location of Pokhara, Sabche glacier and peaks over 7000 m asl. The background image is a Landsat Operational Land Imager and Thermal Infrared Sensor (OLI TIRS) pan-sharpened composite image from 01/12/2015.

1.2 Study region

The study region for the thesis is the ACA (28.70° N, 84.00° E), which is located in central Nepal, in the central Himalayas (Figure 1.2). The region has some of the highest peaks in the world, including Annapurna I (8,091 m asl), and hosts >170 glaciers covering ~450 km^2 (in 2014/15) (Lovell *et al.*, 2019) that receive most of their precipitation during the monsoon (Maussion *et al.*, 2014).

There were several reasons for choosing the ACA as a study region for this project. First, the ACA hosts glaciers of different type (e.g. debris-covered and debris-free), size and geometry, making it a useful region to investigate local controls on glacier behaviour. Second, glaciers in the ACA feed into the Kali Gandaki, Seti and Marsyangdi rivers, which are heavily populated basins. Moreover, the Seti river flows through Pokhara, one of the largest cities in Nepal (population: ~400,000) and a major tourist hub. This makes the ACA an important region for local water resources. Understanding how the glaciers in the region are changing is crucial with respect to the future of these water resources. Third, the ACA is included in some HMA-wide glacier change studies (Brun *et al.*, 2017; Dehecq *et al.*, 2018; Maurer *et al.*, 2019), but an in-depth study of the drivers of heterogeneous glacier behaviour has not previously been conducted in the region. Most of the detailed glacier change research in the central Himalayas has focused on the Everest and Langtang regions (Figure 1.1) in east Nepal (e.g. Quincey *et al.*, 2009; Pellicciotti *et al.*, 2015; Ragettli *et al.*, 2016; King *et al.*, 2017; King *et al.*, 2018). Research shows that the climate is variable across this part of the central Himalayas, with much higher mean annual precipitation observed in the ACA compared with the Langtang and Everest regions (Bookhagen and Burbank, 2010). This could potentially affect how glaciers in the ACA have responded to climate change compared with other better-researched regions. For example, recent HMA-wide mass balance studies have shown that the ACA has experienced a less negative mass balance than the regions to the east and west (Brun *et al.*, 2019; Maurer *et al.*, 2019). Therefore, the ACA is an important data gap in the central Himalayan glacier change dataset and merits further attention. This thesis is primarily focused on improving our understanding of the local controls driving recent heterogeneous glacier behaviour in the ACA in the central Himalayas.

1.3 Research aim and objectives

The overall aim of this thesis is to reveal the specific characteristics of recent glacier change behaviour in the Annapurna Conservation Area (ACA) in central Nepal and identify the scale and sources of local variability in the ACA's glacier change signal across a range of spatial and temporal scales. This aim will be achieved using the following objectives:

1) To quantify changes in glacier area, surface elevation, mass and velocity in the ACA between 2000 and 2016, using a range of remotely-sensed data.
2) To assess the scale of local variability (noise) in the glacier change signal in the ACA between 2000 and 2016, and investigate the influence of potential sources of this glacier change variability (e.g. supraglacial debris, hypsometry, elevation and avalanche contributing area), using statistical analysis.
3) To investigate the behaviour of, and controls on, a surge-type glacier in the ACA, as a source of local glacier response variability with potentially significant local impact, using remotely-sensed data.
4) To study the thermal regime of supraglacial debris on a debris-covered glacier in the ACA and evaluate its influence on sub-debris melt rates, using field observations.

This thesis investigates glacier changes and the extent and sources of local variability in the glacier change signal in the ACA at a range of spatial (regional-, glacier- and sub-glacier-scale) and temporal (decadal to hourly) scales, using remote sensing and fieldwork. This approach has several advantages. First, it allows the analysis of the larger-scale trends of glacier change across the ACA, which can be compared with other Himalayan regional glacier change studies, while benefitting from increased understanding of small-scale processes gained from high spatial- and temporal-resolution studies. Second, conducting an initial regional overview study helps to identify areas and glaciers that should be studied in more detail, using higher resolution imagery. This enables expensive resources, such as high spatial and temporal resolution satellite data, and logistically complicated field data collection, to be used more effectively and efficiently. Third, data obtained through field work can be used to ground-truth data collected via remote sensing.

1.4 Thesis structure

Chapter 2 provides a review of the literature on Himalayan glacier change, and our understanding of the local controls influencing the observed changes, followed by a discussion of the key research gaps in the field, some of which this thesis seeks to address. Chapter 3 presents new data on glacier mass balance and changes in glacier area, surface elevation, and ice flow velocity in the ACA. The chapter also assesses the influence of local controls on glacier behaviour, including glacier surface gradient, glacier elevation, glacier hypsometry, potential avalanche contributions and supraglacial debris. This data chapter was published as a paper in *Remote Sensing* (Lovell *et al.*, 2019). The text is largely unchanged apart from light editing to include any information that was put in a supplementary section for publication in the main body of text and to ensure consistency throughout the thesis. Author contributions for this published chapter are outlined at the beginning of the chapter. Chapter 4 presents data on changes in the terminus position, ice surface velocity and surface elevation of Sabche glacier in the ACA, documenting the first observations of surging behaviour in the central Himalayas. The chapter assesses the characteristics of the glacier surges to shed light on the controls modulating its behaviour. This data chapter was also published as a paper in *Remote Sensing of Environment* (Lovell *et al.*, 2018b) and the text is largely unchanged apart from light editing to include supplementary data and to ensure consistency throughout the thesis. Author contributions for this published chapter are outlined at the beginning of the chapter. Chapter 5 presents field data on sub-debris melt rates, supraglacial debris properties, debris thickness, air temperatures, debris temperatures, and debris thermal properties on the ablation zone of Annapurna South glacier (ASG), in the ACA, collected between October/November 2016 and October/November 2017, to investigate the influence of the thermal regime of debris on glacier ablation rates. This data chapter has not yet been submitted for publication. The methods are distinct for each data chapter and are described in detail in each chapter rather than in a separate methods chapter. Chapter 6 summarises and discusses the key themes of the thesis in the wider context of recent Himalayan glacier change and sources of local glacier response variability. It also identifies useful directions for future research. Chapter 7 outlines the main conclusions of the thesis.

Chapter 2: Progress in understanding the variable response of Himalayan glaciers to recent climate change

2.1 Introduction

Himalayan glaciers, defined in this thesis as glaciers in the western, central and eastern Himalaya sub-regions of High Mountain Asia (HMA) (Figure 2.1), have predominantly been losing mass (e.g. Kääb *et al.*, 2012; Gardelle *et al.*, 2013; Maurer *et al.*, 2019) and area (Zemp *et al.*, 2015) since the 1970s. These negative trends have occurred in conjunction with widespread glacier deceleration (Dehecq *et al.*, 2018) and glacier mass loss has increased in HMA since 2000 (Maurer *et al.*, 2019). These glacier changes have important implications for regional water resources (Kraaijenbrink *et al.*, 2017; Pritchard, 2019), cryospheric hazards (Bajracharya and Mool, 2010) and global sea level rise (Zemp *et al.*, 2019). However, within the broader trends, glacier response to climate change has been highly heterogeneous (e.g. Ragettli *et al.*, 2016; King *et al.*, 2017; Robson *et al.*, 2018). This is thought to be driven by local controls specific to each glacier, such as supraglacial debris, geometry, hypsometry, elevation and the likelihood of a glacier being avalanche-fed (e.g. Salerno *et al.*, 2017; Robson *et al.*, 2018; Brun *et al.*, 2019). There are still large uncertainties about the relative importance of different local controls, complicating our ability to project future glacier behaviour (Kraaijenbrink *et al.*, 2017). This review examines current understanding of recent Himalayan glacier change (over the last 40 to 50 years) and the sources of local variability in the glacier change signal.

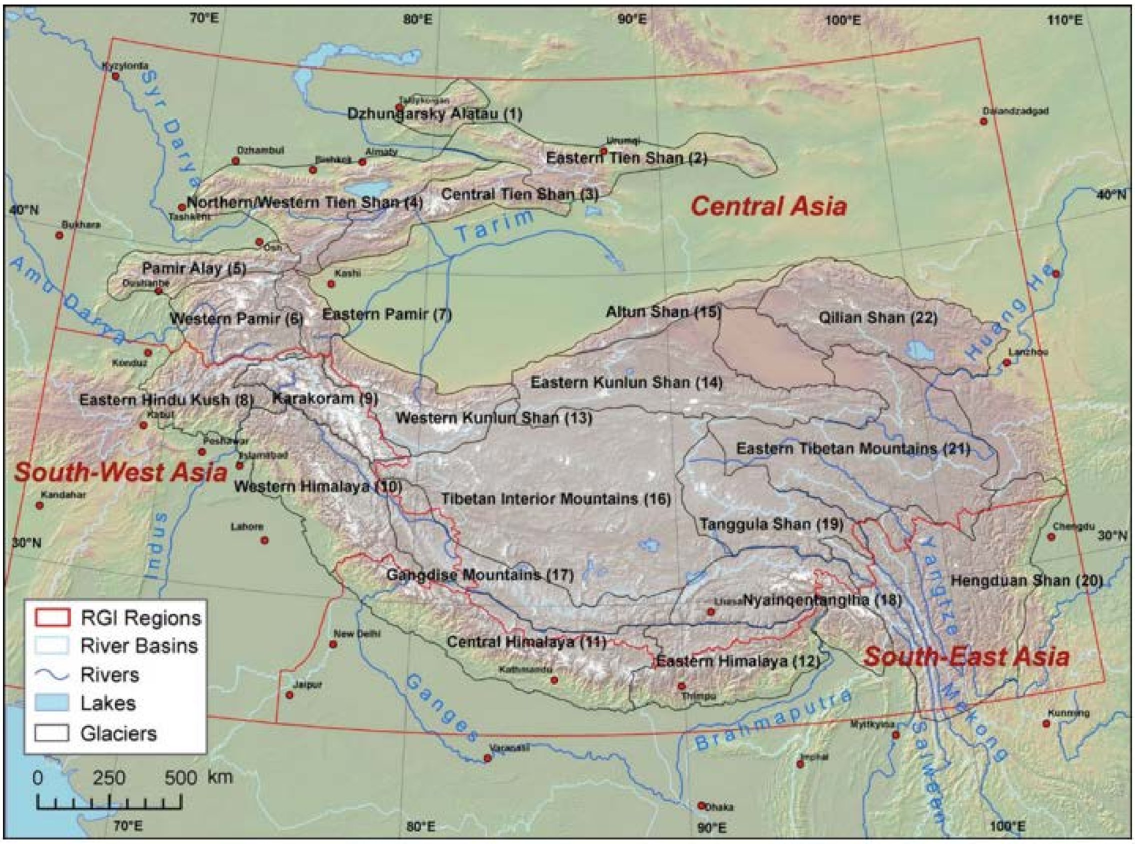

Figure 2.1: Map of HMA divided into 22 glacier sub-regions (from Bolch *et al.*, 2019). In this thesis, Himalayan glaciers are defined as glaciers located within the western Himalaya (10), central Himalaya (11) and eastern Himalaya (12) sub-regions as defined by Bolch *et al.* (2019).

2.2 The importance of Himalayan glaciers

2.2.1 *Water resources*

Himalayan glaciers feed into the Brahmaputra, Ganges and Indus river basins (Figure 1.1) which provide water resources for approximately 800 million people (e.g. Immerzeel *et al.*, 2010; Pritchard, 2019). The glaciers act as natural reservoirs, storing snowfall as ice and releasing meltwater into the catchments during the summer months (Pritchard, 2019). Glacier mass loss is expected to lead initially to increased meltwater inputs to catchments (Kraaijenbrink *et al.*, 2017). This is already being demonstrated by recent evidence that shows that meltwater generated from glacier mass loss is 1.6 times higher than meltwater that would be produced if the glaciers were in balance (Pritchard, 2019). However, as glaciers shrink, their capacity to store water will decrease, ultimately leading to reduced meltwater inputs. In areas with high monsoon rainfall, this meltwater contribution is less important. Nevertheless, in areas where monsoon rainfall is less dominant, or during unusually dry summers, meltwater inputs can play a major role in maintaining water supplies (Molden *et al.*, 2016; Pritchard, 2019). Snow and glacier meltwater generated upstream is a particularly important contributor to the Indus and the Brahmaputra rivers, where it comprises 151% and 27% of the total downstream natural discharge, respectively (Immerzeel *et al.*, 2010). It has been predicted that glacier-related changes to the discharge regimes of these two river catchments could present a food security risk for ~60 million people by 2050 (Immerzeel *et al.*, 2010). These impacts are enhanced in the high-elevation upper catchments of these river systems, where meltwater inputs make up a higher fraction of total river discharge (Molden *et al.*, 2016; Pritchard, 2019).

2.2.2 *Cryospheric hazards*

Himalayan glacier mass loss has led to a growth in the size of glacial lakes in the region (Bajracharya and Mool, 2010; Gardelle *et al.*, 2011; Nie *et al.*, 2017). Between 1990 and 2015, glacial lakes expanded by 14.1%, with the most rapidly expanding lakes located on the southern slopes of the Nepalese Himalayas (Nie *et al.*, 2017). Rapidly growing moraine-dammed lakes present a particular risk of glacial lake outburst floods (GLOFs). This is because the dams are typically unstable and can collapse under growing water pressure (Richardson and Reynolds, 2000; Bajracharya and Mool, 2010) or be triggered by glacier calving, avalanches and rockfalls into the lake (Nie *et al.*, 2017). GLOFs can cause catastrophic damage to settlements and infrastructure in the region (Yamada and Sharma, 1993; Schwanghart *et al.*, 2016; Rounce *et al.*, 2017). However, recent research has shown that although moraine-dammed lakes have grown in both number and area (Nie *et al.*, 2017), the frequency of GLOFs has not changed since the 1980s, suggesting that rapid lake growth alone is not necessarily a good predictor of GLOF risk and more understanding of GLOFs triggers is needed (Veh *et al.*, 2019).

2.2.3 *Global sea level rise*

The contribution to global sea level rise of Himalayan glaciers is relatively small compared with other glacierised regions but not insignificant, with mass balance estimates of -5 ± 2 Gt a^{-1} (South Asia East) compared with -73 ± 17 Gt a^{-1} in Alaska and -34 ± 11 Gt a^{-1} in the Southern Andes between 2006 and 2016 (Zemp *et al.*, 2019). Recent estimates suggest that Himalayan glaciers contain the equivalent of 2.1 ± 0.5 mm of global sea-level rise (Farinotti *et al.*, 2019) and a recent study suggested that all HMA glaciers (including the Karakoram, Pamir, Kunlun and the Tibetan Plateau) could contribute a total potential of 0.046 ± 0.009 mm a^{-1} to global sea level rise (Brun *et al.*, 2017).

2.3 Recent trends in regional climate change

2.3.1 *Himalayan climate*

Himalayan glaciers are principally influenced by two major atmospheric circulation systems (Figure 2.2). The Indian monsoon, which comes from the Bay of Bengal in the south, provides summer precipitation to the central and eastern Himalayas, but its influence decreases rapidly towards the western Himalayas (Barros *et al.*, 2004; Bookhagen and Burbank, 2010; Bookhagen, 2016). The mid-latitude westerlies are more dominant in the north-western Himalayas and provide most precipitation in this area during the winter (Bookhagen and Burbank, 2010; Mölg *et al.*, 2013; Palazzi *et al.*, 2013). This means that the timing of receiving maximum precipitation varies for glaciers along the Himalayan range (Figure 2.3) (Maussion *et al.*, 2014), which can determine their relative sensitivity to changes in regional precipitation and/or air temperatures (Mölg *et al.*, 2013). Glaciers in the central and eastern Himalayas are mainly summer accumulation-type glaciers (Figure 2.3), due to the dominance of the summer monsoon, while glaciers in the north-western Himalayas rely more heavily on winter accumulation (Figure 2.3), due to the stronger influence of the westerlies (Maussion *et al.*, 2014). However, the relative strength of the monsoon and westerlies varies from year to year, driving inter-annual variability in glacier mass balance (Mölg *et al.*, 2013).

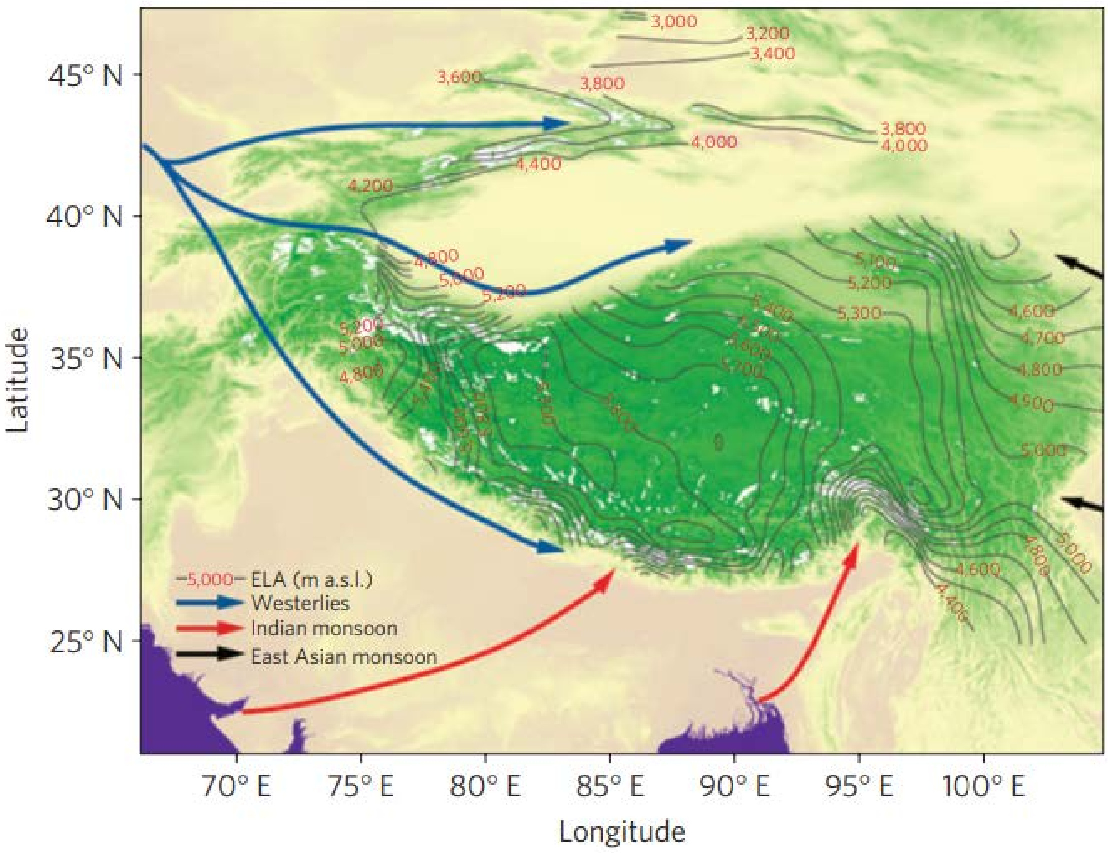

Figure 2.2: The main atmospheric circulation systems influencing HMA (from Yao *et al.*, 2012): the Westerlies, Indian Monsoon and East Asian Monsoon.

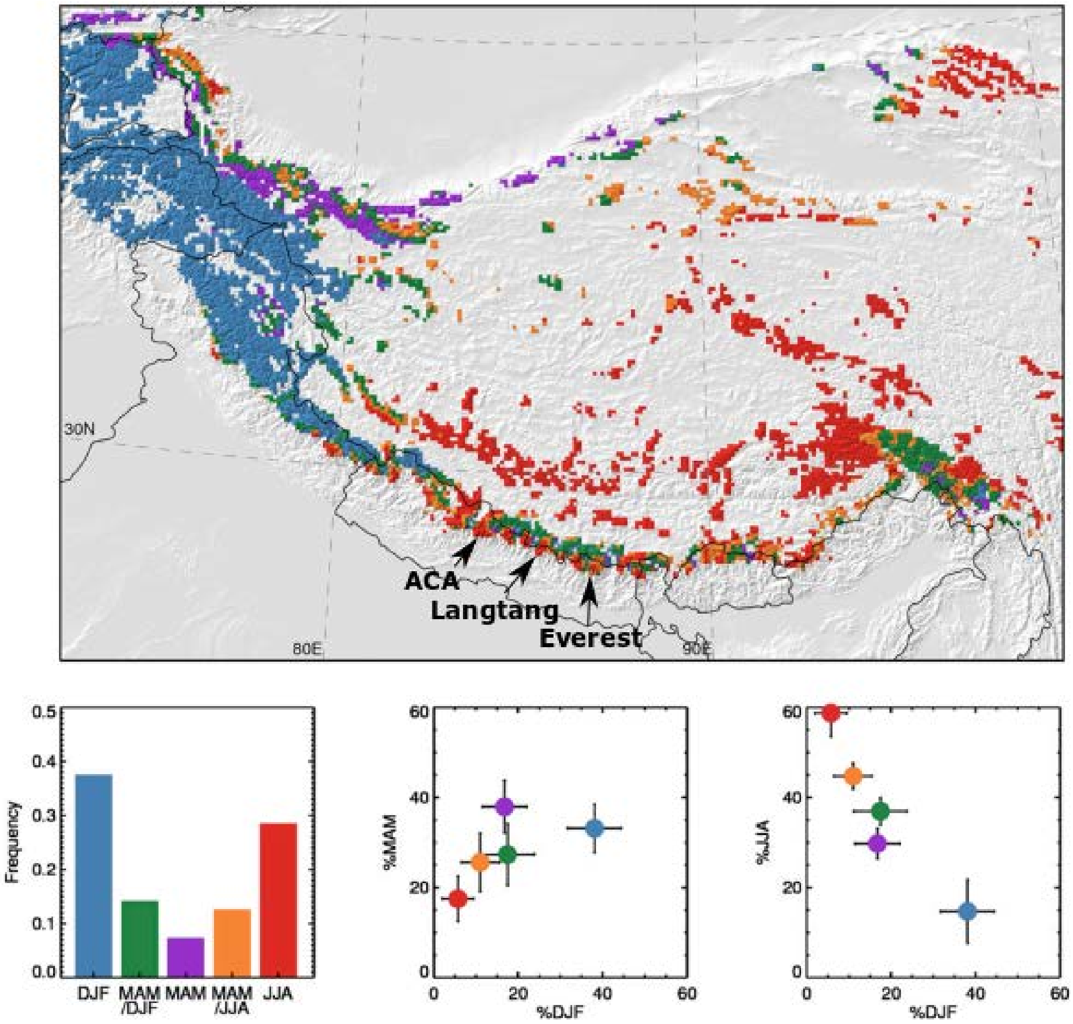

Figure 2.3: Glaciers in HMA categorised into accumulation type (from Maussion *et al.*, 2014). Glacierised grid points across HMA classified according to which season they receive the majority of their precipitation (DJF, MAM, JJA or a combination of two seasons). Note the dominance of winter accumulation-type glacierised area in the northwest and summer accumulation-type glacierised area in the south and east. Also note the high variability of seasonal precipitation classes in the central Himalayas. The locations of the ACA, and Langtang and Everest regions are indicated.

Within the broader climatic trends, the Himalayan climate system is highly heterogeneous. This area of major uplift is home to the highest peaks in the world, with an average altitude of 6,000 m (Benn and Owen, 1998) and several peaks with altitudes over 8,000 m. This topographical complexity has an important influence on local climate variability (Barros *et al.*, 2000; Shea *et al.*, 2015b), producing sharp temperature and precipitation gradients over relatively short horizontal distances, including a ten-fold south-to-north orographic precipitation gradient across the Himalayan range (Singh and Kumar, 1997; Bookhagen and Burbank, 2010). This means that local weather and climate conditions can vary substantially and may not reflect regional trends.

Himalayan climate change studies are hindered by a scarcity of long-term and continuous meteorological datasets in the region. Datasets that are available tend to be biased towards lower elevation locations that are easier to access, resulting in limited observations at higher elevations where glaciers are located (>4000 m asl) (Shea *et al.*, 2015b). Therefore, studies often use climate models that are based on remotely-sensed and/or reanalysis data (Palazzi *et al.*, 2013; Maussion *et al.*, 2014). However, these data tend to have low spatial resolutions (tens of km) (Palazzi *et al.*, 2013; Maussion *et al.*, 2014) which are often unable to capture the smaller-scale topographically-driven climatic variability (Bookhagen and Burbank, 2010), resulting in large uncertainties and weak agreement among climate models in the Himalayas (Krishnan *et al.*, 2019).

2.3.2 *Recent air temperature and precipitation trends*

There is general consensus that air temperatures have been increasing across the Himalayas over the last five decades (Krishnan *et al.*, 2019). From 1951 to 2014, mean air temperatures have been warming at a rate of 0.2 °C decade^{-1} (Ren *et al.*, 2017) and the frequency of extreme warm events has increased (Krishnan *et al.*, 2019). In the western Himalayas, mean air temperatures increased by 2 °C between 1984 and 2007 (Shekhar *et al.*, 2010), and observations indicate that winter air temperatures have increased more rapidly than summer air temperatures (Bhutiyani *et al.*, 2007). Air temperature increases were also observed in several mountain meteorological stations across Nepal between 1980 and 2009 with an average warming of 0.38 °C decade^{-1} and an acceleration of warming between 1997 and 2009 (Kattel and Yao, 2013). However, air temperatures varied considerably between stations, which was attributed to microclimates determined by the local topography (Kattel and Yao, 2013). Air temperatures have warmed more rapidly at higher elevations (Shrestha *et al.*, 1999; Salerno *et al.*, 2015; Krishnan *et al.*, 2019), but more research is needed on elevation-dependent warming, particularly in terms of how it is affected by snow and ice albedo feedbacks (Krishnan *et al.*, 2019).

There is less consensus on long-term precipitation trends in the Himalayas (Krishnan *et al.*, 2019). Models have predicted that increased air temperatures and moisture released into the atmosphere, as a result of anthropogenically-induced climate change, will lead to increased precipitation during the monsoon (Solomon *et al.*, 2007; Annamalai and Sperber, 2016). However, recent trends have been variable, depending on season, location and dataset used. For example, long-term datasets (~1950 to 2010) from the Asian Precipitation Highly Resolved Observational Data Integration Towards Evaluation of Water Resources (APHRODITE) project, the Global Precipitation Climatology Centre, and the Climate Research Unit, showed a significant negative trend in summer precipitation in the Himalayas, but there were no clear winter precipitation trends (Palazzi *et al.*, 2013). Observations from the China Meteorological Administration Global Land-Surface Air Temperature (LSAT-V1.1) and Global Precipitation V1.0 climate datasets show that annual precipitation across the Hindu Kush and Himalayas had a slight, but insignificant, negative trend between 1901 and 2014 (Ren *et al.*, 2017). A more recent trend of decreasing snowfall and cloud cover was observed in the Kashmir region in the Western Himalayas between 1988 and 2008, based on observations from 18 meteorological stations (Shekhar *et al.*, 2010). However, no long-term trends in precipitation were found across Nepal for the period 1948 to 1994 (based on observations from 78 meteorological stations) (Shrestha *et al.*, 2000). In the Gandaki river basin, in central Nepal, precipitation trends outside of the monsoon period (obtained from meteorological stations observations combined with APHRODITE data) decreased significantly but monsoon rainfall increased in the basin between 1981 and 2012 (Panthi *et al.*, 2015). In contrast, station observations in the Everest region showed a decreasing trend in monsoon precipitation between 1994 and 2013 (Salerno *et al.*, 2015). The variation in observed trends shows that much uncertainty remains about long-term precipitation changes across the Himalayas, partly due to the lack of data. To increase certainty of precipitation trends, improved long-term monitoring is needed in a larger number of locations that cover a more representative elevation range.

2.4 Recent and projected Himalayan glacier change trends

2.4.1 *Recent trends in Himalayan glacier area, surface elevation, mass balance and velocity*

Advances in satellite imagery quality and availability have allowed substantial developments in our knowledge of recent (last 20 years) Himalayan glacier change. A number of Himalayan-wide studies have documented area changes (Scherler *et al.*, 2011b), mass balance (Kääb *et al.*, 2012; Gardelle *et al.*, 2013; Brun *et al.*, 2017) and velocity changes (Dehecq *et al.*, 2018) since ~2000. Developments in the automatic processing of declassified spy satellite imagery (Maurer and Rupper, 2015) have also enabled researchers to extend investigations of Himalayan glacier mass changes back to the 1970s (Maurer *et al.*, 2019). This section explores the most up-to-date knowledge of regional glacier changes in the Himalayas.

There has been a clear trend of glacier area loss and fragmentation in the Himalayas over the last few decades (Kulkarni *et al.*, 2007; Ojha *et al.*, 2016). However, within the overall negative trends, there has been variability in measured area loss rates. In the western Himalayas, area change rates ranged from -0.12% a^{-1} (1968 to 2006) to -0.50 % a^{-1} (1962 to 2001/04) (Ye *et al.*, 2006; Kulkarni *et al.*, 2007; Bhambri *et al.*, 2011b). In the central Himalayas, area loss was estimated to be -0.59% a^{-1} from 1999 to 2013 (Robson *et al.*, 2018). In the eastern Himalayas, area changes ranged from -0.12% a^{-1} (1962 to 2005) to -0.50% a^{-1} (for multiple periods) (Bolch *et al.*, 2008; Thakuri *et al.*, 2014; Racoviteanu *et al.*, 2015; Ojha *et al.*, 2016). Moreover, evidence indicates that area loss in the western and eastern Himalayas has accelerated (Ye *et al.*, 2006; Bolch *et al.*, 2008; Bhambri *et al.*, 2011b).

Himalayan glaciers have predominantly thinned and lost mass (Table 2.1). However the existing glacier mass balance and surface elevation change estimates for the region have been calculated using a range of methods and time intervals, leading to variation between estimates (Table 2.1). For example, all methods agree that more mass has been lost in the western Himalayas (Spiti Lahaul) than in East or West Nepal, but there is disagreement about whether glaciers in Bhutan lost the least or the most mass (Table 2.1), which could be due to the smaller glacier sample sizes used by Gardelle *et al.* (2013). The disagreement between mass balance estimates suggests more work is needed to resolve the differences in these areas. However, for the most part, these large-scale studies show the well-known spatial patterns in mass balance across the Himalayas: of moderate mass losses in the central Himalayas and enhanced mass losses in the western Himalayas (Figure 2.4), driven by the competing dominance of the monsoon versus westerlies (Gardelle *et al.*, 2013; Maussion *et al.*, 2014). Similar to glacier area changes, recent research using spy satellite imagery has shown that Himalayan glacier mass loss has accelerated, with mass loss estimates doubling between the periods 1975 to 2000 (-0.22 ± 0.13 m w.e. a^{-1}) and 2000 to 2016 (-0.43 ± 0.14 m w.e. a^{-1}) (Maurer *et al.*, 2019).

Table 2.1: Regional Himalayan glacier mass balance estimates (m w.e. a^{-1}) for Bhutan, East Nepal, West Nepal and Spiti-Lahaul from three recent studies using different methods and satellite imagery. Gardelle et al. (2013) subtracted a Shuttle Radar Topography Mission (SRTM) digital elevation model (DEM) from SPOT 5 DEMs. Kääb *et al.* (2012) subtracted SRTM DEM data from satellite laser altimetry data. Brun *et al.* (2017) differenced ASTER DEMs from 2000 and 2016.

Region	**Gardelle *et al.* (2013)**	**Kääb *et al.* (2012)**	**Brun *et al.* (2017)**
Period	**1999-2011**	**2003-2008**	**2000-2016**
Bhutan	−0.22 ± 0.12	−0.52 ± 0.16	−0.42 ± 0.20
East Nepal	−0.26 ± 0.13	−0.39 ± 0.11	−0.33 ± 0.20
West Nepal	−0.32 ± 0.13	−0.32 ± 0.12	−0.34 ± 0.09
Spiti-Lahaul	−0.45 ± 0.13	−0.38 ± 0.06	−0.37 ± 0.09

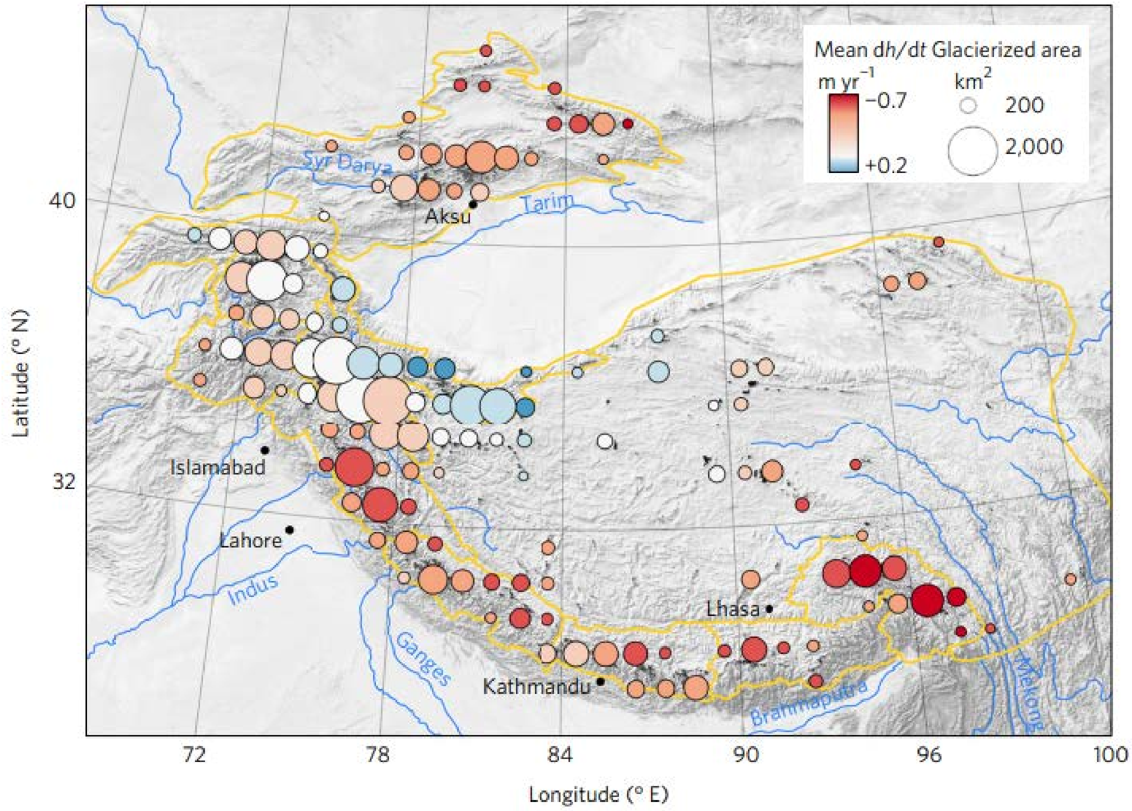

Figure 2.4: Mean glacier elevation change for HMA (2000-2016) (from Brun *et al.*, 2017) on a 1° × 1° grid. The size of the dot represents total glacierised area.

Many Himalayan glaciers have stagnated at their termini in association with mass loss and thinning (e.g. Quincey *et al.*, 2009; Thompson *et al.*, 2016; Bhushan *et al.*, 2018; Dehecq *et al.*, 2018). Some of this glacier-flow deceleration appears to be linked to supraglacial debris (Quincey *et al.*, 2009; Bhushan *et al.*, 2018), which tends to thicken towards the glacier terminus (Mihalcea *et al.*, 2008; Anderson and Anderson, 2018). Ice melt rates are reduced under thicker debris, resulting in an inverted mass balance gradient in the ablation zones of debris-covered glaciers (Rowan *et al.*, 2015). This causes a shallowing of the glacier surface gradient which consequently reduces the driving stress of the glacier, leading to glacier deceleration (Benn *et al.*, 2012). However, a recent study showed that there was a general trend of glacier deceleration across the Himalayas between 2000 and 2017, among both debris-covered and debris-free glaciers (Dehecq *et al.*, 2018), indicating that deceleration is not restricted to debris-covered glaciers. Rather, this trend was predominantly driven by a reduction in gravitational driving stress caused by glacier thinning and the spatial patterns of deceleration across the Himalayas coincided with spatial variations in mass loss (Figure 2.4), with the largest decelerations occurring in the western Himalayas (Figure 2.5) (Dehecq *et al.*, 2018).

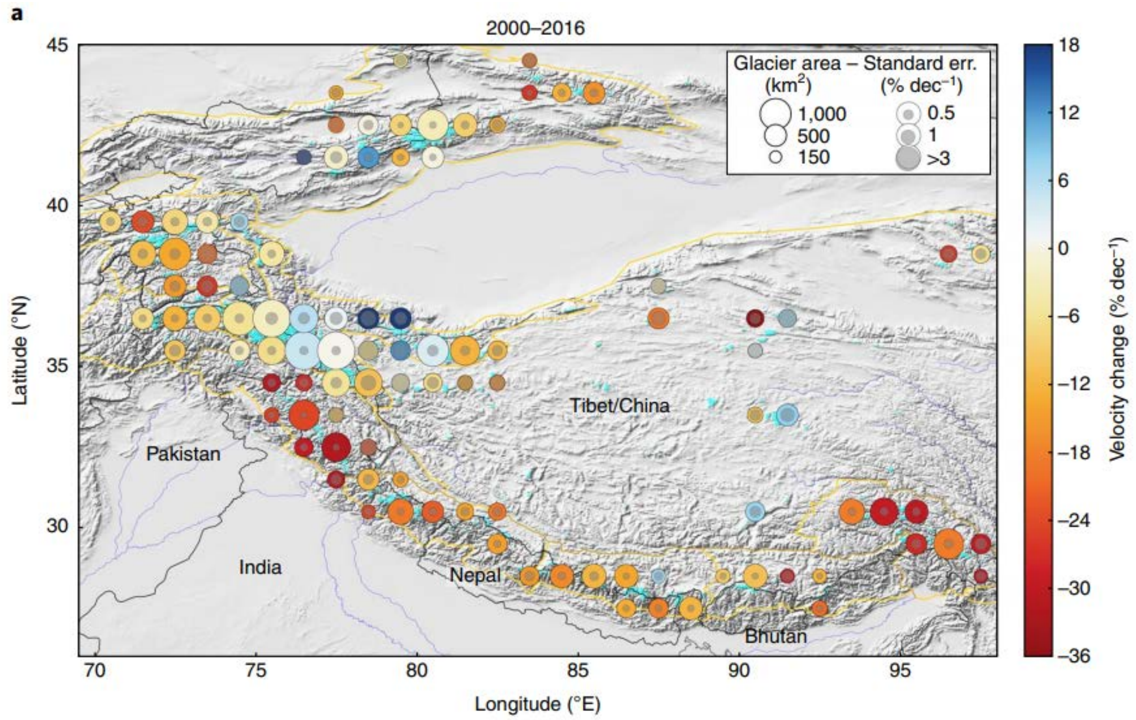

Figure 2.5: Median velocity change for HMA (2000-2016) (from Dehecq *et al.*, 2018) on a 1° × 1° grid. The size of the dot represents total glacierised area. The grey dots represent standard error.

2.4.2 *Projected Himalayan glacier trends*

Modelling has been used to project future Himalayan glacier changes at a range of spatial scales (e.g. Marzeion *et al.*, 2012; Rowan *et al.*, 2015; Shea *et al.*, 2015a; Kraaijenbrink *et al.*, 2017). Bolch *et al.* (2019) reviewed six regional models (Marzeion *et al.*, 2012; Giesen and Oerlemans, 2013; Radić *et al.*, 2013; Zhao *et al.*, 2014; Huss and Hock, 2015; Kraaijenbrink *et al.*, 2017) that projected Himalayan glacier changes for both an RCP4.5 and RCP8.5 emissions scenario at different stages through the 21st century (2030, 2050, 2080 and 2100). These models showed that Himalayan glaciers are expected to lose substantial mass (-8.7% to -32%) under the RCP4.5 and RCP8.5 scenarios by 2030 (Bolch *et al.*, 2019). Mass losses are projected to increase to -30% to -60% by 2050, with a bigger difference between the emissions scenarios (Bolch *et al.*, 2019). By 2100, Himalayan mass losses are projected to be -55% to -90% under a RCP4.5 scenario and -63.7% to -94.7% under a RCP8.5 scenario (Bolch *et al.*, 2019). A recent modelling study showed that even under a RCP2.6 emission scenario, equivalent to a global average temperature increase of 1.5 °C (the target set by 195 countries in the 2015 Paris Agreement), Himalayan glaciers would be expected to lose between -50% and -60% mass by 2100 (Kraaijenbrink *et al.*, 2017).

The considerable variation between the models (Bolch *et al.*, 2019) shows that projections of future glacier change in the Himalayas are subject to much uncertainty. Part of this uncertainty is a result of a relatively poor understanding of how the glaciers interact with the Himalayan climate, largely due to the limited meteorological observations at the same elevations as glaciers in the region (Bookhagen and Burbank, 2010; Wiltshire, 2014). Moreover, regional climate models tend to have coarse spatial resolutions, which poorly represent the complex topography of the Himalayas (Palazzi *et al.*, 2013; Maussion *et al.*, 2014). This leads to large uncertainties in climate modelling in the region (Mishra, 2015). Uncertainty in Himalayan glacier projections also comes from the (in)ability of models to simulate the complex physics, interactions and dynamics that determine glacier evolution (Bolch *et al.*, 2019), including how local controls, such as supraglacial debris and avalanche inputs, modulate these processes. Finally, knowledge of initial ice volumes is a large source of uncertainty for models (Bolch *et al.*, 2019). A recent study modelling global ice thickness indicated that current ice volume in HMA glaciers is 27% less than originally thought (Farinotti *et al.*, 2019). This will have important implications for existing Himalayan glacier projections.

2.5 Recent progress on understanding heterogeneous glacier change and the influence of local controls

Within the broader regional trends of glacier area change, mass balance and velocity change, the response of Himalayan glaciers to climate change has been highly spatially heterogeneous (e.g. Quincey *et al.*, 2009; Ragettli *et al.*, 2016; King *et al.*, 2017; Robson *et al.*, 2018; Brun *et al.*, 2019). Studies have attributed much of this local variability to differences in glacier topography, geometry, supraglacial debris and the presence of proglacial lakes (Ragettli *et al.*, 2016; King *et al.*, 2017; Salerno *et al.*, 2017; Robson *et al.*, 2018). This heterogeneity makes it more challenging to predict how glaciers are going to respond to future climate change. Therefore, improved understanding of the scale and sources of this local variability is vital for future glacier projections in this region. The following section outlines the most recent understanding of the influence of different local controls on Himalayan glacier change signal, followed by a discussion of the key uncertainties that partly motivate the work in this thesis.

The topography and geometry controls most associated with variable glacier change are glacier elevation, surface slope and hypsometry (the distribution of ice with elevation) (e.g.

Racoviteanu *et al.*, 2015; Salerno *et al.*, 2017; Robson *et al.*, 2018). Studies have observed that glacier mass balance and area change have been strongly linked to glacier elevation. For example, in the Kanchenjunga-Sikkim region in the eastern Himalayas, glacier area change was significantly correlated with elevation range and median, minimum and maximum elevation (Racoviteanu *et al.*, 2015). In the Manaslu region in the central Himalayas, glaciers with more positive mass balances tended to have higher median elevations and smaller elevation ranges (Robson *et al.*, 2018). Moreover, mean elevation was strongly positively correlated with glacier mass balance across most HMA regions, apart from in the Nyainqentanglha, Karakoram and Pamir Alay regions (Brun *et al.*, 2019).

Local variability in glacier thinning rates and mass balance have also been attributed to the slope angle of the ablation zone, with the highest thinning rates on glaciers tending to occur where the surface slope of the ablation zone was shallowest (Pellicciotti *et al.*, 2015; Salerno *et al.*, 2017) and glaciers with shallower terminus slopes having more negative glacier-wide mass balances (Brun *et al.*, 2019). Glacier hypsometry is another control that has an important influence on glacier behaviour and glaciers with large and high elevation accumulation areas have higher velocities (Quincey *et al.*, 2009; Robson *et al.*, 2018) and more positive mass balances (King *et al.*, 2017; Robson *et al.*, 2018) than glaciers with more of their glacier mass at lower elevations.

One of the local controls that is most strongly linked to variability in the Himalayan glacier change signal is supraglacial debris (Scherler *et al.*, 2011b; Racoviteanu *et al.*, 2015; Ragettli *et al.*, 2016; Banerjee, 2017). This is because of the varying impact of debris on sub-debris ice melt, which means that sub-debris melt rates are enhanced relative to a debris-free glacier surface under very thin debris but increasingly inhibited under thicker debris (Østrem, 1959; Conway and Rasmussen, 2000; Nicholson and Benn, 2006; Reznichenko *et al.*, 2010; Banerjee, 2017). Research has shown that supraglacial debris alters the spatial patterns of glacier thinning, causing a mass balance inversion in the ablation zone, because thinning rates decrease towards the terminus where debris tends to be thickest (Ragettli *et al.*, 2016; Robson *et al.*, 2018). However, recent large-scale studies have shown that debris-covered and debris-free glaciers are thinning and losing mass at comparable rates (Ragettli *et al.*, 2016; Banerjee, 2017; Salerno *et al.*, 2017; Brun *et al.*, 2019). This has led to suggestions of a debris-covered glacier 'anomaly' (Pellicciotti *et al.*, 2015; Salerno *et al.*, 2017) whereby reduced melting from thicker debris on glacier tongues is compensated by enhanced melting at ice cliffs and supraglacial ponds, which commonly develop on debris-covered glaciers (Kääb *et al.*, 2012; Brun *et al.*, 2016; Watson *et al.*, 2016; Miles *et al.*, 2018). That said, there is some disagreement about whether melting from thermokarst features is sufficient to equal thinning rates on debris-free glaciers when scaled up to the entire ablation zone (Vincent *et al.*, 2016; Banerjee, 2017).

A glacier dynamics explanation has also been proposed for the similar thinning rates whereby the mass balance inversion on the lower part of the glacier causes a shallowing of the glacier surface gradient and reduced gravitational driving stress and glacier deceleration (Benn *et al.*, 2012; Dehecq *et al.*, 2018). Thinning rates on the tongue increase due to a reduction in ice flux from up-glacier and the glacier tongue eventually disconnects from the accumulation area (Rowan *et al.*, 2015). More recent modelling suggested that the influence of supraglacial debris on glacier thinning rates depended on the stage of the glacier’s response to climate forcing and that, at a more advanced stage of evolution, thinning rates on debris-covered glaciers start to exceed debris-free glaciers (Banerjee, 2017). This demonstrates the uncertainty surrounding the evolution of debris-covered glaciers on longer timescales and shows that predicting how debris-covered glaciers will respond to climate change, particularly at larger spatial scales, is still very challenging (Bolch *et al.*, 2019).

The development of glacial lakes is another important modulator of the response of glaciers to climate change. Lake-terminating glaciers tend to have more negative mass balances than land terminating glaciers (King *et al.*, 2017; Brun *et al.*, 2019) because of enhanced melting and calving around supraglacial ponds and proglacial lakes (e.g. Sakai *et al.*, 2000; Sakai *et al.*, 2009; Thompson *et al.*, 2012; Miles *et al.*, 2018). Furthermore, in contrast to debris-covered land-terminating glaciers, which tend to decelerate, develop shallower gradients and undergo the highest rates of thinning part way up the ablation zone, lake-terminating glaciers tend to develop steeper gradients and undergo maximum thinning and retreat at the terminus (King *et al.*, 2018).

2.6 Key uncertainties and future research directions

2.6.1 *Scale and sources of local glacier change variability*

While there has been a recent increase in research focused on explaining spatially variable glacier change in the Himalayas (e.g. Ragettli *et al.*, 2016; King *et al.*, 2017; Salerno *et al.*, 2017; Robson *et al.*, 2018; Brun *et al.*, 2019), there are still gaps in our understanding of the extent and sources of this local variability in glacier behaviour. Specifically, research investigating the controls on variable glacier behaviour at large, Himalayan-wide spatial scales, and using large samples of glaciers, have revealed significant complexity and heterogeneity in the glacier change signal (Scherler *et al.*, 2011b; Brun *et al.*, 2019), making the influence of individual local controls, such as supraglacial debris, challenging to identify within the broader noise (Brun *et al.*, 2019). A recent study showed that while local controls helped to explain heterogeneous glacier change across HMA, the relative influence of the controls varied spatially (Brun *et al.*, 2019). For example, supraglacial debris had a larger influence on glacier change in some regions of HMA than others (Brun *et al.*, 2019). Furthermore, studies that have conducted statistical analyses to test the influence of multiple local controls on glacier change have shown that investigated controls often only partially explained the variability in glacier behaviour (Salerno *et al.*, 2017; Brun *et al.*, 2019). Therefore, there is a need to increase our understanding of the local variability found in the Himalayan glacier change signal and to determine what is the 'normal' level of variability that models should expect when forecasting future Himalayan glacier change.

There is also limited research on how mass inputs from avalanching can be source of variability in the Himalayan glacier change signal (Brun *et al.*, 2019) due to the difficulty of quantifying avalanche inputs on to glaciers (Scherler *et al.*, 2011a; Laha *et al.*, 2017). Most research suggests that avalanche inputs should help maintain glacier mass balance (Rea *et al.*, 1999; Hughes, 2008), but a recent HMA-wide study that looked at the mass balance of glaciers with different sizes of avalanche contributing area, showed that the signal was not particularly strong and was negative in some places and positive in others (Brun *et al.*, 2019). Avalanche inputs are thought to be very important contributors to accumulation on some Himalayan glaciers (Laha *et al.*, 2017), prompting the need for more research on this component of glacier mass balance.

2.6.2 *Field data on the thermal regime of supraglacial debris*

Field data on the influence of supraglacial debris properties on glacier melt in the central Himalayas are limited to a small number of glaciers (Conway and Rasmussen, 2000; Nicholson and Benn, 2013; Rounce *et al.*, 2015; Chand and Kayastha, 2018). This is because obtaining field measurements in this high altitude region is expensive and logistically challenging. Surface energy-balance models have been developed to calculate sub-debris melt rates from a smaller number of more easily measureable variables, such as debris surface temperature and meteorological data (Nakawo and Young, 1982; Nicholson and Benn, 2006). These models make assumptions about the properties of supraglacial debris and how heat is transferred through the debris layer (Nicholson and Benn, 2006; Reid and Brock, 2010). However, the assumptions are based on a relatively limited number of Himalayan field data (Conway and Rasmussen, 2000; Nicholson and Benn, 2013; Rounce *et al.*, 2015) and some uncertainties remain about how the thermal regime of the debris varies with different thickness and physical properties, in different seasons in the year (including winter); and how these variations influence sub-debris melt rates. More data are needed to improve our understanding of how heat is transferred through the debris layer over a full year and how this influences glacier melt.

2.6.3 *Gap in the surge-type glacier record in the central Himalayas*

Surge-type glaciers undergo oscillatory periods of fast and slow velocities which are driven by internal instabilities associated with changing basal conditions (e.g. Meier and Post, 1969; Kamb, 1987; Jiskoot *et al.*, 1998; Murray *et al.*, 2003). Surge-type glacier dynamics are not directly linked to climate change and their behaviour can differ from non-surge type glaciers that are responding to climate change (e.g. surge-type glaciers might undergo terminus advance when the termini of non-surge type glaciers are retreating). This can lead to heterogeneous behaviour in glaciers that confuses the climate change signal when investigating glacier change at regional scales. As yet, no surge-type glaciers have been documented in the central Himalayas. However, a recent study suggested that surge-type glaciers tend to cluster in well-defined climatic envelopes (defined by air temperature and precipitation) and tend to have specific geometry (they were larger, longer and had shallower gradients than their normal glacier counterparts) (Sevestre and Benn, 2015). They used this information to model the distribution of surge-type glaciers around the world and the model predicted some surge-type glaciers in the central Himalayas (Sevestre and Benn, 2015). This suggests that there are surge-type glaciers in the central Himalayas that have not yet been identified. Further research in this area is important for two reasons. First, glacier surge-type behaviour is a potential source of local variability in the regional glacier change signal which could have important implications for local water resources and hazards. Second, surge-type glacier behaviour risks confusing the glacier response to climate change signal in this area. As such, there is a need to identify which glaciers are surge-type so that we can exclude them from studies examining the response of glaciers to climate forcing.

2.7 Summary

Himalayan glaciers have been losing area and mass and decelerating since the 1970s, in association with warming air temperatures across the region. This has important implications for regional water resources and the likelihood of glacial hazards. However, within these overall negative trends, there has been significant local variability in the recent Himalayan glacier change signal. This heterogeneity is thought to be driven by factors that are specific to individual glaciers, such as supraglacial debris and geometry. However, there are still large uncertainties in our understanding of the scale, as well as the sources, of this local variability. In particular, the level of variability in the glacier change signal that can be considered 'normal' is still not well-constrained, which makes it challenging to extract meaningful trends from the noise and presents a challenge for predicting how glaciers in the central Himalayas will respond to future climate forcing. This thesis aims to identify the characteristics of recent glacier change behaviour in the Annapurna Conservation Area (ACA), a region in the central Himalayas which has been under-researched compared with many other Himalayan regions, and put bounds on the local variability observed in the glacier change signal.

Chapter 3: Spatially variable glacier changes in the Annapurna Conservation Area, Nepal, 2000 to 2016

Lovell, A.M., Carr, J.R. & Stokes, C.R. 2019. Spatially variable glacier changes in the Annapurna Conservation Area, Nepal, 2000 to 2016. Remote Sensing, 11, 10.3390/rs11121452.

Author contribution: I conducted the data collection and analysis, led the paper development, wrote the text and designed the figures. Co-authors provided editorial input and guidance on the development of the research. The paper has been published in Remote Sensing and the supplementary information from the paper has been incorporated into the thesis chapter.

Abstract: Himalayan glaciers have shrunk rapidly in recent decades, but the spatial pattern of ice loss is highly variable and appears to be modulated by factors relating to individual glacier characteristics. This hinders our ability to predict their future evolution, which is vital for water resource management. The aim of this study is to assess recent glacier changes in the little-studied Annapurna Conservation Area (ACA; area: 7629 km^2) in Nepal and to explore local controls influencing their behaviour. We map changes in glacier area, surface elevation and ice flow velocity on a large sample of glaciers (n = 162) in the ACA between 2000 and 2016. We found that total glacier area decreased by 8.5% between 2000 and 2014/15. Ice surface velocity changes between 2002 and 2016 were variable with no clear trend of acceleration or deceleration. Mean surface elevation change for a smaller sample of glaciers (n = 72) was -0.33 ± 0.22 m a^{-1} between 2000 and 2013/16, which equates to a mean mass balance of -0.28 ± 0.24 m w.e. a^{-1}. There was a trend of increasingly less negative mass balance towards the north. Glaciers with bottom- and very bottom-heavy hypsometry lost more mass than glaciers with top-heavy hypsometry. Glaciers that lost the most mass in the north of the ACA tended to have lower maximum elevations and were more likely to be avalanche-fed. However, these patterns were not apparent in glaciers in central ACA. Supraglacial debris influenced the spatial patterns of glacier thinning, resulting in inverted mass balance gradients on the ablation zones of some glaciers. Our work shows that glaciers in the ACA are losing area and mass at variable rates but that the

influence of local controls is complex, which introduces large uncertainties when predicting their future evolution.

3.1 Introduction

Glaciers in High Mountain Asia (HMA) are an important component of the global cryosphere (Bolch *et al.*, 2012). Many of these glaciers have lost mass and area and have decelerated over the last few decades in response to climate change (e.g. Bolch *et al.*, 2012; Kääb *et al.*, 2012; Azam *et al.*, 2018; Dehecq *et al.*, 2018), consistent with global trends (Zemp *et al.*, 2019). For example, recent glacier mass balance estimates for HMA were -0.14 ±0.08 m w.e. a^{-1} from 1999 to 2011 (Gardelle *et al.*, 2013), -0.18 ±0.04 m w.e. a^{-1} from 2000 to 2016 (Brun *et al.*, 2017), and -0.21 ±0.05 m w.e. a^{-1} from 2003 to 2008 (Kääb *et al.*, 2012). However, there are broad regional spatial variations in mass balance across HMA: the central and eastern Himalayas (Figure 1.1) show moderate mass losses (-0.22 to -0.33 m w.e. a^{-1}); the western Himalayas have the highest rates of loss (-0.45 to -0.55 m w.e. a^{-1}); and the Karakoram and Pamir (Figure 1.1) are in balance or even showing mass gains (-0.03 to +0.14 m w.e. a^{-1}) (Kääb *et al.*, 2012; Gardelle *et al.*, 2013). These east to west gradients in ice loss are thought to reflect the greater influence of the Indian and East Asian monsoons in the central and eastern Himalayas, versus the prevailing Mid Latitude Westerlies, which provide precipitation for glaciers in the northwest mountain ranges (Yao *et al.*, 2012; Palazzi *et al.*, 2013). In general, glacier area change and mass loss also show north-south variation, due to the sharp orographic precipitation gradient over the Himalayas, caused by the mountains acting as a barrier to the southerly Indian monsoon winds (Shrestha *et al.*, 1999; Bookhagen and Burbank, 2006; Azam *et al.*, 2014; Thakuri *et al.*, 2014). Nonetheless, the impact of this gradient seems to be variable: some studies observe more positive mass balances (Robson *et al.*, 2018), higher velocities (Kääb, 2005) and smaller retreat rates (Kääb, 2005) in the northern Himalayan glaciers compared with southern ones (Kääb, 2005; Robson *et al.*, 2018). However, in the Everest region (Figure 1.1), larger surface lowering rates were observed on glaciers flowing into the Tibetan Plateau, on the north side of the mountain range, compared with glaciers in the southern part of the region (King *et al.*, 2017).

Despite these overall trends relating to climatic gradients, glacier mass loss, area loss and velocity also vary within regions, within catchments, and between neighbouring glaciers (Scherler *et al.*, 2011b; Kääb *et al.*, 2012; Pellicciotti *et al.*, 2015; Racoviteanu *et al.*, 2015;

King *et al.*, 2017; Salerno *et al.*, 2017). This has been attributed to controls specific to individual glaciers, including glacier surface gradient (Pellicciotti *et al.*, 2015; Salerno *et al.*, 2017), glacier elevation (Ojha *et al.*, 2016; Robson *et al.*, 2018), hypsometry (glacier area distribution with elevation) (Kääb, 2005; Quincey *et al.*, 2009; Robson *et al.*, 2018), avalanche inputs (Laha *et al.*, 2017), and supraglacial debris (Gardelle *et al.*, 2013; Pellicciotti *et al.*, 2015). However, this smaller-scale variability is often poorly captured by Himalayan-wide studies, which limits our ability to predict changes in ice volume in the Himalayas and to understand how glaciers will respond to near-future climate change (Kääb *et al.*, 2012; Gardelle *et al.*, 2013). This is important for forecasting cryospheric contributions to water resources, as these glaciers feed into the Indus, Brahmaputra and Ganges river catchments (Figure 1.1) that support ~800 million people (Bolch *et al.*, 2012). Glacier melt helps to maintain baseflows in these catchments outside of the monsoon, reducing the impact of seasonal precipitation variations on discharge (Immerzeel *et al.*, 2010; Bolch *et al.*, 2012; Rowan *et al.*, 2018). A better understanding of how glaciers will respond to climate change will also improve our ability to predict the likelihood of these glaciers generating hazards, particularly the formation and growth of glacial lakes, which can cause high magnitude floods if they break through their moraine dams (Quincey *et al.*, 2007; Rounce *et al.*, 2017).

The Annapurna Conservation Area (ACA) is 160 km northwest of Kathmandu and 30 km north of Pokhara (Figure 1.2). The ACA contains the Annapurna Himal in the south, the Muktinath Himal in the centre and the Damodar Himal in the north (Figure 1.2). These upland areas host more than 170 summer accumulation-type glaciers with varying geometry, hypsometry and supraglacial debris cover (Figure 1.2). The region also extends across a sharp south to north orographic divide and precipitation gradient, with mean annual rainfall ranging from >4 m a^{-1} in the south to <0.5 m a^{-1} in the north (Bookhagen and Burbank, 2010), and is characterised by highly variable topography and elevation, including several mountains over 7000 m asl (Figure 1.2). This makes it an excellent location to investigate the influence of local controls on recent glacier change.

The behaviour (area, surface elevation and velocity changes) of these glaciers has not previously been studied in detail, although hypsometry-driven spatially variable glacier behaviour has been inferred from palaeoglaciology research on the south side of the Annapurna Himal (Pratt-Sitaula *et al.*, 2011). However, glaciers in the ACA covered an area of almost 500 km^2 in 2000 (Table 3.1) and therefore constitute a substantial component of the central Himalayan ice mass which is currently poorly represented in studies of glacier behaviour and mass loss. The ACA glaciers also feed rivers flowing into Pokhara, a large city and tourist hub in Nepal (population ~400 000; Figure 1.2), and therefore contribute to local water resources. Thus, it is crucial to document regional-scale ice losses and their spatial variability. To address this knowledge gap, the objectives of this study are to: (1) investigate recent glacier change between 2000 and 2016 on a large sample of glaciers in the ACA using a range of satellite datasets including Landsat 7 and 8, Shuttle Radar Topography Mission (SRTM), Satellite Pour l'Observation de la Terre (SPOT) 7 and High Mountain Asia (HMA) DEMs; and (2) assess how individual glacier controls (e.g. geometry, hypsometry and supraglacial debris) influence spatial variations in area change and mass loss in the region. This is the first study to simultaneously investigate changes in area, surface elevation and velocity in the ACA and provides a comprehensive picture of recent glacier behaviour in the region.

3.2 Methods

3.2.1 *Data sources and acquisition*

The remotely sensed datasets used in this study are summarised in Table 3.1. We focus on glacier changes between 2000 and 2016 because satellite datasets in this period have greater spatial and temporal resolution, which allows us to measure several glacier variables (e.g. changes in glacier area, surface elevation and ice flow velocity) over a comparable period. A Landsat 7 Enhanced Thermal Mapper Plus (ETM+) scene from 2000 and a Landsat 8 Operational Land Imager (OLI) and Thermal Infrared Sensor (TIRS) scene (2015) from the US Geological Survey (USGS: https://earthexplorer.usgs.gov/) were used to map glacier area changes over the study period (Table 3.1). A Landsat 8 scene from 2014 was used to map a small number of glaciers (n = 10 or 6% of glaciers) that were obscured by shadow in the 2015 scene. The similarity of the time of year between the 2000 and 2015 scenes (14 days apart in December) minimises the effect of seasonal variability. Two Landsat 7 scenes taken in January and December in 2002 and two Landsat 8 scenes from January and December in 2016 were used to calculate glacier surface velocities (Table 3.1). We selected imagery from 2016 for the velocity measurements, rather than 2015, because the image pairs had an appropriate interval for feature tracking (<1 year apart; see Section 3.2.4). All Landsat scenes were chosen because they were cloud-free and had minimal snow-cover.

The non-void-filled 1 Arc-Second Global SRTM digital elevation model (GDEM: USGS) from 2000, was used as the reference elevation dataset in this study because it had the most comprehensive coverage of the study area of any dataset. The absolute geolocation accuracy of the SRTM DEM in Eurasia is 8.8 m and the absolute vertical accuracy is 6.2 m (90% confidence) (Farr *et al.*, 2007) but in some areas it has been shown to be even more accurate (Becek, 2008). An Advanced Spacebourne Thermal Emission and Reflection Radiometer (ASTER) 14 DEM from 2000 (USGS) was used to fill in a large data void over glacierised areas in the Annapurna Himal in the SRTM GDEM, after correcting the DEMs (see Section 3.2.3.2.), to conduct DEM differencing over this area. This DEM was derived from the closest appropriate ASTER scene to the SRTM capture date (Table 3.1). Four HMA 8 m resolution DEMs (from the National Snow and Ice Data Centre: https://nsidc.org/data/highmountainasia) (Shean *et al.*, 2016) were acquired for recent surface elevation datasets. These were chosen for their proximity to 2015 and ranged from 2013 to 2016 (Table 3.1). The HMA DEMs are automatically generated from very-high resolution satellite imagery using NASA Ames Stereo Pipeline open source software (https://ti.arc.nasa.gov/tech/asr/groups/intelligent-robotics/ngt/stereo/) and have a geolocation accuracy of <5 m CE90/LE90 (Circular/Linear Error at a confidence level of 90%) (Shean *et al.*, 2016). Two pairs of 1.5 m resolution SPOT 7 stereo images from 2015 and 2016 (Table 3.1), from the European Space Agency (ESA), were used to create two additional relative 8 m DEMs to fill in voids in the HMA DEMs. Some voids remained in the SRTM DEM, even after filling in with the ASTER DEM. Therefore, glacier hypsometry, gradient and avalanche contribution area were derived from an additional SRTM DEM with all voids filled in with 1:50,000 topographic maps of Nepal, available pre-processed online at Viewfinder Panorama DEMs (http://viewfinderpanoramas.org/) (De Ferranti, 2012; Robson *et al.*, 2018). This version of the SRTM DEM was not used to calculate surface elevation changes because the topographic maps used to fill in the DEM were not from a specific date.

Table 3.1: Summary of the datasets used in this study. A = glacier area, FSCM = firn, snow and clean ice mask, SE = glacier surface elevation, V = glacier velocity, T = topographic controls.

Dataset name	**Date**	**Sensor**	**Spatial resolution (m)**	**Purpose**
LE71420402000350SGS00	15/12/2000	Landsat 7 ETM+	15 to 30	A
LC81420402014284LGN00	11/10/2014	Landsat 8 OLI	15 to 30	A
LC81420402015335LGN00	01/12/2015	Landsat 8 OLI	15 to 30	A
ALOS GLOBAL DSM	Multiple	PRISM	30	A
LE07_L1TP_142040_20001215_20170208_01_T1_sr	15/12/2000	Landsat 7 ETM+	15 to 30	FSCM
SRTM Global DEM non void-filled	11/02/2000 to 22/02/2000	SRTM	30	SE
AST14DEM_00312152000052420	15/12/2000	ASTER	30	SE
HMA_DEM8m_AT_20131120_0508_1020010028D38100	20/11/2013	Worldview-1 panchromatic	8	SE
HMA_DEM8m_AT_20140119_0459_102001002B466800	19/01/2014	Worldview-1 panchromatic	8	SE
HMA_DEM8m_AT_20151001_0511_104001001299E800	01/10/2015	Worldview-3 panchromatic	8	SE
IMG_SPOT7_P_001_A : SPOT 7 2015-10-20:04:30:48.6 SENSOR P	20/10/2015	SPOT 7 NAOMI	1.5	SE
IMG_SPOT7_P_001_C : SPOT 7 2015-10-20:04:31:25.1 SENSOR P	20/10/2015	SPOT 7 NAOMI	1.5	SE
IMG_SPOT7_P_001_A : SPOT 7 2016-02-25:04:47:49.9 SENSOR P	25/02/2016	SPOT 7 NAOMI	1.5	SE
IMG_SPOT7_P_001_B : SPOT 7 2016-02-25:04:48:21.2 SENSOR P	25/02/2016	SPOT 7 NAOMI	1.5	SE
HMA_DEM8m_AT_20161012_0518_103001005E9D8C00	12/10/2016	Worldview-2 panchromatic	8	SE
LE71420402002003SGS00	03/01/2002	Landsat 7 ETM+	15 to 30	V
LE71420402002339SGS00	05/12/2002	Landsat 7 ETM+	15 to 30	V
LC81420402016002LGN00	02/01/2016	Landsat 8 OLI	15 to 30	V
LC81420402016354LGN00	10/12/2016	Landsat 8 OLI	15 to 30	V
SRTM Global DEM void-filled	Multiple	SRTM	30	T

3.2.2 *Glacier area change*

The Annapurna Himal, Muktinath Himal and Damodar Himal upland areas in the ACA (Figure 1.2) span a sharp south (wetter) to north (drier) orographic precipitation gradient (Bookhagen and Burbank, 2010), which might be expected to influence glacier response

(Kääb, 2005; King *et al.*, 2017). We therefore analyse glacier changes in these sub-regions separately to assess the influence of this gradient on glacier change. One glacier previously identified as surge-type (Sabche Glacier, Global Land Ice Measurements from Space - GLIMS ID: G084014E28561N: Figure 1.2), is excluded from the study because its behaviour is driven by internal instabilities that are not directly related to climate forcing (Lovell *et al.*, 2018b). For simplicity, we developed our own numbering system for unnamed glaciers in the ACA. However, the GLIMS IDs for glaciers in this study are included in Appendix A, for reference.

Total glacier area in 2000 and 2015 was mapped using a semi-automated technique in *Esri ArcMap 10.5*. Debris-free glacier areas were mapped using a ratio of the Red (wavelengths: 0.63-0.69 for Landsat 7 and 0.636-0.673 for Landsat 8) and Near Infrared (NIR; wavelengths: 0.77-0.90 for Landsat 7 and 0.851-0.879 for Landsat 8) spectral bands (TM3/TM5) with a threshold value of 2 (Racoviteanu *et al.*, 2009; Paul *et al.*, 2015). We chose this method because it is less time-consuming than manual digitising and because of its high accuracy in similar environments (e.g. Paul *et al.*, 2013). However, we verified the accuracy of each glacier outline derived from the band ratio method visually against the Landsat scenes and edited errors manually. The spectral signature of supraglacial debris is very similar to the surrounding glacier-free terrain and therefore the boundary between debris-covered glacier area and non-glacierised terrain is not clearly identifiable using a band ratio method (Paul *et al.*, 2015). Instead, we mapped debris-covered glacier areas by deriving slope and plan and profile curvatures (Alifu *et al.*, 2015) from the Advanced Land Observing Satellite (ALOS) Global DEM (Japan Aerospace Exploration Agency: https://www.eorc.jaxa.jp/ALOS/en/aw3d30/index.htm) and applying a cluster analysis to the results using *SAGA 2.3.2* software (http://www.saga-gis.org/en/index.html) (Bhambri *et al.*, 2011a). Debris-free and debris-covered glacier areas were combined and edited manually during post processing, using the Landsat imagery for reference. Ten glaciers (6% of mapped glaciers), which were partially obscured by shadow in the 2015 scene, were manually digitised using a Landsat 8 OLI TIRS scene from 11th October 2014 (marked in red in Appendix A). We could not map several glaciers (n = 18, 10%) in the ACA due to consistent shadows caused by topography in the satellite imagery. We calculated absolute total glacier area change (km^2) and percentage total glacier area change (%) for a sample of 162 glaciers (90% of the glaciers in the ACA), which were clearly visible in both measurement years.

3.2.3 *Surface elevation change and mass balance*

3.2.3.1 *SPOT DEM generation*

We generated the 2015 and 2016 SPOT DEMs in *Erdas Imagine 2018 Photogrammetry Suite* using the rational polynomial coefficients (RPCs) included with each stereo scene. Each pair of stereo scenes was tied together with ~100 tie points to minimise the triangulation model root mean square error (RMSE: 0.07 pixels for the 2015 DEM and 0.09 pixels for the 2016 DEM). The output spatial resolution of the generated DEMs was 8 m. The SPOT DEMs were relative DEMs, rather than absolute DEMs, because ground control points (GCPs) were not used in their generation. However, this was deemed sufficient for this study because we assess relative changes only. The geolocation accuracy of SPOT DEMs generated without GCPs is <18 m CE90. This is less than the spatial resolution of the SPOT DEMs once resampled to the 30 m reference 2000 SRTM DEM.

3.2.3.2 *Digital elevation model correction*

To quantify surface elevation change, all DEMs, including the SPOT DEMs, had to be co-registered and corrected to the reference DEM (SRTM DEM), which was chosen as the reference due to its wide spatial coverage (Nuth and Kääb, 2011; Berthier *et al.*, 2014). Prior to co-registration and correction, obvious interpolation artefacts (e.g. spikes and holes) in all DEMs were identified using hill-shade models and removed (Robson *et al.*, 2018). We then resampled all DEMs to 30 m spatial resolution to match the SRTM DEM. Following this, all DEMs were corrected following the 3-step correction procedure by Nuth and Kääb (2011). This included horizontally and vertically co-registering DEMs to the SRTM DEM by minimising the RMSE of the elevation differences between each DEM pair on stable, glacier-free areas and checking for, and correcting, elevation-dependent biases and satellite acquisition biases (Nuth and Kääb, 2011). All DEMs were co-registered separately to the SRTM DEM, apart from the ASTER DEM which was co-registered to the 2016 SPOT DEM (Table 3.2) because of a large data void in the SRTM DEM. The mean, standard deviation and normalised median absolute deviation (NMAD, a measurement of data dispersion which is less sensitive to outliers) (Berthier *et al.*, 2014) of elevation differences on stable off-glacier terrain were calculated for each DEM, before and after correction. These are summarised in Table 3.2.

The SRTM DEM was corrected for C-band penetration into snow and ice (Kääb *et al.*, 2012). A correction of +2.3 m was applied over areas of firn and snow and +1.7 m over clean ice, based on correction values for West Nepal used by Kääb *et al.* (2012: see their Table S2) which they tested against ICESat elevation data (Kääb *et al.*, 2012). A band ratio of (TM4×TM2)/TM5 with a threshold of 200 was used to separate firn and snow areas from clean ice areas using a Landsat 7 ETM+ surface reflectance product (Table 3.1), following methods by Kääb *et al.* (2012).

Table 3.2: DEM correction and uncertainties. The shifts in the x,y and z directions to co-register each DEM to the SRTM with the exception of the ASTER14DEM which was co-registered to the SPOT7 Lower DEM, the mean, standard deviation and NMAD of the off-glacier stable terrain before and after DEM correction and the uncertainty calculated for each DEM of difference.

	Co-registration shifts				**Before correction**			**After correction**			
Imagery name	**x**	**y**	**z**	**Pixel sum**	**Mean (m)**	**SD (m)**	**NMAD (m)**	**Mean (m)**	**SD (m)**	**NMAD (m)**	**dh/dt uncertainty (±m a^{-1})**
AST14DEM_0031215 2000052420	-27.69	5.44	37.82	180717	-42.00	28.55	21.41	0.00	23.46	16.66	0.97
HMA_DEM8m_AT_ 20131120_0508	1.79	-3.34	34.12	682731	-34.48	9.75	6.95	0.00	9.50	6.20	0.23
HMA_DEM8m_AT_ 20140119_0459	4.22	-4.44	34.69	756258	-35.33	13.76	7.38	0.09	13.61	7.17	0.23
HMA_DEM8m_AT_ 20151001_0511	4.67	-2.62	29.65	141775	-30.16	7.55	5.32	-0.51	7.55	5.32	0.33
SPOT7_UPPER_DEM	2	-7.02	32.55	391993	-32.26	10.25	6.95	0.29	10.25	6.95	0.34
SPOT7_LOWER_DEM	4.88	-1.8	18.82	617871	-18.43	11.01	8.75	0.00	10.86	8.73	0.77

3.2.3.3 *DEM differencing and post-processing*

Elevation change maps were created by differencing the corrected DEMs from the SRTM DEM. The ASTER DEM was differenced from the 2016 SPOT DEM (Figure 3.1) because of a large data void in the SRTM DEM. Glaciers with surface elevation changes derived from the ASTER and SPOT DEMs were excluded from the calculation of mean surface elevation change for the region and analysed separately, due to the different 2000 data source. We divided the elevation changes by the interval (in years) between the two DEMs to get an annual surface elevation change rate in m a^{-1}. Unrealistic surface elevation changes, classified as pixels that exceeded ±120 m a^{-1}, were removed following methods by King *et al.* (2017). These pixels were scattered across the study area and tended to be located in areas of very steep terrain and probably resulted from the larger errors that occur on steeper slopes during DEM generation (Toutin, 2002). However, these pixels amounted to <1% of total pixels. In addition, we filtered the elevation change data for outliers, defined as a pixel with a mean value that was more than three standard deviations away from the mean of the surrounding pixels in a moving 21 × 21 pixel (~600 × 600 m) window. We chose this kernel size because it provided the best balance between removing outliers and not removing real (but large) surface lowering values on the glacier tongues. Although the glacier surface elevation changes are derived from elevation difference maps spanning a range of intervals (2000 to 2013-2016), we analysed the data together after converting the surface elevation changes to a rate (in m a^{-1}) to gain the most complete picture of regional elevation change possible, given the limited data availability. The footprints and intervals of the elevation difference maps are shown in Figure 3.1.

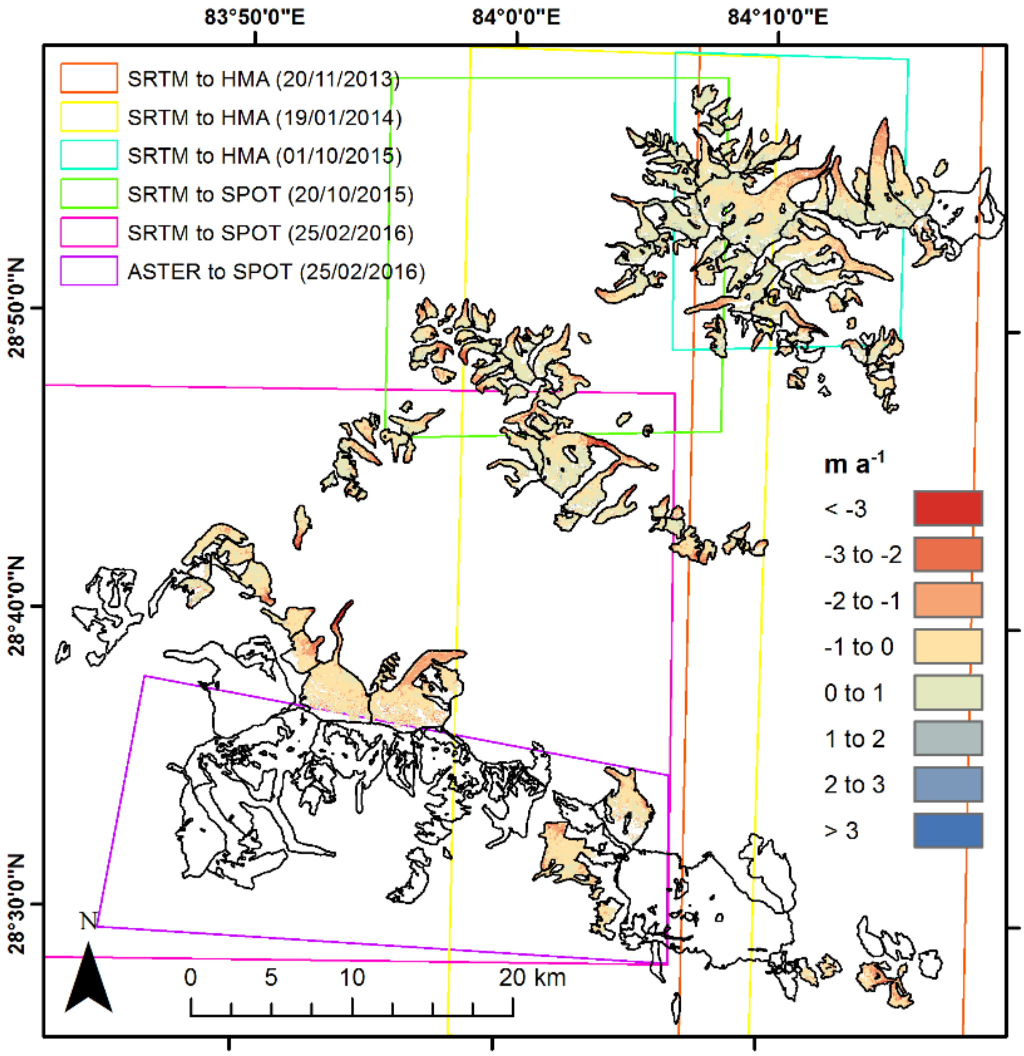

Figure 3.1: Footprints of the different DEM difference maps and surface elevation changes (2000 to 2013/16).

Voids in the surface elevation change data, derived from gaps in the HMA DEMs and the removal of obvious DEM errors and outliers, were filled in to estimate glacier mass balance. Small voids in the elevation change data were filled using the Elevation Void Fill function in ArcMap which uses an inverse distance weighted algorithm and plane fitting to fill in small holes (<2×2 pixels) (Ragettli *et al.*, 2016). Larger voids (>2×2 pixels) were filled using mean elevation change for the 100 m elevation band in which the pixel was located (Gardelle *et al.*, 2013). An example workflow of DEM correction, outlier filtering and void filling is provided in Figure 3.2. Glaciers with voids equating to more than 10% of total glacier area prior to infilling, and glaciers with surface elevation changes derived from the ASTER and SPOT DEMs were excluded from mass balance calculations. After removing glaciers with missing data, a final sample of 72 glaciers (41% of the glaciers in the ACA) was used to calculate glacier mean surface elevation change and geodetic mass balance. The glaciers in this smaller sample span a range of sizes and elevations (Figure 3.9). However, the majority of these glaciers are in the Muktinath Himal and the Damodar Himal with only three in the Annapurna Himal. This means they are not fully representative of the ACA and we focus on the Damodar Himal and Muktinath Himal when interpreting our mass balance results. Geodetic mass balance was calculated from the filled surface elevation change data, assuming an ice density of 850 kg m^{-3} to convert volume change to mass balance (Huss, 2013).

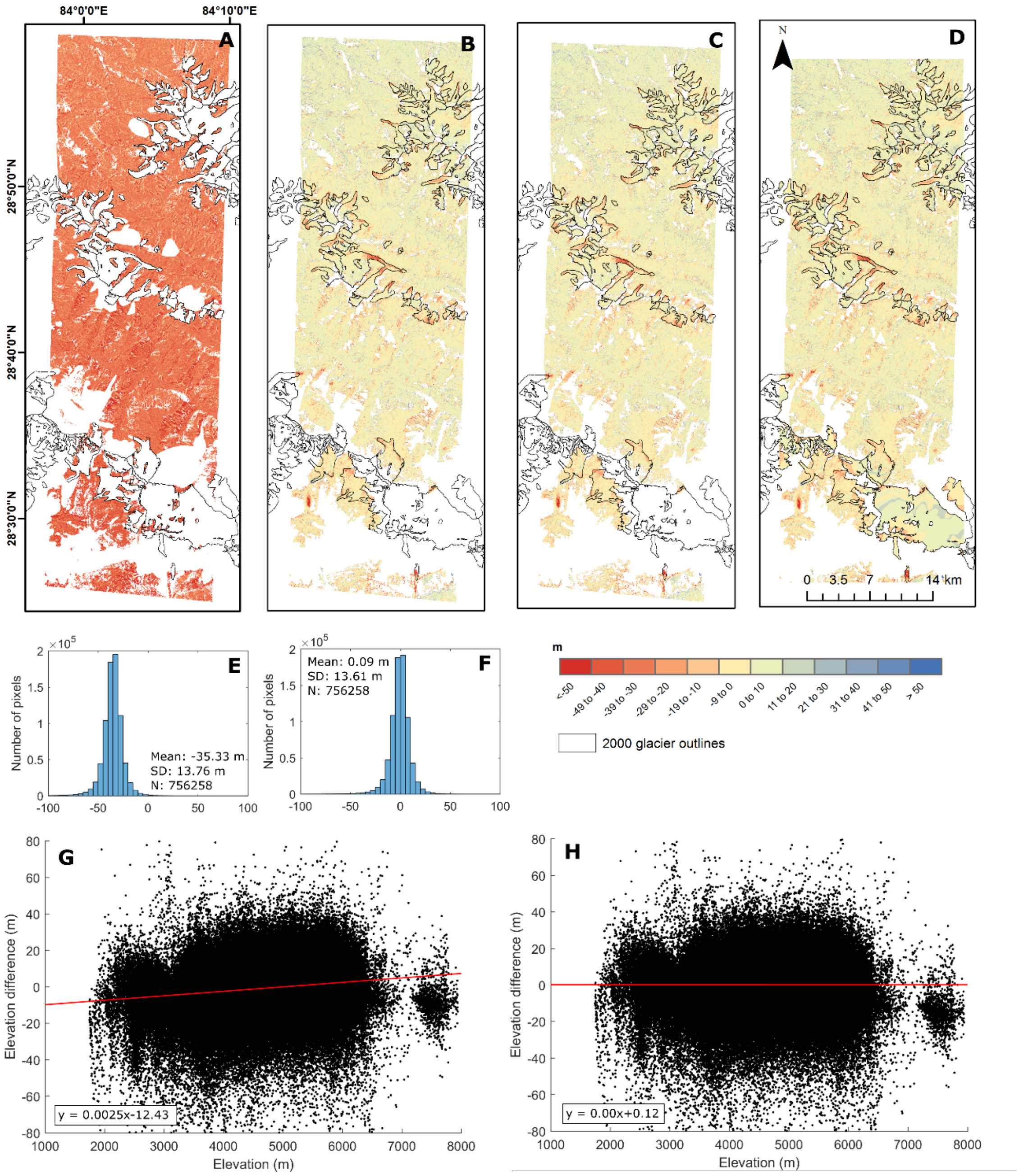

Figure 3.2: Example workflow to correct, filter and fill the surface elevation difference maps using the surface elevation difference map derived from the SRTM GDEM and the HMA_DEM8m_AT_20140119_0459 DEM. A) Elevation differences on stable terrain prior to co-registration and correction, B) after co-registration and correction, C) after filtering, D) after filling, E) off-glacier statistics of surface elevation difference on stable terrain before correction and F) after correction, G) elevation difference plotted against elevation on stable terrain where the trend-line shows an elevation-dependent bias and h) elevation difference plotted against elevation on stable terrain after the elevation-dependent bias has been corrected.

3.2.4 *Glacier surface velocity*

Surface displacement maps in the north/south and east/west directions were generated from pairs of Landsat panchromatic scenes from 2002 and 2016 (Table 3.1) using *COSI-Corr* software (http://www.tectonics.caltech.edu/slip_history/spot_coseis/download_software.html) (Sam *et al.*, 2015). Noise was filtered out by removing pixels with a signal-to-noise ratio <0.9 (Scherler *et al.*, 2008), and striping in the correlation maps inherited from the source imagery was removed using the software's in-built de-striping tool. Annual displacements were calculated and then converted to absolute velocity using Pythagoras theorem. An additional magnitude and direction filter was applied to the data by removing displacement vectors that varied in magnitude or direction by more than 30% from the mean value in a 3 ×3 pixel (90 × 90 m) moving window filter (Robson *et al.*, 2018). Any remaining correlation mismatches due to snow, cloud cover and shadow were identified by cross-referencing the velocity maps with the original imagery and removed manually. The velocity processing workflow is shown in Figure 3.3. The remotely sensed velocities measured on the lower half of the Annapurna South glacier tongue in 2016 (ranging from 0 to 21 m a^{-1}), were very similar to stake velocity measurements we obtained in the field in the same area between October 2016 and October 2017 (Lovell *et al.*, 2018a), providing us with confidence in the accuracy of our data. Due to voids in the data in both years, it is not possible to quantify area averaged velocity change. However we make qualitative observations of velocity change between the two years.

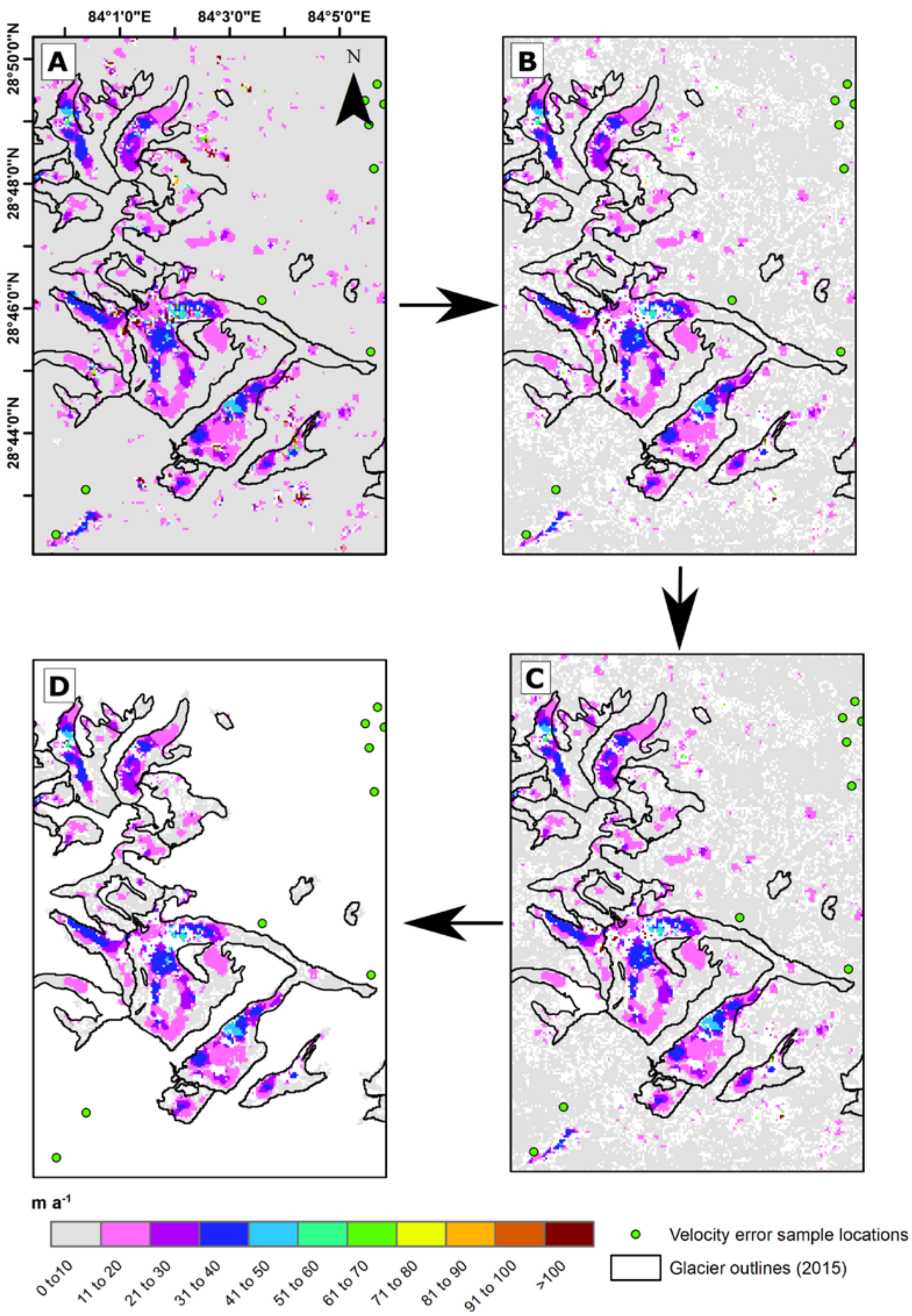

Figure 3.3: Surface velocity processing workflow, A) shows the velocities before post-processing, B) velocities after the magnitude and direction filter was applied, C) velocities after additional manual editing was applied and D) final velocity map. Glacier outlines from 2000.

3.2.5 *Quantification of uncertainties*

To estimate glacier area measurement uncertainty, we manually digitised a random sample of 10 debris-free and 10 debris-covered glaciers in the ACA five times and compared the variation (standard deviation) in area between each outline, following Paul *et al.* (2013). The variation between digitised outlines for individual glaciers ranged from <1% to 5% (Table 3.3) and the mean variation was 2%. The same individual digitised all of the glaciers to ensure consistency in glacier interpretation (Paul *et al.*, 2013).

Table 3.3: The variation (standard deviation) of repeat digitised glacier outlines for 10 debris-free and 10 debris-covered glaciers, selected at random.

Glacier	**Debris covered**	**Area (km2)**	**Std (%)**
Kawache	Y	0.40	1.75
KG003	N	1.81	4.25
KG005	Y	7.68	2.51
KG016	Y	7.22	0.56
KG033_1	N	0.16	1.43
KG040	N	0.45	5.13
M002	Y	4.31	0.85
M003	Y	17.35	0.43
M005_2	N	0.30	0.66
M008	Y	6.59	1.80
M011	N	1.29	2.50
M017	Y	2.26	1.56
M024	N	1.78	0.54
M025	N	0.30	1.60
M042_1	N	0.93	1.26
M045	N	2.85	0.53
M063	Y	2.35	4.00
M100	N	0.25	2.37
MSM002	Y	0.83	2.64
MSM023	Y	1.75	0.93
Mean			**1.87**

Glacier surface elevation change uncertainty was estimated for each elevation difference map using the standard error (*SE*; standard deviation of mean elevation change) of each 100 m elevation band combined with error estimates for the C-band penetration and seasonal variation (Gardelle *et al.*, 2013; Ragettli *et al.*, 2016; King *et al.*, 2017; Robson *et al.*, 2018).

The standard error per 100 m elevation band was calculated by

$$SE = \frac{SD_{STABLE}}{\sqrt{N}} \tag{3.1}$$

where SD_{STABLE} is the standard deviation of stable terrain for each elevation band and N is the effective number of observations, calculated by

$$N = \frac{N_{tot} \times PS}{2d} \tag{3.2}$$

where N_{tot} is the total number of pixels, *PS* is pixel size and *d* is the spatial autocorrelation distance for which we used the value 600 m, following Bolch *et al.* (2011) and King *et al.* (2017). We excluded elevation bands with fewer than 100 pixels because these added a strong bias to the uncertainty estimates. The total standard error per elevation change map is the sum of *SE*.

Additional errors associated with C-band penetration (wavelength: ~5.6 cm; frequency: 5.7 GHz) (Rignot *et al.*, 2001; Gardelle *et al.*, 2013) and seasonal variation were 1.5 m and 0.15 m w.e. per winter month, respectively (Gardelle *et al.*, 2013; Robson *et al.*, 2018). These three uncertainty elements were summed quadratically (King *et al.*, 2017) to give a final glacier surface elevation uncertainty per elevation difference map, summarised in Table 3.2. We also calculated uncertainty per glacier by weighting the error per elevation band by the hypsometry of each glacier (Ragettli *et al.*, 2016; Robson *et al.*, 2018). This means that each glacier has an individual error which takes into account the glacier's specific area-altitude distribution and the spatial variation of uncertainty (Appendix A). DEM uncertainty tends to increase with elevation and therefore glaciers at higher elevations have larger errors to reflect this (Ragettli *et al.*, 2016).When converting from volume to mass balance, an additional 7% error was added to account for uncertainty associated with the density conversion factor (Huss, 2013).

We estimated glacier velocity uncertainty from ~200 points randomly selected on areas of stable terrain (vegetated, shallow slope) across the region (locations are shown in Figure 3.4). The mean velocity error was 4.32 m a^{-1} for 2002 and 2.07 m a^{-1} for 2016 (Table 3.4).

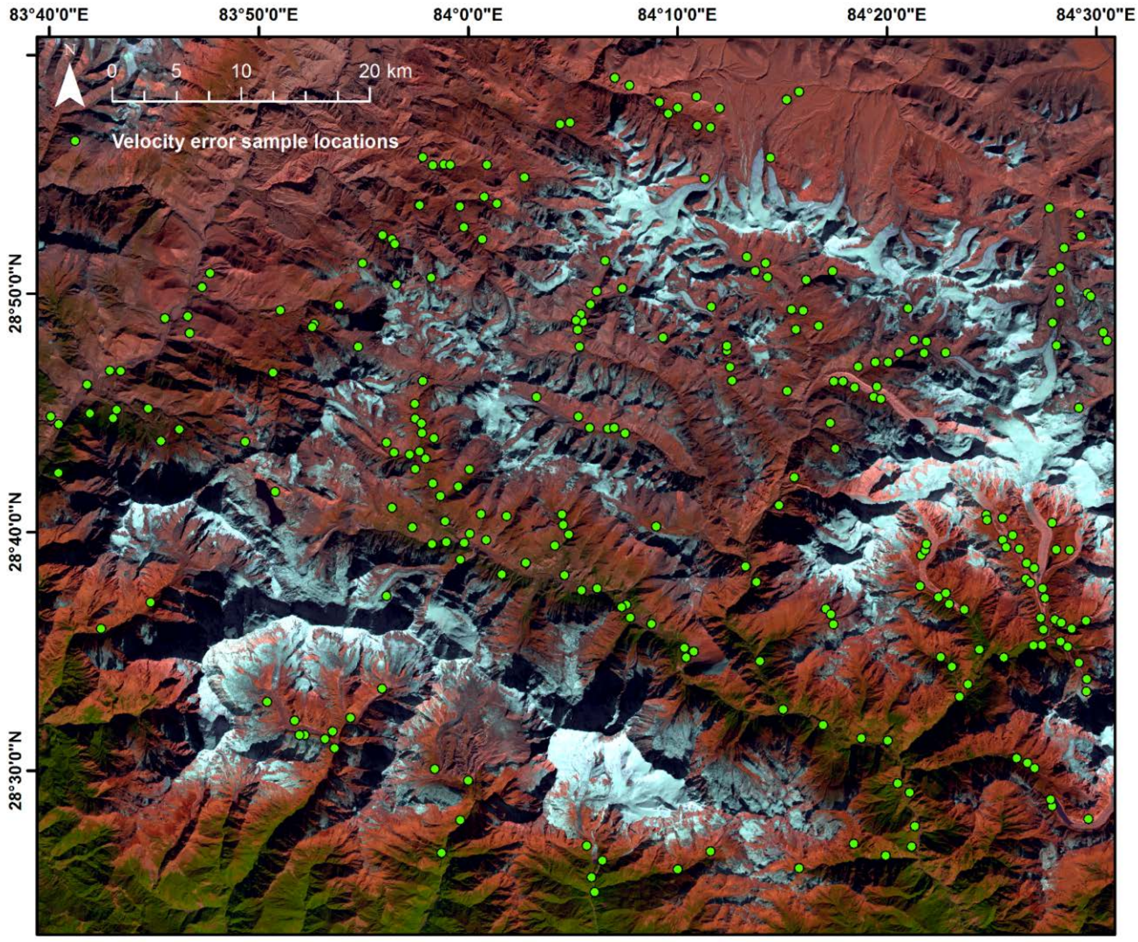

Figure 3.4: Velocity error sampling point locations.

Table 3.4: The mean and standard deviation of point-sampled velocities on stable terrain (vegetated and with shallow slopes) in the ACA for the 2002 and 2016 velocity maps and the number of points sampled in each map. The disparity in the number of sampled points between the maps is due to the pre-determined points coinciding with data voids in one or other of the maps.

Interval	Mean velocity error (m a^{-1})	St dev (m a^{-1})	Number of sampling points
03/01/2002 to 05/12/2002	4.32	4.08	177
02/01/2016 to 10/12/2016	2.07	2.49	251

3.2.6 *Topographic controls*

Glacier hypsometry (distribution of glacier area with elevation) has been identified as a control on glacier change rates (Jiskoot *et al.*, 2009; Robson *et al.*, 2018). Hypsometric curves were calculated for each glacier, using the 2000 glacier outlines, by dividing the glacier area into 100 m elevation bands, based on the filled in SRTM DEM, and calculating the area per elevation band. A hypsometric index, to categorise the glaciers into different hypsometry types, was subsequently calculated based on Jiskoot *et al.* (2009) by

$$\mathrm{HI} = \frac{H_{max} - H_{med}}{H_{med} - H_{min}} \tag{3.3}$$

where $H_{\max}$ is the maximum glacier elevation, $H_{\min}$ is the minimum glacier elevation and H_{med} is the median glacier elevation.

Following this,

$$\text{if } 0 < \mathrm{HI} < 1 \text{ then } \mathrm{HI} = \frac{-1}{\mathrm{HI}} \tag{3.4}$$

The indices were characterised into very top-heavy (HI < -1.5), top-heavy (-1.5 < HI < -1.2), equidimensional (-1.2 < HI < 1.2), bottom-heavy (1.2 < HI < 1.5) and very bottom-heavy (HI > 1.5) glaciers (Jiskoot *et al.*, 2009).

We assumed that the Equilibrium Line Altitude (ELA) for each glacier was equal to the glacier's median elevation: the balanced-budget ELAs of glaciers are highly correlated with their median elevations (Braithwaite and Raper, 2009; King *et al.*, 2017). We note that the median glacier altitude tends to be slightly higher than the balanced-budget ELA and should therefore be considered a maximum estimate (Braithwaite and Raper, 2009). Accumulation and ablation zones for each glacier were derived from the ELAs.

Mean total surface gradient and mean gradients for the ablation and accumulation zones of each glacier were calculated as the gradient of a line drawn between i) the glacier terminus and the top of the accumulation zone, ii) the glacier terminus and the ELA, and iii) the ELA and the top of the accumulation zone, respectively (Quincey *et al.*, 2007; Salerno *et al.*, 2017).

An avalanche ratio was calculated to assess the importance of avalanche inputs to overall glacier accumulation (Hughes, 2008). This was the ratio between the total area susceptible to avalanche, defined as areas with >30° slopes that lead directly onto the glacier accumulation zone, derived from the pre-processed void-filled SRTM DEM (De Ferranti, 2012), and the total glacier area (Hughes, 2008). We acknowledge that this is a simplification, but this is necessitated by the data available and the area and number of glaciers. We also note that these high altitude areas, which tend to have steeper slopes, may be affected by a larger error in the DEM (Becek, 2008). As such, it is used as an overall indicator of the potential relative contribution of avalanche inputs.

3.3 Results

3.3.1 *Glacier area change (2000 to 2014/15)*

Between 2000 and 2014/15, total glacier area in the ACA decreased by 41.33 km^2 (-8.46%; -0.6% a^{-1}; n = 162; Table 3.5). Individual glacier percentage area change ranged from +0.73% (MSM019) to -79.02% (M039; Figure 3.5). Some of the largest percentage area decreases were due to glacier fragmentation (e.g. M039: -79.02%; Figure 3.5), which added a further nine glaciers to the region over the period (Appendix A). The largest percentage decreases in glacier area occurred in the Muktinath Himal and the Damodar Himal (Figure 3.5) with mean percentage decreases of -11.89% and -11.15%, respectively, compared to -6.07% in the Annapurna Himal (Table 3.5 and Figure 3.6A). A Kruskal-Wallis test showed that percentage glacier area change was significantly smaller and less negative in the Annapurna Himal compared with the other two sub-regions ($p<0.05$; Figure 3.6A). There was no significant difference in the rank means of percentage area change in the Muktinath Himal and the Damodar Himal.

Table 3.5: Glacier changes in the ACA and per sub-region. Glacier area changes (2000 to 2014/15; n=162) and mean surface elevation change and mass balance measured for the smaller sample of 72 glaciers (indicated by *) in the ACA and per sub-region between 2000 and 2013/16. Surface elevation change and mass balance uncertainty for the elevation difference maps are summarised in Table 3.2.

Region	**Number of glaciers**	**Total glacier area (2000) (km^2)**	**Total glacier area (2014/15) (km^2)**	**Total glacier area change (%)**	**Mean dh (m a^{-1}) (void-filled)**	**Mass balance (m w. e. a^{-1})**	**Number of glaciers***
ACA	162	488.45	447.13	-8.46	-0.33 ± 0.22	-0.28 ± 0.24	72*
Damodar Himal	64	144.06	127.99	-11.15	-0.19 ± 0.32	-0.16 ± 0.34	29*
Muktinath Himal	54	75.29	66.37	-11.85	-0.43 ± 0.15	-0.37 ± 0.16	40*
Annapurna Himal	44	269.11	252.77	-6.07	-0.31 ± 0.31	-0.26 ± 0.33	3*

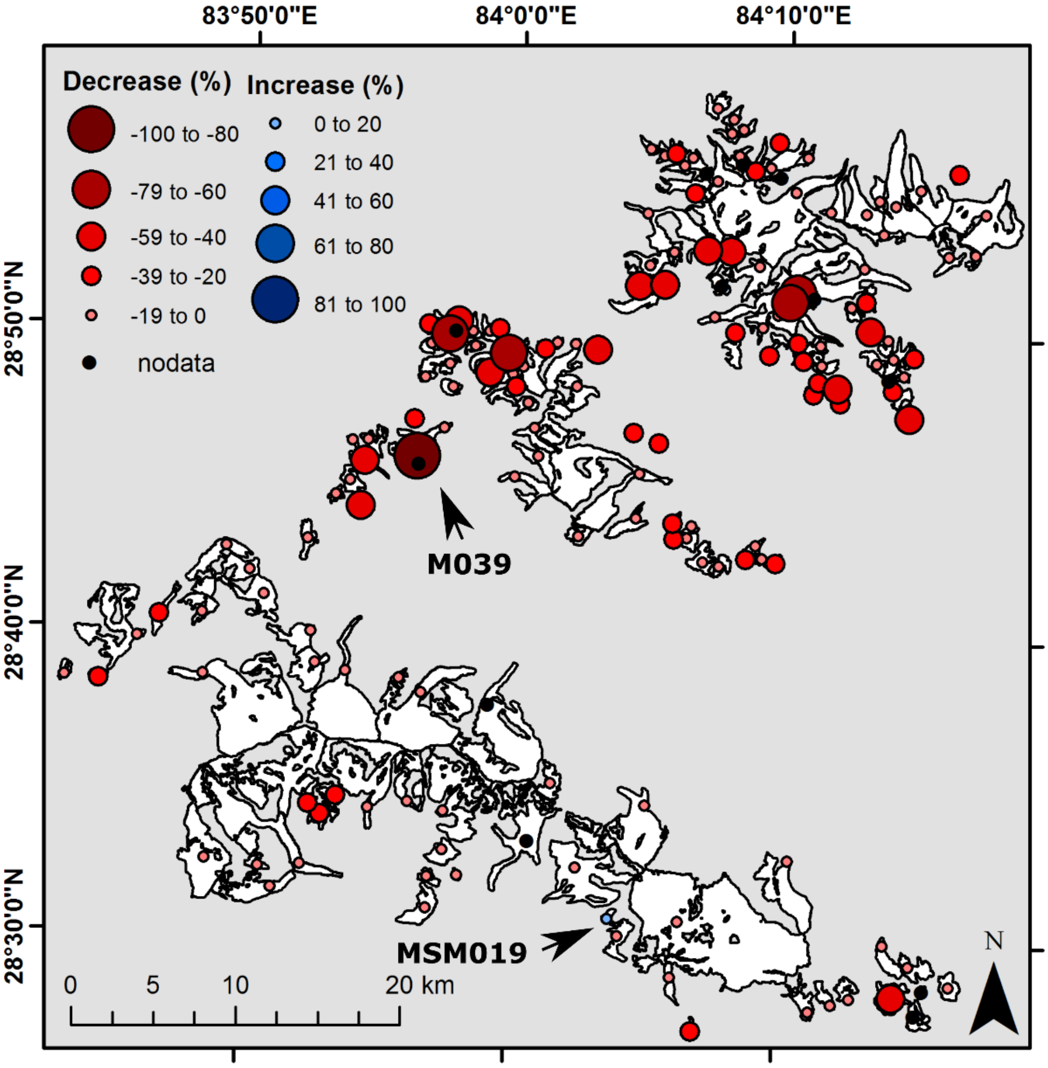

Figure 3.5: Percentage total glacier area change in the ACA from 2000 to 2014/15. Glaciers that underwent the most positive and negative area changes are highlighted. Glacier outlines are from 2015.

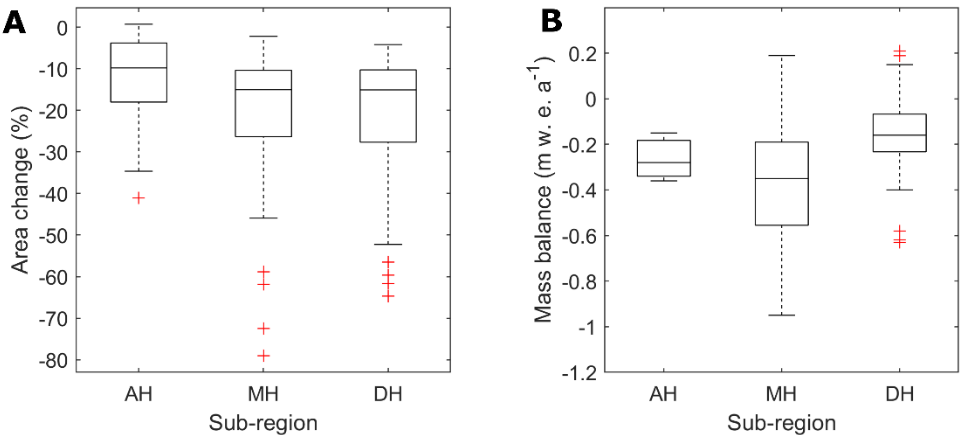

Figure 3.6: Boxplots of glacier change per sub-region. A) percentage area change and B) mass balance for glaciers in the Annapurna Himal (AH), Muktinath Himal (MH) and Damodar Himal (DH) sub-regions. The outliers (red crosses) are values that are >1.5 times the interquartile range from the box.

3.3.2 *Glacier surface elevation change and mass balance (2000 to 2013/16)*

Mean glacier surface elevation change (calculated from 72 glaciers: Appendix A) was -0.33 ± 0.22 m a^{-1} between 2000 and 2013/16 (Table 3.5). However, note that this mean value only includes three glaciers from the Annapurna Himal and, as such, may not be representative of the wider ACA region (Table 3.5). Mean surface elevation change rates on individual glaciers ranged from -1.12 ± 0.01 m a^{-1} on M134, located in the north-west of the Muktinath Himal (Figure 3.7B) to +0.24 ± 0.91 m a^{-1} on KG016, located in the west of the Damodar Himal (Figure 3.7A). Mean surface elevation change rate was most negative in the Muktinath Himal (-0.43 ± 0.15 m a^{-1}), followed by the Annapurna Himal (-0.31 ± 0.31 m a^{-1}) and the Damodar Himal (-0.19 ± 0.32 m a^{-1}; Table 3.5). As expected, most glaciers experienced more negative elevation changes towards the glacier terminus (Figure 3.7). Surface elevation changes on Annapurna South Glacier and MSM005 (Figure 3.8), derived from the ASTER and 2016 SPOT DEMs (footprint location shown in Figure 3.1), also show distinctive surface lowering on the glacier tongues. However, on some glaciers (e.g. M018, MSM018 and M005: Figure 3.7), maximum surface lowering occurred part-way up the glacier tongue with less negative surface changes at the terminus. The majority of these glaciers were debris-covered (Figure 3.7). Glacier thickening occurred in the accumulation zones of several glaciers and was most pronounced on glaciers in the Damodar Himal (Figure 3.7A).

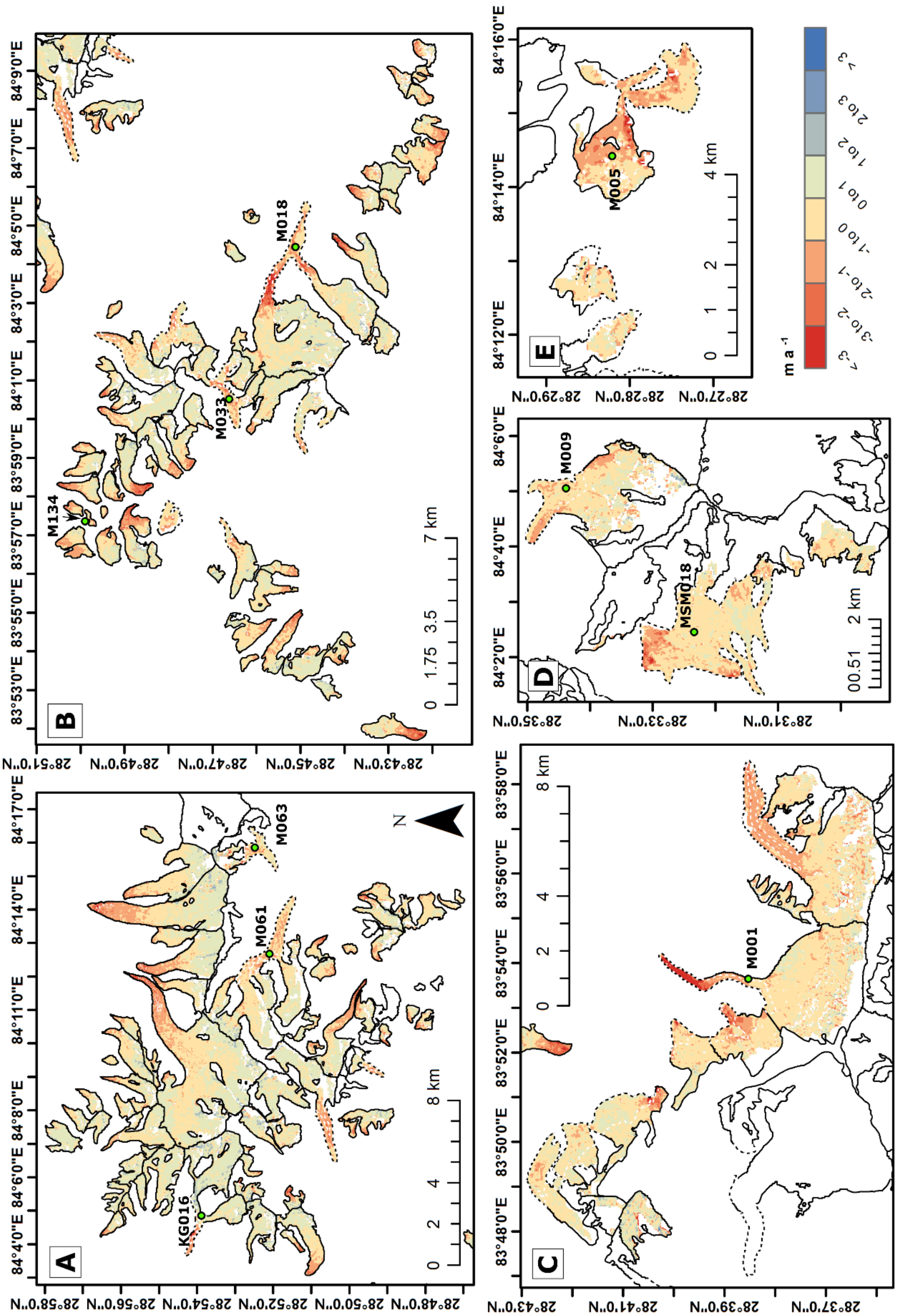

Figure 3.7: Surface elevation change (m a^{-1}) from 2000 to 2013/16 in A) the Damodar Himal, B) the Muktinath Himal and C-E) the Annapurna Himal. Glaciers mentioned in the text are labelled. Dashed black and white lines indicate debris-covered parts of the glaciers. Glacier outlines are from 2000.

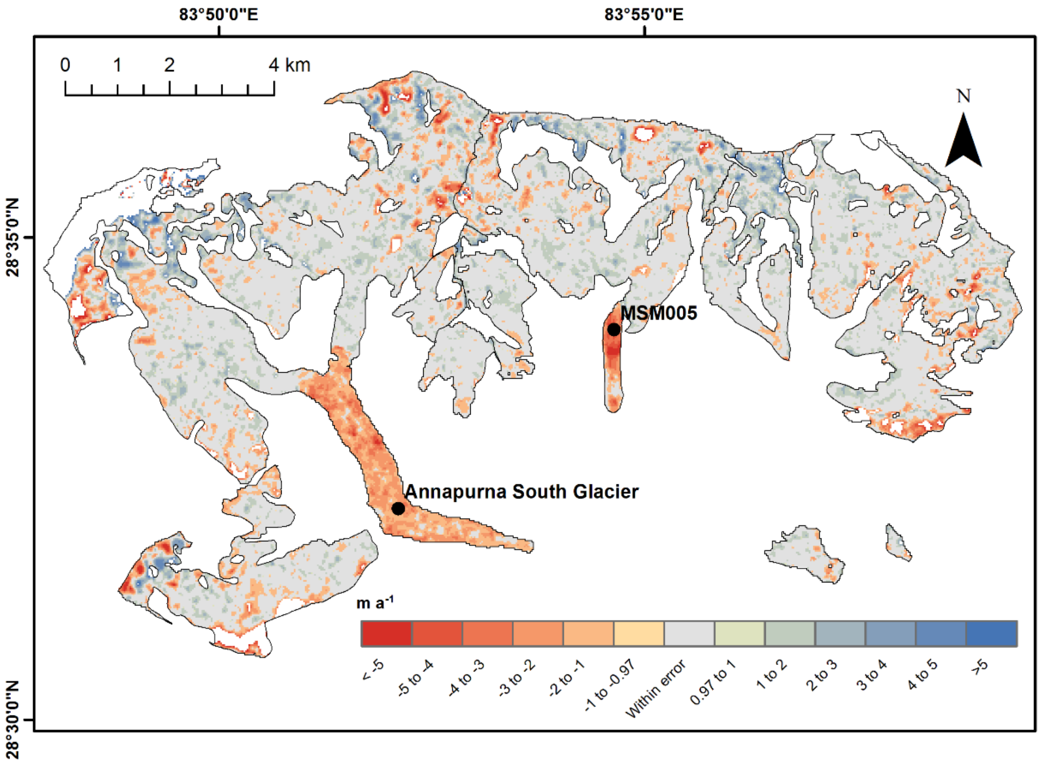

Figure 3.8: Glacier surface elevation change in the Annapurna Himal (2000 to 2016) derived from the ASTER and 2016 SPOT DEMs. Elevation change (m a^{-1}) values within the elevation change uncertainty (0.97 m a^{-1}) are grey. Clear surface elevation lowering is observed on the ablation zones of Annapurna South Glacier (GLIMS ID: G083858E28587N) and MSM005 (G083912E28572N). Glacier outlines are from 2000.

Mean glacier mass balance was -0.28 ± 0.24 m w.e. a^{-1} between 2000 and 2013/16, based on a sample of 72 glaciers (Table 3.5). Individual glacier mass balances ranged from -0.95 ± 0.02 (M134) to +0.21 ± 0.97 m w.e. a^{-1} (KG016: Figure 3.9). Mean mass balance for the Muktinath Himal (-0.37 ± 0.16 m w.e. a^{-1}) was significantly more negative than for the Damodar Himal (-0.16 ± 0.34 m w.e. a^{-1}; Kruskal Wallis: $p<0.05$; Table 3.5 and Figure 3.6B). The mean mass balance in the Annapurna Himal (-0.26 ± 0.33 m w.e. a^{-1}) was not significantly different from the other sub-regions. Ten glaciers in the ACA had negligible or slightly positive mass balances (0 to 0.21 m w.e. a^{-1}; Figure 3.9). Six of these were located in the Damodar Himal and were clustered in the north-west of the sub-region (e.g. KG016 and KG024; Figure 3.9). The other four glaciers with no discernible change or positive mass balances were located in the Muktinath Himal, including M025 and M109 (Figure 3.9). Glaciers with the most negative mass balances were also located in the Muktinath Himal and the majority of these were clustered on the west side of the sub-region (e.g. M012 and M134; Figure 3.9). Mass balance was weakly correlated with area change over the entire region (R^2=0.19, p<0.05; Table 3.6 and Figure 3.10). Mass balance was strongly correlated with area change in the Damodar Himal (R^2=0.51, p<0.05) but there was no significant relationship in the Muktinath Himal (R^2=0.08, p=0.07; Table 3.6). There were not enough observations to assess whether mass balance and area change were related in the Annapurna Himal.

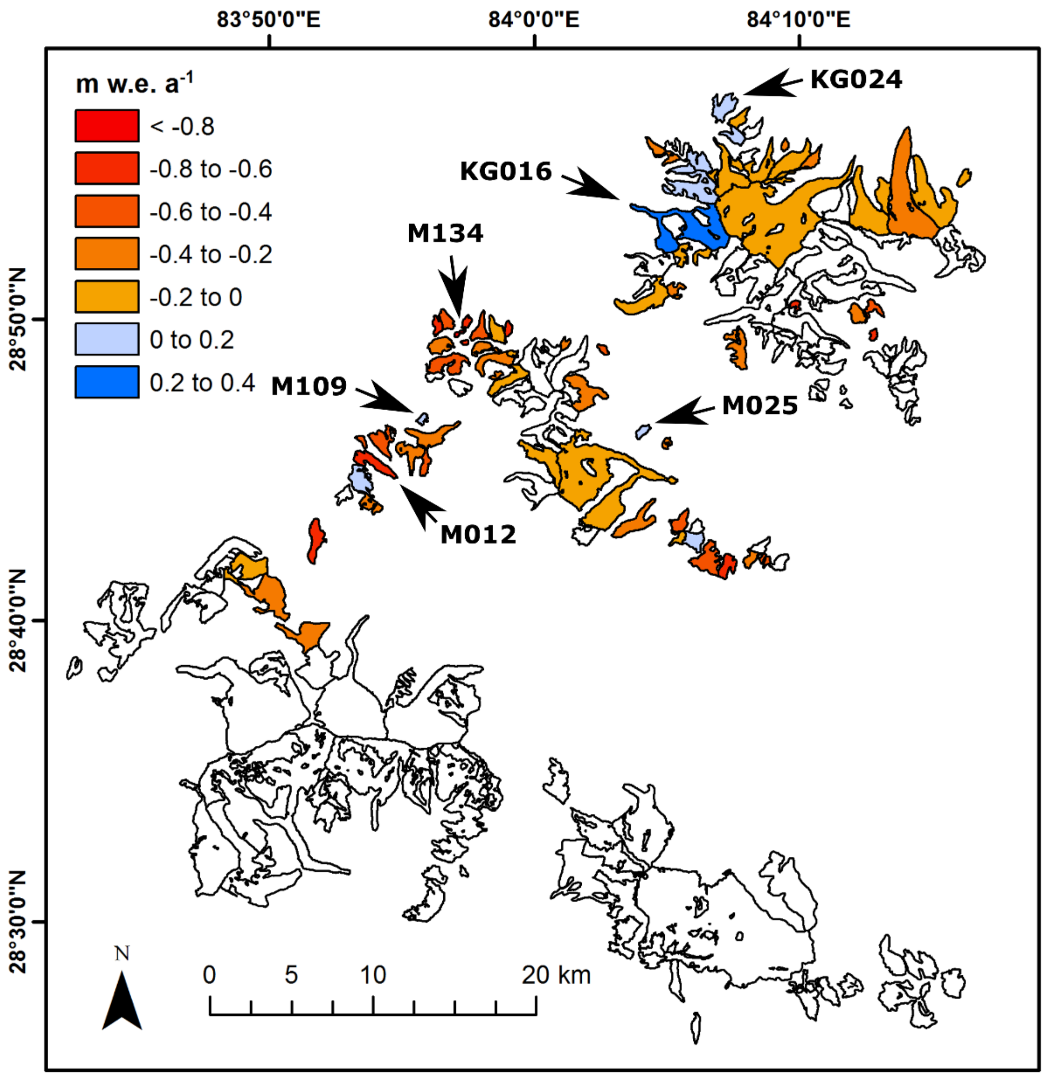

Figure 3.9: Glacier mass balance (m w.e. a^{-1}) (2000 to 2013/16) for a sample of 72 glaciers in the ACA. Glaciers with the most positive and most negative mass balances are labelled. Glacier outlines are from 2000.

Table 3.6: Linear regression results for different controls on glacier area change, surface elevation change and mass balance.

Mass balance vs. area change		
Sub-region	**R^2**	**p-value**
All glaciers	0.19	<0.05
Damodar Himal	0.51	<0.05
Muktinath Himal	0.08	0.07
Surface elevation change vs. surface gradient		
Sub-region	**R^2**	**p-value**
All glaciers	0.10	<0.05
Damodar Himal	0.10	0.10
Muktinath Himal	0.19	<0.05
Mass balance vs. maximum elevation		
Sub-region	**R^2**	**p-value**
All glaciers	0.17	<0.05
Damodar Himal	0.27	<0.05
Muktinath Himal	0.00	0.87
Area change vs. maximum elevation		
Sub-region	**R^2**	**p-value**
All glaciers	0.16	<0.05
Damodar Himal	0.34	<0.05
Muktinath Himal	0.11	<0.05
Mass balance vs. avalanche ratio		
Sub-region	**R^2**	**p-value**
All glaciers	0.08	<0.05
Damodar Himal	0.49	<0.05
Muktinath Himal	0.00	0.80
Area change vs. avalanche ratio		
Sub-region	**R^2**	**p-value**
All glaciers	0.09	<0.05
Damodar Himal	0.46	<0.05
Muktinath Himal	0.09	0.06

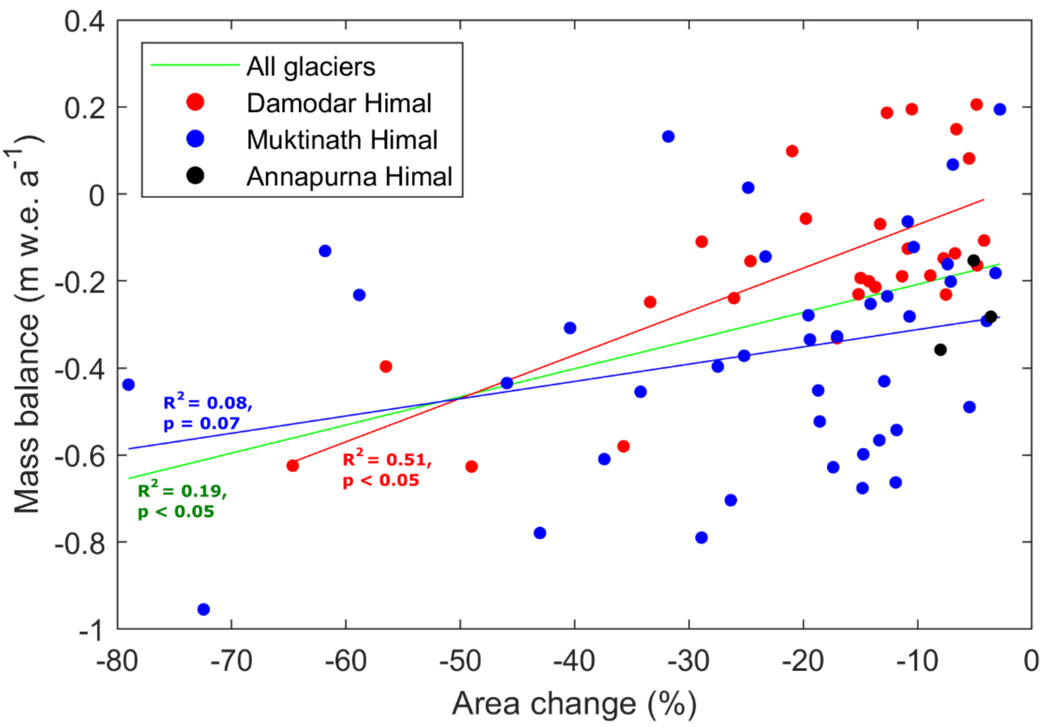

Figure 3.10: Scatterplot of percentage glacier area change against mass balance (n = 72) in the ACA. The green line is the line of best fit for all glaciers and the red and blue lines are the lines of best fit for the Damodar Himal and the Muktinath Himal, respectively. The Annapurna Himal did not have enough data for a line of best fit. Each line is labelled with its R^2 and p-values, in corresponding colours.

3.3.3 *Glacier surface velocities (2002 to 2016)*

Surface velocities on glacier tongues in the ACA ranged from 0 to 70 m a^{-1} in both 2002 (Figure 3.11A, C & E) and 2016 (Figure 3.11B, D & F). Surface velocity patterns in the upper glacier areas were less coherent but they exceeded 100 m a^{-1} on at least one glacier (MSM021; Figure 3.11E & F). The highest velocities (50 to >100 m a^{-1}) occurred in the Annapurna Himal (Figure 3.11E & F). Lower velocities (0 to 70 m a^{-1}) were observed on glaciers in the Muktinath Himal and the Damodar Himal and the tongues of several glaciers in these two sub-regions were stagnant or near-stagnant (0 to 10 m a^{-1}), for example M018 (Figure 3.11C and D). We could not quantify velocity change between 2002 and 2016 because of data voids, but from visual inspection of the velocity maps, we identify seven glacier that underwent deceleration in the area closest to the termini (indicated by red arrows in Figure 3.11). These glaciers were located across the ACA, but most were in the Damodar Himal (Figure 3.11A & B).

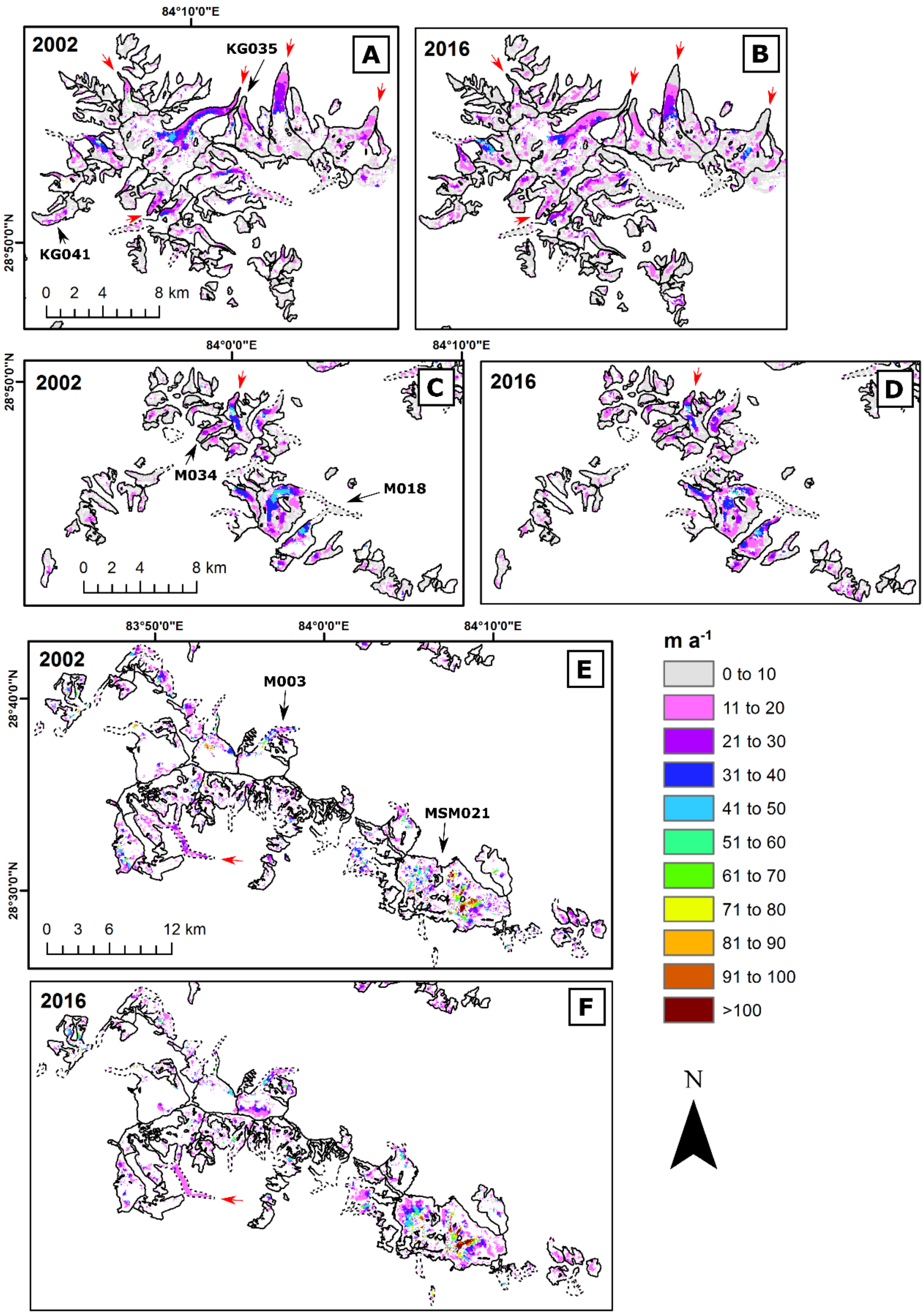

Figure 3.11: Glacier surface velocities (m a^{-1}) in the ACA measured between 03/01/2002-05/12/2002 and 02/01/2016-10/12/2016 in A) the Damodar Himal: 2002, B) the Damodar Himal: 2016, C) the Muktinath Himal: 2002, D) the Muktinath Himal: 2016, E) the Annapurna Himal: 2002 and F) the Annapurna Himal: 2016. Red arrows highlight glaciers that decelerated in their

ablation zones during this period. Dashed black and white lines indicate debris-covered glacier areas. Glacier outlines are from 2000.

3.3.4 *Local controls on glacier change*

3.3.4.1 *Glacier surface gradient*

Mean glacier surface gradient has been highlighted as an important control on glacier surface elevation change, specifically that surface lowering is highest on glaciers with low surface gradients (Pellicciotti *et al.*, 2015; Salerno *et al.*, 2017). We tested this relationship on our sample of 72 glaciers using linear regression (Figure 3.12). There was no significant relationship between mean glacier gradient, accumulation zone gradient or ablation zone gradient and glacier mass balance or area change. We also used linear regression to test the relationship between the mean gradient and mean surface elevation change of the ablation zone. There was a very weak positive relationship between the gradient and mean surface elevation change rate in glacier ablation zones in the ACA (R^2=0.10, $p<0.05$; Table 3.6). This relationship was slightly stronger in the Muktinath Himal (R^2=0.19, $p<0.05$; Table 3.6), but no significant relationship was found in the Damodar Himal. There were not enough data to test this relationship in the Annapurna Himal. Overall, our data suggest that mean surface gradient had limited impact on glacier elevation change.

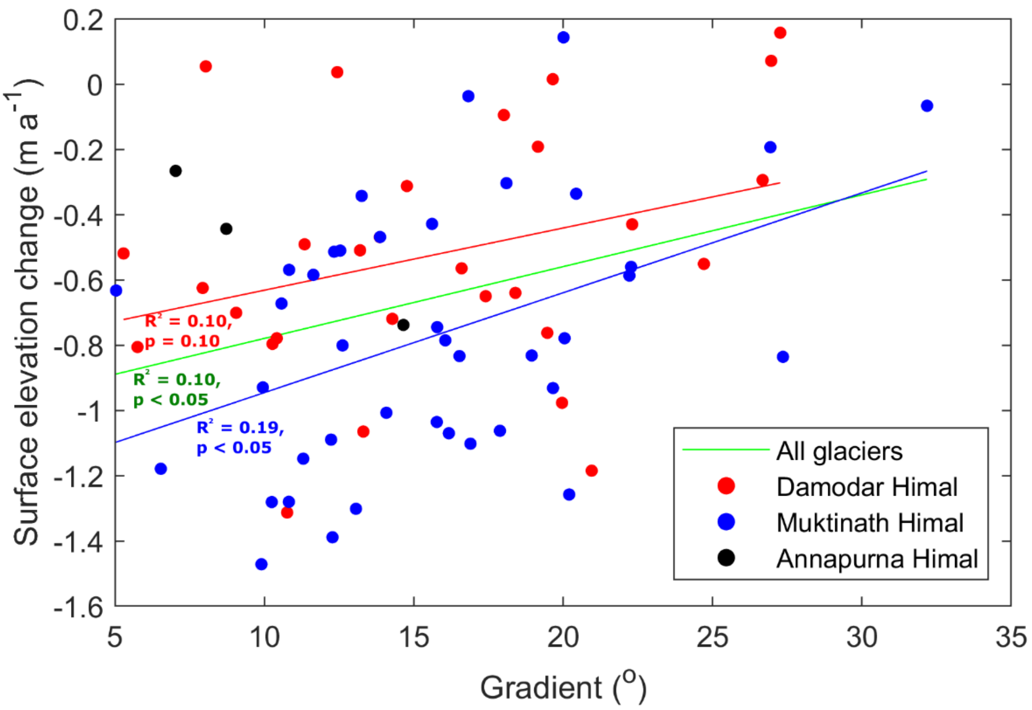

Figure 3.12: Scatterplot of mean gradient of the ablation zone and mean surface elevation change of the ablation zone (n=72). The green line is the line of best fit for all glaciers and the red and blue lines are the lines of best fit for the Damodar Himal and Muktinath Himal, respectively. The Annapurna Himal did not have enough data points for a line of best fit. Each line is labelled with its R^2 and p-values, in corresponding colours.

3.3.4.2 *Glacier elevation*

We used linear regression to assess the relationship between maximum glacier elevation and i) mass balance (Figure 3.13A); and ii) area change (Figure 3.13B). We repeated this analysis for minimum elevation. We hypothesised that glaciers with lower minimum and maximum elevations have more negative mass balances and lose more area for a given climate forcing (Ojha *et al.*, 2016). We found no clear relationship between minimum elevation and mass balance or minimum elevation and area change. There was a very weak positive correlation between maximum elevation and mass balance (R^2=0.17, p<0.05; Table 3.6) and maximum elevation and area change (R^2=0.16, p<0.05; Table 3.6). These relationships were strongest in the Damodar Himal: maximum elevation and mass balance (R^2=0.27, p<0.05; Table 3.6) and maximum elevation and area change (R^2=0.34, p<0.05; Table 3.6). There was no significant relationship between maximum elevation and mass balance (Table 3.6) and a weak positive relationship between maximum elevation and area change (R^2=0.11, p<0.05; Table 3.6) in the Muktinath Himal (Figure 3.13B). There were not enough data to test this relationship in the Annapurna Himal. Our data suggest that glaciers in the Damodar Himal with higher maximum elevations lost less area and mass, but maximum elevation did not have a strong influence on glacier change in the Muktinath Himal.

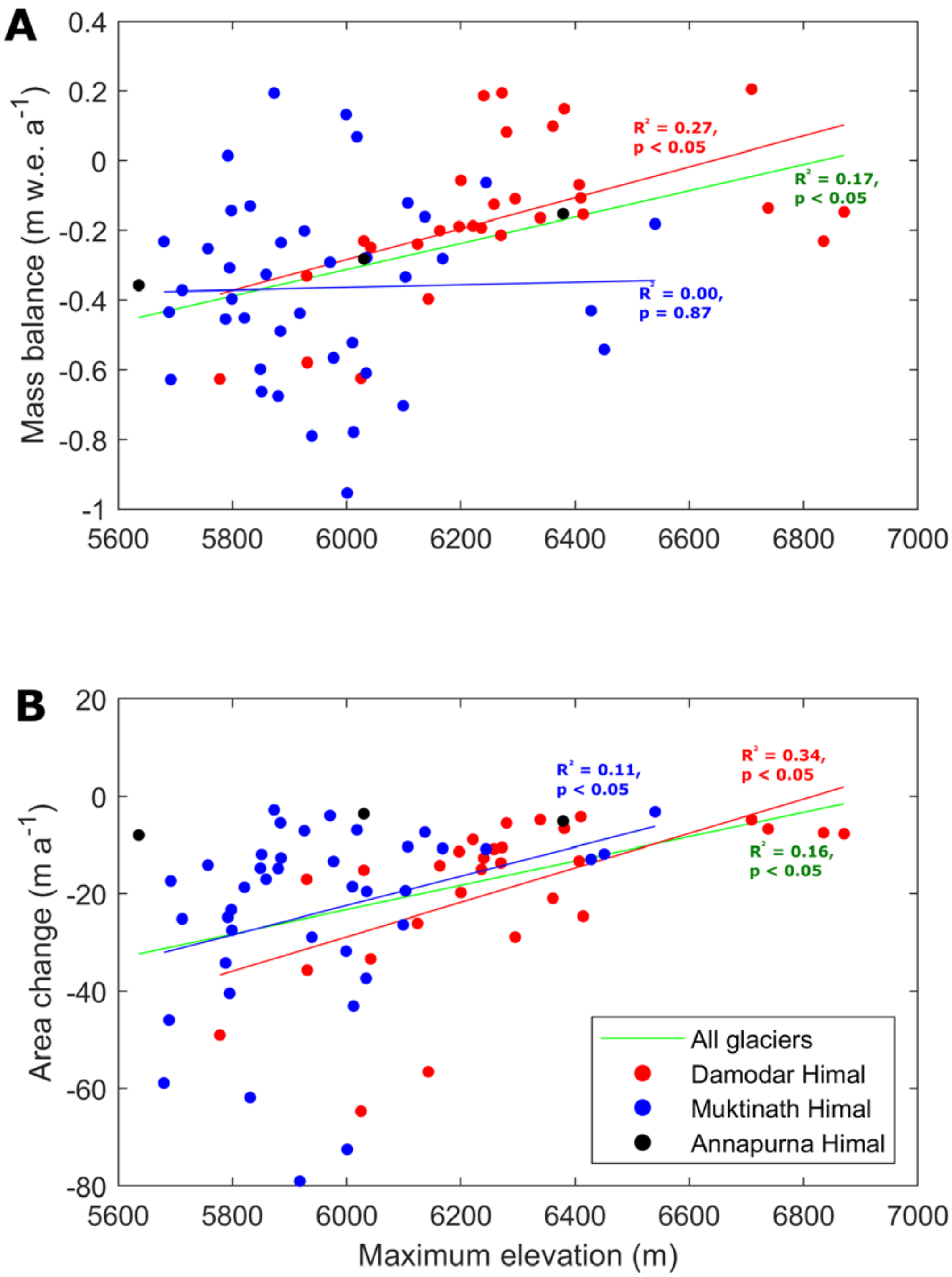

Figure 3.13: Scatterplots of maximum elevation against glacier change. A) mass balance against maximum elevation (n=72) and B) area change against maximum elevation (n=72). The green line is the line of best fit for all glaciers and the red and blue lines are the lines of best fit for the Damodar Himal and Muktinath Himal, respectively. The Annapurna Himal did not have enough data points for a line of best fit. Each line is labelled with its R^2 and p-values, in corresponding colours.

3.3.4.3 *Glacier hypsometry*

We tested the influence of glacier hypsometry on mass balance, hypothesising that glaciers with high and wide accumulation zones (top-heavy) should have more positive mass balances than bottom-heavy glaciers (Jiskoot *et al.*, 2009; Pratt-Sitaula *et al.*, 2011; Robson *et al.*, 2018). The boxplots in Figure 3.14 show that bottom or very bottom-heavy glaciers had more negative mass balances than top or very top-heavy glaciers, and equidimensional glaciers had positive and negative mass balances. A Kruskal Wallis test revealed that the differences in the rank means of the five hypsometry classes were not significant when considered together (Figure 3.14). However, individual Wilcoxon rank sum tests identified significant differences in the mean mass balance of top-heavy and bottom-heavy glaciers ($p<0.05$) and between top-heavy and very bottom-heavy glaciers ($p<0.05$; Figure 3.14). This suggests that top-heavy glaciers had significantly less negative mass balance than bottom- or very bottom-heavy glaciers.

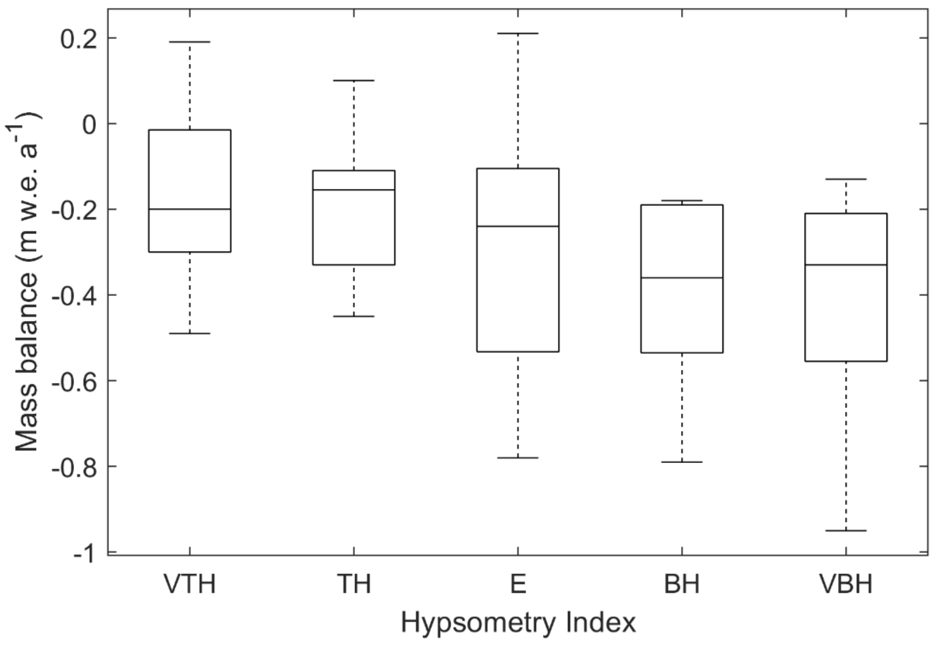

Figure 3.14: Boxplots of mass balance against hypsometric index class (n=72). VTH = very top-heavy, TH = top-heavy, E = equidimensional, BH = bottom-heavy and VBH = very bottom-heavy.

3.3.4.4 *Avalanche contributions*

We assessed the influence of potential avalanche contribution on glacier mass balance and area change by using linear regression to test the hypothesis that glaciers with a higher avalanche likelihood ratio had less negative mass balance and area changes (Figure 3.15) (Hughes, 2008; Laha *et al.*, 2017). We found no significant relationship between mass balance and avalanche ratio in all glaciers or in the Muktinath Himal (Table 3.6). However, there was a significant negative relationship between mass balance and avalanche ratio in the Damodar Himal (R^2=0.49, $p<0.05$; Table 3.6). No significant relationship was found between area change and avalanche ratio for all glaciers, or for glaciers in the Muktinath Himal, but a significant negative relationship was found between area change and avalanche ratio in the Damodar Himal glaciers (R^2=0.46, $p<0.05$; Table 3.6). There were not enough data to test these relationships in the Annapurna Himal. Overall, glaciers that were more likely to be avalanche fed in the Damodar Himal lost more area and mass, but the avalanche contributing area did not have an influence on glacier change in the Muktinath Himal.

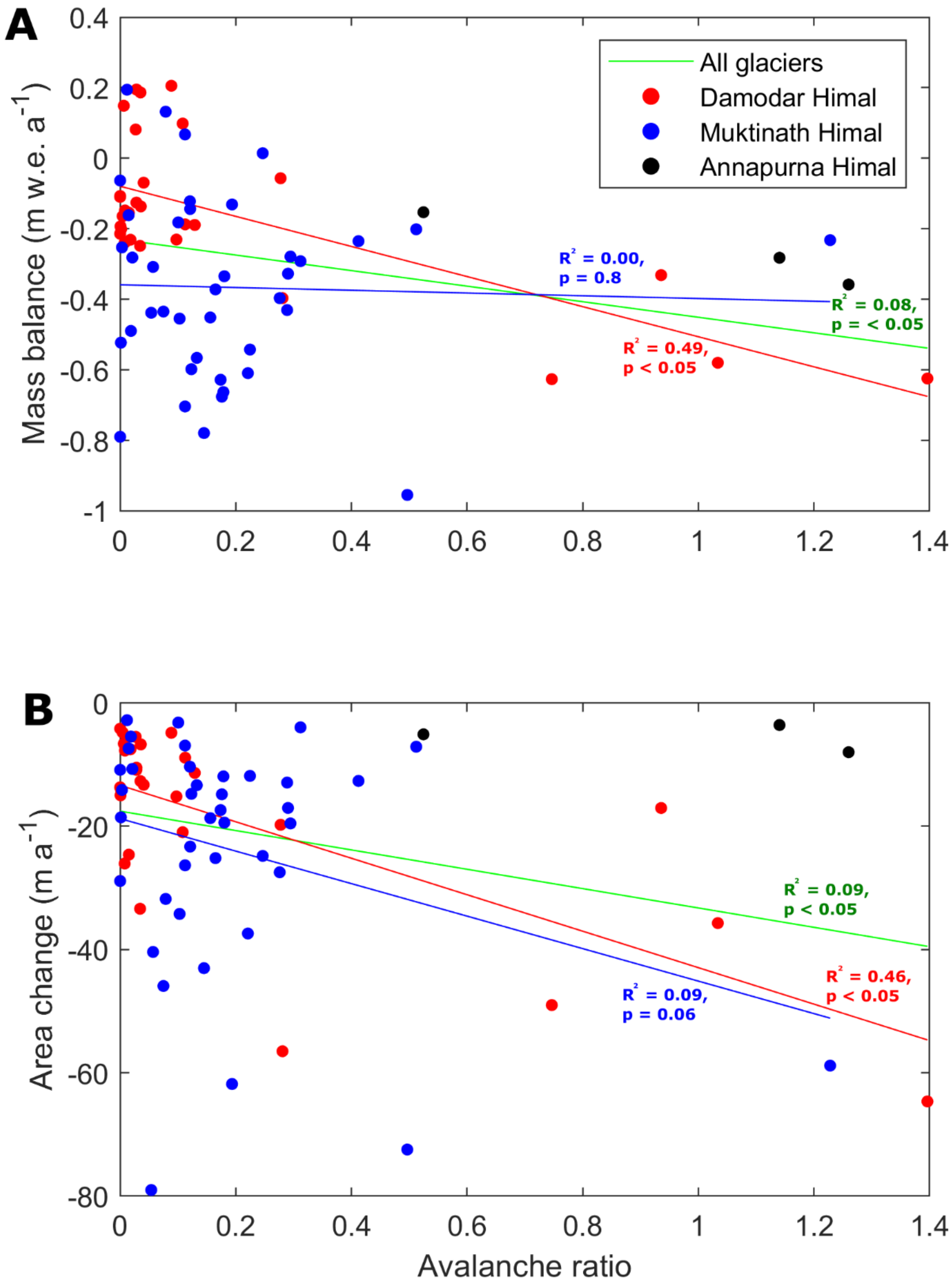

Figure 3.15: Scatterplots of avalanche ratio against glacier change, A) mass balance against avalanche ratio (n=72) and B) area change against avalanche ratio (n=72). The green line is the line of best fit for all glaciers and the red and blue lines are the lines of best fit for the Damodar Himal and Muktinath Himal, respectively. The Annapurna Himal did not have enough data points for a line of best fit. Each line is labelled with its R^2 and p-values, in corresponding colours.

3.3.4.5 *Supraglacial debris*

We tested the hypothesis that surface lowering rates are similar on debris-covered and debris-free glacier areas (Gardelle *et al.*, 2013; Banerjee, 2017). There was no significant difference in mean surface elevation change rate on the ablation zones of debris-covered glaciers compared with debris-free glaciers (Figure 3.16A). While some glaciers with debris-covered ablation zones underwent strong surface lowering (< -3 m a^{-1}) e.g. M001 (Figure 3.7C) and M018 (Figure 3.7B), several other debris-covered glaciers down-wasted more slowly (-2 to 0 m a^{-1}). Many debris-free glaciers showed comparable surface lowering rates (<-3 to -2 m a^{-1}) at their termini (Figure 3.7). We plotted mean surface elevation change rate per 100 m elevation band for both debris-covered and debris-free glacier areas in the ACA to compare surface lowering rates on the different glacier surface types per elevation band (Figure 3.16B). There was a strong positive correlation between mean surface elevation change rate and elevation band for debris-free glacier areas (R^2=0.82, $p<0.05$; Figure 3.16B), showing that surface lowering rates are greatest at lower elevations. This relationship was weaker on debris-covered glacier areas (R^2=0.32, $p<0.05$). Between elevation bands 4600-4700 m and 5000-5100 m, where debris-covered and debris-free glacier areas overlapped, mean elevation change on the debris-free glacier areas was significantly more negative (0.5 m a^{-1} on average, $p<0.05$) than on debris-covered areas. Above the 5000-5100 m elevation band, elevation changes on both debris-covered and debris-free glacier areas were similar (Figure 3.16B). While most glaciers had increasingly negative surface elevation changes towards their termini (Figure 3.7), some glaciers (e.g. M018 and MSM018; Figure 3.7B & D) had more negative surface elevation changes further up-glacier from the terminus. These surface-lowering patterns tended to coincide with debris-covered areas or the transition areas between debris-covered and debris-free ice (Figure 3.7). Our data show that although mean surface lowering rates are similar when directly comparing debris-covered and debris-free glacier ablation zones, the spatial patterns of surface lowering between debris-covered and debris-free glacier areas differ when comparing the surface cover types at the same elevations.

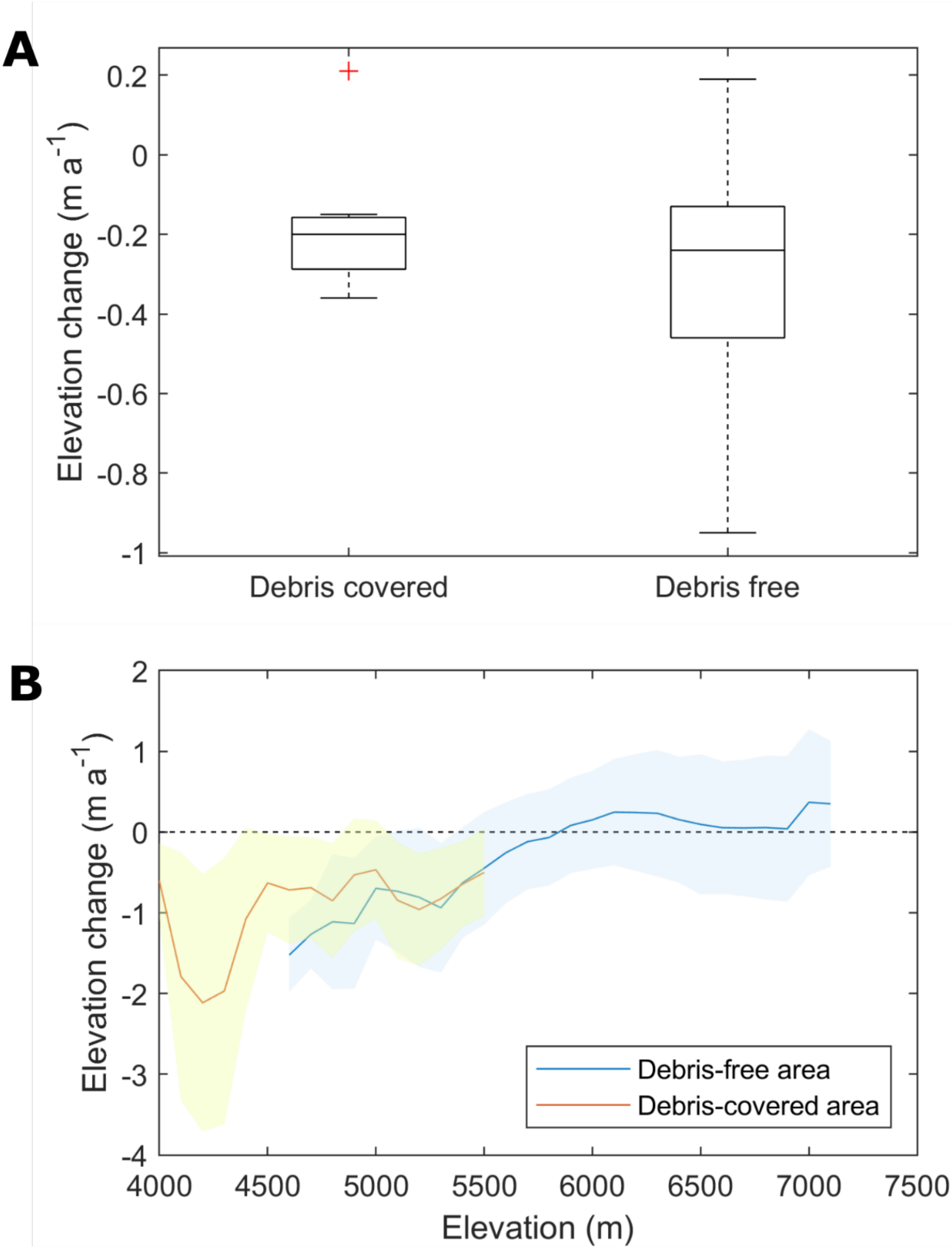

Figure 3.16: Influence of supraglacial debris on glacier surface elevation change: A) boxplots of mean elevation change in the ablation zones of debris-covered and debris-free glaciers and B) plots of mean elevation change against 100 m elevation band for the debris-free (blue) and debris-covered (orange) components of glacier area in the ACA. The shaded areas are 1 standard deviation.

3.4 Discussion

3.4.1 *Overall glacier changes in the ACA*

3.4.1.1 *Area change*

Between 2000 and 2014/15, most glaciers in the ACA lost area (total area change: -8.5% and 0.6% a^{-1}) and several glaciers fragmented, creating new, smaller glaciers (Table 3.5 and Figure 3.5). This is consistent with general trends of glacier shrinkage across the Himalayas over the last ~50 years (Kulkarni *et al.*, 2007; Bolch *et al.*, 2008; Ojha *et al.*, 2016; Robson *et al.*, 2018). Glacier area in the neighbouring Manaslu region decreased by -8.2% for a comparable period (1999/2000 to 2013) (Robson *et al.*, 2018). Between 1962 and 2000, glaciers in the Kanchenjunga-Sikkim region in the eastern Himalayas lost area at a rate of 0.5% a^{-1} (Racoviteanu *et al.*, 2015). Glacier area in the Everest region decreased by 0.4% a^{-1} between 1962 and 2011 (Thakuri *et al.*, 2014), and glaciers in the Himachal Pradesh region decreased by 0.5% a^{-1} between 1962 and 2001 (Kulkarni *et al.*, 2007).

Glacier area shrinkage was variable across the ACA. Glaciers in the Muktinath Himal (-11.85%) and the Damodar Himal (-11.15%) lost significantly larger mean percentage areas than glaciers in the Annapurna Himal (-6.07%; Figure 3.6A). We think this is because glaciers in the Annapurna Himal are significantly larger than in the other two sub-regions (Kruskal Wallis: $p<0.05$; Figure 3.17A) and therefore have slower response times to climate forcing (Bahr *et al.*, 1998).

Although overall mean percentage glacier area change in the ACA (-8.5%) and Manaslu region (-8.2%) was similar, sub-regional patterns of area change differed between the regions. Glaciers in the south of the Manaslu region lost a larger mean percentage area than glaciers in the north (Robson *et al.*, 2018), whereas our data demonstrate the opposite trend (Figure 3.5). Moreover, glaciers in the north of the ACA (the Damodar Himal) shrank more (-11.15%) than the northern glaciers in the Manaslu region (-6.7%) (Robson *et al.*, 2018). However, glaciers in the northern part of the Manaslu region are mostly larger than glaciers in the Damodar Himal, and therefore are probably responding more slowly to climate forcing.

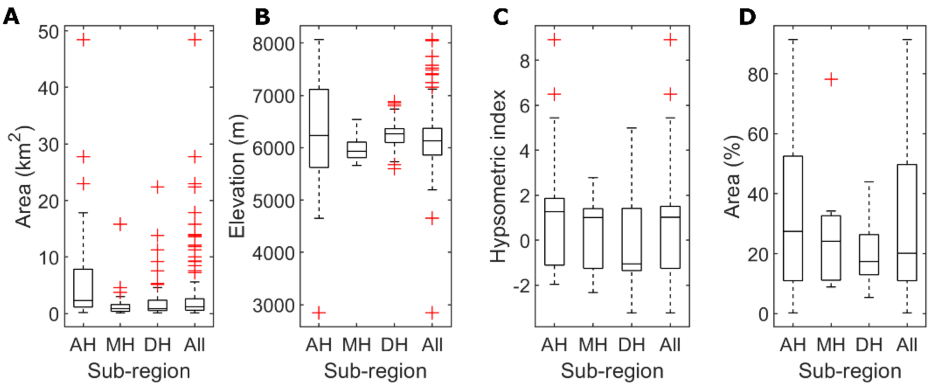

Figure 3.17: Boxplots of glacier characteristics for all glaciers in the ACA (All) and in the Annapurna Himal (AH), Muktinath Himal (MH) and Damodar Himal (DH) sub-regions: A) glacier area, B) maximum elevation, C) hypsometric index and D) debris-covered glacier area (%) (measured in 2000). The outliers (red crosses) are values that are >1.5 times the interquartile range from the box.

3.4.1.2 *Surface elevation change and mass balance*

Between 2000 and 2013/16, mean surface elevation change and mean mass balance of glaciers in the ACA were -0.33 m a^{-1} and -0.28 m w.e. a^{-1}, respectively (Table 3.5). This is more negative than the overall mass balance estimates for HMA for similar periods (-0.14 to -0.21 w.e. a^{-1}) (Kääb *et al.*, 2012; Gardelle *et al.*, 2013; Brun *et al.*, 2017) but consistent with moderate mass loss estimates for the central and eastern Himalayas (-22 to -0.33 m w.e. a^{-1}) (Kääb *et al.*, 2012; Gardelle *et al.*, 2013), and more positive than the strong mass loss in the western Himalayas (-0.45 to -0.55 m w.e. a^{-1}) (Kääb *et al.*, 2012; Gardelle *et al.*, 2013). In comparison to other regions in the Nepalese Himalayas for a similar period, mean mass balance in the ACA was more positive than in the Everest region (-0.52 m w.e. a^{-1} between 2000 and 2015) (King *et al.*, 2017) and the Langtang region (-0.38 ± 0.17 m w.e. a^{-1} between 2006 and 2015) (Ragettli *et al.*, 2016). However, the ACA was more negative than the Manaslu region, where mean surface elevation change was -0.25 m a^{-1} and mean mass balance was -0.21 m w.e. a^{-1} between 1999/2000 and 2013 (Robson *et al.*, 2018). This highlights important variability in the central Himalayas, within the broad east to west gradient of mass loss in HMA. However, note that glaciers in the Annapurna Himal are not well represented in our sample, which may influence our mean mass balance estimate for the ACA.

Mean mass balance in the Damodar Himal was significantly less negative than in the Muktinath Himal (Figure 3.6B), suggesting that mass balance in the ACA became increasingly less negative with distance north. Similar north/south glacier change trends have been observed in other parts of HMA. In the Manaslu region, northern glaciers had a significantly more positive mean mass balance than southern glaciers (Robson *et al.*, 2018). This was attributed to the higher elevations of the northern glaciers, relative to the southern glaciers, which meant the northern glaciers were less vulnerable to warming air temperatures (Robson *et al.*, 2018). In the Bhutan Himalayas, glaciers on the northern slopes had lower retreat rates and higher velocities than glaciers on the southern slopes (Kääb, 2005). This was attributed to the decreasing monsoon influence and increasing continentality of glaciers towards the north, controlled by the orographic barrier, making the northern glaciers less sensitive to changing precipitation and air temperatures (Kääb, 2005). In the Western Kunlun mountains on the Tibetan Plateau, less negative surface lowering rates on north-facing glaciers compared with south-facing glaciers were thought to be controlled by aspect and/or orographically-driven differences in precipitation (Phan *et al.*, 2017). Interestingly, these trends differ from the Everest region where glaciers north of the orographic divide had a more negative mean mass balance than glaciers in the south (King *et al.*, 2017). This was attributed to the sharp decrease in precipitation over the divide causing the northern glaciers to be both snow-deprived and subject to increased insolation, due to cloud-free conditions (King *et al.*, 2017).

Our data show that although glaciers in the Damodar Himal have higher maximum elevations than in the Muktinath Himal (Figure 3.17), glacier mass balance and maximum elevation were only weakly related across the ACA (Table 3.6). This suggests that increased glacier elevation, alone, is not an important control on the more positive mass balances observed in the north of the ACA. We hypothesise that these variable spatial patterns of mass balance are also due to the decreasing sensitivity of glaciers to monsoonal variations towards the Tibetan Plateau. However, meteorological data is needed to test this hypothesis. To summarise, glaciers in the northern part of the ACA had more positive mass balances than glaciers further south, which may be due to a decreasing sensitivity to changes in precipitation.

3.4.1.3 ***Regional climate trends***

Area changes (Figure 3.5) and mass balance (Figure 3.9) in the ACA are broadly consistent with Himalayan trends in precipitation and air temperature (Kattel and Yao, 2013; Panthi *et al.*, 2015). Since 1950, a significant decreasing trend in summer precipitation has been observed across the Himalayas (Palazzi *et al.*, 2013) and, between 1981 and 2012, there was a decreasing trend in annual precipitation in the Trans Himalayan and Mountain sections of the Gandaki river basin, in which the ACA is located (Panthi *et al.*, 2015). Although long-term air temperature data are not available specifically for the ACA, air temperature increases were observed across several mountain stations in Nepal between 1980 and 2009, with an acceleration in warming during the last decade (Kattel and Yao, 2013). There was also a significant increase in air temperature, including at elevations above 5000 m asl, in the Everest region between 1994 and 2013 outside of the monsoon period (Salerno *et al.*, 2015). The coincidence of recent glacier area reduction and mean negative mass balance in the ACA and long-term regional trends of increasing air temperature and decreasing precipitation suggests that the recent glacier change trends are related to climate change.

3.4.1.4 *Relationship between area change and mass balance*

There was a weak positive relationship between glacier mass balance and area change in the ACA (Table 3.6). This relationship was strong in the Damodar Himal but not significant in the Muktinath Himal (Table 3.6). This indicates that glaciers with the most negative mass balances in the Damodar Himal also lost the most area, but that this was not necessarily the case in the Muktinath Himal. Glaciers in the Muktinath Himal that underwent the smallest area changes (<30%) had some of the most positive and negative mass balances (Figure 3.10). This suggests that glaciers in this sub-region underwent diverse morphological changes over the period, with concurrent area and mass loss occurring on some glaciers, while on other glaciers, these changes were de-coupled. This is particularly interesting because the Muktinath Himal had the smallest variability (range) of area, maximum elevation and hypsometric index values of the sub-regions, so we would expect similar glacier responses to climate change (Figure 3.17A-C). This complicates predictions of future glacier change in the sub-region.

3.4.1.5 *Ice flow velocities*

Velocities at most glacier termini in the ACA were <10 m a^{-1} (Figure 3.11), indicating that these glaciers were very slow-flowing or stagnant in these areas. However, several glaciers had maximum glacier tongue velocities of between 40 and 70 m a^{-1} (Figure 3.11). This is slower than the maximum speeds observed on some of the glacier tongues in the Manaslu region (Robson *et al.*, 2018) and on the north side of the Himalayan range in Bhutan (Kääb, 2005), but faster than the velocities observed on the glacier tongues in the Everest region (Quincey *et al.*, 2009) and on the south-facing Bhutan mountain slopes (Kääb, 2005). It indicates that although many glaciers in the ACA lost mass and area over this period, some glaciers, particularly larger glaciers and those located in the Annapurna Himal, were still flowing relatively rapidly across their whole length. Glaciers with some of the highest velocities in the Annapurna Himal originated at the highest elevations in the region and had wide accumulation zones (e.g. M003 and MSM021; Figure 3.11E and F), suggesting that elevation and hypsometry were controls on flow speeds, as has been observed in the Everest region (Quincey *et al.*, 2009).

Despite apparent slow-downs on certain glacier tongues in the ACA, others continued to flow at speeds of 11 to 30 m a^{-1} in 2016 (e.g. KG035, KG041 and M034; Figure 3.11). These tended to be in balance or have only slightly negative mass balances (Figure 3.9). Velocity change patterns between 1999 and 2014 in the Manaslu region were similarly variable, with some glaciers accelerating, others decelerating and the remainder maintaining constant velocities (Robson *et al.*, 2018). This indicates that unlike in other Himalayan regions where widespread stagnation has been observed in combination with glacier thinning and mass loss (Dehecq *et al.*, 2018) (e.g. the Everest region (Quincey *et al.*, 2009; King *et al.*, 2017)), the health of glaciers in the ACA (and Manaslu) is more variable, which is consistent with less negative mean mass balances observed in these regions (Robson *et al.*, 2018).

3.4.2 *Local controls modulating glacier behaviour in relation to regional trends*

We investigated the influence of several local controls on glacier change in the ACA to assess their relative importance. These were glacier surface gradient (Pellicciotti *et al.*, 2015; Salerno *et al.*, 2017), minimum and maximum elevation (Robson *et al.*, 2018), hypsometry (Robson *et al.*, 2018), avalanche inputs (Hughes, 2008; Laha *et al.*, 2017) and supraglacial debris (Gardelle *et al.*, 2013; Banerjee, 2017). We discuss the significant relationships.

Previous observations in the Himalayas have shown that glaciers located at higher elevations tend to have more positive mass balances and less shrinkage because these elevations have cooler temperatures and more precipitation (Ojha *et al.*, 2016; Robson *et* *al.*, 2018). We found a significant relationship between maximum elevation and glacier change in the Damodar Himal but this relationship was less strong, or insignificant, in the Muktinath Himal (Table 3.6). Mean maximum elevation in the Damodar Himal was significantly higher than in the Muktinath Himal (Wilcoxon rank sum test: $p<0.05$; Figure 3.17B) which may mean that maximum elevation influences glacier behaviour but only at higher maximum elevations.

Glaciers in the bottom or very bottom-heavy hypsometric classes had more negative mass balances than top or very top-heavy glaciers (Figure 3.14). Our data are consistent with observations in the Manaslu region, where glaciers losing most mass in the region tended to have bottom-heavy hypsometries (Robson *et al.*, 2018) and in the Everest region, where glaciers with more of their ice located in high altitude and wide accumulation zones tended to flow faster (Quincey *et al.*, 2009). This suggests that glaciers with most of their ice at lower elevations are more vulnerable to climate change, both in the ACA and across the Himalayas. These findings are supported by previous research in the Annapurna Himal which showed that a glacier with a high altitude accumulation zone advanced while a neighbouring lower altitude glacier retreated during the onset of the Holocene (Pratt-Sitaula *et al.*, 2011). The influence of hypsometry could be due to both warming air temperatures at lower elevations and bottom-heavy glaciers having smaller accumulation zones, which are more affected by changing precipitation trends, leading to shorter response times.

Glaciers with very steep and glacier-free headwalls are more likely to gain mass from avalanches (Laha *et al.*, 2017). The contribution of avalanches to Himalayan glacier mass balance is poorly constrained because measurement of these events is very difficult (Scherler *et al.*, 2011a; Laha *et al.*, 2017) but it is thought that avalanches can contribute >95% to total accumulation on some glaciers, allowing them to maintain higher velocities, and lower surface lowering rates than if they were not avalanche-fed (Hughes, 2008; Laha *et al.*, 2017). However, we found significant negative correlations between glacier avalanche ratio and both mass balance and area change (Table 3.6) in the Damodar Himal, indicating that in this sub-region, glaciers that were more likely to receive avalanche inputs had more negative mass balances and lost more area. This could be because glaciers that were predominantly avalanche-fed were able to exist in locations that would not have been possible if they relied on precipitation inputs alone, and these locations may have become more vulnerable under changing climatic conditions. However, we acknowledge that the avalanche ratio is only a simplified proxy for avalanche inputs which is potentially susceptible to large uncertainties associated with steep slopes, and similar relationships between avalanche ratio and glacier change were not found in the Muktinath Himal (Table 3.6).

While supraglacial debris over a critical thickness threshold (~2 cm) is thought to inhibit glacier melt (Østrem, 1959; Mattson, 1993; Kayastha *et al.*, 2000; Vincent *et al.*, 2016), several multi-glacier remote sensing studies have observed similar surface lowering rates on debris-covered and debris-free glaciers (Kääb *et al.*, 2012; Gardelle *et al.*, 2013; Banerjee, 2017). This demonstrates that its role in accelerating or inhibiting melt over larger spatial scales is still not fully understood (Gardelle *et al.*, 2013; Pellicciotti *et al.*, 2015). We found no significant difference between surface elevation lowering rates in the ablation zones of debris-covered and debris-free glaciers in the ACA (Figure 3.16A), supporting these previous studies (Kääb *et al.*, 2012; Gardelle *et al.*, 2013; Ragettli *et al.*, 2016; Banerjee, 2017; Salerno *et al.*, 2017). This is attributed to differential melting on debris-covered ice and the development of ice cliffs and supraglacial meltwater pools, which can significantly enhance melt over larger spatial scales (e.g. Brun *et al.*, 2016; Watson *et al.*, 2016; Miles *et al.*, 2018). However, we found that while surface elevation change was strongly linearly correlated with elevation on debris-free glacier areas, the same relationship on debris-covered glacier areas was much weaker (Figure 3.16B). In the lower elevation bands, between 4500-4600 and 5000-5100 m asl, the surface elevation change rate on the debris-covered glacier areas was more positive than on the debris-free areas. However, above the 5000-5100 elevation band, surface elevation change on both debris-covered and debris-free areas was very similar (Figure 3.16B). This is consistent with the notion that the mass balance gradient on the lower sections of debris-covered glaciers is inverted due to the increasing protective effects of thicker debris towards the terminus (Benn *et al.*, 2012; Vincent *et al.*, 2016). Several debris-covered glaciers underwent maximum surface lowering at mid-elevations, rather than at the terminus, further supporting this theory (Figure 3.7). Similarly, non-linear relationships between surface lowering and elevation on debris-covered glacier areas have been observed in other parts of the Himalayas (Ragettli *et al.*, 2016; Banerjee, 2017; Robson *et al.*, 2018). However, it should be noted that debris extent does not give an indication of supraglacial debris thickness on these glaciers, which is an important control on sub-debris ablation rates (Nicholson *et al.*, 2018).

A number of Himalayan glacier change studies looking at smaller sample sizes (5 to 30 glaciers) have identified relatively strong links between individual glacier controls and recent glacier change (Pellicciotti *et al.*, 2015; Ragettli *et al.*, 2016; Salerno *et al.*, 2017). However, our study suggests that when looking at larger data samples (>70 glaciers), the influence of these controls can be less clear, due to a more complex dataset (in terms of size, location etc.). This highlights the difficulty of predicting the future evolution of large samples of glaciers and, in particular, those located within the ACA.

3.5 Conclusions

Our study shows that glaciers in the Annapurna Conservation Area (ACA), central Nepal, thinned, lost mass and lost area between 2000 and 2016. Glaciers underwent an 8.5% reduction in area (2000 to 2014/15; n = 162) and we recorded a mean surface elevation change of -0.33 m a^{-1} and a mean mass balance of -0.28 m w.e. a^{-1} for a smaller sample of 72 glaciers (2000 to 2013/16). These changes are consistent with recent trends in increasing air temperature and decreasing precipitation across the Nepal Himalayas. However, no region-wide trend in velocity was apparent (2002 to 2016) and several glacier tongues were still flowing >10 m a^{-1}, indicating that widespread glacier stagnation has not yet occurred in the ACA as has been reported elsewhere in the Central Himalayas (Dehecq *et al.*, 2018). We observed north to south trends in glacier area change and mass balance, which we attribute to differences in glacier geometry and the orographic divide. The largest glacier mass and area losses occurred in the Muktinath Himal, suggesting that this sub-region will be most vulnerable to future increases in air temperature and decreases in precipitation.

Within these regional trends, glacier changes were heterogeneous, modulated by local controls. Surface elevation change rates on the ablation zones of debris-covered and debris-free glaciers across the ACA were not significantly different, but supraglacial debris influenced the spatial patterns of glacier surface lowering at specific elevations, promoting inverted mass balance gradients in the ablation zone. Glaciers with bottom-heavy hypsometry lost more mass than those with top-heavy hypsometry. In the Damodar Himal, glaciers that had lower maximum elevations and were more likely to receive inputs from avalanches, tended to have more negative mass balances. However, in the Muktinath Himal, these relationships were weak or did not exist, and glacier area change and mass balance were decoupled. This difference between the sub-regions shows that the strength of the influence of local controls on individual glacier behaviour in the ACA is complex and varies spatially, especially across large samples of glaciers, presenting an important challenge to predicting their future behaviour. Further research is needed to assess how glacier changes in the ACA relate to local climate conditions and influence local water resources.

Chapter 4: Topographic controls on the surging behaviour of Sabche glacier, Nepal (1967 to 2017)

*Lovell, A.M., Carr, J.R. & Stokes, C.R. 2018. Topographic controls on the surging behaviour of Sabche glacier, Nepal (1967 to 2017). Remote Sensing of Environment, 210**,** 434-443, 10.1016/j.rse.2018.03.036.*

Author contribution: I conducted the data collection and analysis, led the paper development, wrote the text and designed the figures. Co-authors provided editorial input and guidance on the development of the research. The paper has been published in Remote Sensing of Environment and the supplementary information from the paper has been incorporated into the thesis chapter.

Abstract: Using a combination of Landsat, Pléiades and CORONA satellite imagery from 1967 to 2017, we map changes in the terminus position, ice surface velocity and surface elevation of Sabche glacier, and report the first observations of surging behaviour in central Nepal. Our observations show that Sabche glacier surged four times over the last 50 years. The three most recent surges occurred at 10 to 11-year cycles, which is one of the shortest surge cycles ever recorded. Detailed analysis of the most recent surge (2012 onwards), indicates that the glacier advanced 2.2 km and experienced maximum velocities of 1.6 ± 0.10 m day^{-1}. During this surge, there was a surface elevation gain at the terminus of up to 90 ± 6.19 m a^{-1}, with a corresponding surface lowering of between 10 ± 6.19 and 60 ± 6.19 m a^{-1}, 3 km up-glacier of the terminus. This transfer of mass amounted to a volume of ~2.7 × 10^{7} ± 0.1 × 10^{7} m^{3} a^{-1}. Sabche glacier is the first surge-type glacier to be observed in the central Himalayas, but this is consistent with a previous global analysis which indicates that surge-type glaciers should exist in the region. We hypothesise that the surge is at least partially controlled by subglacial topography, whereby a major subglacial overdeepening and constriction 3 km up-glacier of the terminus provides resistance to glacier flow from the accumulation area to the ablation area. This overdeepening appears to store mass until a threshold is crossed, after which the glacier flows out of the subglacial depression and rapidly surges over a bedrock lip and down the valley. Thus, whilst the surges are likely to be facilitated by subglacial processes (e.g. changes in subglacial hydrology and/or basal

thermal regime), the topographic setting of the glacier appears to be modulating both the timing and duration of each surge.

4.1 Introduction

Surge-type glaciers fluctuate between long periods (10s to 100s of years) of slow flow and shorter periods (1 to 10 years) of faster flow, during which ice surface velocities increase by up to three orders of magnitude (e.g. Meier and Post, 1969; Clarke *et al.*, 1984; Jiskoot *et al.*, 1998). These oscillations are not thought to be directly triggered by external climate forcing, but rather by internal instabilities, linked to changing conditions at the glacier bed (Meier and Post, 1969; Sharp, 1988; Sevestre and Benn, 2015). During the slow, or quiescent, phase of the surge cycle, ice builds up in a reservoir area, and is then transferred rapidly down-glacier to a receiving area, during the fast, or surge, phase (e.g. Meier and Post, 1969; Murray *et al.*, 2000). There is a distinct pattern in the global distribution of surge-type glaciers, with large clusters found in Alaska-Yukon, Arctic Canada, Greenland, Iceland, Svalbard, and High Mountain Asia, while very few have been recorded in other regions such as the European Alps or Scandinavia (Sharp, 1988; Jiskoot *et al.*, 1998; Sevestre and Benn, 2015). While the lengths of the surge and quiescent phases tend to be consistent for individual surge-type glaciers, marked differences have been observed between these different geographic regions (e.g. Meier and Post, 1969; Murray *et al.*, 2003; Sevestre and Benn, 2015). Glaciers in Svalbard tend to have surge periods lasting between 3 and 10 years and quiescent periods lasting between 50 and 500 years (Dowdeswell *et al.*, 1991). In contrast, surge-type glaciers in Alaska-Yukon, the Pamirs, and Iceland, have much shorter surge (1 to 3 years) and quiescent (20 to 40 years) phases (Dowdeswell *et al.*, 1991; Murray *et al.*, 2003). These observed differences have led to the development of two main theories to explain surge-type glacier behaviour through either a thermal (Clarke *et al.*, 1984; Murray *et al.*, 2003) or hydrological (Kamb, 1987) mechanism. Thermally-driven glacier surges, common in Svalbard, are thought to be triggered by changes in the basal thermal regime, whereby a surge-front of warm-based and fast-flowing ice propagates down-glacier into stagnant cold-based ice and activates it into surging (Clarke *et al.*, 1984; Murray *et al.*, 1998). Thermal glacier surges can also be influenced by changes in the amount of bed deformation occurring under the glacier (Clarke *et al.*, 1984; Jiskoot *et al.*, 1998). In contrast to thermally-driven surges, temperate glaciers, such as Variegated glacier (Kamb *et al.*, 1985) and West Fork glacier (Harrison *et al.*, 1994) in Alaska, are thought to surge due to changes in their basal hydrology. Specifically, surging occurs when an efficient subglacial hydrological system switches to an inefficient cavity system generating increased water pressures at the bed and promoting rapid basal sliding (Kamb, 1987).

While surge-type glaciers are rare, constituting less than 1% of glaciers worldwide (Jiskoot *et al.*, 1998), they can provide valuable insight into glacier dynamics and the mechanisms triggering surge-type behaviour and fast glacier flow (Clarke, 1987). They can also present major hazards in populated areas through their influence on glacial lake outburst floods (GLOFs), rapid meltwater and sediment release, and the overriding of infrastructure (Richardson and Reynolds, 2000; Haeberli *et al.*, 2002; Kääb *et al.*, 2005). Moreover, knowledge of the spatial distribution of surge-type glaciers is vital for separating internal glacier dynamics from the climate change signal. This is especially important in High Mountain Asia, as the spatial distribution of surge-type glaciers in the region is highly variable (Sevestre and Benn, 2015) and the region is undergoing accelerated glacier changes due to climatic forcing (Gardelle *et al.*, 2012; Kääb *et al.*, 2012; Gardelle *et al.*, 2013).

Surge-type glaciers in High Mountain Asia have been well-documented in the Karakoram (Gardner and Hewitt, 1990; Hewitt, 2007; Copland *et al.*, 2009; Copland *et al.*, 2011; Quincey *et al.*, 2011), Pamirs (Dolgoushin and Osipova, 1975; Kotlyakov *et al.*, 2008) and Tien Shan (Dolgoushin and Osipova, 1975; Pieczonka and Bolch, 2015). However, no glacier surges have been recorded in the central Himalayas, which we define as the section of the Himalayan range extending from Northern India to Bhutan (Figure 4.1). Despite this, Sevestre and Benn (2015) predicted that surge-type glaciers should occur in this region, using the species distribution model Maxent. The model used climatic (mean annual temperature (MAT) and mean annual precipitation (MAP)) and geometric (glacier length and slope) data to predict the global distribution of surge-type glaciers. This is based on the compilation of a geodatabase of known surge-type glaciers which revealed that they preferentially cluster within a distinct climatic envelope (with a MAT range of -12 to +8°C and a MAP range of 165 to 2155 mm a^{-1}) and that they tend to be longer and have shallower mean surface slopes than normal glaciers in these regions (Figure 4.2) (Sevestre and Benn, 2015). In High Mountain Asia, the model accurately predicted the likelihood of surge-type glaciers in the Pamirs, Karakoram and Tien Shan. It also predicted surge-type glaciers in the central Himalayas, but they noted the absence of observations of surging in this region and speculated that the model might be over-predicting their occurrence (Sevestre and Benn, 2015).

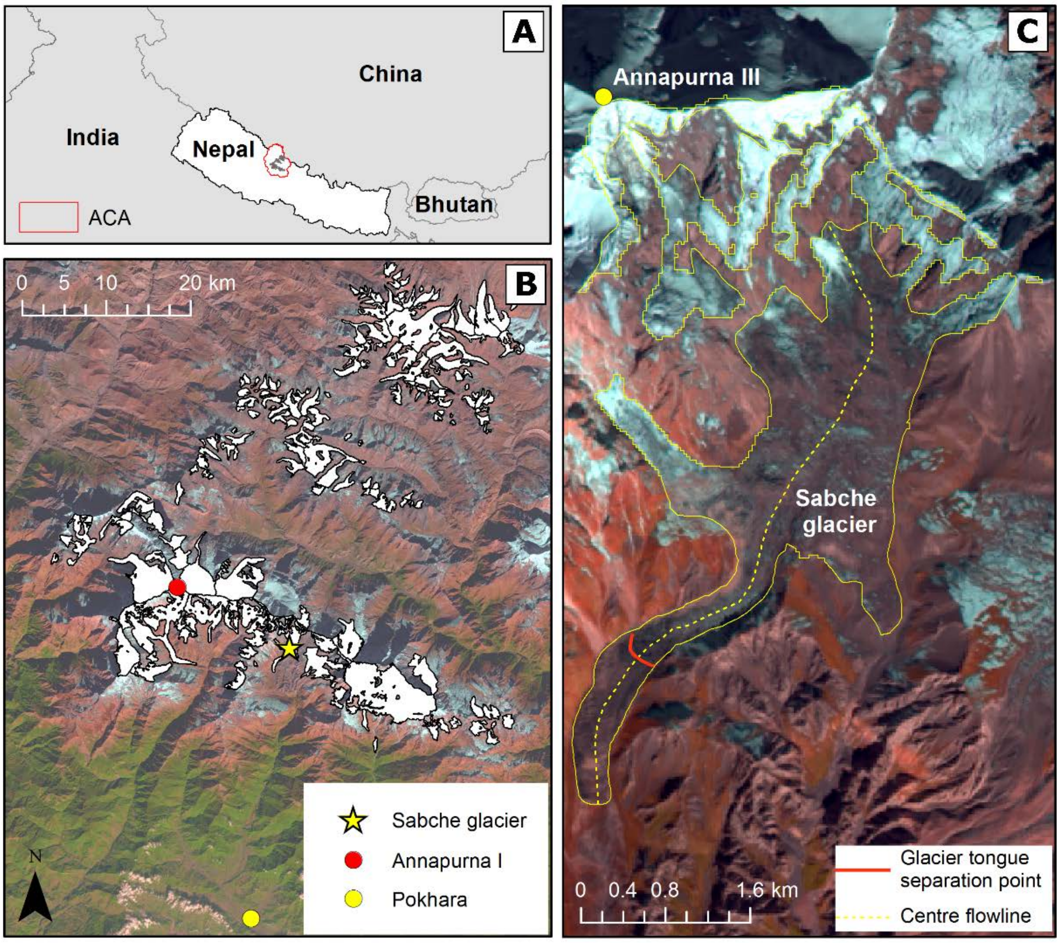

Figure 4.1: Study area map of Sabche glacier. A) Location of the central Himalayas and the Annapurna Conservation Area (ACA) in Nepal, B) location of Sabche glacier in the ACA and Pokhara and C) map of Sabche glacier with the central flowline (yellow dotted line), the approximate position of the recurring separation point between the main body of the glacier and its tongue (red line) and the location of Annapurna III. The white arrow indicates the location of the glacier terminus. The base image is a pan-sharpened Landsat 8 scene from 1st December 2015, courtesy of USGS.

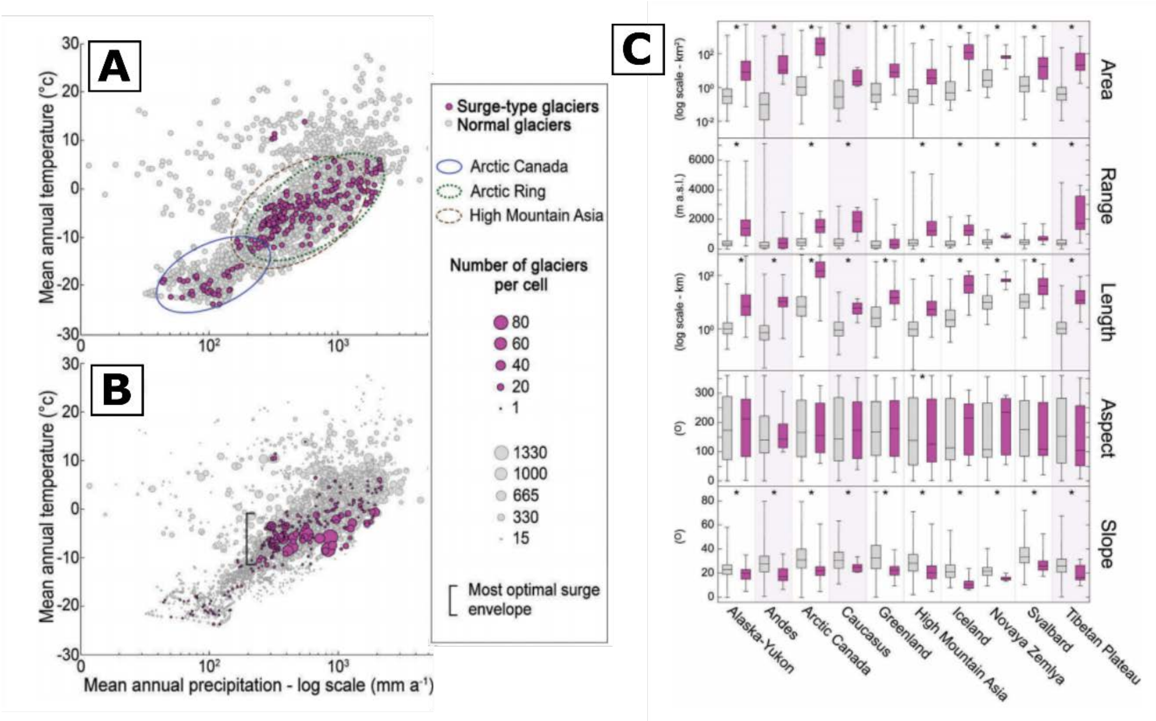

Figure 4.2: The climatic ranges and geometric properties used in Sevestre and Benn (2015) to predict the presence of surge-type glacier using the Maxent species distribution model (modified from Sevestre and Benn, 2015). This range is based on a global geodatabase of 2317 known surge-type glaciers. A) the climatic distributions of the populations of non-surge type (grey) and surge-type (pink) glaciers for mean annual precipitation against mean annual temperature, B) the same as plot A with additional information on the number of glaciers present in each 0.75° × 0.75° cell of the climate data, and C) the difference in glacier geometry between non-surge-type (in grey) and surge-type (in pink) glaciers across the main surge cluster. The final Maxent model output used to predict the presence of surge-type glaciers was based on four variables: mean annual temperature, mean annual precipitation, length and slope.

In this paper, we use observations of frontal position, ice surface velocity and surface elevation change to identify a surge-type glacier in the large (10 km wide) Sabche cirque basin in the Annapurna Conservation Area (ACA) region in central Nepal, hereafter referred to as Sabche glacier. This represents the first surge-type glacier to be recorded in the central Himalayas. We compare its characteristics to surge-type glaciers elsewhere in High Mountain Asia and other geographic regions, and discuss the possible mechanisms controlling its behaviour.

4.2 Study site

Sabche glacier (28.56° N, 84.01° E) (Figure 4.1) is in the south-west of the ACA, on the south-east facing slope of Annapurna III (location in Figure 4.1C). It is one of the larger glaciers in the ACA with an area of 9.1 km^2 in 2014. It has a mean surface slope of 28.2°, a mean aspect of 178° and descends across a large altitudinal range, from 7489 to 3773 m asl, based on a glacier outline we digitised from a Landsat 8 scene from 1st December 2015 (Table 4.1). Over half of the glacier's area (5.2 km^2, 57%) is covered in supraglacial debris and it sits in the steep-sided, bowl-shaped Sabche basin, and flows into a narrow outlet, forming a long (3 km) glacier tongue (Figure 4.1C).

Sabche glacier is located at the head of, and feeds into, the Seti river, which flows through highly populated areas, including Pokhara (population ~400,000), located 30 km down-stream. The Seti river has a history of dramatic, and occasionally deadly, flooding events (Fort, 1987; Oi *et al.*, 2014). Between 1000 and 500 years ago, catastrophic debris-flows led to the formation of the large sediment-filled basin upon which Pokhara is located (Yamanaka, 1982). Sedimentological studies indicate that the majority of clasts (90%) deposited by these events were provided by perched glacial tills in the large Sabche cirque, originally derived from the glaciated cirque headwall (Fort, 1987). While it has been suggested that the debris-flows were triggered by a series of earthquakes between A.D. 1100 and 1344 (Schwanghart *et al.*, 2015), the mechanisms capable of transporting sufficiently large volumes of debris down-valley are still open to debate, with GLOFs and rock-ice avalanches proposed as potential agents (Fort, 1987; Schwanghart *et al.*, 2015). More recently, in May 2012, hyper-concentrated floods in the Seti river killed 13 people, triggered by a massive rock and ice avalanche from Annapurna IV (Oi *et al.*, 2014; Evans and Delaney, 2015; Schwanghart *et al.*, 2015).

The impact of Sabche glacier's behaviour on river outputs and the related flooding events has not been assessed. However, surge-related outburst floods have been observed in other regions, including: i) Skeiðarárjökull in Iceland where, in 1991, a glacier surge led to the partial drainage of the subglacial lake Grímsvötn (Björnsson, 1998); ii) Bering glacier in Alaska, where an outburst flood coincided with the termination of the first of a two-stage surge between 1993 and 1995 (Fleisher *et al.*, 1998; Burke *et al.*, 2010); and iii) Medvezhiy glacier, in the Pamirs (Dolgoushin and Osipova, 1975). Based on the severity of previous floods in the Seti river, the potential contribution of Sabche glacier to major flooding events warrants further investigation.

Table 4.1: Summary of satellite imagery used. The Landsat and CORONA imagery was obtained from the USGS and the Pléiades imagery was obtained from ESA.

Scene name	Date	Satellite	Spatial resolution (m)

DS1038-2134DA068	23/01/1967	CORONA KH-4A	3
DS1112-1007DF179_179	19/11/1970	CORONA KH-4B	2
DZB1209-500033L023001	04/11/1974	CORONA KH-9	6
LT51420401988325BKT01	20/11/1988	Landsat 5	30
LT51420401989311BKT00	07/11/1989	Landsat 5	30
LT51420401990026BKT00	26/01/1990	Landsat 5	30
LT05_L1TP_142040_19910926_20170125_01_T1	26/09/1991	Landsat 5	30
LT51420401991349ISP00	15/12/1991	Landsat 5	30
LT51420401992320ISP00	15/11/1992	Landsat 5	30
LT05_L1TP_142040_19921217_20170121_01_T1	17/12/1992	Landsat 5	30
LT51420401993354ISP00	20/12/1993	Landsat 5	30
LT51420401994357ISP00	23/12/1994	Landsat 5	30
LT51420401995312ISP00	08/11/1995	Landsat 5	30
LT51420401996347ISP00	12/12/1996	Landsat 5	30
LT51420401998256BIK00	13/09/1998	Landsat 5	30
LE71420402000350SGS00	15/12/2000	Landsat 7	15
LE71420402002003SGS00	03/01/2002	Landsat 7	15
LE71420402002339SGS00	05/12/2002	Landsat 7	15
LE71420402003006SGS00	06/01/2003	Landsat 7	15
LE71420402003022SGS00	22/01/2003	Landsat 7	15
LE71420402003326ASN01	05/10/2003	Landsat 7	15
LE71420402004345PFS00	10/12/2004	Landsat 7	15
LE71420402004361PFS00	26/12/2004	Landsat 7	15
LE71420402005363PFS00	29/12/2005	Landsat 7	15
LE71420402006318PFS00	14/11/2006	Landsat 7	15
LE71420402007305PFS00	01/11/2007	Landsat 7	15
LE71420402008308SGS00	03/11/2008	Landsat 7	15
LE71420402009342SGS00	08/12/2009	Landsat 7	15
LE71420402010345PFS00	11/12/2010	Landsat 7	15
LE71420402010361PFS00	27/12/2010	Landsat 7	15
LE71420402011332PFS00	28/11/2011	Landsat 7	15
LE71420402011348PFS00	14/12/2011	Landsat 7	15
LE71420402011364PFS00	30/12/2011	Landsat 7	15
LE71420402012287PFS00	13/10/2012	Landsat 7	15
LE71420402012303PFS00	29/10/2012	Landsat 7	15
LE71420402013337EDC00	03/12/2013	Landsat 7	15
LC81420402013361LGN00	27/12/2013	Landsat 8	15
DIM_PHR1A_P_201410120519086_SEN_2284096101-001	12/10/2014	Pléiades 1A	0.5
DIM_PHR1A_P_201410120519323_SEN_2325847101-001	12/10/2014	Pléiades 1A	0.5

LC81420402014284LGN00	11/10/2014	Landsat 8	15
LE71420402014340EDC00	06/12/2014	Landsat 7	15
LC81420402015095LGN0	05/04/2015	Landsat 8	15
LC81420402015127LGN00	07/05/2015	Landsat 8	15
LC81420402015319LGN00	15/11/2015	Landsat 8	15
DIM_PHR1B_P_201511190518545_SEN_2284098101-001	19/11/2015	Pléiades 1B	0.5
DIM_PHR1B_P_201511190519139_SEN_2301729101-001	19/11/2015	Pléiades 1B	0.5
LC81420402015335LGN00	01/12/2015	Landsat 8	15
LC81420402015351LGN00	17/12/2015	Landsat 8	15
LC81420402016002LGN00	02/01/2016	Landsat 8	15
LC81420402016018LGN00	18/01/2016	Landsat 8	15
LC81420402016034LGN00	03/02/2016	Landsat 8	15
LC81420402016306LGN00	01/11/2016	Landsat 8	15
LC81420402016354LGN00	19/12/2016	Landsat 8	15
LC81420402017020LGN00	20/01/2017	Landsat 8	15
LC81420402017084LGN00	25/03/2017	Landsat 8	15
LC08_L1TP_142040_20170613_20170628_01_T1	13/06/2017	Landsat 8	15

4.3 Methods

4.3.1 *Data acquisition*

Landsat satellite images were obtained at annual to sub-annual intervals from 1988 to 2017 (Landsat 5 to 8) from the US Geological Survey (USGS: https://earthexplorer.usgs.gov/) (details of individual scenes are summarised in Table 4.1). The spatial resolution of the Landsat scenes varied from 15 to 30 m (Table 4.1). Where possible, scenes were chosen between October and February of each year to minimise the likelihood of cloud and snow cover associated with the Asian monsoon (see Table 4.1 for exact dates). There were no discernible seasonal differences in terminus position (<15 m) between October and February during the quiescent phases. CORONA satellite imagery from the KH-4A, KH-4B and KH-9 satellite missions were obtained from the USGS for the years 1967, 1970 and 1974, with spatial resolutions ranging from 2 to 6 m (Table 4.1). These dates were dictated by the availability of cloud-free imagery. In order to minimise topographic distortion, a subset image of each CORONA scene was created to cover the glacier terminus area and these were then geo-referenced to a Landsat 8 base image (LC81420402015335LGN00)

(Table 4.1) by matching easily recognisable, stable features around the terminus in the two scenes using tie-points. This yielded root mean square (RMS) values between 11 and 20 m, which is comparable to the pixel resolution. The co-registration error for the CORONA imagery was calculated by measuring the displacement between 15 points on known stable ground between the CORONA images and the Landsat base image. Mean co-registration error was 35 m for the 1967 scene, 36 m for the 1970 scene and 24 m for the 1974 scene. These errors are much smaller than the observed terminus changes. Two pairs of Pléiades satellite panchromatic stereo scenes, from 12th October 2014 and 19th November 2015, were also obtained from the European Space Agency (ESA) (Table 4.1). The scenes were chosen to capture the before- and after-surge configuration of the glacier and for their minimal snow and cloud cover. These scenes had a spatial resolution of 0.5 m. The 2014 stereo pair had along-track angles of -9.6°and 4.8° (convergence angle of 14.4°) and the 2015 pair had along-track angles of -8° and 3.4° (convergence angle of 11.4°).

4.3.2 *Glacier terminus position change*

Glacier terminus positions were digitised manually from CORONA scenes in 1967, 1970 and 1974 and from Landsat scenes between 1988 and 2017 at roughly annual intervals, and sub-annually (1- to 6-month intervals) where cloud-free images were available (Table 4.1). Glacier terminus position change was calculated using the well-established box method (e.g. Moon and Joughin, 2008), using a curvilinear box to account for a bend in the valley (Lea *et al.*, 2014). The rate of terminus position change was calculated in both m day^{-1} and m a^{-1} to allow comparisons with other studies. Manual digitising was conducted by the same person to maximise consistency in the method and interpretation of the glacier terminus position. The digitising error for the glacier terminus position changes was assessed by repeatedly digitising the terminus and measuring the maximum variation between the digitised lines from a representative scene per satellite data type. Digitising errors ranged from 11 to 26 m.

4.3.3 *Glacier velocities*

East/west and north/south surface displacements were mapped using feature tracking in COSI-Corr software (Leprince *et al.*, 2007) on four pairs of band 8 panchromatic scenes from the Landsat 7 ETM+ and Landsat 8 OLI TIRS sensors (15 m resolution) taken between 2011 and 2016. The intervals between the images in each pair used to calculate the velocity measurements depended on image availability. Some scenes were affected by cloud or snow cover and therefore could not be used. Consequently, intervals between scenes ranged from 16 to 48 days. Glacier velocities were not calculated for the period prior to 2011 due to the lack of suitable imagery. Before calculating velocity, the displacement maps were post-processed using tools in COSI-Corr to filter out noise with a signal-to-noise ratio of less than 0.9, following methods by Scherler *et al.* (2008) (Figure 4.3). The correlations derived from the Landsat 7 scenes required additional filtering to remove striping introduced by attitude effects in the satellite imagery (Scherler *et al.*, 2008) (Figure 4.4). Shadow, cloud, and areas affected by snowfall, especially where snow was present in one scene of the pair and not the other, tended to generate noise in the velocity output and were masked out and a simple directional filter was applied to remove erroneous displacement values that clearly contradicted the direction of general glacier flow (Figure 4.3). Daily velocities (m day^{-1}) were calculated by dividing the velocity maps by the number of days in each interval. Error was estimated for each map by calculating the mean of the velocity values extracted from 30 points located off-glacier around Sabche glacier (location of points in Figure 4.5). The same points were used for each velocity map and they were placed on terrain that was judged to be stable (e.g. vegetated or with shallow slopes where possible). Errors for individual velocity maps ranged from ± 0.06 m day^{-1} to ± 0.12 m day^{-1} (Figure 4.5). The glacier outline, separating on- and off-glacier areas was manually digitised from Landsat imagery.

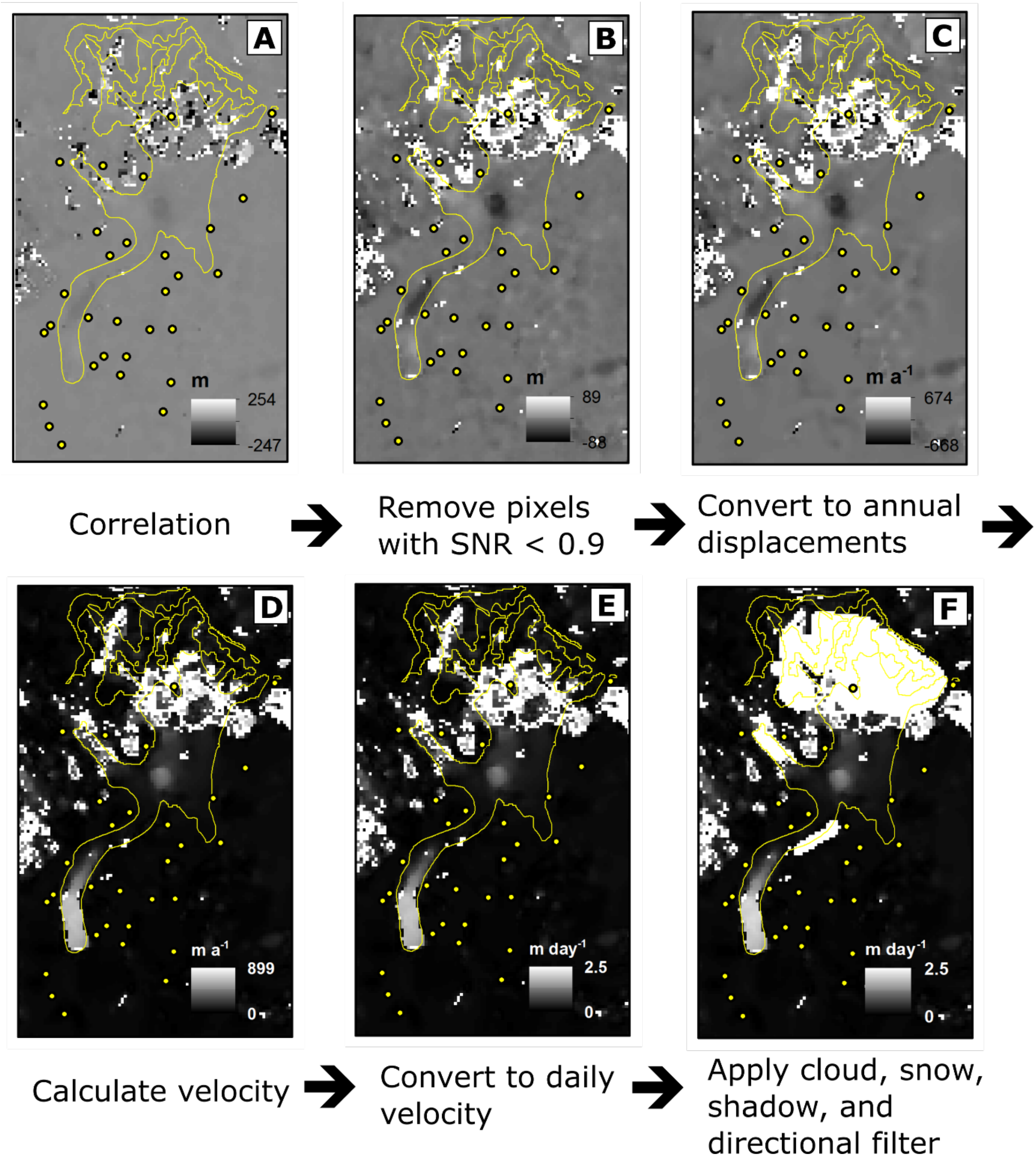

Figure 4.3: Example flow chart of velocity calculation and correction between the 1st November 2016 and 19th December 2016 Landsat 8 panchromatic scenes. A) Initial correlation map (East/West displacement), B) correlation map with Signal-to Noise ratio values < 0.9 removed (East/West displacement), C) conversion to annual displacements (East/West displacement), D) velocity calculation, E) conversion to daily velocity and F) final velocity map after cloud, snow, shadow and directional filters have been applied.

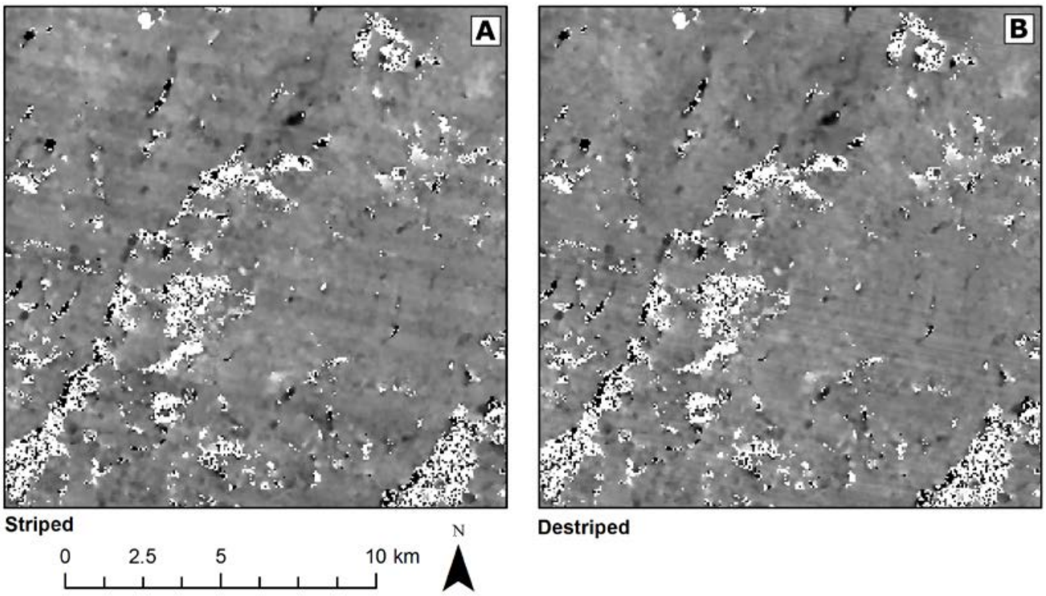

Figure 4.4: Example of de-striping on the East/West displacement map derived from Landsat 7 panchromatic scenes from 28th November 2011 and 30th December 2011.

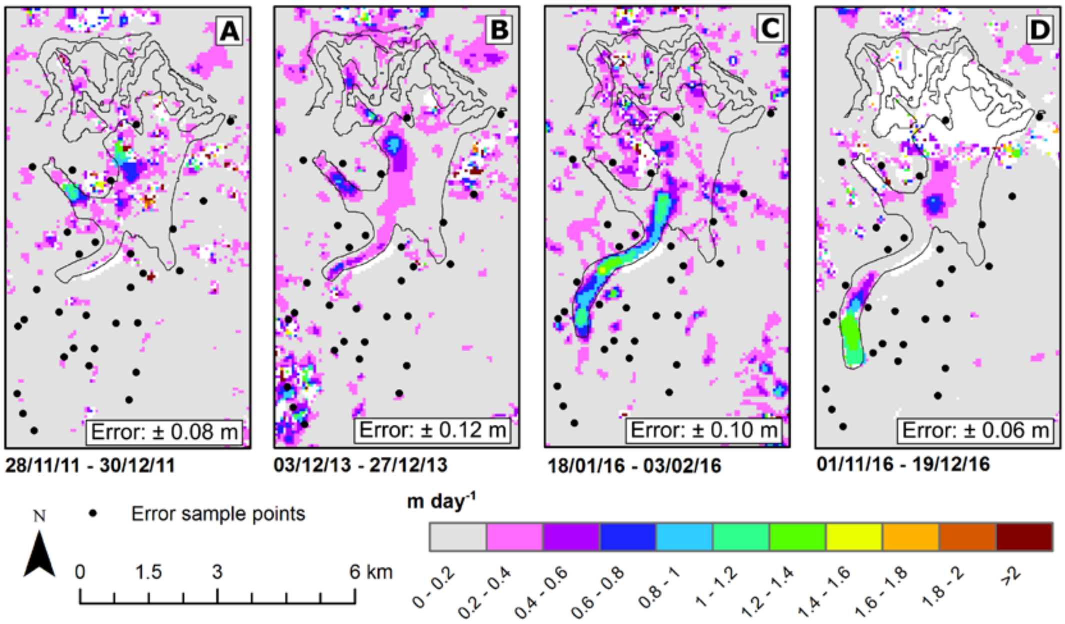

Figure 4.5: Calculating velocity error. Velocity fields both on- and off-glacier for velocity calculated between pairs of Landsat panchromatic scenes using feature tracking methods. A) 28th November 2011 to 30th December 2011, B) 3rd December 2013 to 27th December 2013, C) 18th January 2016 to 3rd February 2016 and D) 1st November 2016 to 19th December 2016. The black

dots indicate the off-glacier sample locations of velocity error. Mean off-glacier errors are quoted in the boxes.

4.3.4 *Digital elevation models and changes in glacier surface elevation and volume*

Digital elevation models (DEMs) of Sabche glacier were generated from the 12th October 2014 and 19th November 2015 Pléiades stereo pairs using Erdas Imagine's Photogrammetry Suite. The Pléiades scenes, which were obtained at primary processing level, were georeferenced using just the rational polynomial coefficients (RPCs) provided with each scene because we did not have any ground control points (GCPs) for the area. Over 100 tie-points were used on each stereo pair to minimise the root mean squared error (RMSE) of the triangulation models. Both stereo pairs had RMSE values of 0.07 pixels. Following Berthier *et al.* (2014), we chose an output spatial resolution of 4 m for the DEMs to decrease processing time but maintain sufficient detail for analysis. Due to the lack of accurate GCPs on Sabche glacier, it was only possible to generate relative DEMs using tie-points rather than absolute DEMs. However, a previous assessment of the quality of a pair of absolute DEMs generated with GCPs and a pair of relative DEMs generated without GCPs, revealed that the mean off-glacier elevation differences between the absolute and relative pairs were very similar (within 0.03 m) once both pairs had been horizontally and vertically co-registered using the stable (off-glacier) terrain (Berthier *et al.*, 2014).

The Pléiades DEMs were assessed and corrected following Nuth and Kääb (2011) (Figure 4.6). First, areas in the DEMs affected by noise due to cloud cover and shadow were filtered out. Next, the DEMs were horizontally and vertically co-registered by iteratively minimising the root mean square height difference of stable (off-glacier) terrain (Nuth and Kääb, 2011) (Figure 4.6A and B). It was calculated that the 2014 Pléiades DEM needed to be shifted 45.34 m, -18.47 m and -201.25 m in the x, y and z direction, respectively, to align the DEMs. Following this, the DEMs were assessed for an elevation-dependent bias by plotting elevation differences against elevation on stable terrain only (Nuth and Kääb, 2011). However, no obvious bias was observed and, as such, no correction was undertaken (Figure 4.6F). Due to the lack of GCPs and other high resolution DEMs of the area, it was not possible to validate the quality of the DEMs against an independent dataset. However, the relative error between the DEMs was assessed using the mean, median and standard deviation of the differences between the two datasets on stable terrain (see Nuth and Kääb,

2011) (Table 4.2). The normalised median absolute deviation (NMAD) was used as an additional assessment of vertical precision between the datasets which is less sensitive to outliers compared with the standard deviation (see Berthier *et al.*, 2014) (Table 4.2). Error in the text is quoted as the standard deviation (m a^{-1}) of elevation differences on stable terrain (Nuth and Kääb, 2011).

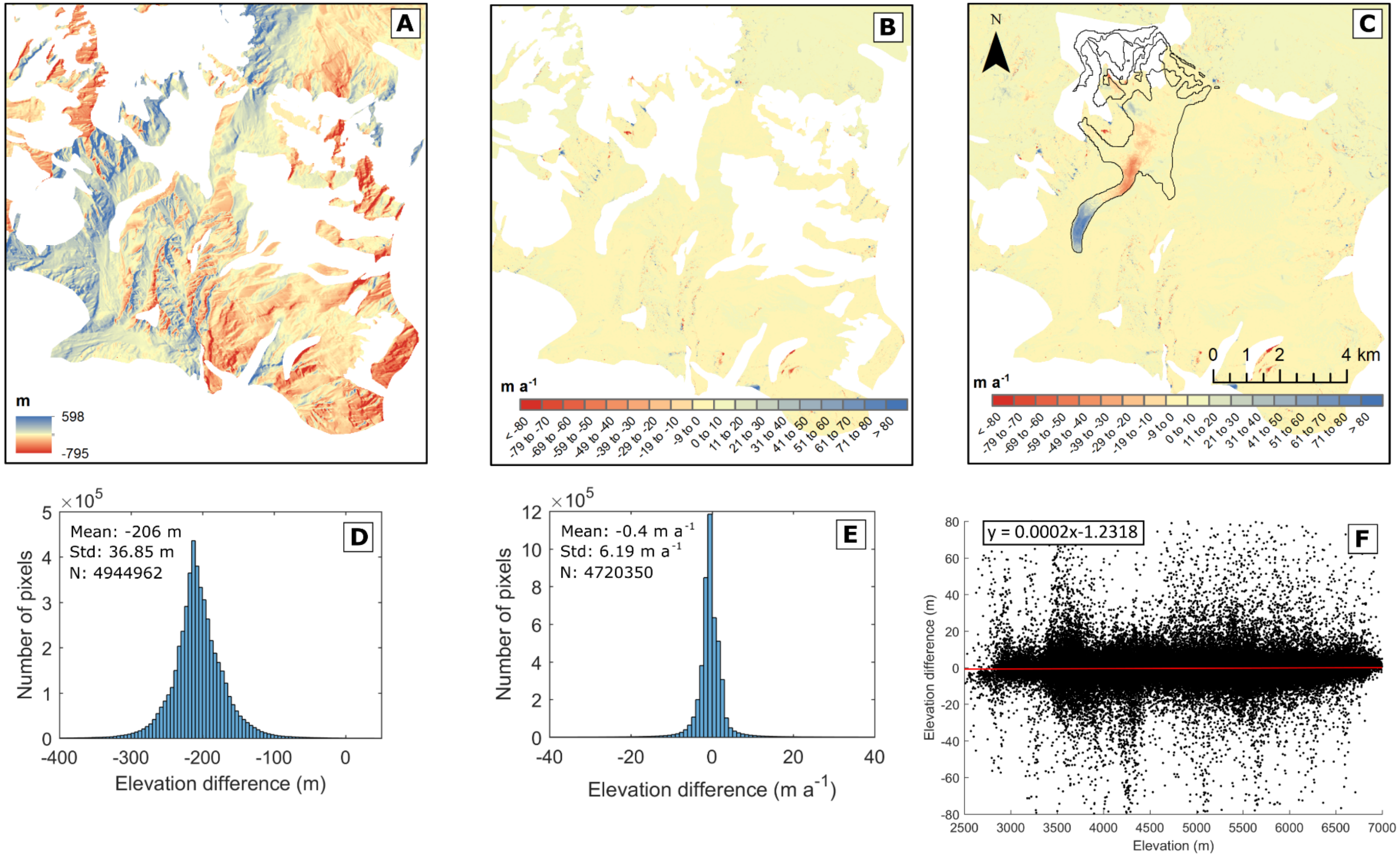

Figure 4.6: DEM co-registration and off-glacier statistics. A) DEM of difference of off-glacier and shadow/cloud masked areas before co-registration, B) DEM of difference of off-glacier and shadow/cloud masked areas after co-registration, converted to m a-1, C) DEM of difference of off- and on-glacier areas with areas affected by shadow/cloud masked out, D) off-glacier statistics of DEM of difference before co-registration, E) off-glacier statistics of DEM of difference after co-registration (m a^{-1}) and F) elevation difference plotted against elevation on stable (off-glacier) terrain. The equation of the trendline shows no obvious elevation-dependant bias following co-registration of the 2014 and 2015 Pléiades DEMs.

Table 4.2: Statistics of the off-glacier elevation differences between the two DEMs (mean, median, standard deviation and NMAD), calculated for ~4 900 000 pixels, before and after co-registration and converted to m a^{-1}.

	DEM before co-registration	**DEM after co-registration**	**DEM after co-registration (m a^{-1})**
Mean (m)	-206.01	-0.42	-0.37
Median (m)	-208	-0.6	-0.54
Standard deviation (m)	36.85	6.83	6.19
NMAD (m)	27.43	1.99	1.81

The large horizontal and vertical shifts required to co-register the DEMs were most likely a result of the tools we used to process the DEMs. Much smaller shifts can be obtained using alternative tools (E. Berthier, personal communication, 2018), but this does not affect the relative differences in elevation that we report in this paper. The DEM corrections, following established correction procedure by Nuth and Kääb (2011), reduced the standard deviation of elevation differences on stable terrain from 36.85 m to 6.83 m (6.19 m a^{-1}) and the mean elevation difference from -206.01 to -0.42 m (-0.37 m a^{-1}) (Table 4.2 and Figure 4.6D and E). This error is much smaller than the on-glacier surface elevation changes we expect to observe and is consistent with the error values of corrected DEMs in other studies (Nuth and Kääb, 2011; King *et al.*, 2017). We are therefore confident that DEM co-registration has reduced geolocation errors sufficiently to obtain useful surface elevation change data. Figure 4.6D and E show summaries of elevation differences on the stable terrain before correction and after correction. Glacier surface elevation change was calculated by subtracting the 2014 DEM from the 2015 DEM and was converted into annual elevation change for comparison with other studies. Only relative, rather than absolute, surface elevation change was calculated, due to the lack of GCPs. However, this is sufficient for our analysis which aims to assess how Sabche glacier's surface elevation on 19th November 2015 has changed relative to 12th October 2014. Mean glacier elevation changes per 200 m elevation band were calculated for the lower and intermediate elevations on the glacier (3600-4800 m elevation). Mean elevation changes were not calculated for the upper elevation bands due to large gaps in the data.

Surface elevation change was converted into volume change for the area of maximum elevation loss and the area of maximum elevation gain (locations in Figure 4.7) by multiplying the on-glacier elevation differences by the area of the glacier sub-sections. We did not calculate volume change for the upper glacier area due to a large number of data gaps. The upper and lower error boundaries of volume change were calculated by adding/subtracting the mean off-glacier error from the mean elevation change of each glacier sub-section and multiplying by its area. Glacier geometry including area, centre flowline length, hypsometry, altitudinal range and aspect were calculated for Sabche glacier using Landsat imagery and the ASTER GDEM v2.

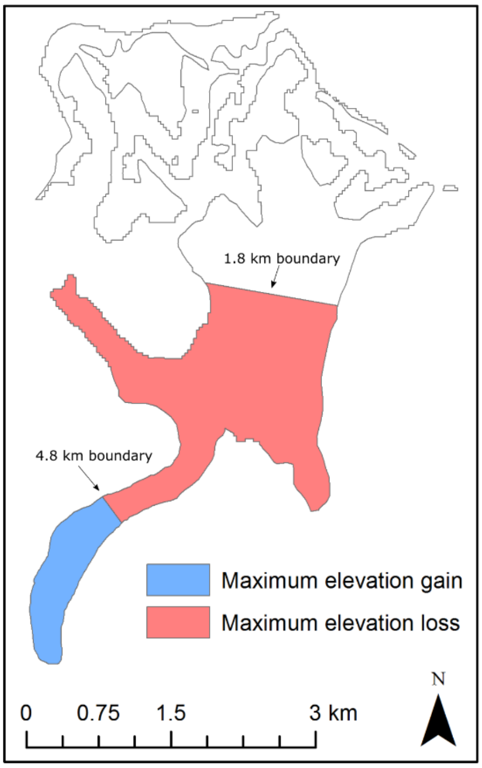

Figure 4.7: The locations of the areas of maximum elevation loss and maximum elevation gain used to calculate volume change. The area of maximum elevation loss was between 1.8 and 4.8 km distance from the headwall and the area of maximum elevation gain was between 4.8 km distance from the headwall to the terminus.

4.4 Results

4.4.1 *Glacier frontal position change (1967 to 2017)*

Terminus position measurements show that Sabche glacier advanced four times between 1967 and 2017 (Figure 4.8). There was an interval of at least 17 years between the first period of advance (measured in 1974) and the beginning of the second period of advance (1991) and the last three advance periods occurred at 10 to 11-year intervals (Figure 4.8). However, we may have missed an additional advance due to the data gap between 1974 and 1988, given the interval between the three most recent advances. The maximum distance of terminus advance varied between the first three surges (Figure 4.8). During both the second and third advance periods, the terminus had an initially rapid advance (~1 m day^{-1}, ~365 m a^{-1}) lasting several months, reducing into a less rapid advance (<0.5 m day^{-1}, <180 m a^{-1}) and followed by retreat. The most recent advance period, from 2012 onwards, was of a much greater magnitude and more rapid than the previous three, with a maximum advance rate of 5.2 m day^{-1} (1900 m a^{-1}) between May and November 2015 and a maximum advance of 2.2 km, relative to 1967, at the most recent measurement date (25th March 2017) (Figure 4.8). This advance also slowed down towards the end of the measurement period (~0.5 m day^{-1}, ~180 m a^{-1} between January and March 2017). High magnitude and rapid retreats in terminus position followed the first three periods of advance in 1974 (-1.5 km), 1995 (-1 km) and 2008 (-0.8 km) (Figure 4.8). These retreat events occurred where the glacier tongue disconnected from the main glacier body as a result of localised acceleration and glacier extension caused by a large increase in slope (Figure 4.1C, Figure 4.9 and Figure 4.11D).

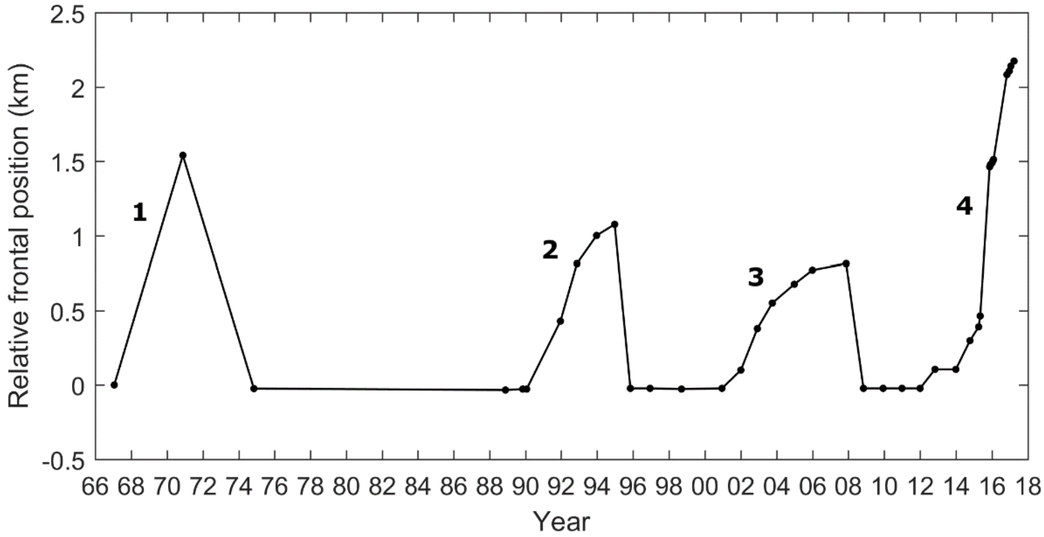

Figure 4.8: Glacier frontal position changes of Sabche glacier relative to 1967 with individual advance (surge) periods numbered (1 to 4). Circles plot measurement dates.

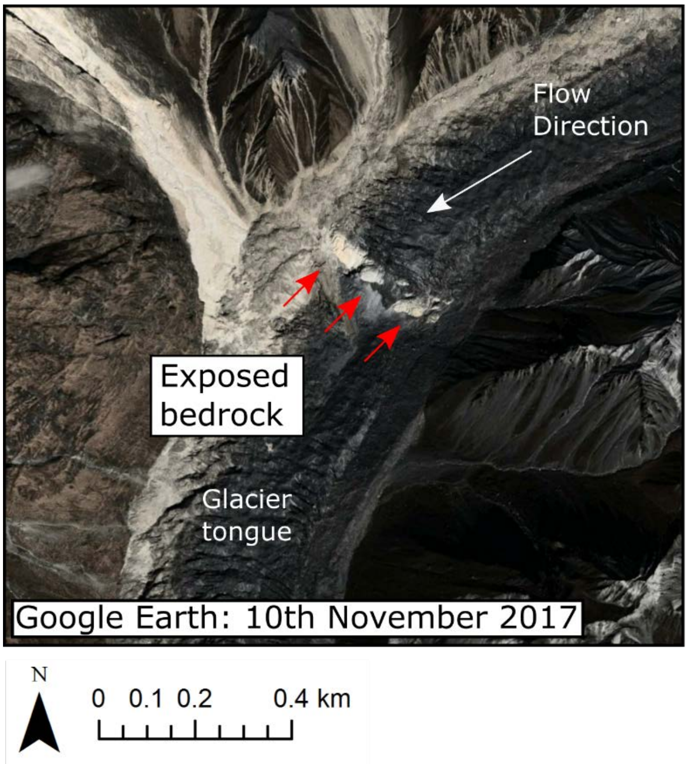

Figure 4.9: A large increase in slope encouraging localised acceleration and extension, leading to the separation of Sabche glacier's tongue from the main part of the glacier and the exposure of bedrock in November 2017. See Figure 4.1 for the position of the recurring separation point on Sabche glacier. Background image: Digital Globe imagery on Google Earth on 10th November 2017.

4.4.2 *Ice surface velocities (2011 to 2016)*

Ice surface velocities were calculated between 2011 and 2016, covering the most recent advance period. In November and December 2011, before the most recent terminus advance, glacier tongue velocities ranged from 0 to 0.8 ± 0.08 m day^{-1} (~290 m a^{-1}) and there were minimal changes in terminus position (Figure 4.10B). By December 2013, coinciding with the beginning of the most recent advance period (Figure 4.10A), higher velocities (0.4 to 0.8 ± 0.12 m day^{-1}; ~140 to 290 m a^{-1}) had spread over a large area of the glacier tongue (Figure 4.10C). Between January and February 2016, velocities at the tongue ranged between 0 and 1.6 ± 0.10 m day^{-1} (580 m a^{-1}) and increased velocities extended throughout most of the glacier tongue and up to a distinct bowl-shaped area 3 km up-glacier of the terminus (Figure 4.10D). This period of increased velocities coincided with rapid terminus advance (Figure 4.10A). By November and December 2016 (Figure 4.10E), the highest velocities had shifted to the lower section of the tongue, and the upper section had reverted to slow-flow, with velocities of < 0.2 ± 0.06 m day^{-1} (~70 m a^{-1}).

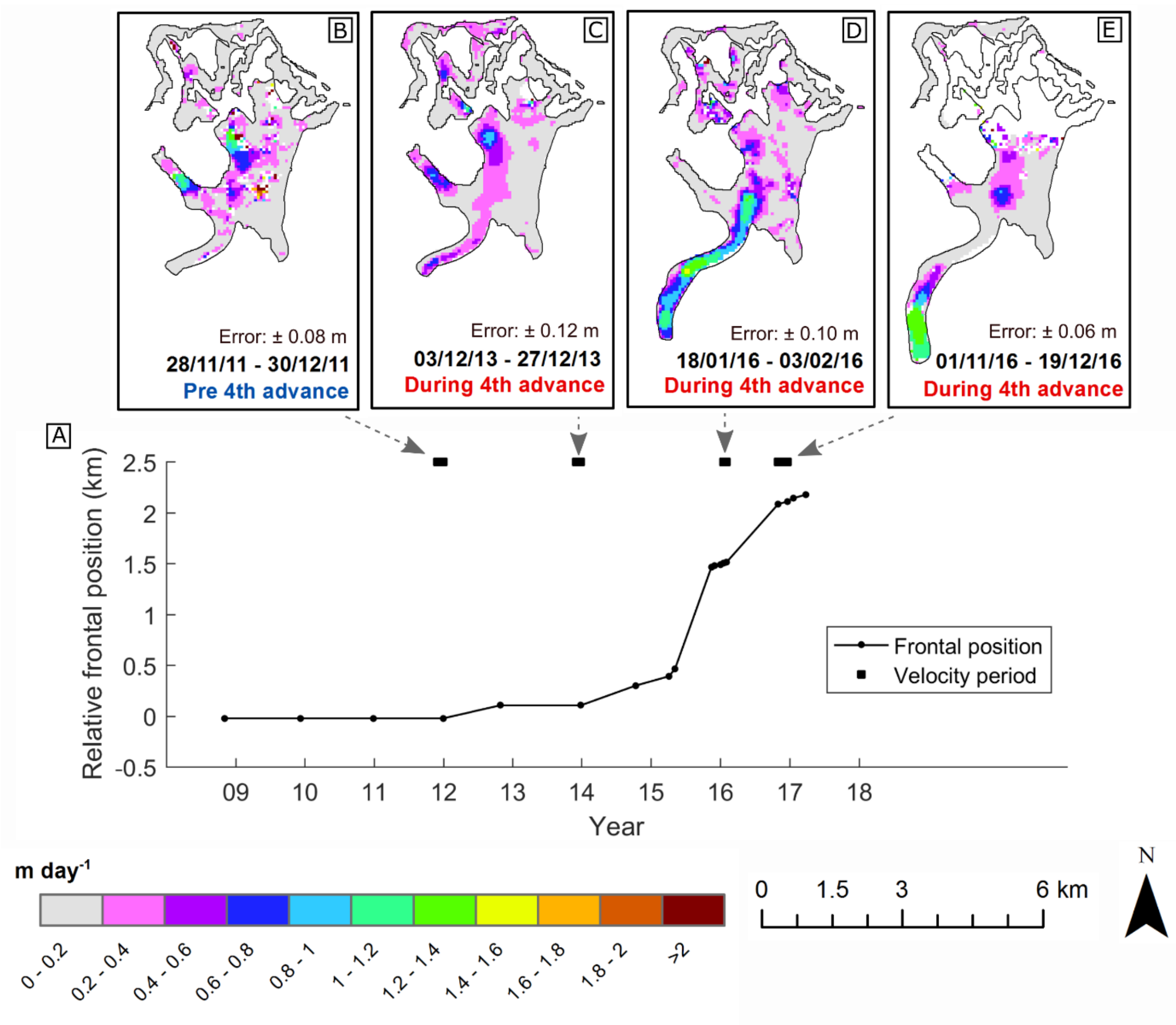

Figure 4.10: Velocities (m day^{-1}) on Sabche glacier during 2011, 2013 and 2016 (B-E), arranged along a timeline with frontal position changes (A) for the same period. The glacier outlines show changes in the frontal positions of the glacier. The velocities were calculated using 15 m resolution imagery.

4.4.3 *Glacier surface elevation and volume changes (12th October 2014 to 19th November 2015)*

Between 12th October 2014 and 19th November 2015, Sabche glacier experienced a surface elevation gain of up to 90 ± 6.19 m a^{-1} at the glacier terminus and surface lowering of between 10 ± 6.19 and 60 ± 6.19 m a^{-1}, 2-3 km further up-glacier, with the maximum surface lowering occurring in a distinct bowl-shaped area at the top of the glacier tongue (Figure 4.11A). This change in elevation coincided with the advance of the terminus

(Figure 4.11B and C). The largest surface lowering along the centre line occurred between 1.8 and 4.8 km from the glacier headwall (Figure 4.11A and D), and the largest surface elevation gain occurred from 4.8 km onwards (Figure 4.11A and D). Mean glacier elevation change per 200 m elevation band was positive near the glacier terminus (3600-4200 m elevation), ranging from 22 ± 6.19 m a^{-1} to 54 ± 6.19 m a^{-1} (Figure 4.11E). In the intermediate elevation bands, between 4200 and 4800 m elevation, mean elevation change was negative, with a maximum mean surface lowering of -18 ± 6.19 m a^{-1} (Figure 4.11E). The area of maximum elevation loss, between 1.8 and 4.8 km distance from the headwall had a net volume change of $-2.8 \times 10^7 \pm 0.1 \times 10^7$ m^3 a^{-1} and the area of maximum elevation gain at the glacier terminus, from 4.8 km onwards, had a net volume change of $+2.7 \times 10^7 \pm 0.3 \times 10^6$ m^3 a^{-1} (Figure 4.11A and D).

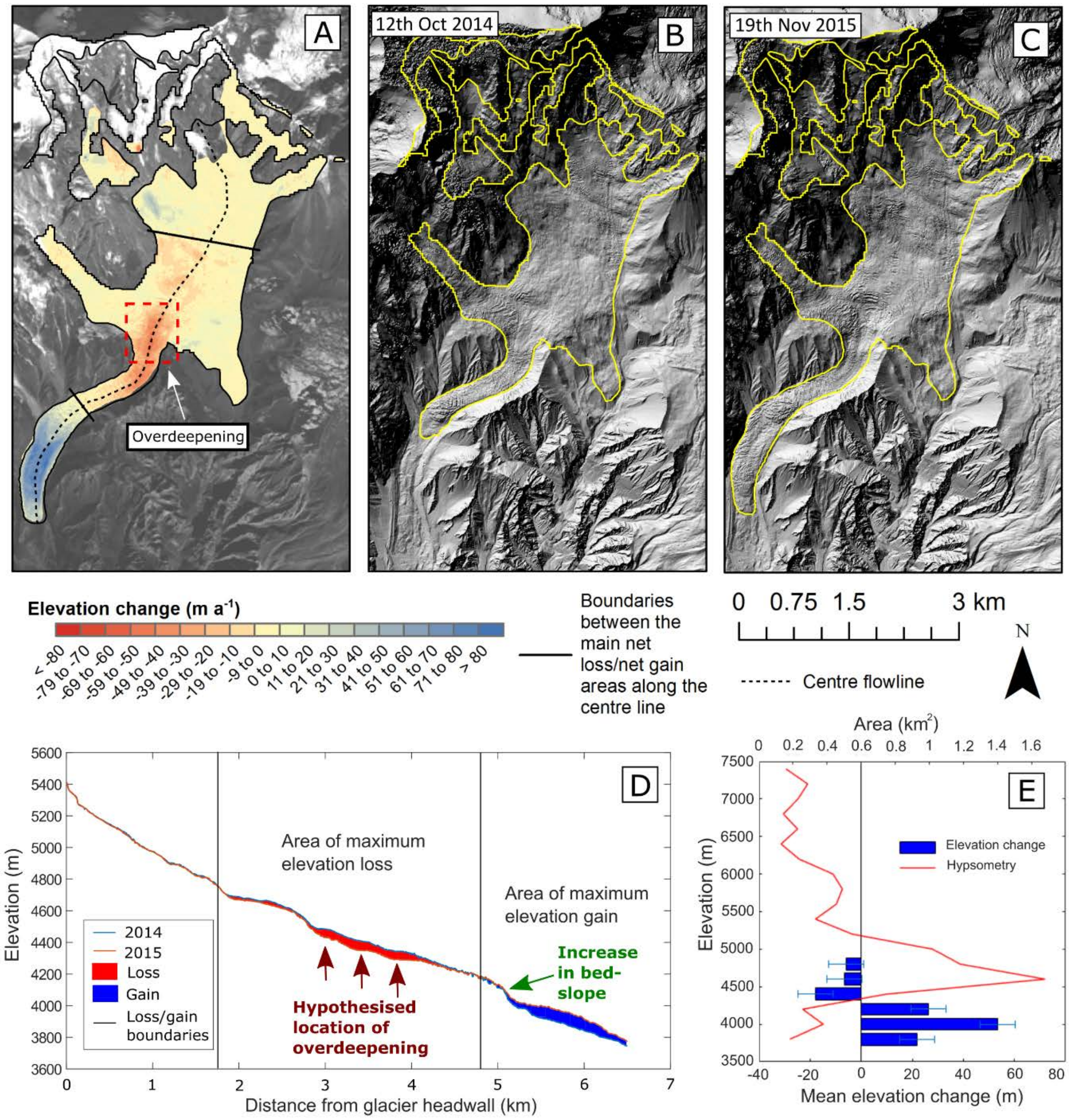

Figure 4.11: Surface elevation change on Sabche glacier. A) Surface elevation change (m a-1) calculated from the 12th October 2014 (towards the beginning of the surge) and 19th November 2015 (middle of the surge) Pléiades DEMs, and the location of the glacier central flowline, the red dashed box indicates the location of the overdeepening B) 2014 DEM hill-shade (beginning of surge), C) 2015 DEM hill-shade (middle of surge) and D) central flowline long profiles of the 2014 and 2015 DEMs revealing surface elevation changes between the two dates, as the surge progressed. Red areas show net elevation loss, blue areas show net elevation gain. The black lines show the boundary between the sections of loss and gain at 1.8 and 4.8 km distance from the headwall. The large increase in slope in the bed topography at the location where the glacier tongue repeatedly disconnects is indicated with a green arrow. The location of the hypothesised subglacial overdeepening is indicated with a maroon arrow. E) Mean elevation change (m a^{-1}) on Sabche glacier calculated between 12th October 2014 and 19th November 2015 per 200 m elevation band and the distribution of glacier area with elevation (red line).

4.4.4 *Glacier surface morphology*

Changes in the glacier's surface morphology were analysed using the Pléiades DEMs. Between 12th October 2014 (towards the beginning of the surge) and 19th November 2015 (midway through the surge), several striking morphological changes occurred on the glacier surface (Figure 4.12). On 12th October 2014, the glacier tongue and west tributary were heavily crevassed, but most of the upper glacier area had a relatively smooth, crevasse-free surface (Figure 4.12A). By 19th November 2015, the crevassing had propagated up-glacier to cover most of the glacier surface with large extensional crevasses appearing in the upper glacier area and compressional crevasses occurring at the glacier terminus (Figure 4.12B). In 2014, a distinctive lobe-shaped surface feature, approximately 200 m wide and with a smooth surface, was observed just up-glacier of the tongue (Figure 4.12A and C). By 2015, this feature had been replaced by a large and heavily crevassed bowl-shaped depression with an area of ~0.3 km^2 (Figure 4.12B and D). This bowl-shaped area is also visible in the same location on the glacier in a CORONA satellite image from 19th November 1970 and comparison of the 1970 image with the 2015 Pléiades scene shows very similar crevasse patterns (Figure 4.13B and C). This includes crescentic extensional crevassing on the north-east side and a line of intense crevassing across the narrow valley at the top of the glacier tongue (highlighted in yellow in Figure 4.13B and C).

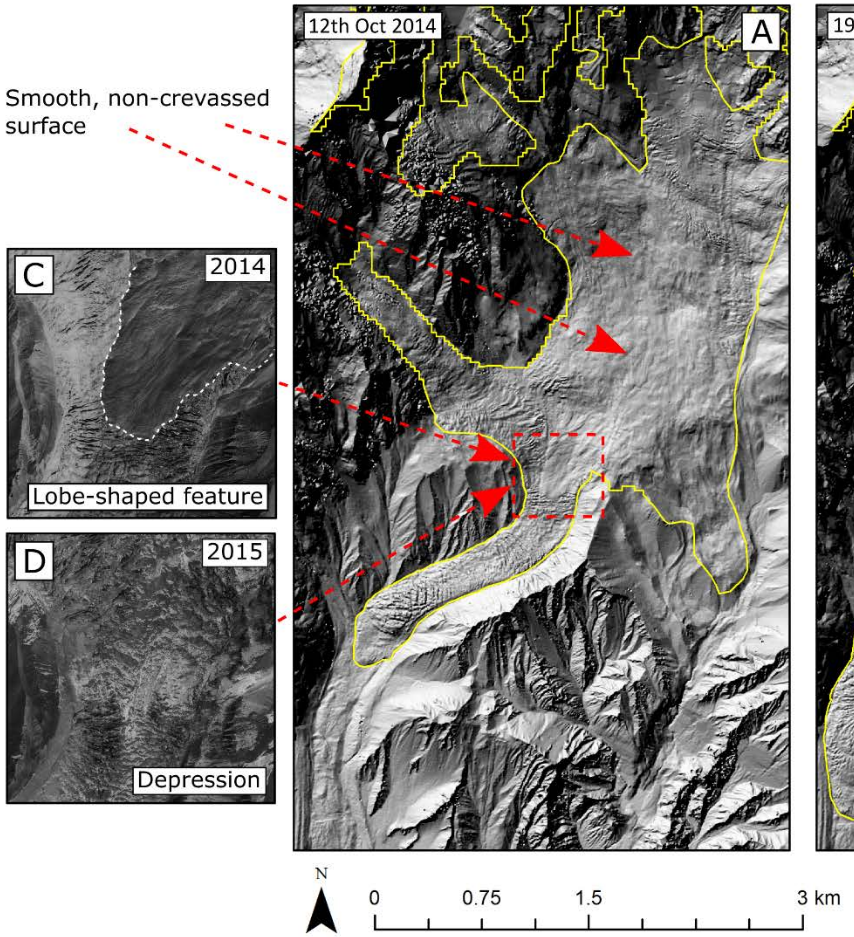

Figure 4.12: Morphological changes on the surface of Sabche glacier between A) 12th October 2014 and B) 19th November 2015 (background image: hill-shades of Pléiades DEMs). C) Magnified view of the lobe-shaped feature on 12th October 2014 and D) same view on 19th November 2015 with the heavily crevassed depression (background images: Pléiades panchromatic scenes of the same dates).

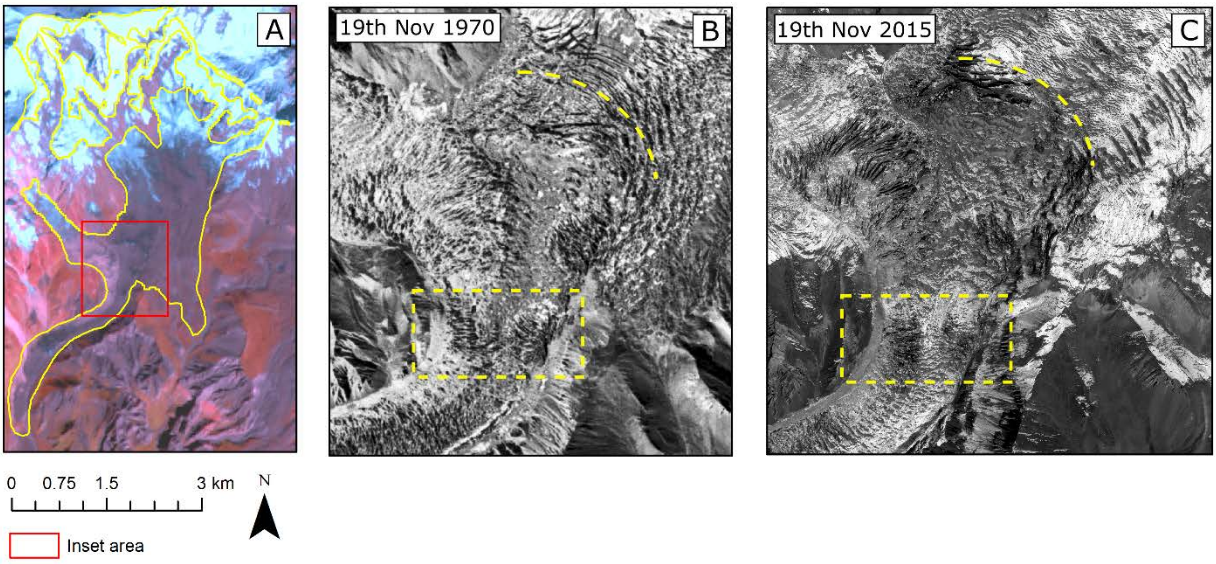

Figure 4.13: Repeated appearance of a bowl-shaped depression and similar crevasse patterns, 3 km up-glacier of the terminus in 1970 and 2015. (A) Location of bowl-shaped depression, (B) crevasse patterns in a CORONA satellite image from 19th November 1970 and (C) in a Pléiades satellite image from 19th November 2015. The yellow dashed curved lines highlight similar crescentic crevassing and the yellow dashed boxes highlight similar intense crevassing at the point where the glacier flows into the narrow valley.

4.5 Discussion

4.5.1 *Sabche glacier surge characteristics*

Several independent lines of evidence strongly suggest that Sabche glacier is a surge-type glacier. These include: i) regularly fluctuating terminus positions; ii) rapid ice surface velocity acceleration and deceleration; iii) large and rapid surface elevation changes, and; iv) widespread propagation of crevassing on the glacier surface (Meier and Post, 1969; Sharp, 1988; Murray *et al.*, 2003; Grant *et al.*, 2009). Our data suggest that the glacier surged up to four times during the last 50 years and, from 1991 onwards, surged every 10 to 11 years (Figure 4.8). However, a gap in the terminus position change dataset, between 1974 and 1988, may mean an additional surge was missing from the record: based on the 10 to 11-year cycle of the three most recent surges, we would expect another surge to have initiated between 1978 and 1980.

Based on the terminus position change chronology (from 1991 to 2017) (Figure 4.8), Sabche glacier has one of the shortest surge cycles (10 to 11 years; Table 4.3) and quiescence phases (4 to 7 years) ever recorded. For comparison, between 1905 and 1995, the surge cycle of Variegated glacier in Alaska ranged from 13 to 18 years and between the 1982/3 and 1995 surges, it had a quiescence phase of 12 years (Kamb *et al.*, 1985; Eisen *et al.*, 2005). Shokal'sky glacier in the Zailai-Alatau mountain range in Kazakhstan has a surge cycle of 11 to 12 years, and Medvezhiy glacier and North Tanymas glacier in the Pamirs have surge cycles of 12 to 14 years and 13 years, respectively (Dolgoushin and Osipova, 1975). Sabche glacier could therefore represent an end-member of a spectrum of observed glacier surge cycle lengths ranging from slow surge cycles (40 to 130 years) in Svalbard and Arctic Canada (Murray *et al.*, 2003; Frappé and Clarke, 2007) to rapid surge cycles (11 to 40) in the Pamirs, Karakoram, North America and Iceland (Table 4.3) (Dolgoushin and Osipova, 1975; Dowdeswell *et al.*, 1991; Kotlyakov *et al.*, 2008; Copland *et al.*, 2011). Therefore, it is important to understand Sabche glacier's surging mechanism to capture the full range of surge-type glacier behaviour globally.

Table 4.3: Summary of the surge and surge cycle lengths, maximum velocity (m day^{-1}) and terminus advance (km) for surge-type glaciers in different regions. Those in Arctic Canada and Svalbard tend have slow surge cycles, while those in the Pamirs, Karakoram, northwest North America and Iceland, tend to have rapid surge cycles. Sources: (Desio, 1954; Dolgoushin and Osipova, 1975; Dowdeswell *et al.*, 1991; Murray *et al.*, 2000; Murray *et al.*, 2003; Frappé and Clarke, 2007; Kotlyakov *et al.*, 2008; Copland *et al.*, 2011).

Glacier region	**Surge duration (yr)**	**Surge cycle duration (yr)**	**Maximum Velocity (m day^{-1})**	**Terminus advance (km)**
Arctic Canada and Svalbard	3 to 10	40 to 130	0.1 to 16	0 to 3
Pamirs, Karakoram, northwest North America, Iceland	1 to 2	11 to 40	3 to 110	0 to 7.5
Sabche glacier, Nepal	3 to 5	10 to 11	2	2.2

4.5.2 *Potential influence of subglacial topography on surge timing and duration*

The short surge cycle length of Sabche glacier is more common in glacier surges driven by a hydrological trigger such as Variegated glacier (~15 years) (Kamb, 1987; Eisen *et al.*, 2005), Bering glacier in Alaska (~26 years) (Fleisher *et al.*, 1998) and Lowell glacier in Yukon, Canada (~15 years) (Bevington and Copland, 2014). In contrast, thermally-triggered surge cycles tend to be longer (> 50 years) (Dowdeswell *et al.*, 1991; Frappé and Clarke, 2007; Benn *et al.*, 2009). However, Sabche glacier's surging behaviour reveals some unusual characteristics compared to other hydrologically-triggered surge behaviour. First, the length of its surge phases (3 to 5 years) are more typical of the thermally triggered surges of Svalbard (3 to 10 years) (Dowdeswell *et al.*, 1991) than hydrologically-controlled ones (1 to 2 years) (Kamb *et al.*, 1985; Harrison *et al.*, 1994; Björnsson, 1998). The quiescent phase (4 to 7 years) is also far shorter than surge-type glaciers controlled by either thermal or hydrological basal conditions (Meier and Post, 1969; Dowdeswell *et al.*, 1991; Eisen *et al.*, 2005). These, together with the unusual rapidity of the surge cycle (10-11 years), suggest that other factors might be influencing the cyclicity of the surges.

During the most recent surge, the coincidence of surface lowering (Figure 4.11), intense crevassing (Figure 4.12B) and increased velocities (Figure 4.10D) in a distinct bowl-shaped area 3 km up-glacier from the terminus, strongly suggests that the ice responsible for terminus advance originated in this relatively localised reservoir mid-way along the glacier central flowline, rather than coming from further up-glacier. This bowl-shaped depression appears in satellite imagery from 1970 and 2015 (both years when the glacier was surging) (Figure 4.13), and we hypothesise that its development is related to a subglacial basin, or overdeepening, in the bed topography (Cook and Swift, 2012). A slight concavity is visible in the 2015 ice surface long profile in Figure 4.11D. We also note the raised bump in the surface topographic expression at the down-glacier extent of the bowl in Figure 4.12B and the transverse line of intense extensional crevassing, visible in both 1970 and 2015 (yellow, dashed box in Figure 4.13B and C) from which we infer the location of the down-glacier lip, or adverse slope, of a subglacial overdeepening. This leads us to hypothesise that Sabche glacier's surging behaviour is, in part, controlled by subglacial topography. In particular, we suggest that the narrow valley and adverse slope of the overdeepening provide resistance to glacier flow (Cook and Swift, 2012), allowing ice to build up in the overdeepening to a sufficient thickness to cause surging. This leads to a much shorter quiescence phase than for surge-type glaciers controlled solely by thermal or hydrological basal conditions. If ice was not trapped in the overdeepening, it might not be able to accumulate enough to surge. No other glacier surges have been observed in the region to date, despite favourable climatic conditions (Sevestre and Benn, 2015), so we speculate that the behaviour is specific to Sabche glacier, i.e. the subglacial topography.

Based on our observations, we propose a conceptual model to explain the potential role of subglacial topography in Sabche glacier's surge cyclicity.

1. Quiescent phase: ice accumulates in the overdeepening on the glacier. The down-glacier lip of the overdeepening and narrow valley provide resistance to glacier flow further down-valley. Velocities on the glacier tongue are low and there is minimal change in terminus position.
2. Surge phase 1 (rapid advance): sufficient ice accumulates to allow ice to flow out of the overdeepening (Figure 4.12C), leading to rapid down-stream ice flow. The narrow and steep subglacial topography facilitates rapid advance and high flow velocities.
3. Surge phase 2 (moderate advance): The ice reservoir in the overdeepening becomes depleted and the surging ice continues down-glacier. Maximum ice velocities propagate down-glacier. Eventually the glacier tongue thins and the lower part disconnects from the upper part and begins to stagnate and down-waste.

A similar topographic mechanism was predicted to influence the slow surge of a small, unnamed glacier in the Yukon region in Canada, monitored between 2006 and 2009 (Flowers *et al.*, 2011). Using an ice flow model, they demonstrated that a bedrock ridge on the down-glacier side of an overdeepening on the glacier, could provide added resistance to ice flow. This promoted growth in the overdeepening during quiescence, allowing the glacier to surge, even under negative mass balance conditions. Bedrock also played an important role in glacier surging in the glacier flowline modelling of Budd and McInnis (1974), who showed that steeper bedrock profiles led to surges at lower velocities and in thinner glaciers. This suggests that some glacier surges are strongly influenced by subglacial topography, and not solely controlled, or even triggered by, hydrological or thermal basal changes. Given the steep subglacial topography found in many high mountain regions, topographically-influenced surging may be important elsewhere, and potentially produce very rapid and hazardous surges.

A subglacial overdeepening might also preferentially collect unconsolidated sediments (subglacial till) (Cook and Swift, 2012), which could have an additional influence on the temporal pattern of surges observed on Sabche glacier. When water pressure in the till increases sufficiently to support the overlying ice, it can dilate and deform, leading to glacier surging (Turrin *et al.*, 2014). For example, subglacial till deformation has been inferred to generate regular (every ~7 years between 1973 and 2012) pulses of glacier acceleration observed on Ruth Glacier in Alaska (Turrin *et al.*, 2014). Till failure is also thought to have influenced periodic (every 12 years) accelerations on Black Rapids glacier in Alaska during its quiescence phase (Nolan, 2003). However, subglacial observations (e.g. geophysical data of bed topography and substrate) are required to test this hypothesis for Sabche glacier, and they do not currently exist.

It is also possible that basal hydrology played a key role in Sabche glacier's surging behaviour. In particular, meltwater could accumulate in a bowl-shaped depression as the ice thickens, or through seasonal change (Cook and Swift, 2012). Moreover, once the glacier thickens sufficiently to overcome the resistance offered by the topography, it is likely to trigger a positive feedback whereby the initial basal sliding across the bedrock promotes frictional/strain heating that generates further meltwater and further increases basal sliding. However, our data are not at a high enough temporal resolution to test whether there is a seasonal influence on the onset and termination of the surges and we cannot analyse changes to meltwater outflow due to limited hydrological data.

While we acknowledge that it is not possible to test our hypothesis of a subglacial topographic control on Sabche glacier's surge-type behaviour with the current available data, we suggest that future research should prioritise surveying the bed to confirm the presence/absence of a bedrock overdeepening and subglacial till and the configuration of subglacial meltwater drainage.

A question still arises as to why, despite occurring at regular (approximately 10 years) intervals, there are marked differences in the size of the two most recent surges on Sabche glacier. The most recent surge, from 2012 onwards, advanced twice the distance of the previous surge at the last measured date (25th March 2017) (Figure 4.8). This suggests that the size of the surge is not necessarily related to surge-cycle length. A possible explanation is that a larger proportion of the glacier overcame resistance and became involved in the surge. Additional data, such as accumulation rates, subglacial topography and surface elevation change covering the three most recent surges would be required to test this hypothesis.

4.5.3 *Implications for the presence of other surge-type glaciers in the central Himalayas*

While there has been no previous record of glacier surges in the central Himalayas to our knowledge, this new discovery of a surge-type glacier is consistent with a recent model that predicted surge-type glaciers in this region (Sevestre and Benn, 2015). However, although the Maxent model predicts the presence of surge-type glaciers with relatively high probability in some parts of the central Himalayas, Figure 4.14 shows that in the area where Sabche glacier is located, the model output suggests that there is a low probability of surge-type glacier presence (Sevestre and Benn, 2015).

There are a couple of reasons why the model may not be predicting surge-type glaciers in the area where Sabche glacier is present. First, it could be that Sabche glacier does not fit the geometry requirements used to predict surge-type glaciers in the model (e.g. surge-type glaciers tend to be longer and have shallower gradients than non-surge-type glaciers in the same region). Although we do not have length data for glaciers in the ACA, glacier length is strongly correlated with glacier area and elevation range (Sevestre and Benn, 2015). Therefore, we compared the area and elevation range of Sabche glacier (measured in 2002) to other glaciers in the ACA (Appendix A). Sabche glacier was in the 10% of largest glaciers in the ACA in terms of area (with an area in 2002 of 9.05 km^2) and in the top 2.5% of ACA glaciers in terms of elevation range (with an elevation range of 3402 m asl), indicating that it is therefore also probably one of the longest glaciers in the region. However, Sabche glacier also had one of the steepest gradients in the region (28.2°), sitting in the top 15% of steepest glaciers in the ACA (Appendix A), which does not fit the model's criteria for surge-type glaciers, which tend to have shallower gradients.

Second, it could be that the area that Sabche glacier is located in does not fit within the climatic range of the Maxent model. The geodatabase that Sevestre and Benn (2015) used to inform the model indicates that surge-type glaciers in High Mountain Asia fit within a climatic envelope characterised by a MAT range of -12 to +8°C and a MAP range of 165 to 2155 mm a^{-1}. Reliable and consistent mean annual temperature data are not available for the ACA. However, precipitation measured between 1998 and 2007 using Tropical Rainfall

Measurement Mission (TRMM) indicates that mean annual precipitation data in the southern part of the ACA, where Sabche glacier is located, ranged between 3000 and over 4000 mm a^{-1} (Bookhagen and Burbank, 2010). Therefore, although we do not have data on the microclimate around Sabche glacier, it is likely that mean annual precipitation on the glacier exceeds the predictor range used in the Maxent model (Sevestre and Benn, 2015).

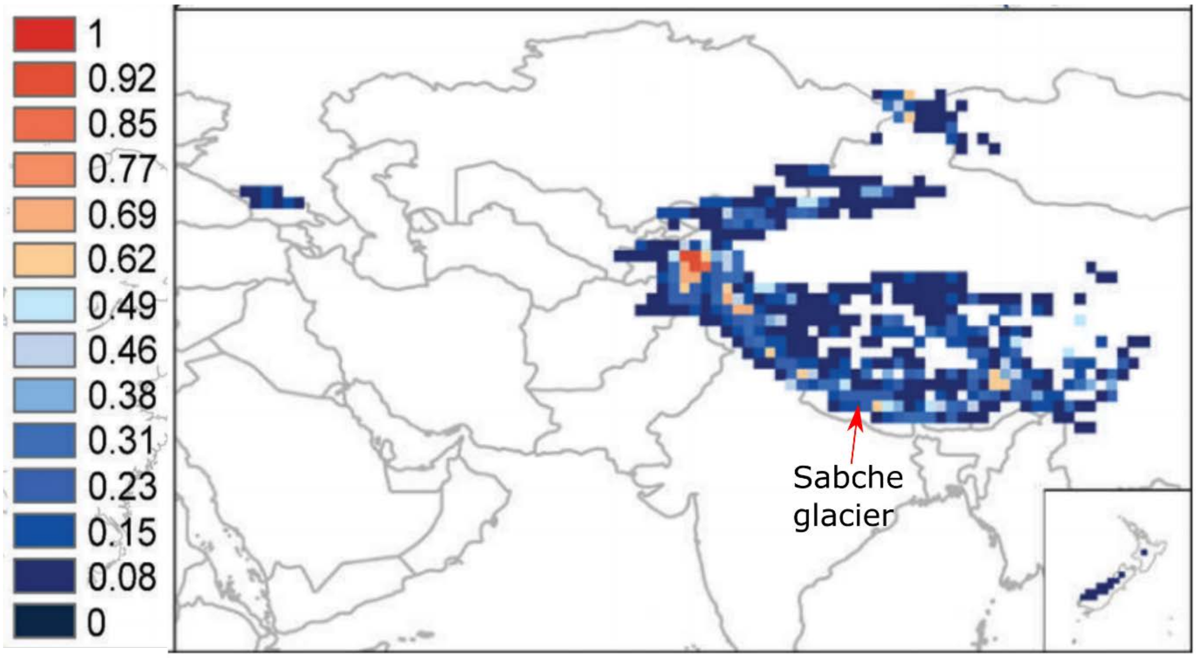

Figure 4.14: Final model output from the Maxent species distribution model in Sevestre and Benn, 2015 displaying the probabilities of presence of the population of surge-type glaciers across HMA (modified from Sevestre and Benn, 2015). Four variables were used for this model: mean annual temperature, mean annual precipitation, glacier length and slope. The figure also shows the approximate location of Sabche glacier in the ACA. The figure shows that the Maxent model predicts with a relatively high probability the presence of surge-type glaciers in some parts of Nepal, but that where Sabche glacier is located, the probability predicted by the model is relatively low.

This suggests that although the Maxent model is predicting surge-type glaciers in the central Himalayas, Sabche glacier does not appear to fit the model's ranges. This may be because of the additional topographic control on Sabche glacier which enables it to surge despite not necessarily meeting the climatic and geometric criteria of the majority of surge-type glaciers in the global geodatabase that was used to inform the model.

More research is needed to understand the role of local controls such as topography in modulating glacier surge behaviour, where surge-type glaciers influenced by these controls might be present, and whether these controls can be incorporated into models such as the

Maxent model in Sevestre and Benn (2015) to improve the global prediction of surge-type glaciers with similar characteristics to Sabche glacier.

4.6 Conclusions

In this paper, we report a newly-discovered surge-type glacier, the presence of which is consistent with previous work predicting the occurrence of surge-type glaciers in the central Himalayas (Sevestre and Benn, 2015). Using a combination of manual digitisation, feature tracking and DEM differencing, we mapped changes in the terminus position, velocity and surface elevation of Sabche glacier in the ACA from 1967 to 2017. Our results show that Sabche glacier surged four times in the last 50 years. The three most recent surges occurred at 10 to 11-year cycles, making it one of the shortest surge-cycles ever recorded. Its unusual surge-type characteristics (very short surge cycle, but relatively long surge phase of 3 to 5 years), do not fit clearly with the established paradigms for hydrologically- or thermally-driven surge mechanisms. Rather, the persistent reappearance of a bowl-shaped depression above a narrow valley constriction lead us to suggest that Sabche glacier's surge-type behaviour is influenced by subglacial topography. Specifically, we propose that the configuration of bedrock above the glacier tongue promotes the accumulation of mass in the overdeepening and leads to a more rapid surge cycle than would otherwise be possible. On this basis, our data highlight the importance of topography in controlling surge-type glacier behaviour, which may be relevant to glacier surging in other mountainous regions.

Chapter 5: The thermal regime of supraglacial debris and its influence on glacier melt on Annapurna South glacier, Nepal

5.1 Introduction

Many Himalayan glaciers are partially covered with debris, which reaches the glacier through rockfalls and landslides and/or subglacial and englacial emergence (Kirkbride and Deline, 2013; Anderson and Anderson, 2018; Berthier and Brun, 2019) and accumulates in the ablation zone (Benn *et al.*, 2012; Bolch *et al.*, 2012). Supraglacial debris influences glacier surface melt by modulating how atmospheric radiation is transferred to the ice surface, which is largely controlled by debris thickness (e.g. Østrem, 1959; Fujii, 1977; Inoue and Yoshida, 1980; Brock *et al.*, 2010). Glacier melt is enhanced, relative to a debris-free glacier surface, under a thin layer (less than a few centimetres) of supraglacial debris, due to lowering of the surface albedo (Mattson, 1993). Beyond this critical threshold, surface melt decreases with increasing debris thickness. This is because thicker debris has an enhanced capacity to block the transfer of heat to the ice surface (Østrem, 1959; Nakawo and Rana, 1999; Reznichenko *et al.*, 2010).

The relationship between debris thickness and ice melt can cause non-linear responses to climate forcing on debris-covered glaciers compared to their debris-free counterparts (Benn *et al.*, 2012; Nicholson and Benn, 2013). For example, the tendency for debris to increase in thickness towards the terminus generates a reversed mass balance gradient in the ablation zone where the highest mass loss occurs mid-way up the ablation zone rather than at the terminus (Benn *et al.*, 2012; Rowan *et al.*, 2015). This can reduce the glacier surface gradient, leading to lower driving stress, glacier deceleration, and eventually stagnation (Rowan *et al.*, 2015). This response means that debris-covered glacier ablation zones tend to lose mass by thinning rather than undergoing terminus retreat, which is more commonly observed on debris-free glaciers (Scherler *et al.*, 2011b; Benn *et al.*, 2012). Observations suggest that supraglacial debris cover has expanded in the Himalayas since the 1960s, as a result of climate change (Bolch *et al.*, 2008; Gibson *et al.*, 2017; Jiang *et al.*, 2018; Shukla and Garg, 2019), and so the impact of debris cover on ice melt is likely to be an important component of future glacier change in the region.

Although it is established that debris cover impacts ablation rates, the critical threshold in debris thickness between accelerated and inhibited sub-debris melt, relative to a debris-free glacier, is highly variable, ranging from 3 cm on Rakhiot glacier (Mattson, 1993) to 9 cm on Lirung glacier (Rana *et al.*, 1998). These variations are thought to arise from: i) differences in meteorological conditions (e.g. solar radiation intensity and turbulent heat fluxes), which determine how much energy the debris surface receives (Mattson, 1993; Reznichenko *et al.*, 2010); and ii) the physical properties of the debris (e.g. effective thermal conductivity, albedo and aerodynamic roughness), which determine how heat enters and is transferred through the debris layer (Conway and Rasmussen, 2000; Nicholson and Benn, 2013; Rounce and McKinney, 2014; Juen *et al.*, 2016; Steiner *et al.*, 2018). The influence of supraglacial debris on glacier melt is further complicated by the spatial heterogeneity of the thickness and physical properties of the debris (Reznichenko *et al.*, 2010; Anderson and Anderson, 2018; Nicholson *et al.*, 2018). This can result in highly variable sub-debris melt rates over small spatial scales, which are often missed when investigating the influence of supraglacial debris on melt rates at larger spatial scales using satellite data (Mihalcea *et al.*, 2008).

Understanding the small-scale influence of supraglacial debris on melt rates, particularly how heat is transferred through the debris and how this varies over time and for different debris thicknesses and properties, is vital for accurately predicting how debris-covered glaciers will respond to future changes in meteorological conditions (Nicholson and Benn, 2013; Rounce *et al.*, 2015; Juen *et al.*, 2016). However, field measurements of debris properties and sub-debris melt rates are scarce in the Himalayas, due to the difficulty of accessing these remote glaciers (Nicholson and Benn, 2013). As such, they tend to be restricted to a few benchmark glaciers in the Everest and Langtang regions (Figure 1.1) in east Nepal (e.g. Nakawo and Rana, 1999; Adhikary *et al.*, 2000; Conway and Rasmussen, 2000; Kayastha *et al.*, 2000; Nicholson and Benn, 2013; Rounce *et al.*, 2015; Quincey *et al.*, 2017) and in the Lahaul-Spiti region (Figure 1.1) in the western Himalayas (Patel *et al.*, 2016; Sharma *et al.*, 2016). Therefore, available field measurements are not fully representative of the Himalayan region, which has highly spatially variable topography and climate (Bookhagen and Burbank, 2010). This could impair efforts to model debris-covered glaciers at the regional scale.

Moreover, there are few assessments of the thermal regime of supraglacial debris in the Himalayas (Conway and Rasmussen, 2000; Nicholson and Benn, 2013; Rounce *et al.*, 2015; Chand and Kayastha, 2018). Of the existing studies, observations revealed spatial and temporal variations in temperature and thermal properties of the debris cover

(Nicholson and Benn, 2013; Rounce *et al.*, 2015; Chand and Kayastha, 2018; Gibson *et al.*, 2018). Debris surface temperatures were spatially variable, influenced by local topography and physical properties of the debris (Gibson *et al.*, 2018). Effective thermal diffusivity (the rate of temperature change in the debris in response to a temperature change at the surface) and effective thermal conductivity (the ability of a material to conduct heat) of the debris varied through time and were higher during the monsoon than winter (Nicholson and Benn, 2013). Heat was transferred through the debris primarily by conduction during the monsoon, but non-conductive heat transfer and phase changes were prevalent during transitional periods between different seasons (Nicholson and Benn, 2013). Modelling studies have shown that debris porosity and moisture also influence thermal transfer and the amount of energy available for ice melt at the ice-debris interface (Collier *et al.*, 2014; Evatt *et al.*, 2015). However, there are no direct observations of how the thermal regime of supraglacial debris influences sub-debris melt, and there are few studies that investigate how the debris thermal regime varies with different debris thicknesses and physical properties over a full annual cycle (Nicholson and Benn, 2013). Our understanding of the thermal regime of supraglacial debris and its influence on ice melt outside of the monsoon season (in winter and spring) is therefore limited.

Given the above, the aim of this chapter is to investigate the thermal regime of supraglacial debris and its influence on melt rates on the ablation zone of Annapurna South glacier (ASG; Figure 5.1) continuously for a year. ASG is a debris-covered glacier in the Annapurna Conservation Area (ACA), central Nepal. Results from Chapter 3 demonstrated that glaciers in the ACA recently shrank in area, thinned and lost mass (Table 3.5). However, supraglacial debris was identified as an important local control on the spatial patterns of glacier thinning in the ACA (Chapter 3; Figure 3.16). This chapter investigates the influence of supraglacial debris on glacier melt in this region in more detail (at both higher temporal and spatial resolutions). ASG was chosen for the study because its tongue is characterised by highly heterogeneous supraglacial debris and it has recently undergone substantial down-wasting (Chapter 3; Figure 3.8) (Lovell *et al.*, 2019). ASG feeds into the Modi Khola river and is an important tourist attraction in Nepal. The glacier also acts as a route to several of the trekking peaks in the Annapurna Sanctuary basin. Therefore, glacier changes are likely to have an important impact on local water resources and tourism.

This chapter presents *in situ* measurements of supraglacial debris properties and ablation rates on ASG, which has not been previously studied. Air temperatures, debris thickness, aerodynamic roughness, clast size, debris temperatures, debris thermal properties and sub-debris ablation rates are measured between November 2016 and October/November 2017. This work provides new field observations that contribute to a limited dataset on the thermal regime of supraglacial debris in the central Himalayas. It allows a detailed investigation into processes occurring in the debris throughout the year, and their impact on glacier ablation. The key objectives of this chapter are to:

1. Characterise the spatial variability of supraglacial debris properties and thickness, sub-debris ablation rates and velocity on ASG.
2. Assess the relationship between ablation rates and debris properties and thickness on ASG.
3. Examine the temporal variation of debris temperatures and thermal properties on ASG over a year.
4. Assess how the thermal regime of debris on ASG differs between sites with different debris thicknesses and physical properties.
5. Analyse temporal changes in the thermal regime of debris on ASG to infer the timing and magnitude of ablation during the winter, spring and monsoon seasons.

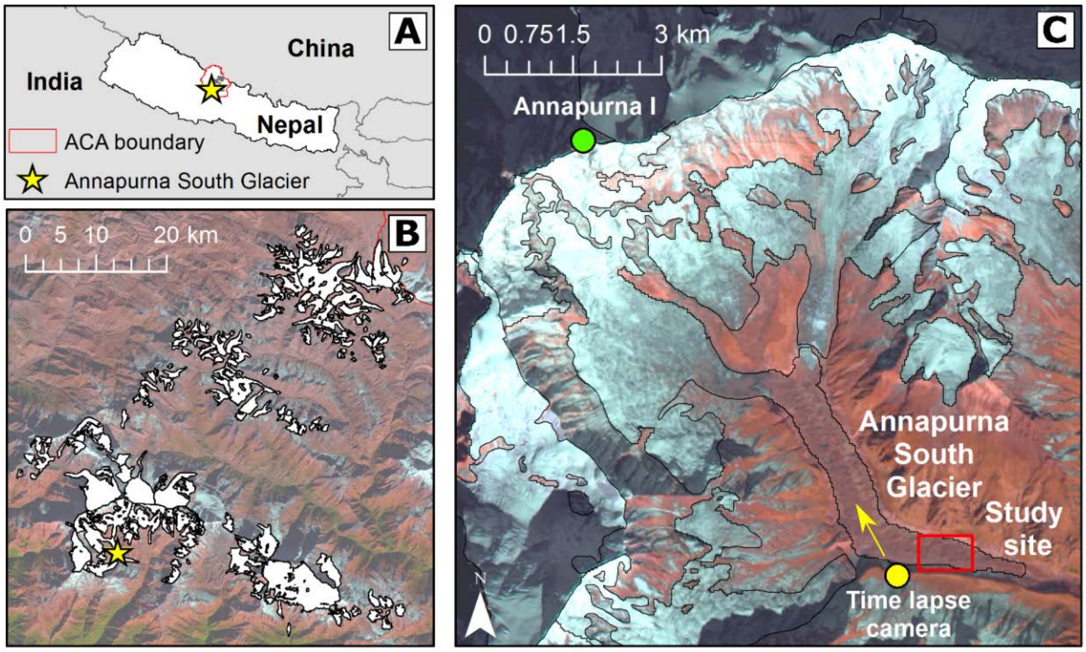

Figure 5.1: Map of the study area and Annapurna South glacier(ASG): A) location of Annapurna Conservation Area (ACA) in Nepal, B) location of ASG in the ACA and C) map of ASG with the location of the study site (in red box), location and orientation (yellow arrow) of the time lapse camera and location of Annapurna I. Glacier outlines from 2000 (Lovell *et al.*, 2019).

5.2 Study area

ASG is located on the southern flank of the Annapurna Himal in the ACA (28°31′48″N 83°52′40.8″E; area: ~27 km^2; Figure 5.1), a region that underwent 8.5% glacier area loss between 2000 and 2014/15 and experienced a mean mass balance rate of -0.28 ± 0.24 m w.e. a^{-1} between 2000 and 2013/16 (Chapter 3; Table 3.5) (Lovell *et al.*, 2019). The glacier has a very steep headwall and one of the largest elevation ranges (from 3780 to 8050 m a.s.l.) of any glacier in the region (Lovell *et al.*, 2019). The glacier tongue is ~5 km in length and is fed by a steep accumulation zone, but three of the four largest accumulation areas are no longer connected to the ablation zone and contribute ice and snow via avalanching.

ASG has a predominantly debris-covered ablation zone (supraglacial debris covers 16% of the total glacier area, but mantles almost all of the main glacier tongue: Figure 5.1C). Observations made in the field suggest that the main sources of debris input are rockfalls and avalanches in the upper part of the glacier near the accumulation zones and lateral moraine degradation on the glacier tongue on the lower part of the glacier. The local geology is a rose-coloured Nilgiri sandstone, which forms a band on the north side of the study site, and a dark grey Nilgiri limestone on the south side, which are derived from the accumulation zone and transported down-glacier to the ablation zone (Waltham, 1972) (Figure 5.2). The supraglacial debris is generally heterogeneous and poorly sorted but there is some stratification with a predominantly matrix-supported lower layer with smaller clasts and higher moisture content and a drier, clast-supported upper layer with larger clasts.

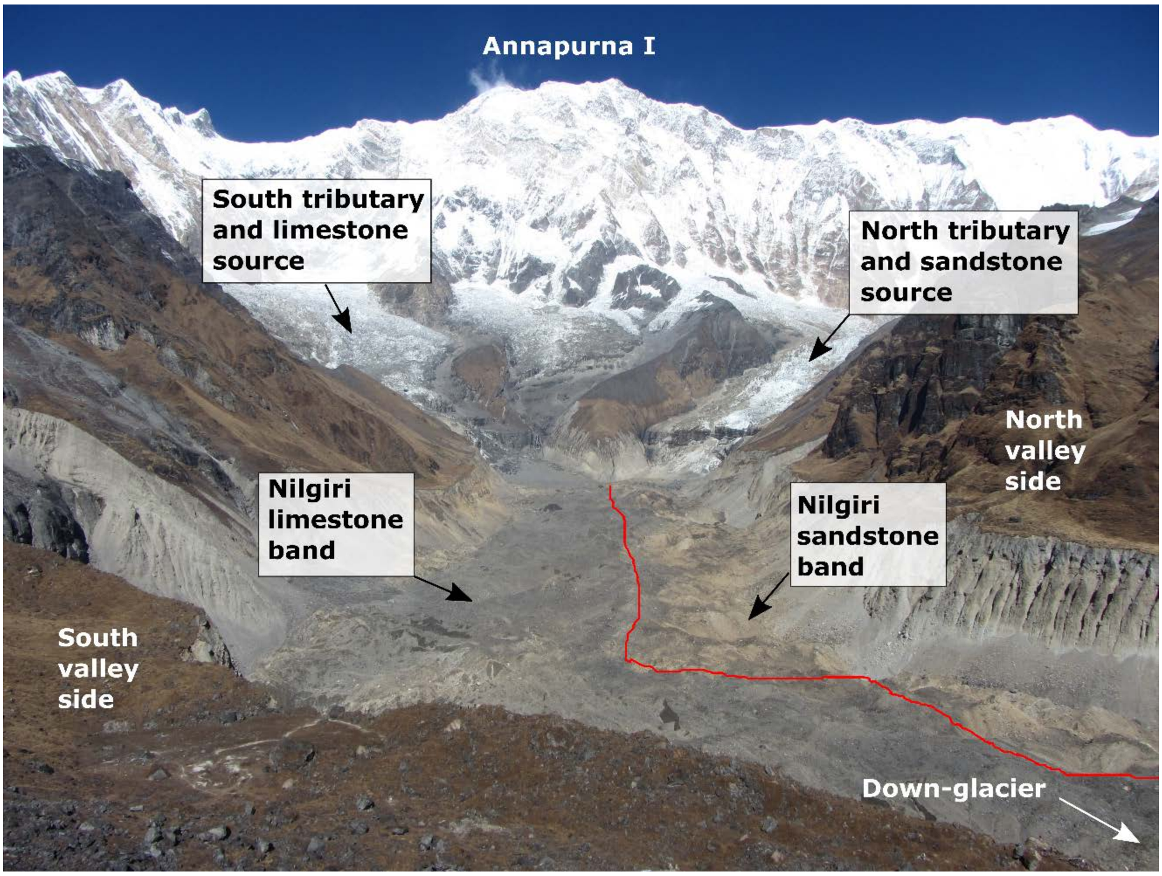

Figure 5.2: Annotated photograph of ASG looking up-glacier showing the separate bands of predominantly rose-coloured Nilgiri sandstone and predominantly dark grey Nilgiri limestone in the ablation zone and the north-side tributary (disconnected from the ablation zone) and south-side tributary (still connected to the ablation zone; photograph: Arminel Lovell).

Remotely-sensed data (Chapter 3; Figure 3.8) showed that the ablation zone of ASG underwent down-wasting rates of up to 5 ± 0.97 m a^{-1} between 2000 and 2015 (Lovell *et al.*, 2019) and the ~100-metre-high lateral moraines flanking the glacier tongue show that ASG has experienced substantial down-wasting over longer timescales. In 2016, the glacier tongue was still flowing (~20 m a^{-1}) but qualitative remotely-sensed data showed that deceleration occurred on the tongue between 2002 and 2016 (Lovell *et al.*, 2019). The study site was a 1 km × 0.5 km debris-covered section of the ablation zone located ~1 km up-glacier of the terminus, with an elevation of ~4000 m asl (Figure 5.1). This site was chosen because it was accessible and relatively crevasse-free, which was important for safety. The site was characterised by uneven surface topography as a result of differential melt, with multiple ice cliffs and meltwater ponds (Figure 5.3).

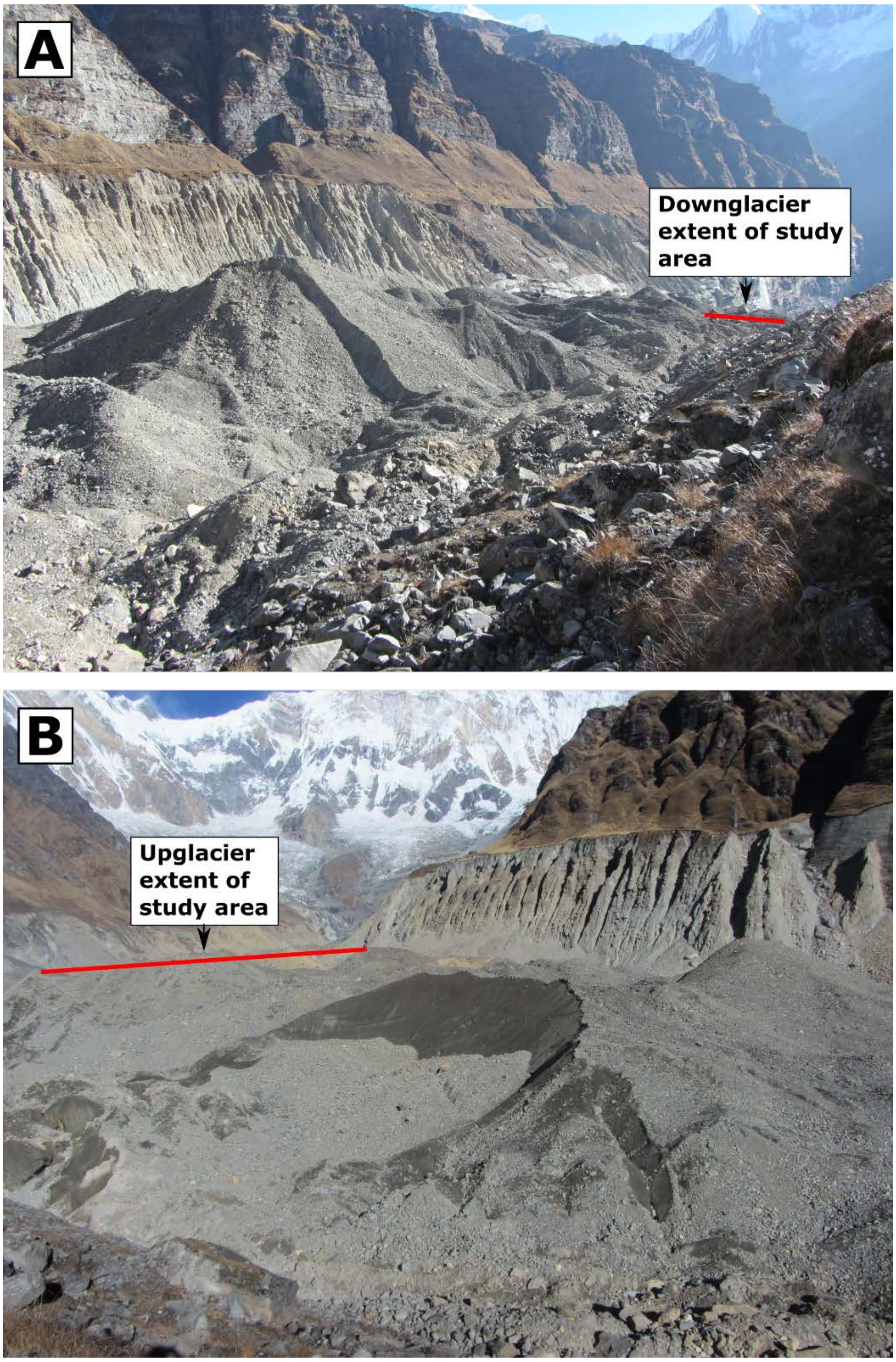

Figure 5.3: Photographs of the lower part of the ablation zone illustrating the varied topography and supraglacial debris. A) Looking down-glacier towards the terminus and B) looking up-glacier towards Annapurna I. The approximate upglacier and downglacier extents of the study area have been marked on the photographs (photograph: Arminel Lovell).

5.3 Methods

5.3.1 *Ablation rates*

In November 2016, ~2 m bamboo (chosen because it is a poor conductor of heat) stakes were installed at 14 sites across the study area. The initial plan was to install the stakes in a network of transects across the study area. However, the sampling strategy had to be modified in the field to account for obstacles on the glacier surface (e.g. ponds and ice cliffs) and to avoid areas of debris thicker than 1 m, where it was very challenging to access the ice surface. Thus, debris was only excavated to a maximum depth of 1 m at any location because the digging was physically challenging and melting under debris thicker than 1 m is assumed to be negligible (Nicholson and Benn, 2013). At each stake, the debris was excavated down to the ice surface and a Kovacs ice drill attached to a power drill was used to drill ~1.5 m into the ice. The distance from the highest point of each ablation stake to the ice surface on the down-glacier side of each stake was measured. This careful measurement procedure was followed to minimise the ablation measurement error. Maximum ablation measurement errors were assumed to be small (±1 cm) and much smaller than the ablation rates measured in the field. Following measurement of the stake, the debris was replaced to the original thickness, taking care to refill it in the same stratigraphic order in which it was excavated. After 11 months, in October/November 2017, each stake was re-visited, the debris was re-excavated to access the ice surface and the distance from the highest point on each bamboo stake to the ice surface was re-measured. Six of the 14 stakes could not be re-measured because they had disappeared or had moved from where they were originally installed as a result of ice cliff collapse (marked as ‘No Data’ in Figure 5.4). Of the remaining stakes, six had melted out and therefore, the ablation rates from these stakes are considered to be minimum melt rates (marked in red in Figure 5.4).

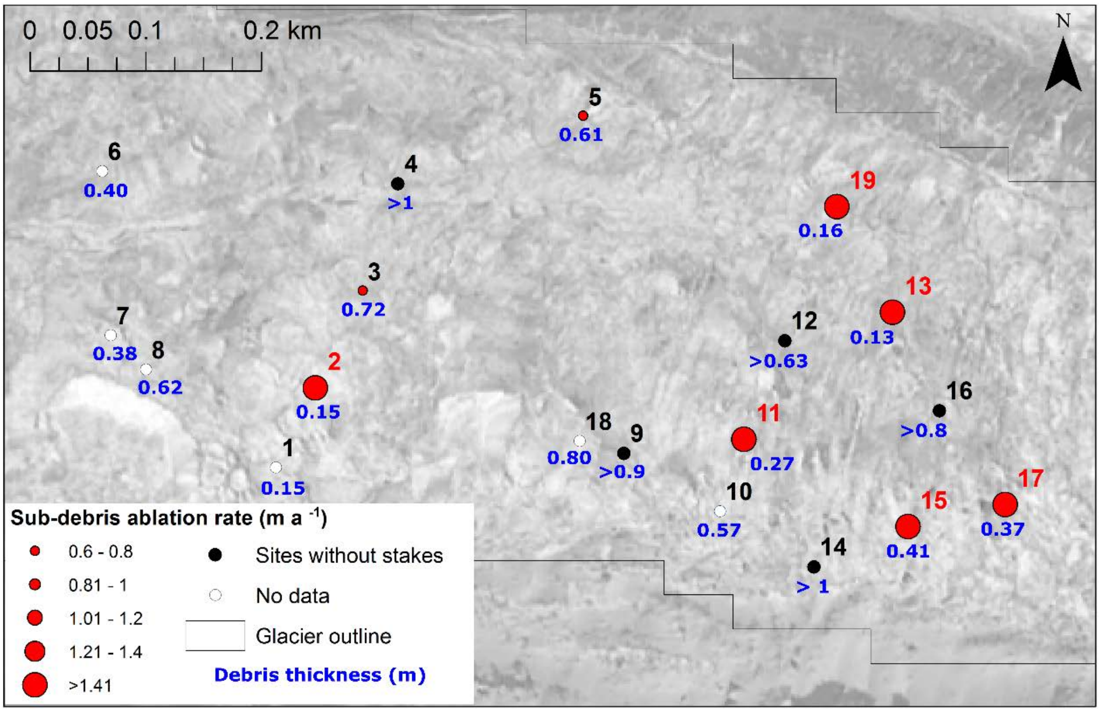

Figure 5.4: Stake measurements of ablation rates and debris thickness, and debris thickness for 5 sites where stakes were not installed (sites 4, 9, 12, 14, 16). The stakes at sites 2, 11, 13, 15, 17 and 19 (labelled in red) had melted out and are therefore minimum ablation rates. The sites indicated with a white dot are where the stakes were missing in the October/November 2017 field season.

5.3.2 *Supraglacial debris thickness, aerodynamic roughness and clast morphology*

To determine supraglacial debris thickness, the distance from the top of the debris to the ice surface at each stake was measured and marked on the stake. Following this, the debris was refilled to the mark on the stake, taking care to refill the hole in the same order as it was excavated to retain stratigraphic structure. A plastic lid was placed on the debris to get a level surface and the distance from the top of the stake to the lid was measured. Minimum debris thicknesses at several sites where it was not possible to reach the ice surface were also measured (Sites 4, 9, 12, 14 and 16). The maximum measurement error of debris thickness was estimated to be ±2-3 cm, due to uneven surface of large and blocky debris.

A cloud-based approach developed by Smith *et al.* (2016) was used to measure the aerodynamic roughness length (the height above the ground at which the extrapolated horizontal wind velocity falls to zero; z_0) of the glacier surface from microtopography.

Estimates of z_0 for glacier surfaces using microtopography commonly use an equation developed by Lettau (1969):

$$z_0 = 0.5h^* \left(\frac{s}{S}\right) \tag{5.1}$$

where h^* is the effective obstacle height, or average vertical extent (m), s is the silhouette area (m^2) facing in the upwind direction, S is the frequency or density of the roughness elements per unit area (m^2) and 0.5 is the average drag coefficient (Lettau, 1969; Smith *et al.*, 2016; Quincey *et al.*, 2017). The cloud-based approach was chosen instead of alternative methods commonly used to estimate z_0, such as a profile-based method or a DEM-based method (Rounce *et al.*, 2015; Smith *et al.*, 2016; Quincey *et al.*, 2017). This was because tests showed that z_0 calculated using the cloud-based method fluctuated the least with changing spatial scales and most closely matched with wind profiles z_0 measurements on the glacier (Quincey *et al.*, 2017). It also made use of the large amount of data available in a point cloud rather than simplifying down to a rasterised DEM (Smith *et al.*, 2016).

Measurements of z_0 were undertaken in 5 m × 5 m plots around each of the stakes remaining after 12 months using Structure-from-Motion (SfM) and following the methods in Smith *et al.* (2016) and Quincey *et al.* (2017). A 5 m × 5 m plot size was chosen because it was found to most closely resemble meteorologically measured aerodynamic values, compared with larger and smaller plot sizes, in a previous study on Khumbu glacier (Quincey *et al.*, 2017). The corners of the plots were clearly marked with ground control points and surveyed with a Leica dGPS. Between 150 and 200 overlapping photographs were taken at different angles around each site at an approximate height of 1.5 m using a Canon Digital SLR (Westoby *et al.*, 2012). Dense point clouds were generated for each site from the photographs in Agisoft Photoscan and georeferenced using the ground control points. The georeferencing root mean square error (RMSE) for the different point clouds ranged from 0.27 m to 0.48 m. Each point cloud was subsequently sub-sampled (using an octree filter) in CloudCompare (https://www.danielgm.net/cc/) to generate a cloud of uniform point density. The point cloud was then fitted to a detrended plane, to remove the effects of any surface slope, and h^* was calculated as the mean height of points above the detrended plane. Normal vectors were calculated for each point and s was estimated as the number of normal vectors facing each cardinal direction. Points below the detrended plane and points with a normal vector >80° (considered to be flat), were rejected. S was estimated as the total number of all points in the cloud (Smith *et al.*, 2016; Quincey *et al.*, 2017). Calculations of z_0 were made for an up-glacier (anabatic) prevailing wind, which typically occurs during the day, and a down-glacier (katabatic) prevailing wind, which typically occurs at night, outside of the monsoon season (Bollasina *et al.*, 2002; Quincey *et al.*, 2017).

The B-axis of clasts was measured at 36 locations in a grid of six transverse transects and six longitudinal transects across the study area. At each site, 50 clasts were measured, sampled at random within a 1 m^2 area using a Wolman grain size measurement plate. Mean and median grain size were calculated for each site. Spatial autocorrelation was calculated using Moran's I statistical test in ArcMap to assess whether there were significant spatial patterns in mean and median grain size across the study site.

5.3.3 *Stake displacements and time lapse camera*

The location of each stake was surveyed using a Leica dGPS. Each stake was re-surveyed during the following field season to measure horizontal displacement. The location accuracy of the stakes surveyed in 2016 was <5 mm. However, due to a problem with the dGPS during the 2017 field season, the positional accuracy of the second stake survey was much larger, ranging from 0.22 m to 0.78 m. This error is still much smaller than the horizontal stake displacements observed, typically of the order of 10 m.

A Browning Recon Force trail camera was set up in time lapse mode to capture images of the glacier once a day (see Figure 5.1 for location and direction of camera) and to observe the weather conditions on the glacier. The camera took photos from 6th November 2016 to 22nd July 2017 (~8 months) when the camera battery was depleted.

5.3.4 *Air and debris temperatures*

Maxim iButton® DS1922L-F5 temperature data loggers (range: -40 °C to +85 °C; accuracy: 0.5 °C) were installed at Site 3 and Site 17 on ASG to measure hourly temperatures at varying depths through the debris layer under different thicknesses of debris. iButtons were chosen because they are relatively cheap and have previously been used successfully in studies of both permafrost and debris-covered glacier environments (Gubler *et al.*, 2011; Gibson *et al.*, 2018). Prior to installation, the sensors were tested at room temperature and in refrigerated conditions to assess the variability of temperature measurements between sensors. These were within the manufacturer's stated measurement error (± 0.5 °C). The iButtons were placed in plastic bags to make them waterproof, following similar methods by Roznik and Alford (2012) and Gibson *et al.* (2018). The influence of the bags on the temperature sensors was tested and 90% of the time, the measurement error on iButtons inside the bags was within the manufacturer's stated measurement error (± 0.5 °C). The measurement precision of the iButtons was 0.5 °C.

At Site 3, which had thicker debris, the sensors were installed on 1st November 2016 at the surface, 0.24 m, 0.36 m, 0.48 m, 0.6 m and 0.72 m depth, the lowest of which was at the ice-debris interface. At Site 17, which had thinner debris, sensors were installed on 4th November 2016 at the surface, 0.06 m, 0.14 m, 0.22 m, 0.3 m and 0.38 m depth, which was at the ice-debris interface. The sensors placed on the surface at all sites were covered by ~2 cm of debris to protect the sensors from direct solar radiation. Sensors were also installed in radiation shields placed 1 m above the glacier surface on bamboo stake platforms at both Site 3 and Site 17 to measure near-surface air temperature. The sensors were re-excavated from Site 3 on 29th October 2017 and from Site 17 on 31st October 2017. All of the iButtons stopped recording on the 1st October 2017, when their memories were full. This provided almost a year-long dataset.

Some of the iButtons at Site 17 shifted position during the measurement period. From 20th May 2017 onwards, the debris layer at Site 17 began to collapse and the sensor that had originally been installed at the ice-debris interface was found level with the sensor placed at the surface. The second lowest sensor had also migrated towards the surface. Therefore, some of the data have been omitted after this date at Site 17.

Prior to any data analysis, the first three days of the hourly temperature measurements were removed to account for the sensors adjusting to the temperature of the debris. Daily mean temperature was calculated from the hourly time series and seasonal variations in temperature were also analysed. The winter (1st December 2016 to 28th February 2017) and spring (1st March to 11th June 2017) seasons were defined based on similar intervals used in previous Nepalese studies (Nicholson and Benn, 2013; Pokharel and Hallett, 2015). Precipitation data were not available for the study period. Thus, it was not possible to identify the exact date of the onset of the summer monsoon on ASG. Therefore, the monsoon is defined using the official onset (12th June 2017) and withdrawal (16th October 2017) dates for Nepal as published by the Nepal Department of Hydrology and Meteorology (DHM, 2017).

5.3.5 *Debris thermal properties and ablation estimates*

Effective thermal diffusivity (K) was calculated as a ratio of the change in hourly debris temperature with time (in seconds) against the change in the rate of hourly debris temperature change with depth (Conway and Rasmussen, 2000; Nicholson and Benn, 2013; Rounce *et al.*, 2015). The estimated thermal diffusivity (in $m^2\ s^{-1}$) was the gradient of the linear regression of this relationship at different depths in the debris. Mean diffusivity for the bulk layer was also calculated.

Effective thermal conductivity (k) was estimated using equation:

$$k = K\rho C(1-\varphi) \tag{5.2}$$

Where ρ is density of the debris (2700 kg m^{-3}), C is specific heat capacity of the debris, for which a standard value for rock (750 J $kg^{-1}\ K^{-1}$) is used, and φ is bulk effective porosity (0.33) (Conway and Rasmussen, 2000; Nicholson and Benn, 2013). The error associated with density, debris specific heat capacity and porosity was estimated to be 10% (Conway and Rasmussen, 2000; Nicholson and Benn, 2013).

Ablation (M) in m s^{-1} was estimated by:

$$M = \frac{Q_c}{\rho_i L_f} \tag{5.3}$$

Where ρ_i is ice density (900 kg m^{-3}), L_f is latent heat of fusion (334 000 J kg^{-1}) and Q_c is the conductive energy flux (W m^{-2}). The conductive energy flux (Q_c) was estimated by:

$$Q_c = -k\frac{\partial T_d}{\partial z} \tag{5.4}$$

Where ∂T_d is the difference between the mean debris surface temperature and mean ice-debris interface temperature and ∂z is the change in depth (m). Mean effective thermal diffusivity, effective thermal conductivity and ablation rates were calculated for the entire measurement period (4th November 2016 to 1st October 2017 and the monsoon season (12th June to 1st October).

5.4 Results

5.4.1 *Ablation rates, supraglacial debris thickness and properties, and glacier velocity*

5.4.1.1 *Spatial variability of observed ablation rates, supraglacial debris properties and debris thickness on ASG*

Ablation rates, debris thickness and debris properties were spatially variable across the study site (Table 5.1). Annual sub-debris melt rates measured between November 2016 and October/November 2017 ranged from 0.66 m a^{-1} to more than 1.58 m a^{-1} (Table 5.1 and Figure 5.4). The lowest ablation rates occurred at Sites 3 and 5 towards the up-glacier end of the study site (Figure 5.4). The ablation stakes at Sites 2, 11, 13, 15, 17 and 19 melted out during the measurement period (they were still held in place by the debris but the base of the stake was no longer in the ice), and should be considered minimum melt rates (labelled in red in Figure 5.4). The stakes at Sites 6 and 10 were displaced from their original locations (they had rolled downhill and were lying on the glacier surface) and the stakes at Sites 1, 7, 8 and 18 had disappeared (Figure 5.4). Data from these sites were therefore excluded.

Table 5.1: Debris thickness, aerodynamic roughness and ablation rates (amount of surface lowering in m a^{-1} and cm day^{-1}) at the sites. *Minimum ablation rates, where the stake melted out.

Site	**Debris thickness (m)**	**z_0 (m)**		**Ablation rate (m a^{-1})**	**Ablation rate (cm day^{-1})**
		Up-glacier	**Down-glacier**		
2	0.15	0.0054	0.0055	1.56*	0.43*
3	0.72	0.0109	0.0114	0.68	0.19
5	0.61	0.0093	0.0086	0.66	0.18
11	0.27	0.0046	0.0042	1.55*	0.42*
13	0.13	0.0060	0.0078	1.44*	0.39*
15	0.41	0.0053	0.0064	1.49*	0.41*
17	0.37	0.0064	0.0128	1.52*	0.41*
19	0.16	0.0113	0.0086	1.58*	0.43*

Debris thicknesses ranged between 0.13 m and 0.72 m at the remaining stakes (including the stakes that melted out but were not displaced; Table 5.1), and exceeded 0.8 m at Sites

4, 9, 14 and 16, where it was not possible to excavate down to the ice surface (Figure 5.4). Aerodynamic roughness (z_0) values ranged from 0.0053 to 0.0113 m for an up-glacier wind and 0.0042 to 0.0128 m for a down-glacier wind (Table 5.1). Grain size was spatially variable across the study site (Figure 5.5) and spatial autocorrelations of the distribution of median and mean grain size were not statistically significant, indicating that the spatial patterns were random.

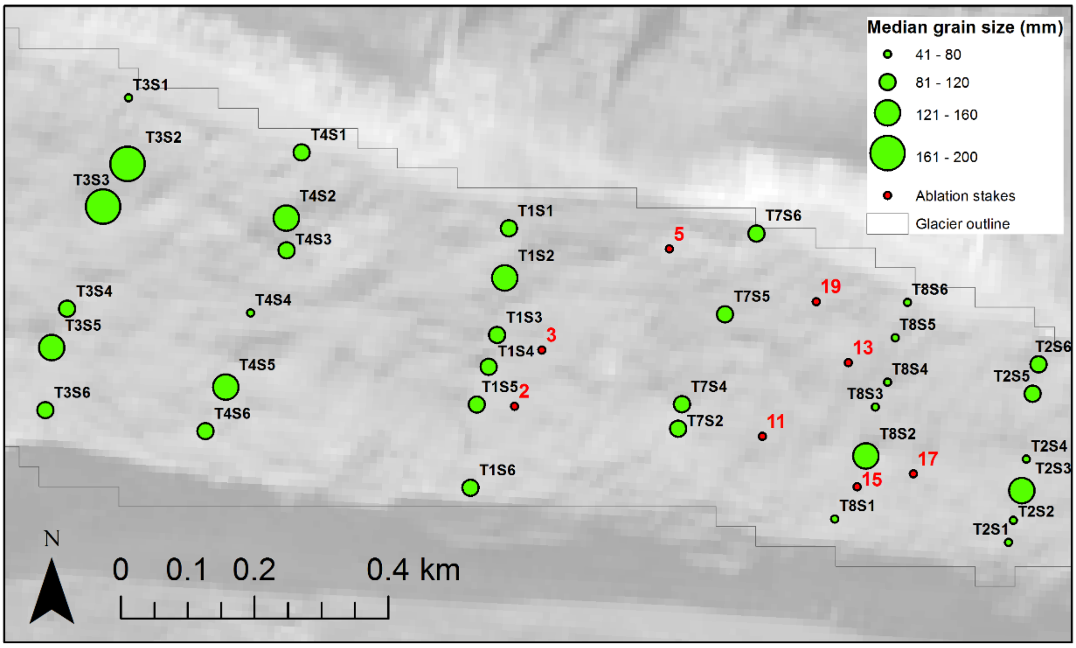

Figure 5.5: Median grain size distribution across the study site. The red dots show the locations of the ablation stakes.

5.4.1.2 *Relationships between ablation rates and aerodynamic roughness and supraglacial debris thickness*

Sites 3 and 5, which had the lowest ablation rates, had some of the largest z_0 values in the study site (Table 5.1). However, the sites that had the largest ablation rates had both the smallest and largest z_0 values (Table 5.1), indicating that the relationship between z_0 and ablation was not clear. The relationship between ablation rates and debris thickness was stronger. A plot of ablation versus debris thickness (Figure 5.6) shows that the stakes under debris thicknesses ranging from 0.13 to 0.41 m had the largest ablation rates (the stakes melted out) but the stakes with the thickest debris (>0.6 m; Sites 3 and 5) had lower ablation rates (0.68 m a^{-1} and 0.66 m a^{-1}; Table 5.1).

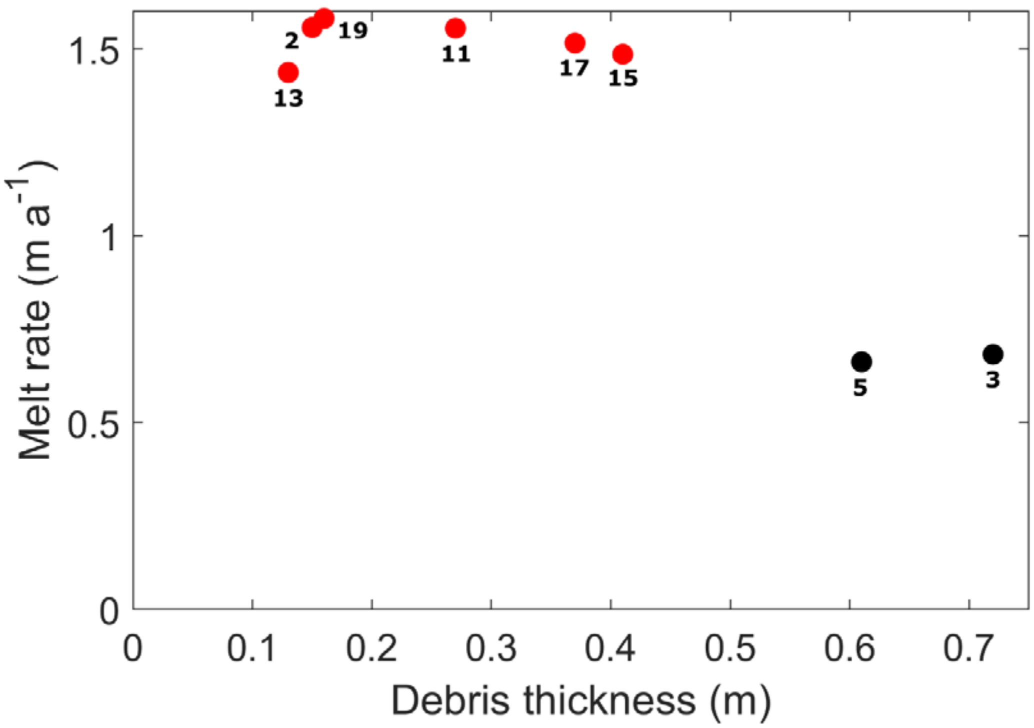

Figure 5.6: Østrem curve of ablation rates vs debris thickness measured at the stakes on ASG. The points are labelled with the site numbers. The points in red are the stakes that melted out and are minimum melt rates. See Figure 5.4 for location.

5.4.1.3 *Glacier velocity*

Stake displacements, measured between November 2016 and November 2017, ranged from 9.9 m a^{-1} to 21.2 m a^{-1} across the study site (Figure 5.7), with a mean horizontal displacement of 16 m a^{-1}. Displacement lengths increased towards the down-glacier end of the study area (Figure 5.7). However, there were not enough data points to test the statistical significance of this trend. The smallest displacement (9.9 m a^{-1}) was measured at Site 5, near the glacier margin (Figure 5.7).

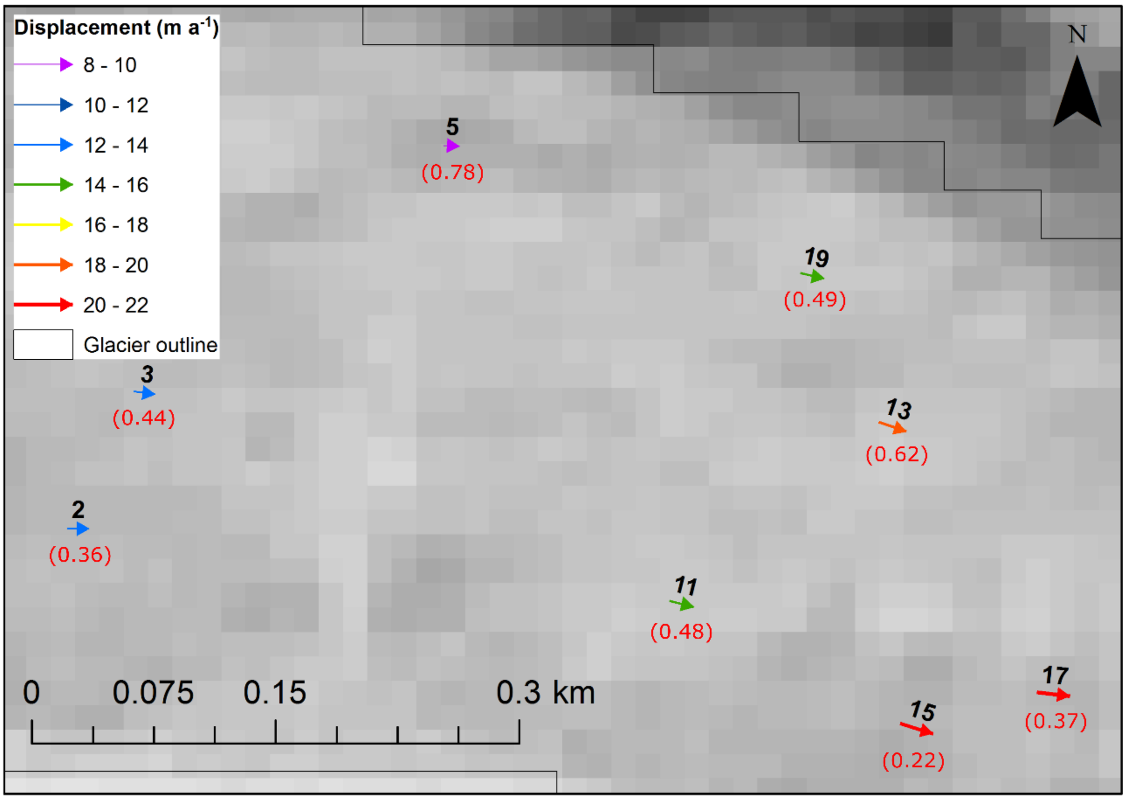

Figure 5.7: Stake displacements (m a^{-1}) in the study area, measured between November 2016 and November 2017. The colour scale and length of the vectors indicate the magnitude of displacement. The site number is labelled above each stake displacement vector. The red number in brackets below each vector is the positional accuracy of the stake locations surveyed in 2017 using the dGPS (in metres). The positional accuracy of all stake locations surveyed in 2016 using the dGPS was <5 mm).

5.4.2 *Debris temperatures, debris thermal properties and air temperatures on ASG*

In this section, the temporal variability of debris temperatures (T_d), debris thermal properties and air temperatures (T_a) are analysed at Sites 3 and 17 between November 2016 and October 2017, to conduct a detailed investigation of how heat was transferred through the debris during the year. A similar approach to Nicholson and Benn (2013) is followed in order to directly compare the data in this chapter to their data. The debris thermal regime data is used to model ablation rates for the period from November 2016 to October 2017 and for the monsoon season. Sites 3 and 17 had distinct surface topography, debris thicknesses and ablation rates (Table 5.1), making them a useful comparison for understanding how processes in the debris influenced sub-debris glacier melt.

5.4.2.1 *Site characteristics*

Site 3 was on a large, exposed debris peak (Figure 5.8A) near the centre flow-line of the glacier (Figure 5.4). The surface layer of the debris was characterised by clast-supported, unsorted angular and sub-angular diamict, ranging from coarse pebbles to large boulders (>1 m). Below the surface, the debris was matrix-dominated, with sub-angular to sub-rounded, fine to very coarse pebbles. The lithology was mixed but dominated by limestone and sandstone. The thickness of the debris was 0.72 m and z_0 was 0.01 m.

Site 17 was in a depression on a north-facing slope, below a large debris peak (Figure 5.8B) and was the furthest down-glacier site (Figure 5.4). The surface debris was predominantly matrix-supported, unsorted angular diamict, ranging from coarse pebbles to very large boulders (>5 m). The sub-surface debris was matrix-dominated sands and cobbles. Patches of low-lying vegetation were present, indicating soil development. Similarly to Site 3, the lithology was very mixed but was dominated by limestone and sandstone. The thickness of the debris was 0.37 m and z_0 was 0.006 m in the up-glacier direction and 0.013 m in the down-glacier direction.

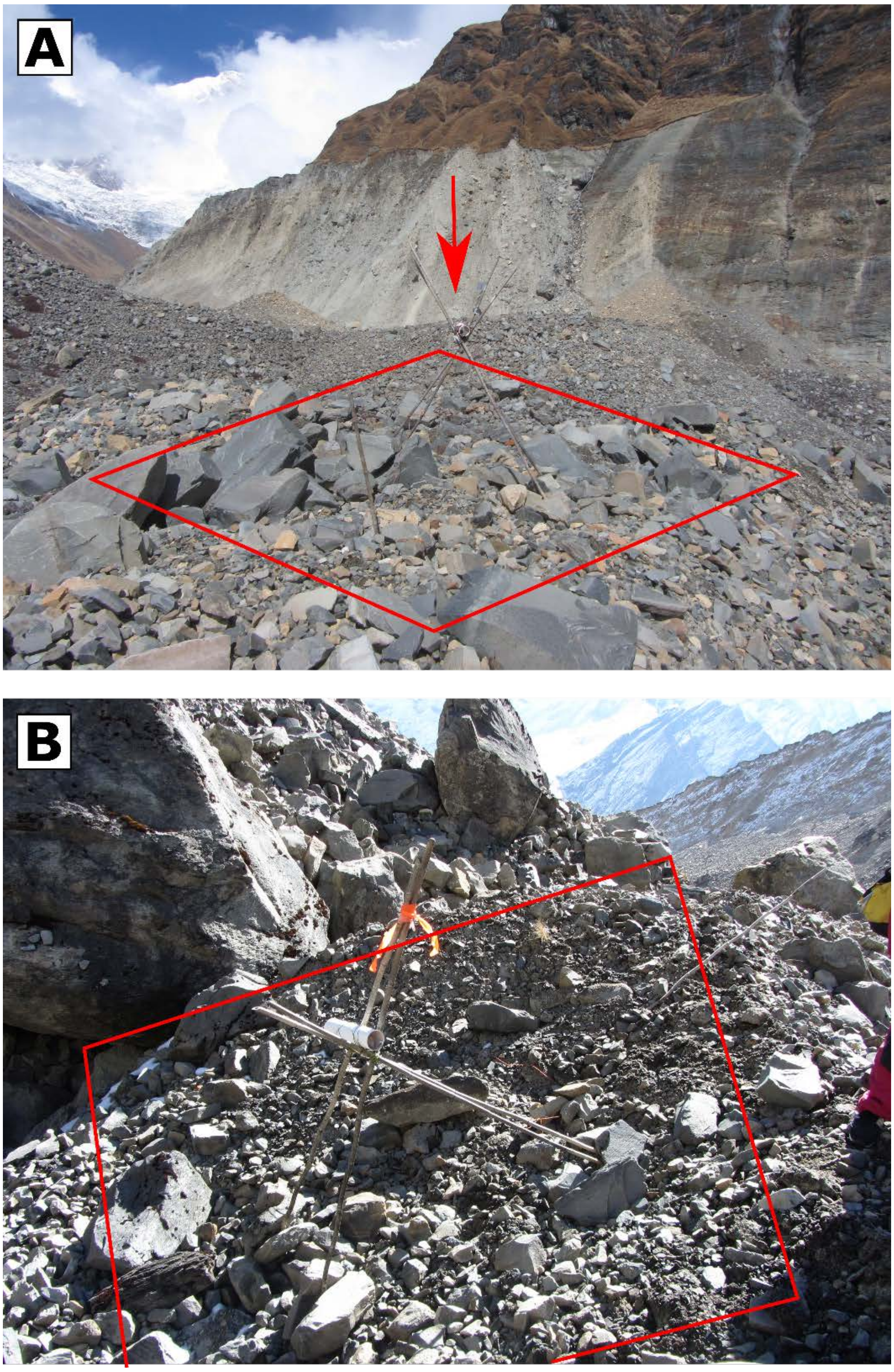

Figure 5.8: Locations where air and debris temperatures were measured: (A) Site 3 was on an exposed debris peak (red arrow shows location) and (B) Site 17 was on a north-facing slope of a depression, behind a large debris peak. See Figure 5.4 for location. The red boxes show the approximate location of the 5 m x 5 m grid used to measure aerodynamic roughness (photograph: Arminel Lovell).

5.4.2.2 *Temporal variability of debris temperatures (T_d) at Sites 3 and 17*

There were phases of strong diurnal cycles in T_d at Sites 3 and 17 throughout the measurement period (Figure 5.9). One of these phases occurred for a month in December. Then, from April until the end of the measurement period there were almost continuous strong diurnal temperature cycles (Figure 5.9). The diurnal temperature cycles were less clear in the debris during the winter and early spring (5th January 2017 to 26th March 2017; Figure 5.9), when photographs from the time lapse camera indicate that the ablation zone underwent extended periods of snow-cover. The data at the two lowest depths at Site 17 are excluded from further analysis after 20th May 2017, due to the shifting of the iButtons following the collapse of the debris profile (Figure 5.9B). The maximum penetration depth of the diurnal cycles varied between the sites and over time. In December, diurnal temperature oscillations penetrated down to >0.6 m at Site 3 and 0.35 m at Site 17. However, from May onwards, diurnal cycles penetrated down to the deepest iButton at the ice surface at both sites (Figure 5.9). The shape of the diurnal waves was narrower at Site 17 than at Site 3 due to T_d at all depths warming and cooling more rapidly in each 24-hour period at Site 17 (Figure 5.9).

Seasonal variations in T_d occurred at both sites and at all depths. During the winter, throughout most of December, there was a clear diurnal cycle in the debris and T_d at both sites regularly exceeded 0 °C. However, in January and February, during the period of snow-cover, the hiatus of diurnal warm temperature inputs into the debris led to temperature equilibration and a gradual cooling of T_d at all depths to well below 0 °C, with slightly cooler T_d at Site 3 than Site 17 (Figure 5.9). During the early part of spring (March), T_d of the bulk debris layer also stayed close to 0 °C (Figure 5.9), although the diurnal cycles had stopped at both sites. From April onwards, mean daily T_d at both sites began to increase, coinciding with increasing mean daily T_a (Figure 5.10B and Figure 5.11B), but underwent large fluctuations. During the monsoon, mean daily T_d throughout the bulk layer at Site 3 settled into a stable period of positive temperatures (Figure 5.10A). At Site 17, mean daily T_d in the upper layers also stabilised into warmer temperatures but they were less warm than at Site 3 at the same depths (Figure 5.11A).

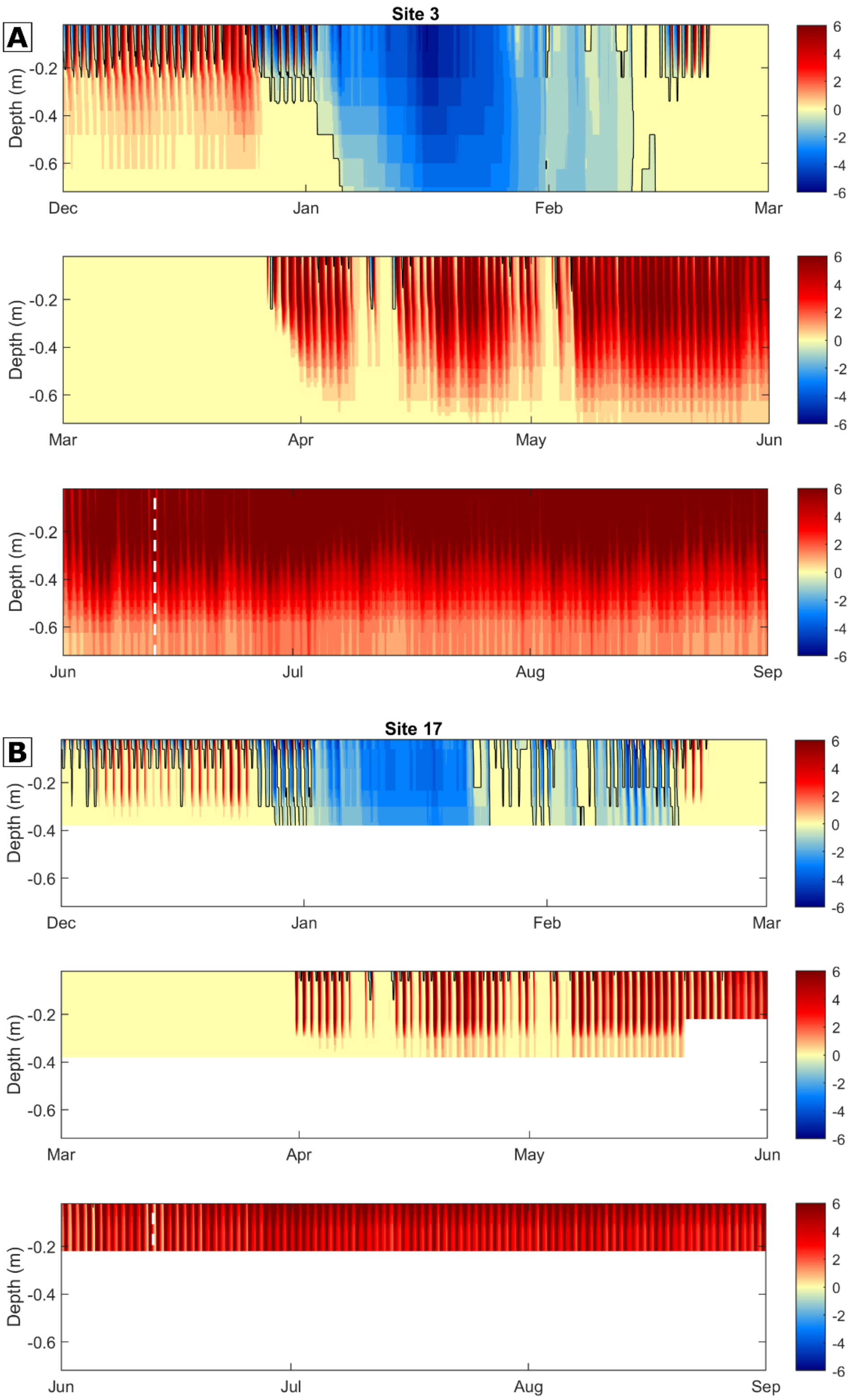

Figure 5.9: Hourly temperatures (°C) at different depths through the debris at A) Site 3 and B) Site 17 from November 2016 to September 2017. The onset of the monsoon (12th June 2017) is marked with a white dashed line.

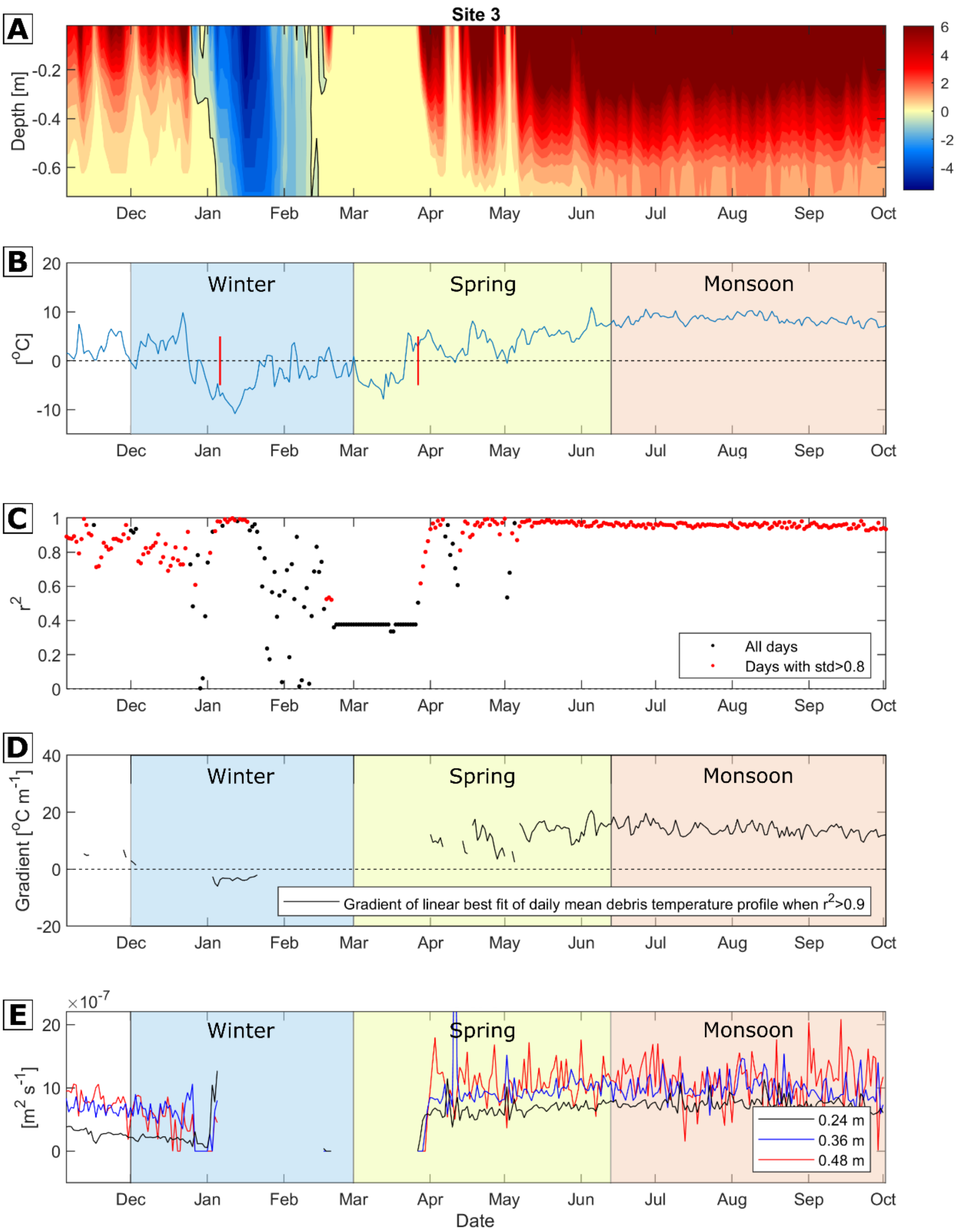

Figure 5.10: Changes in the thermal regime of supraglacial debris at Site 3 from November 2016 to October 2017. A) Mean daily temperature (°C) at different depths through the debris, B) mean daily air temperature (°C), the red lines indicate the beginning and end of the inferred period of snow cover (5th January to 26th March 2017), C) r^2 values of the 24-hour vertical temperature-depth linear profiles, D) linear gradients of the 24-hour vertical temperature profiles, and E) mean daily diffusivity for the upper four depths at Site 3. Data during the period of snow-cover between January and March, identified as when diurnal temperature oscillations stopped entering the debris, have been removed.

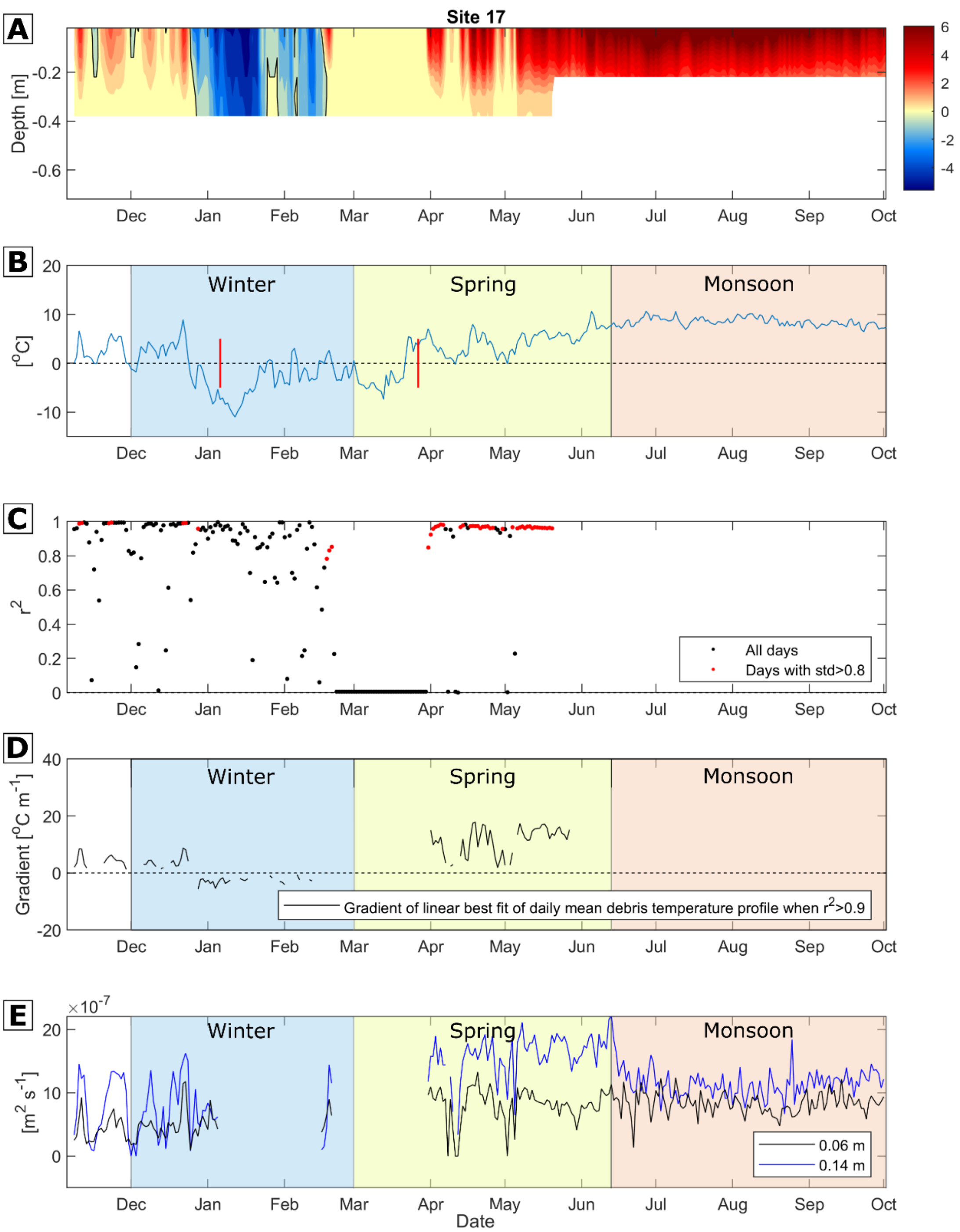

Figure 5.11: Changes in the thermal regime of supraglacial debris at Site 17 from November 2016 to October 2017. A) Mean daily temperature (°C) at different depths through the debris, B) mean daily air temperature, the red lines indicate the beginning and end of the inferred period of snow cover (5th January to 26th March 2017), C) r^2 values of the 24-hour vertical temperature-depth linear profiles, D) linear gradients of the 24-hour vertical temperature profiles, and E) mean daily diffusivity for the upper three depths. Data during the period of snow-cover between January and March, identified as when diurnal temperature oscillations stopped entering the debris, have been removed.

It is not possible to pinpoint the exact moment that temperatures at the ice-debris interface (T_i) exceeded 0 °C, due to the sensor resolution. As such, a more conservative estimate (T_i was equal to, or exceeded, 0.5 °C) was used to infer ice melt. Hourly T_i exceeded 0.5 °C at Site 17 (on 13th April 2017) and almost consistently exceeded 0.5 °C every day after that until measurements stopped, apart from a few days in the transition from April to May (Figure 5.9). Hourly T_i exceeded 0.5 °C at Site 3, eight days later than at Site 17 (on 21st April 2017), but only exceeded 0.5 °C in four days in April and did not start to consistently exceed 0.5 °C on a daily basis until 5th May 2017 (Figure 5.9). Mean daily T_i first exceeded 0.5 °C at Site 17 (on 18th April; Figure 5.11A) but did not exceed 0.5 °C until three weeks later at Site 3 (on 7th May; Figure 5.10A).

5.4.2.3 *Comparison of debris surface temperatures (T_s) and their relationship with air temperatures (T_a) at Sites 3 and 17*

T_s is a function of energy transfer at the surface of the debris and an important control on heat transfer through the debris layer (Nakawo and Young, 1981; Gibson *et al.*, 2018). In order to examine how T_s varies between sites with different topography and properties, T_s was compared between Sites 3 and 17 and the relationship between T_s and T_a was also assessed at both sites. Hourly T_s at both Sites 3 and 17 were strongly correlated between November 2016 and October 2017 (r = 0.94). However, there were distinct differences in T_s between the sites; mean T_s was warmer at Site 3 (mean and standard deviation: 8.6 ± 6.6 °C) and cooler at Site 17 (5.1 ± 5.4 °C). A Wilcoxon signed rank test showed that this difference in T_s between the sites was statistically significant ($p<0.05$).

The relationship between T_a and T_s was assessed at Sites 3 and 17 through correlations of the hourly datasets (the highest temporal resolution of the data) for maximum detail. The period of snow-cover between January and March prevented diurnal temperature oscillations in the debris so the temperature data was removed from this period before analysing the datasets. T_a and T_s were strongly correlated at both Site 3 (0.78; $p<0.05$) and Site 17 (0.81; $p<0.05$). However, Wilcoxon signed rank tests showed that at Site 3, T_s (mean and standard deviation: 8.0 ± 4.0 °C) was significantly warmer than T_a (5.5 ± 3.6 °C; $p<0.05$; Table 5.2) whereas at Site 17, T_s (4.7 ± 3.1 °C) was significantly cooler than T_a (5.5 ± 3.7 °C; $p<0.05$).

To examine these differences in the relationship between T_a and T_s at both sites in more detail, the temperatures were separated into day hours (6:00 to 17:00) and night hours (18:00 to 5:00). At Site 3, day time T_s (10.9 ± 4.5 °C) was significantly warmer than T_a (6.9 ± 3.5°C; $p<0.05$). During the night period, T_s (5.0 ± 4.0 °C) was also significantly warmer than T_a (4.2 ± 3.9 °C; $p<0.05$) but the difference was less significant (Table 5.2). At Site 17, there was no significant difference between day time T_s (6.5 ± 3.5 °C) and T_a (7.0 ± 3.6 °C) but at night, T_s (2.9 ± 2.8 °C) was significantly cooler than T_a (4.0 ± 4.0°C; $p<0.05$; Table 5.2). The differences between T_a and T_s, for both day time and night time, were more significant during the monsoon and less, or not significant, during the winter months at both sites (Table 5.2).

Table 5.2: Wilcoxon signed rank test results for T_a vs T_s at Sites 3 and 17 for 24-hour, day time and night time periods and for the whole measurement period and winter, spring and the monsoon. Note that at Site 3, mean T_s was significantly warmer than mean T_a for the whole period, whereas at Site 17, mean T_a was significantly warmer than mean T_s apart from during the day when there was no significant difference.

	Site 3: T_a vs T_s								
	24-hour			**Day**			**Night**		
	T_a mean	**T_s mean**	**p-value**	**T_a mean**	**T_s mean**	**p-value**	**T_a mean**	**T_s mean**	**p-value**
Whole period	5.54	7.95	<0.001	6.85	10.89	<0.001	4.23	5.01	<0.01
Winter	1.13	2.53	0.13	2.92	5.47	<0.01	-0.67	-0.41	0.77
Spring	4.51	7.85	<0.001	6.12	11.41	<0.001	2.90	4.29	<0.001
Monsoon	8.48	10.80	<0.001	9.32	13.04	<0.001	7.63	8.55	<0.001
	Site 17: T_a vs T_s								
	24-hour			**Day**			**Night**		
	T_a mean	**T_s mean**	**p-value**	**T_a mean**	**T_s mean**	**p-value**	**T_a mean**	**T_s mean**	**p-value**
Whole period	5.50	4.70	<0.001	6.96	6.47	0.06	4.04	2.94	<0.001
Winter	0.61	0.32	0.21	2.30	1.58	0.12	-1.07	-0.93	0.57
Spring	4.60	4.47	0.80	6.51	6.77	0.14	2.69	2.18	0.06
Monsoon	8.51	7.20	<0.001	9.53	8.86	<0.001	7.49	5.54	<0.001

5.4.2.4 *Temporal variability of the linearity and gradient of debris temperature-depth profiles at Sites 3 and 17*

Instantaneous temperature-depth profiles through debris layers more than several centimetres thick, tend to be non-linear (Conway and Rasmussen, 2000; Nicholson and Benn, 2006). This is because the diurnal temperature cycles do not allow enough time for the debris to reach a steady state temperature (Conway and Rasmussen, 2000; Reznichenko *et al.*, 2010). However, there is an assumption that the relationship between temperature and depth averaged over a 24-hour period should be linear, if heat transfer through the debris is predominantly via conduction (Conway and Rasmussen, 2000; Nicholson and Benn, 2006; Nicholson and Benn, 2013). This assumption was used when assessing temporal variations in temperature-depth relationships at Site 3 (Figure 5.10C) and Site 17 (Figure 5.11C) from November 2016 to October 2017. At Site 3, 58% of days had linear 24-hour profiles (defined as r^2 >0.95 and standard deviation >0.8 °C). Most of the non-linear days (when non-conductive processes were more prevalent) occurred in December and February to May, but there was a period of linear profiles in January and profiles were predominantly linear from May onwards (Figure 5.10C), indicating heat transfer by conduction. Site 17 had very few linear 24-hour temperature-depth profiles (as defined earlier) in winter but had mostly linear profiles in April and May up until measurements ended on 20th May due to collapse of the debris (Figure 5.11C).

The gradients of the temperature-depth profiles at Site 3 (Figure 5.10D) and Site 17 (Figure 5.11D) were positive in November and December, ranging between 1 and 10 °C m^{-1}, and also positive from April onwards but with larger magnitude (1 and 20 °C m^{-1}). This indicates heat flux towards the ice surface. However, in January and February the gradients were negative at both sites and of smaller magnitude (-1 and -10 °C m^{-1}) than the gradients in the spring and monsoon (Figure 5.10D and Figure 5.11D), indicating a small heat flux away from the ice surface.

5.4.2.5 *Temporal variability of debris thermal properties at Sites 3 and 17*

Effective thermal diffusivity was estimated for the upper five depths at Site 3 and upper four depths at Site 17 (Figure 5.12). Diffusivity was not measured at the lowest depth at either site because the temperature changes for a large part of the measurement period were very small at these depths and not captured by the iButtons, which had a precision of 0.5 °C (Nicholson and Benn, 2013). At both sites and at all sampled depths, diffusivity was higher in the monsoon than in the winter (Figure 5.12). Diffusivity was generally higher at Site 17 than Site 3, but it should be noted that the depths at which diffusivity was measured in the debris differed between the two sites (Figure 5.12).

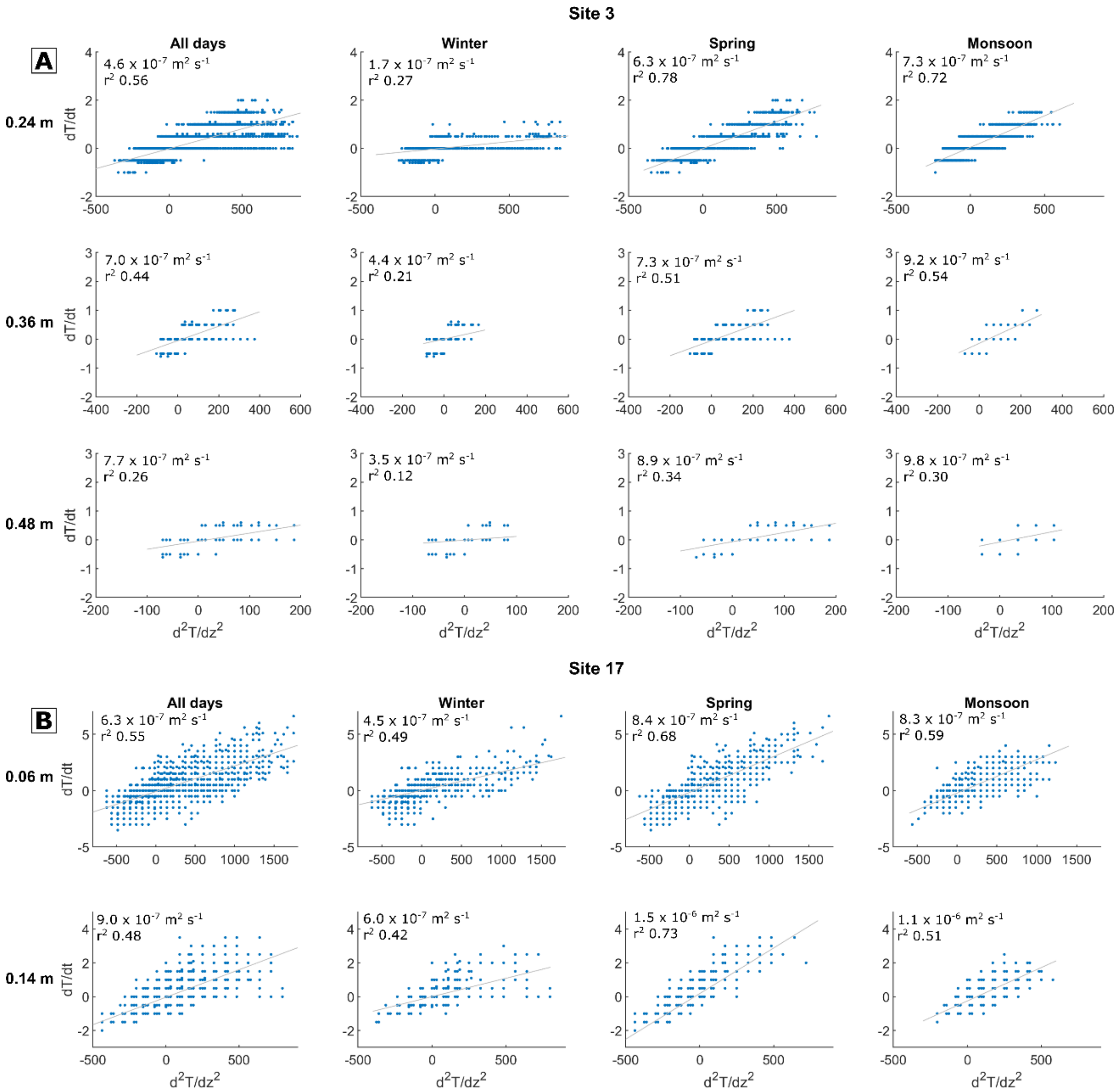

Figure 5.12: The first derivative of change in temperature with time against the second derivative of change in temperature with depth for the whole measurement period (4th November 2016 to 1st October 2017), winter, spring and the monsoon for A) Site 3 and B) Site 17. The gradient and r^2 value of the lines of best fit for each plot are given. The gradients of each line of best fit are the values used for effective thermal diffusivity.

At Site 3, mean daily effective diffusivity increased in magnitude and amplitude with depth in the debris (Figure 5.10E). Diffusivity decreased between November and January and stabilised at all depths from April on into the monsoon. At Site 17, daily diffusivity at 0.14 m depth underwent large fluctuations in winter and reached a peak during the spring before decreasing and stabilising during the monsoon (Figure 5.11E). Comparison of mean daily diffusivity, averaged for the upper depths at both sites, shows that diffusivity at Site 17 regularly exceeded Site 3 in November and December, and again from April until the onset of the monsoon (Figure 5.13). During the monsoon, the difference in diffusivity between the sites decreased but diffusivity at Site 17 was still significantly higher than at Site 3 (Wilcoxon signed rank test: $p<0.05$).

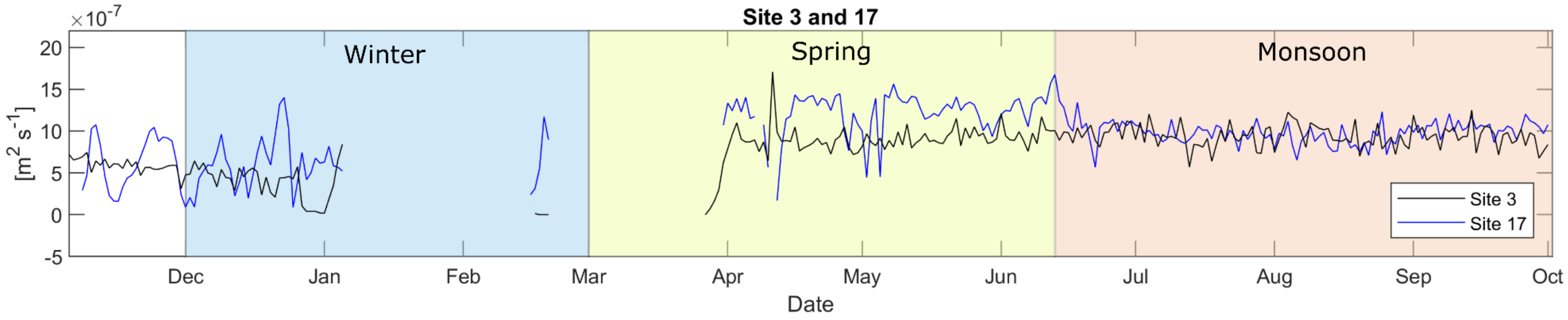

Figure 5.13: Mean daily diffusivity for the upper five depths at Site 3 and upper four depths at Site 17 from November 2016 to October 2017. Data during the period of snow-cover between January and March, identified as when diurnal temperature oscillations stopped entering the debris, have been removed.

5.4.2.6 *Modelled ablation rates for the full measurement period and the monsoon at Sites 3 and 17*

The debris temperature data from Sites 3 and 17 were used to model ablation rates for the full measurement period (November 2016 to October 2017). The modelled rates were compared to the observed ablation rates (also measured from November 2016 to October 2017) to check that they were of similar magnitudes. Following this, ablation rates were modelled for the monsoon season, when meteorological conditions were most stable and heat was predominantly transferred via conduction (Figure 5.10C and Figure 5.11C), to assess the magnitude of melt that occurred during this season.

Mean effective thermal diffusivity for the upper five depths at Site 3, from 4th November 2016 to 1st October 2017, was 6.4×10^{-7} m^2 s^{-1} (Table 5.3). The mean effective thermal conductivity was estimated to be 0.87 ± 0.09 W m^{-1} K^{-1}. The modelled ablation rate was 0.19 cm per day, equating to an annual ablation rate of 0.69 m a^{-1} (Table 5.3). This was very similar to the observed ablation rate (0.68 m a^{-1}; Figure 5.6). Mean effective thermal diffusivity for the upper four depths at Site 17, between 7th November 2016 and 1st October 2017, was 7.67×10^{-7} m^2 s^{-1} and mean effective thermal conductivity was 1.04 ± 0.10 W m^{-1} K^{-1} (Table 5.3). The modelled ablation rate was 0.35 cm per day, equating to an ablation rate of 1.27 m a^{-1} (Table 5.3). This was less than the observed ablation rate (>1.52 m a^{-1}; a minimum value because the stake melted out; Figure 5.6). The disparity between them could be because heat transfer during part of the winter and spring seasons was predominantly via non-conductive processes (Figure 5.10C and Figure 5.11C) and the modelled rate is based on the temperature values of the upper four iButtons only. For the monsoon period (12th June to 1st October 2017), the modelled ablation rate at Site 17 (3.23 m a^{-1}) was almost double the ablation rate at Site 3 (1.64 m a^{-1}; Table 5.3).

Table 5.3: Modelled ablation rates at Sites 3 and 17 derived from thermal properties. Mean effective thermal diffusivity and mean effective thermal conductivity calculated from the debris temperatures in the upper five depths at Site 3 and the upper four depths at Site 17 for the entire measurement period (4th November 2016 to 1st October 2017) and the monsoon (12th June to 1st October).

	Site	**Diffusivity ($m^2 s^{-1}$)**	**Conductivity ($W m^{-1} K^{-1}$)**	**Ablation rate (cm day^{-1})**	**Ablation rate ($m a^{-1}$)**
4th Nov 2016 - 1st Oct 2017	Site 3	6.4×10^{-7}	0.87 ± 0.09	0.19	0.69
	Site 17	7.67×10^{-7}	1.04 ± 0.10	0.35	1.27
Monsoon	Site 3	8.76×10^{-7}	1.19 ± 0.12	0.45	1.64
	Site 17	9.61×10^{-7}	1.3 ± 0.13	0.88	3.23

5.5 Discussion

5.5.1 *Supraglacial debris properties, ablation rates, and velocity on ASG*

5.5.1.1 *Spatial variability of supraglacial debris properties and thickness and the relationship between sub-debris ablation rates and debris thickness on ASG*

The spatial variability of debris thickness, surface roughness and grain size across the study site (Table 5.1, Figure 5.4 and Figure 5.5) shows that the supraglacial debris on this part of the glacier was highly heterogeneous. This is due to a combination of debris transfer processes which tend to be very variable over small spatial scales, such as localised debris inputs from mass movements (Gibson *et al.*, 2017), melt out of englacial debris (Kirkbride and Deline, 2013) and gravitational reworking of debris (Nicholson *et al.*, 2018).

Ablation rates under debris thicknesses of up to 0.41 m were high (>1.5 m a^{-1}; Table 5.1) between November 2016 and October 2017. However, substantially reduced melt rates (>50% less) occurred at Sites 3 and 5, which had debris thicknesses of >0.6 m. This indicates that ablation was inhibited more effectively under thicker debris and is consistent with established theory on the influence of debris thickness on ablation derived from field observations (e.g. Østrem, 1959; Mattson, 1993; Kayastha *et al.*, 2000; Nicholson and Benn, 2006), laboratory experiments (Reznichenko *et al.*, 2010) and modelling studies (Evatt *et al.*, 2015; Anderson and Anderson, 2016).

It is not possible to directly compare the ablation rates under debris thicknesses <0.41 m on ASG with Østrem curves from other studies because they are minimum ablation rates and the actual melt at these sites may have been larger. However, the ablation rates at the sites with thicker debris (0.18 cm day^{-1} under 0.61 m and 0.19 cm day^{-1} under 0.72 m; Table 5.1) are slightly smaller than ablation rates observed on Larsbreen (Svalbard) under similar debris thicknesses (~0.3 cm day^{-1} under ~0.58 m debris) (Nicholson and Benn, 2006). They are also of a smaller magnitude than Østrem curves fitted to data from multiple ablation studies (~0.3 cm day^{-1} to ~0.7 cm day^{-1} under debris thicknesses between 0.6 m and 0.7 m) (Anderson and Anderson, 2016), and results from a model that incorporated debris layer porosity and airflow (~0.4 cm day^{-1} under ~0.6 m debris) (Evatt *et al.*, 2015). This disparity is probably because the ablation rates on ASG are averaged over the winter, spring and monsoon seasons while many studies measure ablation rates only during the summer months (e.g. Østrem, 1959; Khan, 1989; Kayastha *et al.*, 2000; Mihalcea *et al.*, 2006). Regular monitoring through the year and/or longer ablation stakes would be needed to measure the ablation rates under thinner debris on ASG more accurately.

5.5.1.2 *Ice flow velocity on ASG*

There were relatively high velocities (mean displacement: 16 m a^{-1}) across the study site on ASG during the measurement period (Figure 5.7), compared with many debris-covered glaciers in the Himalayas which have no detectable flow in the lower ablation area (Quincey *et al.*, 2009; Thompson *et al.*, 2016). This shows that although the ablation zone of ASG melted more than 1.5 m a^{-1} in multiple areas (Figure 5.6), and was disconnected from most of the glacier accumulation areas, it had not yet stagnated, which commonly occurs in conjunction with rapid down-wasting on debris-covered glacier tongues (Quincey *et al.*, 2009; Benn *et al.*, 2012; Nicholson and Benn, 2013; Rowan *et al.*, 2015). This indicates that ASG may still be in a relatively early phase of response to climate change (Benn *et al.*, 2012). It is likely that the glacier is entering the second regime of debris-covered glacier evolution defined in Benn *et al.* (2012), in which the ablation zone is subject to reduced ice flux from the accumulation zone, enhanced mass loss, and an inverted mass balance gradient. It is expected that this will eventually lead to substantial deceleration and stagnation in the ablation zone of ASG.

The stake displacements suggest a trend of increasing glacier velocity towards the down-glacier end of the study site (Figure 5.7). This is inconsistent with many observations of debris-covered glaciers in the Himalayas, which show that glacier velocities tend to decrease towards the terminus (Quincey *et al.*, 2009; Immerzeel *et al.*, 2014; Robson *et al.*, 2018), due to down-wasting and reduced driving stresses on the glacier tongue (Benn *et al.*, 2012). This trend could be due to a localised control on glacier velocity in this area, such as an increase in the gradient of the bedrock. However, the data were not available to test this hypothesis.

5.5.2 *Temporal variations in debris temperatures (T_d) and thermal properties on ASG*

The thermal regime of the supraglacial debris on ASG underwent substantial and complex changes between November 2016 and October 2017 at both diurnal and seasonal timescales. T_d at Sites 3 and 17 was subject to strong diurnal temperature oscillations for large sections of the measurement period (Figure 5.9). This shows that a portion of the heat transferred into the debris during the day was released back into the atmosphere during the night and that the debris rarely reached a steady state heat flux (Reznichenko *et al.*, 2010).

Large seasonal changes also occurred in T_d and debris thermal properties, coinciding with seasonal variations in T_a and the timing of periods of snow cover. During the winter months, diurnal oscillations at Sites 3 and 17 did not penetrate down to the ice surface (Figure 5.9), demonstrating that heat flux into the debris from the surface was not sufficient to warm the lowest depths of the debris (Figure 5.9). Diurnal cycles at both sites reached the ice-debris interface in April 2017, as changes in T_d occurred at all depths in the debris, and this continued into the monsoon (Figure 5.9).

Apart from the period of negative T_d in January and February, which coincided with sub-zero T_a (Figure 5.10B and Figure 5.11B) and snow-cover, temperatures at most depths in the debris in winter and the beginning of spring were close to or above 0 °C (0 to 0.5 °C; Figure 5.9, Figure 5.10A and Figure 5.11A) at both sites. These debris temperatures were relatively warm compared with debris temperatures on Ngozumpa glacier, a debris-covered glacier in the Everest region, where debris temperatures were recorded to well below 0 °C through most of the winter (Nicholson and Benn, 2013). This temperature difference may be due to the different elevations of the sampling areas: the debris temperatures at Ngozumpa glacier were sampled at ~4800 m elevation (Nicholson and Benn, 2013) whereas the study site on ASG was ~3900 m elevation. The gradual increase in T_d at all depths in the second half of the spring season coincided with warming T_a (Figure 5.10 and Figure 5.11). During the monsoon season at Site 3, T_d at all depths were positive and stable.

Most energy-balance models calculate ablation under debris with the assumption that heat transfer occurs via conduction (Nakawo and Young, 1981; Nicholson and Benn, 2006; Reid and Brock, 2010). However, heat can also be transferred through supraglacial debris by convection, advection, radiation and/or phase changes (Humlum, 1997; Nicholson and Benn, 2013; Evatt *et al.*, 2015). Previous studies of supraglacial debris temperature on Khumbu and Ngozumpa glaciers showed that, during the summer, heat was transferred through the debris layer primarily via conduction (Conway and Rasmussen, 2000; Nicholson and Benn, 2013). However, during seasonal transition periods, or when water was present, non-conductive processes were more likely to be dominant (Nicholson and Benn, 2013). The data in this chapter support those previous studies because non-conductive processes occurred at both Sites 3 and 17 in winter and the beginning of spring, which is attributed to changeable weather and latent heat transfer from phase changes (Conway and Rasmussen, 2000; Nicholson and Benn, 2013). However, heat was predominantly transferred via conduction from May until October at Site 3, and from April until measurements ended at Site 17 (Figure 5.10C and Figure 5.11C). The temperature data indicate that these periods of conductive heat transfer coincided with ablation (Figure 5.10A and Figure 5.11A). These results lend support to the assumptions made by energy-balance models that during periods of ablation, heat transfer is dominated by conduction.

Observations from the Everest region showed that effective thermal diffusivity and conductivity of the supraglacial debris layer varied over time (Nicholson and Benn, 2013; Rounce *et al.*, 2015) and, on Ngozumpa glacier, conductivity was ~30% higher in the summer than winter (Nicholson and Benn, 2013). The data on ASG support these findings as effective diffusivity at Sites 3 and 17 was higher in spring and the monsoon than in winter (Figure 5.10E, Figure 5.11E and Figure 5.12). This seasonal variation is probably a result of changes in temperature and moisture content, phase changes due to the different conductivity of ice and water, and the temperature dependence of conductivity (Nicholson and Benn, 2013; Rounce *et al.*, 2015).

5.5.3 *Similarities and differences in the supraglacial debris thermal regimes of Sites 3 and 17*

The data in this chapter show that Sites 3 and 17, which had different debris thicknesses, properties and surface topography, and underwent different rates of ablation (Table 5.1), had distinct debris thermal regimes. In this section, these differences and their potential influence on glacier ablation are discussed.

First, the diurnal oscillations were narrower at Site 17 than at Site 3 throughout the measurement period (Figure 5.9), indicating that over each 24-hour period, the heat was transferred into, and back out of, the debris more rapidly at Site 17 than at Site 3. It is hypothesised that this is due to the reduced heat capacity of the thinner debris at Site 17 compared with Site 3 (Table 5.1) (Reznichenko *et al.*, 2010). Second, although T_s at Sites 3 and 17 strongly correlated with each other (Table 5.2

Table 5.2), indicating that their periodicity and seasonality were very similar (Gibson *et al.*, 2018) and that the sites were subject to similar external changes, T_s at Site 3 was significantly warmer than at Site 17. This disparity is probably due to the different topographic settings of the sites (especially in terms of aspect and slope), which also influenced spatial variations in T_s on Khumbu glacier (Gibson *et al.*, 2018), and Lirung glacier in the Langtang region (Steiner and Pellicciotti, 2016). Site 3, which was located on an exposed debris peak, most likely received more direct solar radiation than Site 17, the latter being located on a north-facing slope in a hollow (Figure 5.8). T_s is a key control on the thermal regime of supraglacial debris (Nicholson and Benn, 2006) and cooler T_s may help to explain the cooler T_d at Site 17, compared with Site 3, during the spring and monsoon seasons (Figure 5.9). Site 17 also had thinner debris which tends to have cooler T_s than thicker debris, due to the greater influence of the ice surface below (Nakawo and Young, 1981; Brock *et al.*, 2010). During the period of snow-cover between January and February, Site 17 had less extreme cold T_d compared with Site 3 (Figure 5.9). It is hypothesised that this is a result of a lower sensitivity to external temperatures at Site 17. This is consistent with its location in a hollow on the glacier surface where it is likely to be more protected from changes in meteorological conditions than at Site 3.

Third, the relationships between T_s and T_a were different at Sites 3 and 17 (Table 5.2). These differences appeared to be driven by significantly warmer T_s than T_a during the day at Site 3; and significantly cooler T_s than T_a during the night at Site 17 (Table 5.2). Gibson *et al.* (2018) investigated similar relationships on Khumbu glacier and found that T_s tended to be warmer than T_a at all sampled locations. Meanwhile, on Lirung glacier, T_s was warmer than T_a during the day and cooler than T_a during the night because of the higher conductive capacity of debris (Steiner and Pellicciotti, 2016). The data show that T_s at Site 17 was either not significantly different from T_a or was significantly cooler than T_a during the day time (Table 5.2). This is probably because Site 17 was in a shaded hollow and received very little direct solar radiation and, as a result, the debris would have only heated up as much as the surrounding T_a during the day. T_s at Site 3 exceeded T_a during the day, as would be expected from a site that received more direct shortwave radiation. It is hypothesised that T_s was warmer than T_a at night at Site 3 (in contrast to Site 17 where T_s was cooler than T_a at night; Table 5.2) because of the higher specific heat capacity of the thicker debris. This meant that T_s cooled more slowly at night at Site 3 than at Site 17, as demonstrated by the wider diurnal oscillations at Site 3 in Figure 5.9A. Fourth, Site 17 tended to have higher effective thermal diffusivity than Site 3 for large sections of the measurement period (Figure 5.13), which could be due to differences in moisture content, phase of water, debris pore space and/or debris temperature (Nicholson and Benn, 2013; Rounce *et al.*, 2015).

Despite generally cooler temperatures and a lower heat capacity, the data show that ablation started earlier at Site 17 than Site 3 (Figure 5.10A and Figure 5.11A), and Site 17 underwent more than twice the amount of melt as Site 3 between November 2016 and October 2017 (Figure 5.6). Comparison of the thermal regime at both sites suggest that this can be partially explained by the diurnal temperature cycles (Figure 5.9) and mean daily temperature (Figure 5.10A and Figure 5.11A). They showed that although Site 17 was located in a shaded hollow on the glacier and had cooler T_d than Site 3, energy had less distance to travel through the thinner debris at Site 17 to reach the ice surface. Moreover, Site 17 generally had higher thermal diffusivity than Site 3 (Figure 5.13). It can therefore be assumed that Site 17 had higher thermal conductivity, which is directly proportional to thermal diffusivity (Eq. 5.2), than Site 3. This indicates that heat was conducted more quickly through the debris at Site 17 than at Site 3 and that less energy was needed to raise the temperature of the debris and melt ice at Site 17. This shows that even across relatively small distances on a glacier ablation zone, the debris thermal regime can be very diverse, due to varying topography and debris properties, and this can have an important influence on ablation rates.

5.5.4 *Seasonal variation of timing and magnitude of ablation on ASG*

During the winter, T_i did not exceed 0.5 °C (the temperature threshold used to define ablation in this study) at Site 3 or Site 17. Therefore, the data suggest that no melt occurred in this season. However, T_i was between 0 °C and 0.5 °C during December, most of January, March, and the first half of April (Figure 5.9). These warm temperatures at the ice-debris interface indicate that the ice was almost always close to the melting point and that some melt may have occurred during the winter and early spring but cannot be detected because of the temperature resolution of the iButton sensors. Higher resolution temperature sensors would be needed to assess whether ablation occurred during the winter and early spring on ASG. If there was any melting during this period, it would probably have been very minor. The debris temperature data suggest that ablation began at both sites in mid-April (when T_i started to exceed 0.5 °C; Figure 5.9). However, melt occurred more consistently at Site 17 than Site 3 during April whereas regular daily melting did not occur at Site 3 until the beginning of May (Figure 5.9). It was not possible to model ablation rates during the spring because of the lack of stable meteorological conditions (Nicholson and Benn, 2013). However, T_i was cooler in May than from June onwards at Site 3 (Figure 5.9), suggesting that the magnitude of ablation was less in the spring than during the monsoon. T_i at Site 3 indicates that ablation continued consistently through the monsoon. Although T_i data for Site 17 are not available during this period, it is assumed that ablation also continued at this site.

Previous studies that have investigated ice surface temperatures and sub-debris ablation rates in the Himalayas tend to focus on the monsoon season, with measurements taken at various points between the end of May and November of a given year (e.g. Mattson, 1993; Conway and Rasmussen, 2000; Takeuchi *et al.*, 2000; Rounce *et al.*, 2015). However, the data on ASG indicate that melt was underway at both Sites 3 and 17 much earlier than this (Figure 5.9) and suggest that ablation during the spring could be an important component of annual ablation, particularly on glaciers with relatively low-elevation ablation zones.

The modelled ablation rates for the monsoon season at Site 3 (0.45 cm day^{-1} under 0.72 m debris thickness) and Site 17 (0.88 cm day^{-1} under 0.37 m debris thickness; Table 5.3) fit within the range of Østrem curves compiled from multiple ablation studies, almost all of which derive their data from the summer months (Anderson and Anderson, 2016). This shows that sub-debris ablation on ASG during the monsoon was of a similar magnitude to other glaciers during the peak ablation season.

5.6 Conclusions

The properties and thermal regime of supraglacial debris and its influence on ablation were investigated on Annapurna South glacier (ASG) in the Annapurna Conservation Area (ACA), Nepal over a year. The aim of this chapter was to characterise debris properties and ablation rates on ASG, analyse temporal variations in the thermal regime of the debris, assess how the thermal regime varied under different debris properties, and infer the timing and magnitude of ablation.

The results show that supraglacial debris characteristics and thickness were highly variable over short distances, and temporal variations in the thermal regime of the debris occurred on both diurnal and seasonal timescales, influencing the timing and magnitude of ablation through the year. Measured ablation rates ranged from 0.66 m a^{-1} to >1.58 m a^{-1} from November 2016 to November 2017, and ablation was reduced under thicker debris (>0.6 m). Heat was predominantly transferred through the debris via conduction during the period of glacier ablation, supporting findings from previous studies and assumptions of heat transfer commonly used in energy-balance modelling. The thermal regime at Sites 3 and 17 had distinct differences, controlled partially by surface topography and debris thickness. However, despite generally cooler debris temperatures, ablation started earlier, and was of higher magnitude, at Site 17 than Site 3, due to thinner debris and higher thermal conductivity. This provides a clear illustration of how, despite similar meteorological conditions, spatially variable debris cover can result in differential melting on a glacier surface.

The data in this chapter suggest that ablation at both sites started in April 2017. Previous Himalayan ablation studies have tended to focus on measuring melt during the monsoon months, but this chapter suggests that on glaciers with low-elevation ablation zones (such as ASG), spring ablation could represent an important component of annual ablation. Indeed, the temperatures at the ice-debris interface on ASG were close to the melting point through most of the winter and early spring, suggesting that some melt may have occurred even earlier than this but was not detected because of the resolution of the temperature sensors. The magnitude of ablation increased towards the monsoon and modelled ablation rates for the monsoon season at Sites 3 and 17 were of a similar magnitude to monsoon/summer ablation on other debris-covered glaciers.

This chapter contributes new field observations to a very limited dataset on the temporal variations of supraglacial debris thermal regimes in the Himalayas. It provides rare and useful insight into the processes occurring in the debris, and their influence on melt, at high temporal resolutions and across different seasons. This work supports findings from Chapter 3 that shows that supraglacial debris is an important control on the spatial pattern of glacier ablation in the ACA, and demonstrates that this influence also occurs at much smaller spatial scales and timescales, due to differing debris properties and thickness.

Chapter 6: Discussion

The overall aim of this thesis was to reveal the specific characteristics of recent (2000 to 2016) glacier change in the Annapurna Conservation Area (ACA) in central Nepal, and identify the scale and sources of local variability in the ACA's glacier change signal at a range of spatial and temporal scales (Chapter 1: Section 1.3). This chapter summarises the main findings of the thesis, discusses some of the lessons learned, and outlines directions for further research.

6.1 Glacier change in the ACA

A key finding of this project is that glaciers in the Annapurna Conservation Area (ACA) have been shrinking, down-wasting and losing mass since 2000 (Chapter 3). These results contribute to addressing the overall project aim and the first objective of the project (Chapter 1: Section 1.3). Chapter 3 shows that from 2000 to 2016, glaciers in the ACA lost 8.5% of their area, had a mean down-wasting rate of -0.33 ± 0.22 m a^{-1} and mass balance declined by -0.28 ± 0.24 m w.e. a^{-1} (Chapter 3: Table 3.5) (Lovell *et al.*, 2019). This is consistent with widespread glacier shrinkage and mass loss across most of High Mountain Asia (HMA) (Kulkarni *et al.*, 2007; Scherler *et al.*, 2011b; Kääb *et al.*, 2012; Gardelle *et al.*, 2013; Brun *et al.*, 2017), and worldwide (Zemp *et al.*, 2015; Zemp *et al.*, 2019) during this period. This trend has important implications for global sea-level rise. Since 1961, global glacier mass loss (excluding the ice sheets) has contributed an estimated 27 ± 22 mm to global sea-level rise (Zemp *et al.*, 2019) and this trend is accelerating (Wouters *et al.*, 2019; Zemp *et al.*, 2019). By the end of the 21st century, glaciers worldwide are expected to contribute a further 148-217 mm to global sea-level rise, depending on the emissions scenario used (Marzeion *et al.*, 2012). Although recent mass loss from HMA glaciers have been moderate compared to some other glacierised regions, such as Alaska and the Southern Andes (Wouters *et al.*, 2019; Zemp *et al.*, 2019), future contributions to sea level from glaciers in HMA are still expected to be important, with estimates ranging from 2 mm to 11 mm global sea-level equivalent by 2100 (Marzeion *et al.*, 2012).

Perhaps of greater significance than their sea-level contribution, meltwater from glaciers in HMA plays a vital role in maintaining inputs to Asian river systems during summers of drought (Pritchard, 2019). Meltwater inputs from recent glacier mass loss are 1.6 times larger than normal summer glacier meltwater inputs and these contributions are projected to increase in the next few decades as glaciers continue to lose mass (Pritchard, 2019). However, as glaciers shrink, their capacity to act as a reservoir will decline and their meltwater contributions will subsequently decrease (Pritchard, 2019). Therefore, HMA glacier mass loss has important implications for the sustainability of water resources in this region, which support ~800 million people (Immerzeel *et al.*, 2010).

Glacier mass loss (-0.28 ± 0.24 m w.e. a^{-1}) and down-wasting (-0.33 ± 0.22 m a^{-1}) rates in the ACA between 2000 and 2013/16 (Chapter 3; Table 3.5) were smaller than in the Everest region (mean mass balance: -0.52 ± 0.22 m w.e. a^{-1}, between 2000 and 2015) (King *et al.*, 2017), and the Langtang region (mean mass balance: -0.38 ± 0.17 m w.e. a^{-1} and mean surface lowering: -0.45 ± 0.18 m a^{-1}, between 2006 and 2015) (Ragettli *et al.*, 2016). Moreover, in the Everest region, glaciers have undergone widespread stagnation close to their termini (Quincey *et al.*, 2009). However, our data do not show a comparable trend in the ACA. Results from Chapter 3 show that there was no clear trend of deceleration in glacier velocities in the ACA, and Chapters 3 and 5 confirm that several glaciers in the ACA did not have stagnant tongues (velocities in the ablation zone of ASG ranged from 8 to 22 m a^{-1} between 2016 and 2017). These results are important because they indicate that glaciers in the ACA are perhaps at a less advanced stage of mass loss compared with these other central Himalayan regions, despite the regions often being grouped together in mass balance studies (Gardelle *et al.*, 2013; Brun *et al.*, 2017; Brun *et al.*, 2019).

Rather, the mass loss and down-wasting rates measured in the ACA are of a similar magnitude to the neighbouring Manaslu region (Robson *et al.*, 2018). This demonstrates a clear mass balance and surface lowering disparity between the ACA/Manaslu regions in central Nepal and the regions in east Nepal (Figure 6.1). This difference was also apparent in a HMA-wide analysis of glacier surface-lowering rates (Brun *et al.*, 2017). Furthermore, a recent Himalayan mass balance study, showed that, since 2000, mass loss in the Langtang and Everest regions had accelerated more than in the ACA and Manaslu region (Figure 6.1), increasing the mass balance difference between these Nepalese areas (Maurer *et al.*, 2019). These results strongly indicate that glaciers in these regions are undergoing different responses to climate forcing.

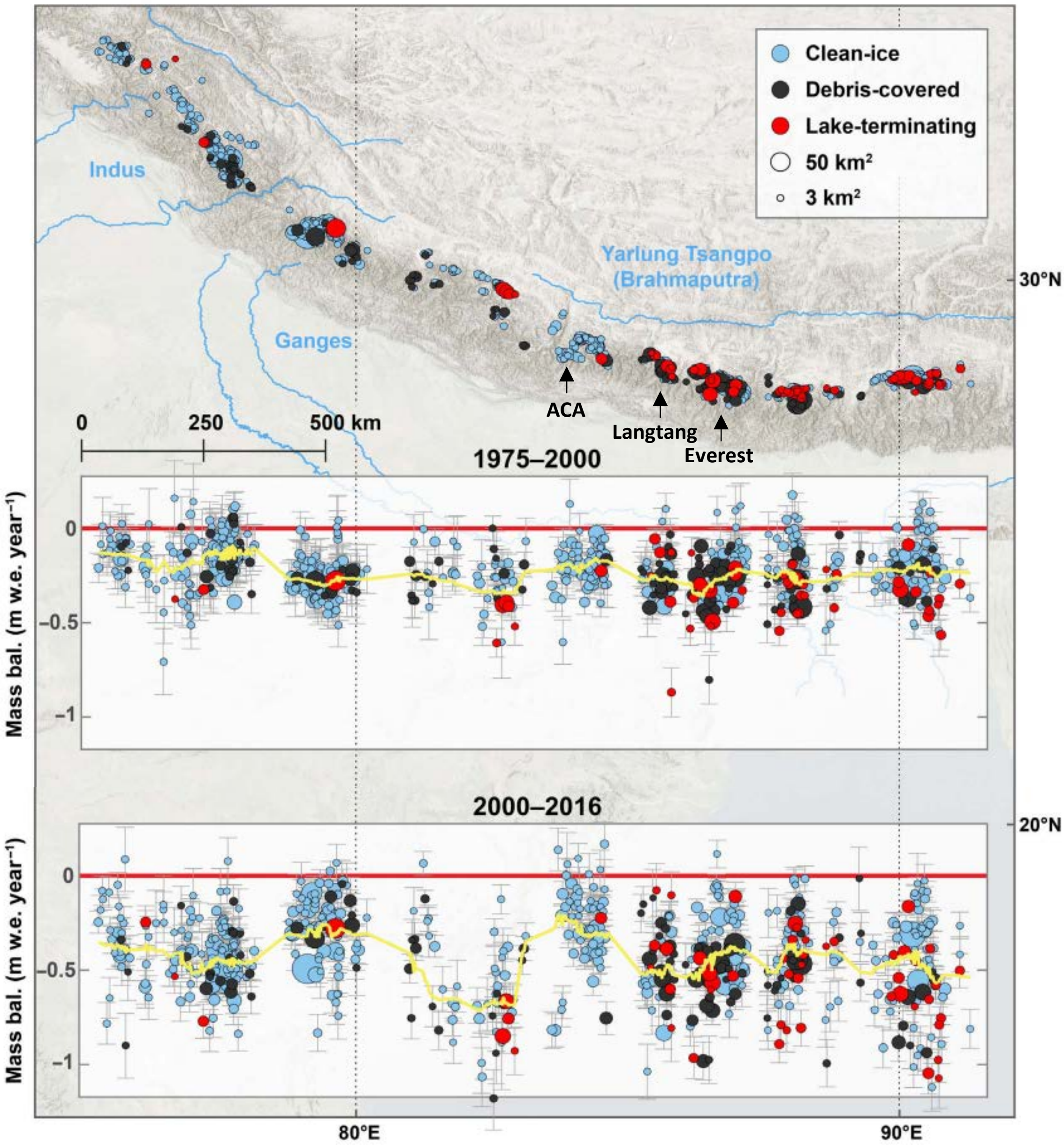

Figure 6.1: Glacier locations and geodetic mass balances in the Himalayas using Hexagon and ASTER DEMs, from Maurer *et al.* (2019), annotated to show the location of the ACA, Langtang and Everest regions. Circle sizes are proportional to glacier areas. Insets show mass balance of individual glaciers from 1975 to 2000 and 2000 to 2016 along a longitudinal transect, horizontally aligned with the map view. The yellow line represents the area-weighted moving-window mean (window size: 30 glaciers). Note the increased difference in mass balance between the ACA and Langtang and Everest regions between the two measurement periods.

The drivers of this regional mass balance discrepancy are not fully understood but it is most likely a result of local climate variability within the overarching climate regime in the central Himalayas. Data from the Tropical Rainfall Measurement Mission showed that between 1998 and 2007, there was higher precipitation in the Greater Himalayan sections of the drainage basins surrounding the ACA and Manaslu regions (the Kali Gandaki, Seti and Marshyangdi rivers) compared with the Everest and Langtang regions (Barros *et al.*, 2000; Bookhagen and Burbank, 2010). This difference in precipitation was attributed to topography (Barros *et al.*, 2000; Bookhagen and Burbank, 2010). First, the topographic relief of the Lesser Himalayas at this point along the range is particularly low, allowing more moisture-rich air to enter the Greater Himalayas (Barros *et al.*, 2000). Second, the topographic relief of the Greater Himalayas in this area is much higher than to the east or west, forcing more moisture out of the air as it passes over (Bookhagen and Burbank, 2010). Higher precipitation availability may help to make glaciers in the ACA and Manaslu regions more resilient to climate change compared with the Langtang and Everest regions, where glaciers are thought to be particularly sensitive to precipitation changes (Salerno *et al.*, 2015). These findings demonstrate the heterogeneity of regional glacier response to climate change in the central Himalayas, and its potential link to highly variable regional climate.

The trend of glacier shrinkage and mass loss in the ACA is highly likely to continue with projected increases in air temperatures across Nepal (Wiltshire, 2014; Dimri *et al.*, 2018; Bolch *et al.*, 2019). Numerical modelling is needed to predict how much mass loss will occur in each sub-region of the ACA, but results from Chapter 3 show that between 2000 and 2016, glaciers in the Muktinath Himal lost the most area and mass (Lovell *et al.*, 2019), and therefore are likely to be the least resilient to future climate change. In contrast, glaciers in the Damodar Himal, which lost less area and mass, are expected to be more resilient (Lovell *et al.*, 2019).

Glaciers in all three sub-regions feed into the populated valleys of the Marshyangdi to the southeast and the Kali Gandaki to the west. In the Kali Gandaki river basin, there was an increasing (although not significant) trend in river discharge from 1964 to 2006 in the dry pre-monsoon and post-monsoon seasons (Manandhar *et al.*, 2012). This was attributed to enhanced melting of snow and glacier ice (Manandhar *et al.*, 2012). This trend is expected to continue for the next few decades as glaciers in the ACA, particularly in the Muktinath Himal, continue to lose mass. However, the trend may reverse as snow cover in the surrounding mountainous areas decreases and the capacity of glaciers to act as meltwater reservoirs declines. This could lead to reduced inputs of water from glaciers during the ablation period (March to October), particularly in the pre- and post-monsoon periods, and potentially increased water stress in the catchment (Manandhar *et al.*, 2012; Bolch *et al.*, 2019; Pritchard, 2019).

6.2 Scale and potential sources of variability in the glacier change signal in the ACA

As well as revealing the characteristics of recent glacier change in the ACA, this project sought to identify the scale of local variability in the ACA's glacier change signal and to put bounds on this variability for the first time. The rationale for this is that when investigating Himalayan glacier changes at larger spatial scales, there tends to be substantial variability, or noise, in the glacier change signal which complicates efforts to identify local controls on glacier behaviour (Brun *et al.*, 2019). Therefore, there is still a need to identify the range of variability, or noise, in the glacier change signal that should be considered 'normal' when modelling glacier change or projecting future glacier response to climate change. This knowledge can be used to improve the accuracy of numerical modelling of future glacier change, which in turn will benefit water resource management and natural hazard prevention. Furthermore, once these bounds on variability are established, further research can focus on picking out glaciers that share certain characteristics to investigate the reasons of this variability using more controlled samples.

6.2.1 *Scale of variability in the glacier change signal in the ACA*

The results from Chapter 3 showed that while the majority of glaciers in the ACA were losing mass and shrinking, there was a substantial amount of local variability in the glacier area change and mass balance signals in the region, both between sub-regions (Figure 3.6) and between individual glaciers (Figure 3.10 & Figure 3.12 to 3.15) (Lovell *et al.*, 2019). Glaciers in the Muktinath Himal had both the largest range of area change and mass balance over the study period (Figure 3.6), although interestingly this sub-region had the least variation in glacier morphological characteristics (including area, maximum elevation and hypsometry) of the three ACA sub-regions (Figure 3.17). While Himalayan glacier change studies on smaller samples of glaciers tend to be less affected by noise (Pellicciotti *et al.*, 2015; Ragettli *et al.*, 2016; Salerno *et al.*, 2017), the variability in glacier change across the ACA demonstrates the scale of noise in the Himalayan glacier change signal that can be expected, and can be considered normal, when looking at larger samples of glaciers.

Chapter 3 also showed that the local variability in the glacier change signal was not uniform across the region, which complicated efforts to identify the sources of this variability. For example, while glacier mass balance and area change were related to maximum elevation and the likelihood of avalanche inputs in the Damodar Himal, the relationships between these local controls and glacier mass balance were not significant in the Muktinath Himal (Chapter 3; Table 3.6). Similarly, there was no significant relationship between area change and potential avalanche inputs in the Muktinath Himal, and only a weak significant relationship between area change and maximum elevation (Chapter 3; Table 3.6).

Furthermore, the significant correlations between the local controls investigated and mass balance or area change in the ACA (Chapter 3) were not very strong (Lovell *et al.*, 2019), suggesting that they only partially explain the variation in glacier change and that there are other controls, or complex interactions between controls, that were not within the scope of this investigation, that also contribute to the variability in glacier behaviour. This is similar to a study investigating six morphological controls (area, median elevation, slope, easting, northing and aspect) on glacier mass balance across 50 glaciers in the European Alps which found that they only explained 51% of the variance (Huss, 2012). Brun *et al.* (2019) also found that glacier tongue slope, mean glacier elevation, supraglacial debris and avalanche contributing area only explained between 8% and 48% of glacier mass balance variation in a sample of ~6500 glaciers across HMA. These findings demonstrate the scale of variability in the glacier change signal that models and forecasting studies can consider to be ‘normal’ when predicting future Himalayan glacier changes, especially across large samples of glaciers and at large (e.g. regional) spatial scales.

6.2.2 *Interaction between topography, hillslope processes and glacierisation in the ACA*

The ACA extends through a range of topographic landscapes, from the high altitude but low relief of the Tibetan plateau in the north to the high relief of the deeply incised valleys on the edge of the plateau towards the south of the region. This has resulted in different styles of glacierisation across the ACA sub-regions which may help to explain some of the observed variation in the glacier change signal between the sub-regions (Chapter 3).

Scherler *et al.* (2011a) developed a conceptual model to explain these different types of glacierisation through a continuum of the interactions between topography, erosion, hillslope processes and glacial dynamics in High Mountain Asia glaciers (Figure 6.2 & Figure 6.3). According to the model, glaciers on the Tibetan plateau are cold-based, low relief, characterised by large accumulation areas, and predominantly fed by direct precipitation (Figure 6.2A). Hillslope flux onto these glaciers is low and the glaciers are not very erosive (Figure 6.3A). This description is consistent with many of the glaciers in the Damodar Himal in the north, which are relatively low relief, and the region has the most top-heavy glaciers (which tend to be characterised by large accumulation zones) and the smallest percentage of debris-cover of all the sub-regions (Chapter 3, Figure 3.17). Glaciers in the second stage of the conceptual model are polythermal, tend to have a less extensive accumulation zone and receive input both from avalanches and direct precipitation (Figure 6.2B). The hillslope flux has increased, resulting in more debris inputs onto the glaciers and downcutting rates are high (Figure 6.3B). This is consistent with glaciers in the Muktinath Himal, which had an increased percentage area covered with debris and had more bottom-heavy glaciers than the Damodar Himal (Chapter 3, Figure 3.17).

In the third stage of the conceptual model, glaciers tend to be temperate, predominantly avalanche-fed, and debris-covered (Figure 6.2C). Glacial erosion occurs mostly through headwall retreat in accumulation areas which are typically steep and, below the snow line, glaciers act as conveyors of debris (Figure 6.3C). These characteristics are commonly found in the glaciers in the Annapurna Himal, which typically have steep headwalls and heavily debris-covered tongues (e.g. ASG and Sabche glacier). In particular, observations in the field on ASG suggested that very little fresh bedrock was being contributed to the glacier tongue directly from the valley sides in the ablation zone (e.g. there were no fresh rockfall scars), and the different strands of sandstone and limestone geology in the supraglacial debris on ASG indicated that the debris was excavated from different sections of geology in headwall and the glacier tongue was conveying this debris down-glacier (Chapter 5, Section 5.2).

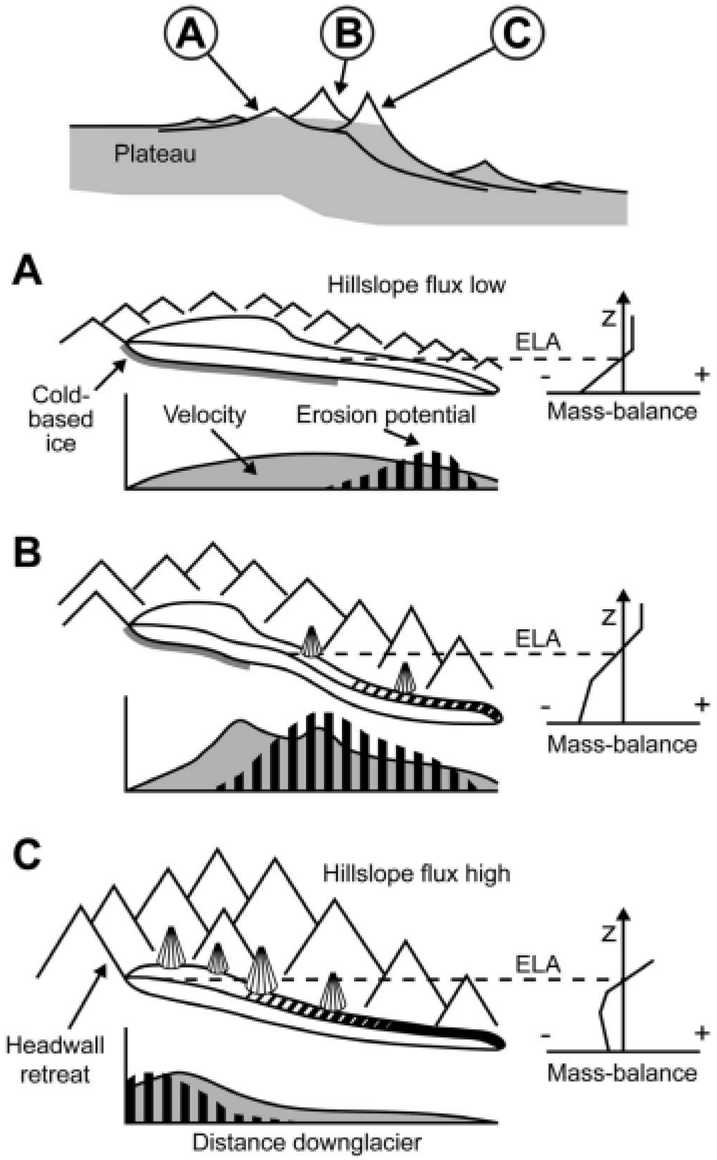

Figure 6.2: Conceptual model of the effect of topography on accumulation types, debris cover, glacier flow velocities and erosion potentials in HMA, from Scherler *et al.* (2011a). A) Mostly cold-based glacier in a low-relief landscape, which is dominantly fed by direct snowfall and has no debris cover (e.g. glaciers in the Damodar Himal); B) polythermal glacier fed by both avalanches and direct snowfall (e.g. glacier in the Muktinath Himal); and C) temperate glacier dominantly fed by avalanches and with abundant debris-cover (e.g. glaciers in the Annapurna Himal).

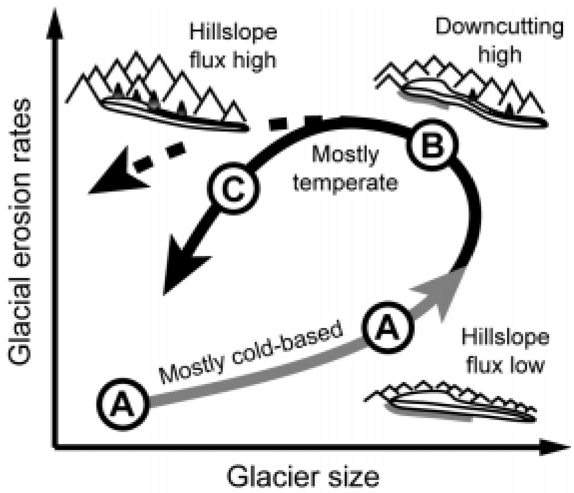

Figure 6.3: Conceptual model showing the morphologic evolution of a plateau-like landscape under glacial influence, from Scherler *et al.* (2011a). A) Initial glacierisation is mostly cold-based and not very erosive; B) progressive glacial down-cutting occurs, starting at the lower end of glaciers, and increases relief and hillslope fluxes; and C) eventually, steep accumulation areas result in significant headwall retreat, but glaciers that are located mostly below the snow line have little erosion potential and mostly act as debris conveyors.

These differences in the glacier characteristics and landscape evolution of the sub-regions in the ACA may help to explain some of the variability in glacier change observed between the sub-regions. For example, the increase in hillslope flux for glaciers in the Annapurna Himal compared with the Damodar Himal and Muktinath Himal has resulted in increased debris-covered area in the Annapurna Himal (Figure 3.17). Alongside glaciers being larger in the Annapurna Himal, probably resulting in slower response times (Chapter 3, Section 3.4.1.1), the increased presence of debris in the ablation zones of glaciers in the sub-region means the glaciers are more likely to lose mass via down-wasting than terminus retreat (Hambrey *et al.*, 2008), which helps to explain why the Annapurna Himal lost significantly less area than the Damodar Himal and Muktinath Himal between 2000 and 2014/15 (Chapter 3, Section 3.3.1).

6.2.3 *Supraglacial debris*

The results from Chapters 3 and 5 show that supraglacial debris is a source of variability in the glacier change signal in the ACA, supporting observations in other parts of the central Himalayas (Ragettli *et al.*, 2016; Robson *et al.*, 2018). Specifically, mean glacier thinning rates on the ablation zones of debris-covered and debris-free glaciers were not significantly different, but supraglacial debris altered the spatial patterns of thinning compared with debris-free glaciers (Lovell *et al.*, 2019). At lower elevations, debris-covered glaciers underwent reduced thinning rates relative to debris-free glaciers (Chapter 3; Figure 3.16), which is attributed to the tendency of debris to be thicker at lower elevations (Anderson and Anderson, 2018). Moreover, on many debris-covered glaciers, maximum thinning rates occurred part-way up the glacier, where debris tends to be thinnest (Chapter 3). This created an inverted thinning profile on the ablation zones of many debris-covered glaciers in the ACA (Chapter 3; Figure 3.7) (Lovell *et al.*, 2019). Numerical modelling of Khumbu glacier in the Everest region showed that the inverted mass balance gradient caused by debris cover will eventually lead to separation of the glacier tongue from the accumulation zone and enhanced glacier mass loss (Figure 6.4) (Rowan *et al.*, 2015). Chapter 5 demonstrates that this process already appears to be underway on ASG, where three of its four accumulation areas are no longer connected to the debris-covered glacier tongue. It is likely that other debris-covered glaciers in the ACA will have similar responses to future climate warming.

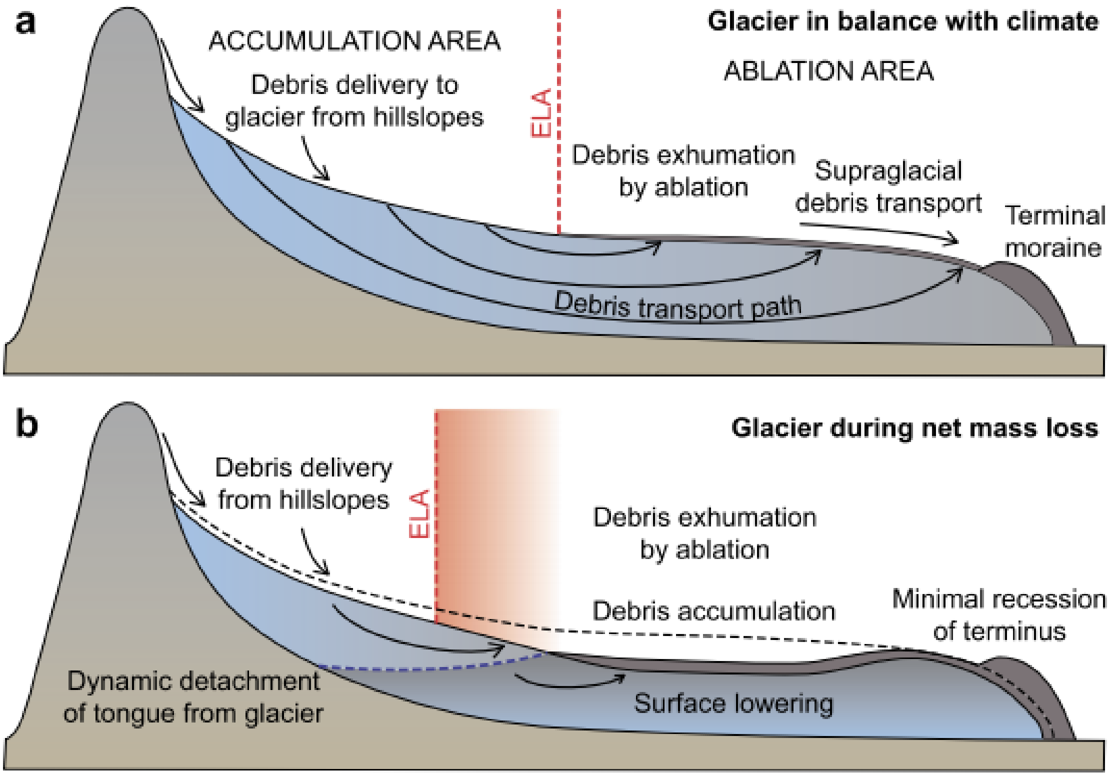

Figure 6.4: A conceptual model illustrating the development of a debris-covered glacier in the Himalayas (from Rowan *et al.*, 2015). a) the glacier is in balance with the climate and b) the glacier is responding to a warming climate, resulting in surface lowering and the development of an inverted mass balance gradient at the terminus.

Chapter 5 presents data from one of a limited number of studies to investigate the thermal regime of supraglacial debris and its influence on ablation rates on a Himalayan glacier over a full year (Nicholson and Benn, 2013). The high temporal resolution of this dataset provides valuable insight into the processes occurring in the debris through time and how they affect melt. The results demonstrate that ablation was influenced by debris thickness and was reduced under the thickest debris (Chapter 5; Figure 5.6). They also show that the thermal regime of the debris varied substantially at both diurnal (Chapter 5; Figure 5.9) and seasonal timescales (Chapter 5; Figure 5.10 and Figure 5.11). The data support previous work in the Himalayas that showed that thermal diffusivity and conductivity varied seasonally (Nicholson and Benn, 2013; Rounce *et al.*, 2015; Chand and Kayastha, 2018) and that conduction was the dominant form of heat transfer through the debris in the monsoon, whereas non-conductive processes were more important during the winter and spring seasons (Nicholson and Benn, 2013). A comparison of two sites on the glacier showed that heat was transferred much more rapidly through one site which had thinner debris with higher thermal conductivity, allowing the ice surface to start melting earlier in the year compared with the other site which had thicker debris with lower thermal conductivity (Chapter 5). This shows that although sites on the same glacier can be exposed to similar external conditions, they can have distinct debris thermal regimes, resulting in different timings and magnitudes of ablation. This chapter confirms that, even on very small spatial scales, supraglacial debris has an important influence on glacier ablation (and consequently mass balance).

6.2.4 *Glacier hypsometry, elevation and avalanche contributions*

Glacier hypsometry, elevation and avalanche contributing area were also found to be potential sources of variability in the glacier change signal (Chapter 3). Glaciers in the ACA with bottom- and very bottom-heavy hypsometry lost significantly more mass than those with top heavy hypsometry (Chapter 3; Figure 3.14). This illustrates the importance of glacier shape and altitudinal distribution in determining the response of a glacier to external forcing and supports other research in the central Himalayas that shows that glaciers with a larger proportion of their mass at lower altitudes are more vulnerable to climate change (Ragettli *et al.*, 2016; Robson *et al.*, 2018). Over a third of glaciers in the ACA have bottom-heavy or very bottom-heavy hypsometries (Appendix A), implying that a substantial number of glaciers in this region are likely to be more vulnerable to climate forcing.

Chapter 3 also shows that variations in both glacier area change and mass balance in the Damodar Himal sub-region were related to maximum glacier elevation and the likelihood of avalanche inputs (Lovell *et al.*, 2019). Very few studies have investigated the influence of avalanche inputs on glacier mass balance because of the difficulty of quantifying these processes (Scherler *et al.*, 2011a; Laha *et al.*, 2017), but avalanche inputs are thought to help sustain glaciers at lower altitudes than would otherwise be possible (Rea *et al.*, 1999; Hughes, 2008). However, the results from Chapter 3 suggest that glaciers in the Damodar Himal sub-region that were more likely to receive avalanche contributions lost more area and mass (Chapter 3; Table 3.6) (Lovell *et al.*, 2019). These findings are supported by a recent HMA-wide study which also showed that in the Kunlun and Inner Tibetan Plateau, glaciers with larger avalanche contributing areas tended to have more negative mass balances (Brun *et al.*, 2019). A possible explanation for this relationship is that glaciers with larger contributions from avalanches can exist in more vulnerable locations where glaciers that rely solely on precipitation inputs are not able to survive. However, their more precarious locations potentially make avalanche-fed glaciers more exposed to changes in climate and, if avalanche contributions decrease or cease, they rapidly begin to retreat and lose mass (Rea *et al.*, 1999; Lovell *et al.*, 2019). One of the limitations of this study is the use of a proxy for avalanche inputs, the ratio of the area susceptible to avalanche and the total glacier area (Hughes, 2008), rather than quantifying avalanche contributions. Therefore, it would be helpful to develop a method to quantify avalanche inputs onto glaciers more accurately, perhaps through the use of time lapse cameras and seismic data.

6.2.5 *Surge-type behaviour and the influence of subglacial topography*

As well as supraglacial debris and glacier morphological properties, Chapter 4 reveals that glacier surge-type behaviour is another, perhaps more unexpected, source of local glacier response variability in the ACA, which has potentially very important implications on local water resources and hazards due to its proximity to Pokhara, one of the largest cities in Nepal (population ~400,000). This merits further understanding of the mechanisms driving Sabche glacier's behaviour, and its inclusion in this body of work.

The glacier surged four times between 1967 and 2017 and the three most recent surges occurred at 10- to 11-year cycles (Chapter 4; Figure 4.8). The characteristics of the surge are somewhat unusual for a surge-type glacier, compared to other surge-type glaciers globally, specifically: i) the brevity of the surge cycle and quiescence phase, and ii) the recurrence of a bowl-shaped depression up-glacier of the tongue (Chapter 4; Figure 4.12). The results suggest that the surge mechanism is modulated by subglacial topography, which restricts regular glacier flow and allows a reservoir to build up above the glacier tongue (Lovell *et al.*, 2018b). These findings are important as surge-type behaviour that is influenced by local controls is not well documented in the literature (Flowers *et al.*, 2011; Abe *et al.*, 2016; Benn *et al.*, 2019). Previous studies have linked surging behaviour to valley topography (Abe *et al.*, 2016; Kochtitzky *et al.*, 2019) and subglacial landforms (Finlayson *et al.*, 2019), but these examples are quite limited.

The surge cycle of an unnamed glacier in Yukon (Flowers *et al.*, 2011) may be modulated by a similar subglacial topography mechanism as Sabche glacier. Modelling showed that a bedrock lip under the Yukon glacier restricted regular flow, leading the glacier to develop a reservoir area behind the ridge and helping it to surge even with a net negative mass balance (Flowers *et al.*, 2011). However, the surge styles of the two glaciers are very different (in terms of speed and frequency), indicating that similar mechanisms can result in diverse surge characteristics, likely dependent on glacier size and the mass balance gradient. This may be determined by the thermal regime of the glacier (e.g. polythermal or temperate) and whether the trigger mechanism is thermal or hydrological (Kamb, 1987; Murray *et al.*, 2003). While the unnamed glacier in Yukon is thought to be polythermal (Flowers *et al.*, 2011), the thermal regime of Sabche glacier has not yet been verified, but showed some characteristics of a temperate glacier (e.g. very short surge cycle) (Lovell *et al.*, 2018b). The results from Chapter 4 confirm that, although rarely recorded, subglacial topography can have an important influence on surging behaviour and it is hoped that this control will be considered when investigating the behaviour of other surge-type glaciers in the future.

Sabche glacier's location at the head of the Seti river, which flows into Pokhara, means that the surge-type behaviour of the glacier could be of potentially significant local importance. The Seti river has already experienced catastrophic and deadly flooding in the past (Fort, 1987; Oi *et al.*, 2014), and the possible influence of Sabche glacier's surge-type behaviour on river discharge in the Seti river should be investigated further.

6.3 Presence of surge-type glaciers in the central Himalayas

In relation to the previous section, it is noteworthy that the work on Sabche glacier in this thesis is the first documentation of a surge-type glacier in the central Himalayas (Chapter 4). While identification of previously undocumented surge-type glaciers is not rare (Bhambri *et al.*, 2017; Chudley and Willis, 2018; Falaschi *et al.*, 2018), it is more unusual to identify surge-type glaciers in a region where no surge-type activity has been recorded previously.

Recent work which modelled the global distribution of surge-type glaciers based on temperature, precipitation and glacier geometry data predicted that surge-type glaciers should be present in the central Himalayas (Sevestre and Benn, 2015). Surge-type glaciers worldwide predominantly cluster within a well-defined climate envelope, where mean annual temperature ranges between -12 °C and +8 °C and mean annual precipitation ranges between 165 and 2155 mm a^{-1} (Sevestre and Benn, 2015). Furthermore, surge-type glaciers tend to share certain geometric characteristics: they tend to be larger and longer and have shallower slopes than their non-surge-type counterparts in the same cluster (Sevestre and Benn, 2015). These characteristics were used to model the location of all potential surge-type glaciers globally and the model predicted the existence of surge-type glaciers in Nepal and other parts of the central Himalayas (Sevestre and Benn, 2015). It should be pointed out that the model did not predict surge-type glaciers in the location of Sabche glacier in the central Himalayas (Section 4.5.3), which may indicate that Sabche glacier's particular surge-type behaviour is enabled by the influence of subglacial topography in an area which did not otherwise match the model's criteria (Sevestre and Benn, 2015). However, the identification of Sabche glacier as a surge-type glacier in this study, in combination with the surge-type glacier distribution model (Sevestre and Benn, 2015), suggests that there may be other surge-type glaciers in the central Himalayas that have not yet been identified.

6.4 Lessons learned

This section of the chapter discusses some of the lessons learned through undertaking this research, including both the challenges encountered and other observations about the ACA that were not within the scope of this research project but are of potential scientific interest.

6.4.1 *Challenges encountered*

6.4.1.1 *Mapping supraglacial debris cover*

As well as measuring changes in glacier area, mass balance and velocity in the ACA, I originally intended to map changes in debris-covered glacier area. This is because as glaciers worldwide shrink, the proportion of debris-covered glacier area is expected to increase and have a greater influence on glacier response to climate change (Scherler *et al.*, 2018). However, we still have a poor understanding of how debris is evolving over time, and is expected to evolve in the future, restricting our ability to model how debris will influence glacier change, especially at broader spatial scales (Herreid and Pellicciotti, 2020).

The challenges of mapping debris-covered glaciers are well-documented (Racoviteanu *et al.*, 2009; Paul *et al.*, 2015) and while debris-free glacier areas can be mapped automatically with relatively high accuracy, debris-covered glacier areas are still commonly edited manually (Mölg *et al.*, 2018). This is because the similar spectral signature between supraglacial debris and the surrounding terrain makes it difficult for automated methods (such as the band ratio method) to accurately differentiate between the two (Paul *et al.*, 2015; Herreid and Pellicciotti, 2020). However, even once I had obtained complete glacier outlines for the ACA (for 2000 and 2014/15), I encountered challenges mapping the separate debris-free and debris-covered sections of each glacier. This was due to changing snow-cover conditions between satellite scenes making it difficult to accurately identify the location of the ice-debris boundary on the glaciers. Although I tried to find scenes for the ACA that had minimal snow-cover, it was challenging to find scenes where snow-cover was consistently low across the entire ACA region. This meant that on some glaciers, the snow-cover was higher in the 2015 image than in 2000, making it look like the debris-covered area on the glacier had decreased over the period. I therefore concluded that the error margins were too large to be confident that I was observing meaningful change in supraglacial debris area over the period.

The challenge of mapping debris cover accurately at large spatial scales is reflected in the recent publication of two global glacier debris-cover maps; one produced using fully automated methods and the other using a semi-automated approach with manual editing (Herreid and Pellicciotti, 2020). First, although both studies used similar (Landsat) satellite imagery and the same glacier outlines (Randolph Glacier Inventory version 6.0), there was significant disagreement between them about the final global percentage of glacier area covered with debris (Scherler *et al.*, 2018; Herreid and Pellicciotti, 2020). A comparison analysis by Herreid and Pellicciotti (2020) indicate that the fully automated method (Scherler *et al.*, 2018) missed 51% of the debris-covered area that Herreid and Pellicciotti (2020) identified in their study and mapped 25% of area as debris-covered which was not identified as debris-covered in their study. This suggests that manual editing of debris-covered glacier areas is still needed to maximise accuracy.

Second, neither attempted to map debris change. This may be because in cases of slow debris expansion, significant changes in debris-cover area are thought to occur only over very long timescales (hundreds of years) (Herreid and Pellicciotti, 2020). However, mapping of debris-cover area on the Miage Glacier in the European Alps suggests that large changes in supraglacial debris cover can occur on much shorter timescales (10 to 20 years) (Deline, 2005), indicating that timescales of debris-cover evolution are still not well understood. Instead, Herreid and Pellicciotti (2020) made an assessment of the stage of debris cover evolution for individual glaciers, using a series of metrics based on geometric properties, and the evolution trajectory of debris cover, based on the current stage of debris evolution and an estimation of debris expansion potential or moraine abundance. However, creating a decisive map of supraglacial debris cover and its evolution at regional, and larger, spatial scales is still a significant challenge.

6.4.1.2 *Field measurements*

Another challenge I encountered undertaking this research was the difficulty of obtaining field measurements on Annapurna South Glacier. Of 14 stakes initially installed in the glacier, almost half (six) were lost between the 2016 and 2017 field seasons due to debris mobilisation and ice cliff collapse, including the three stakes (sites 6, 7 and 8) installed at the up-glacier end of the study site (Chapter 5, Figure 5.4). This meant a significantly reduced number of ablation rate measurements. Moreover, although all iButton temperature sensors were successfully retrieved during the second field season, the bottom two sensors at one of the sites had shifted during the year, most likely due to debris mobilisation and collapse, and could not be used. As a result, the sample size of the data obtained in the field was low. However, the data obtained from Annapurna South Glacier will add value to global community-wide data collections, such as the International Association of Cryopsheric Sciences Debris Covered Glaciers Working Group.

6.4.2 *Other learnings*

6.4.2.1 *Evolution stage of glaciers in the ACA*

The ACA is unusual because it has relatively few glacial (supraglacial and ice-contact) lakes and relatively few glacier lakes that rapidly expanded between 1990 and 2015 compared with other glacierised regions in the central Himalayas, such as the Everest region in East Nepal, the Dolpo and Humla regions in West Nepal, and Bhutan (Figure 6.5) (Nie *et al.*, 2017).

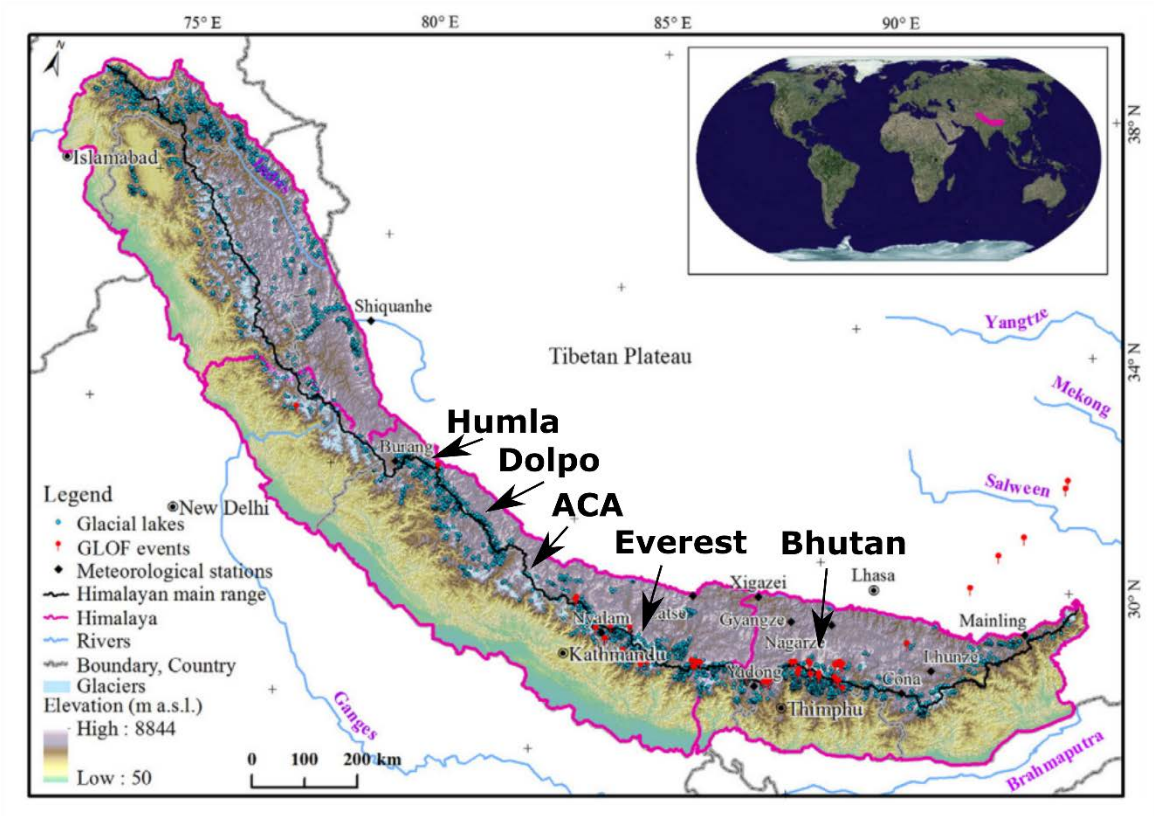

Figure 6.5: Distribution of Himalayan glaciers and glacial lakes in 2015, adapted from Nie *et al.* (2017). The ACA has significantly fewer glacial lakes (blue dots) compared with the Everest region and Bhutan to the east and the Dolpo and Humla regions to the west.

In addition, the velocities on the tongues of a number of debris-covered glaciers in the ACA were relatively active (Chapter 3, Section 3.3.3) compared with other regions, such as the Everest region, where almost all of the tongues of debris-covered glaciers have stagnated (Quincey *et al.,* 2009). This suggests that debris-covered glaciers in the ACA are at an early stage of response to climate change when compared with glaciers in the Everest region (Benn *et al.*, 2012; Rowan *et al.*, 2015). Benn *et al.* (2012) identified three evolution stages for Himalayan debris-covered glaciers based on observations from the Everest region. In the first stage (Regime 1) active flow occurs across the glacier's length, the ablation rate in the lower zone tend to be reversed and the drainage system is relatively efficient meaning that meltwater does not stay stored in the system over multiple years (Figure 6.6). In Regime 2, ice flux from the accumulation zone is reduced, leading to enhanced mass loss. The mass balance in the lower part of the glacier continues to be inverted resulting in a reduced glacier surface gradient, reduced driving stresses in the lower ablation zone, and glacier stagnation. Increased water storage, due to a disrupted drainage system, leads to pond formation on the glacier surface. In Regime 3, base-level proglacial lakes can form. This occurs where a continuous terminal moraine (or equivalent barrier) exists and the glacier surface has lowered to the level of this barrier, resulting in meltwater being stored behind the barrier. These ice-contact lakes can expand rapidly through melting and calving (Benn *et al.,* 2012). Numerical modelling projecting the evolution of Khumbu glacier in the Everest region indicates that in some cases, the mass balance inversion on the glacier tongue could eventually lead to a separation between the glacier tongue and the upper part of the glacier, rapidly accelerating glacier mass loss (Rowan *et al.*, 2015).

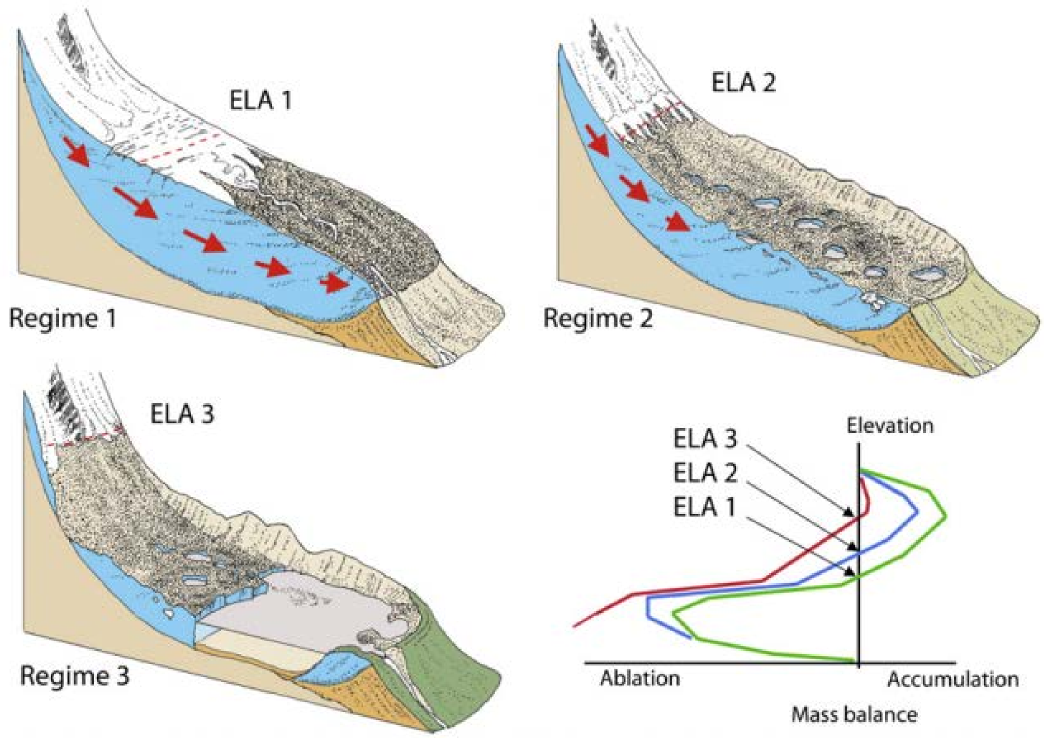

Figure 6.6: A schematic of the three phases of Himalayan debris-covered glacier evolution from Benn *et al.* (2012). The bottom right panel shows idealised mass balance curves and equilibrium line altitudes for the three regimes.

The relative absence of glacial lakes and the presence of debris-covered glaciers that are still actively flowing in their lower ablation zones (Figure 3.11) suggests that glaciers in the ACA are still at an early stage in the debris-covered glacier evolution conceptual model developed by Benn *et al.* (2012), most likely between Regime 1 and Regime 2. This is consistent with the ACA having a less negative mass balance compared with other regions in the central Himalayas, as mentioned above in Section 6.1.

6.4.2.2 *Influence of topography on local climate conditions in the ACA*

As mentioned previously, there are a number of indicators (including a less negative mass balance, glaciers that still have actively flowing glacier tongues, and fewer numbers of glacial lakes) which suggests that glacier response to climate change is at an earlier stage of response in the ACA compared with regions to both the east and west. While investigating the controls on this regional variation in glacier response was not within the scope of this project, it is possible that this variation in part reflects the influence of topography on local climate conditions in the ACA.

Bookhagen and Burbank (2010) hypothesised that the relatively high precipitation rates they observed in the ACA compared with other central Himalayan regions was influenced by the topography of the region allowing moisture-rich air to encroach further into the Greater Himalaya areas at this location along the mountain range. Using the High Asia Reanalysis climate dataset, which has a relatively high spatial resolution (10 km) compared with other regional climate datasets, Maussion *et al.* (2014) observed that the precipitation regimes (and the time of year when glaciers receive the majority of their precipitation) were highly spatially variable across short distances in the central Himalayas (Figure 2.3), influenced by the complex topography. Their analysis also illustrated differences in the precipitation regime between the ACA and other central Himalayan regions. Namely, the ACA had a relatively large proportion of summer-accumulation type glaciers, which extend into the northern parts of the ACA. In comparison, the Everest and Langtang regions, host more winter and spring-accumulation type glaciers, and the summer-accumulation type glaciers in both regions tend to be limited to the southern-most areas of the region (Figure 2.3). The varying proportions of glaciers with different accumulation regimes may help to explain some of the mass balance disparities between the ACA and other central Himalayan regions.

In other parts of HMA (e.g. the Karakoram), the influence of topography on local climate conditions, such as wind direction, precipitation patterns and irradiance, is becoming better understood (Dobreva *et al.*, 2017). However, there is still a gap between the relatively coarse resolution of many regional climate models and the high-resolution of topography data in HMA, which means that the topographic-controlled local climate variability can be missed (Palazzi *et al.*, 2013; Gerlitz *et al.*, 2015; Mishra, 2015; Dobreva *et al.*, 2017). Higher resolution climate models are needed to fully understand the influence of complex topography on precipitation patterns and glacier mass balance in this area (Maussion *et al.*, 2011; Dobreva *et al.*, 2017).

6.4.2.3 *Methodological limitations of analysis of local controls on glacier change*

There are methodological challenges to analysing the controls on local variability in the Himalayan glacier change signal. The strength of the observed relationships between local controls and glacier change can vary depending on the glacier sample size used and the scale of the geographic area covered. Relatively strong relationships have been observed between local controls and Himalayan glacier change in studies that investigated small samples (<30) of glaciers (Pellicciotti *et al.*, 2015; Ragettli *et al.*, 2016; Salerno *et al.*, 2017). For example, in their investigation of the morphological factors controlling the spatial variability of mass balance changes of 28 glaciers on the southern side of Mount Everest, Salerno *et al.* (2017) found a strong relationship between the surface gradients on the downstream sections of glaciers and glacier surface elevation change. In contrast, Brun *et al.* (2019) investigated the influence of glacier morphology on mass balance variability of nearly 6,500 glaciers across HMA and found that the morphological variables only explained a small portion of the variability in mass balance and the strength of the relationships between morphological variables and mass balance varied from region to region. Similarly, analysis of the influence of local controls on the mass balance of 72 glaciers across the ACA (Chapter 3) showed that while the influence of maximum glacier elevation and avalanche contributing area both had significant relationships with mass balance in the Damodar Himal sub-region, neither had a significant relationship with glacier mass balance in the neighbouring Muktinath Himal sub-region (Lovell *et al.*, 2019).

The advantage of looking at smaller samples of glaciers is that it is easier to control for some of the variability, or noise, in the dataset (for example, by choosing glaciers that are within the same valley, or choosing glaciers that share similar morphological characteristics), which can lead to stronger results. However, when attempting to understand broader glacier response to climate change, it is important to test whether these relationships exist over larger glacier samples. Chapter 3 and Brun *et al.* (2019) show that this is complicated because larger glacier datasets tend to be more noisy and undergo more complex interactions between controls (for example, due to varying locations and climatic regimes). This makes it challenging to control for particular glacier characteristics and to pick out individual controls, complicating efforts to identify the drivers of local glacier variation at larger spatial scales.

6.5 Directions for future research

6.5.1 *Complete mass balance estimates for the Annapurna Himal*

Due to a large void in the Shuttle Radar Topography Mission Global DEM in the Annapurna Himal sub-region, and no appropriate alternative datasets covering that region for the same year (Lovell *et al.*, 2019), it was not possible to calculate the mass balance of the majority of glaciers in the Annapurna Himal using geodetic methods. As and when more suitable surface elevation data become available, it would be useful to derive a mass balance estimate for the Annapurna Himal to compare to the other sub-regions to test further the south to north mass balance gradient observed in Chapter 3 (Lovell *et al.*, 2019).

6.5.2 *Conduct numerical modelling of glacier change in ACA*

This project shows that glacier changes in the ACA are complex and spatially variable, and influenced by a range of local controls; but that the strength of local controls can also vary spatially. Future research should focus on using this information to accurately simulate/calibrate numerical models and, if successful, project how glaciers in the ACA will evolve in response to different climate change scenarios by building local control parameters into numerical modelling. A number of studies projecting future glacier changes in the Everest region have included supraglacial debris parameters in their models (Rowan *et al.*, 2015; Shea *et al.*, 2015a; Soncini *et al.*, 2016). However, the introduction of other local control data, including potential avalanche contributions, could improve predictions of how different types of glaciers will respond to future climate change across the central Himalayas.

6.5.3 *Pre-clustering, hypothesis driven approach to analysing the drivers of spatially variable glacier change*

Future analysis of the drivers of local spatial variability in the glacier change signal in HMA would benefit from a pre-clustering, hypothesis-driven approach to complement the 'big-data' approach of Chapter 3 (Lovell *et al.*, 2019) and other previous studies (e.g. Brun *et al.*, 2019). In the ACA, this would mean building on the analysis of the full glacier dataset (Chapter 3) by sorting the glaciers into groups with similar characteristics (such as location, geometry etc.) and conducting further analysis on the spatial variability of glacier changes within these groups of glaciers. This approach would enable the relationships observed in the big data analyses to be tested in more detail on smaller, more controlled samples that are less influenced by noise.

6.5.4 *Investigate Sabche glacier's impact on river discharge*

Sabche glacier is located at the top of the Seti catchment, a river that flows through Pokhara and has a history of important flooding events. Pokhara itself is built on major flood deposits (4 km^3) that originated from the catchment (Fort, 1987) and a more recent flooding event, also triggered in Sabche cirque, resulted in deaths and destruction to infrastructure (Schwanghart *et al.*, 2015). Pokhara is one of the largest cities in Nepal (population ~400,000) and a major tourist hub. Therefore, it is important to clarify what influence the surges have on river discharge, how much extra melt and/or runoff is produced following a surge, and whether the surge-type behaviour increases the risk of flooding down-valley. This would require continuous hydrological data in the upper catchment of the Seti river, which are currently not available (Lovell *et al.*, 2019).

6.5.5 *Conduct systematic search for surge-type glaciers in the central Himalayas*

Systematic searches for other surge-type glaciers in the central Himalayas would be beneficial to continue testing the global distribution model in Sevestre and Benn (2015). This would also help to identify areas that might be subject to future glacier-surge-related hazards and impacts on local water resources, and to improve large-scale studies of glacier response to climate change in this area by removing surge-type glaciers, which are not directly influenced by external forcing (Bolch *et al.*, 2019). Similar surge-type glacier inventories have been conducted in the Karakoram (Copland *et al.*, 2011; Bhambri *et al.*, 2017), West Kunlun Shan (Chudley and Willis, 2018) and Central Andes (Falaschi *et al.*, 2018), leading to the identification of multiple new surge-type glaciers in these regions. With increasing availability of satellite imagery at high temporal resolution (e.g. Landsat, ASTER, Sentinel and Planet data), it would be possible to analyse glaciers across the central Himalayas over multiple years for evidence of surge-type behaviour (Copland *et al.*, 2011). Creating animated sequences of multi-temporal satellite imagery, similar to work in the Karakoram (Paul, 2015), could provide an initial rapid qualitative method to identify glacier surges in the central Himalayas to inform where to focus subsequent quantitative studies on surging behaviour.

Chapter 7: Conclusions

This thesis demonstrates the characteristics of changes in glacier area, surface elevation, mass balance and ice surface velocity in the Annapurna Conservation Area (ACA), central Nepal. Results show an almost universal trend of area loss, thinning, and mass loss across the glaciers in the ACA. Between 2000 and 2014/15, total glacier area decreased by 8.5%, and between 2000 and 2013/16, mean surface elevation change was -0.33 ± 0.22 m a^{-1}. However, there was no clear trend in glacier velocities across the study region (velocities on the glacier tongues ranged from 0 to 70 m a^{-1} in both 2002 and 2016). Together, the ACA had a mean mass balance of -0.28 ± 0.24 m w.e. a^{-1} between 2000 and 2013/16, which was less negative than in other central Himalayan regions (e.g. the Langtang and Everest regions). This is attributed to differing climate conditions in the regions, driven by highly variable and complex topography.

Results demonstrate the scale and complexity of local variability in the glacier change signal across the ACA. Some of this variability can be partly attributed to local glacier characteristics, such as supraglacial debris, glacier hypsometry, maximum glacier elevation and avalanche contributing area. Specifically, debris-covered glaciers had an inverted mass balance gradient in the ablation zone, compared to debris-free glaciers. On debris-covered glaciers, surface lowering rates were lower towards the terminus, where debris tends to be thicker, compared to further up-glacier in the ablation zone, where debris is thinner. Glaciers with bottom-heavy hypsometry also lost more mass than those with top-heavy hypsometry, indicating that they are more vulnerable to climate change. However, while maximum glacier elevation and avalanche contributing area influenced area change and mass balance in the Damodar Himal, in the Muktinath Himal, the only significant relationship was between maximum elevation and area change and this relationship was much weaker than in the Damodar Himal. This shows that the sources of variability in the glacier change signal are not uniform across space, presenting an additional challenge when predicting spatially variable glacier change in response to climate forcing.

This thesis demonstrates that surge-type behaviour is also a key source of variability in the glacier change signal in the ACA with potentially important consequences for local water resources and hazards in the populous city of Pokhara. This is the first record of a surge-type glacier in the central Himalayas, and thus identifies another important mechanism determining variable glacier behaviour in the ACA. Sabche glacier, a steep debris-covered glacier, surged four times between 1967 and 2017. This work is critical because it supports previous predictions that surge-type glaciers could be present in the central Himalayas, and suggests that there could be other surge-type glaciers in this part of the Himalayan range that have not yet been documented. Identifying these surge-type glaciers, which are not directly influenced by climate change, is important to understand their potential impact on local communities and to ensure that their behaviour is not confused with the response of non-surge-type glaciers to climate forcing. The results from this study are also significant because they indicate that the surging behaviour of Sabche glacier is influenced by subglacial topography, a control mechanism that is rarely documented in published literature.

The influence of supraglacial debris on glacier ablation rates was investigated in detail on Annapurna South glacier, in the ACA, to assess how heat is transferred through the debris layer to the ice surface and how it influences sub-debris melt rates. The results showed that the thermal regime of the debris varied seasonally and under different debris thicknesses, influencing the timing and magnitude of ablation. Ablation was reduced under the thickest debris and heat was predominantly transferred through the debris via conductivity during the monsoon, but non-conductive heat transfer was more prevalent during the winter and spring months. The study showed that sites with different debris thicknesses and physical properties had distinct thermal regimes and ablation rates, despite experiencing similar meteorological conditions. This research contributes to a limited dataset on the thermal regime of supraglacial debris in the central Himalayas. It provides useful insight into the processes occurring within debris and demonstrates the importance of these processes on glacier ablation at small spatial scales.

To conclude, the results of this thesis reveal spatially heterogeneous glacier changes within the broader trends of area loss, thinning and mass loss in the ACA. The findings show that the scale of local variability, or noise, in the Himalayan glacier change signal can be substantial when studying large samples of glaciers, and the sources of this variability can be complex and not spatially uniform. This work contributes to putting limits on the extent of ‘normal’ variability that can be expected in the glacier change signal in ACA. A better understanding of the extent of noise that can be considered ‘normal’ in the glacier change signal can help to improve efforts to forecast future Himalayan glacier changes.

Moreover, this research shows that glacier behaviour in the ACA, a previously under-researched region, has some distinctive characteristics compared with other better-researched regions in the central Himalayas (i.e. less negative mean mass balance and the presence of a surge-type glacier). This strongly suggests that the region merits further detailed research to contribute to our understanding of central Himalayan glacier change. This thesis thus contributes to the literature by filling in an important data gap in the central Himalayan glacier change record, and provides a comprehensive platform from which to launch future research projects in the ACA.

References

Abe, T., Furuya, M. and Sakakibara, D. (2016) 'Brief Communication: Twelve-year cyclic surging episodes at Donjek Glacier in Yukon, Canada', *The Cryosphere*, 10(4), pp. 1427-1432.

Adhikary, S., Nakawo, M., Seko, K. and Shakya, B. (2000) 'Dust influence on the melting process of glacier ice: experimental results from Lirung Glacier, Nepal Himalayas', *IAHS Publication*, pp. 43-52.

Alifu, H., Tateishi, R. and Johnson, B. (2015) 'A new band ratio technique for mapping debris-covered glaciers using Landsat imagery and a digital elevation model', *International Journal of Remote Sensing*, 36(8), pp. 2063-2075.

Anderson, L.S. and Anderson, R.S. (2016) 'Modeling debris-covered glaciers: response to steady debris deposition', *The Cryosphere*, 10(3), pp. 1105-1124.

Anderson, L.S. and Anderson, R.S. (2018) 'Debris thickness patterns on debris-covered glaciers', *Geomorphology*, 311, pp. 1-12.

Annamalai, H. and Sperber, K.R. (2016) 'South Asian summer monsoon variability in a changing climate', *The Monsoons and Climate Change*, pp. 25-46.

Azam, M.F., Wagnon, P., Berthier, E., Vincent, C., Fujita, K. and Kargel, J.S. (2018) 'Review of the status and mass changes of Himalayan-Karakoram glaciers', *Journal of Glaciology*, 64(243), pp. 61-74.

Azam, M.F., Wagnon, P., Vincent, C., Ramanathan, A.L., Favier, V., Mandal, A. and Pottakkal, J.G. (2014) 'Processes governing the mass balance of Chhota Shigri Glacier (western Himalaya, India) assessed by point-scale surface energy balance measurements', *The Cryosphere*, 8(6), pp. 2195-2217.

Bahr, D.B., Pfeffer, W.T., Sassolas, C. and Meier, M.F. (1998) 'Response time of glaciers as a function of size and mass balance: 1. Theory', *Journal of Geophysical Research: Solid Earth*, 103(B5), pp. 9777-9782.

Bajracharya, S.R. and Mool, P. (2010) 'Glaciers, glacial lakes and glacial lake outburst floods in the Mount Everest region, Nepal', *Annals of Glaciology*, 50(53), pp. 81-86.

Banerjee, A. (2017) 'Brief communication: Thinning of debris-covered and debris-free glaciers in a warming climate', *The Cryosphere*, 11(1), pp. 133-138.

Barros, A.P., Joshi, M., Putkonen, J. and Burbank, D.W. (2000) 'A study of the 1999 monsoon rainfall in a mountainous region in central Nepal using TRMM products and rain gauge observations', *Geophysical Research Letters*, 27(22), pp. 3683-3686.

Barros, A.P., Kim, G., Williams, E. and Nesbitt, S.W. (2004) 'Probing orographic controls in the Himalayas during the monsoon using satellite imagery', *Natural Hazards and Earth System Science*, 4(1), pp. 29-51.

Becek, K. (2008) 'Investigating error structure of shuttle radar topography mission elevation data product', *Geophysical Research Letters*, 35(15).

Benn, D. and Owen, L. (1998) 'The role of the Indian summer monsoon and the mid-latitude westerlies in Himalayan glaciation: review and speculative discussion', *Journal of the Geological Society*, 155(2), pp. 353-363.

Benn, D.I., Bolch, T., Hands, K., Gulley, J., Luckman, A., Nicholson, L.I., Quincey, D., Thompson, S., Toumi, R. and Wiseman, S. (2012) 'Response of debris-covered glaciers in the Mount Everest region to recent warming, and implications for outburst flood hazards', *Earth-Science Reviews*, 114(1-2), pp. 156-174.

Benn, D.I., Fowler, A.C., Hewitt, I. and Sevestre, H. (2019) 'A general theory of glacier surges', *Journal of Glaciology*, pp. 1-16.

Benn, D.I., Kristensen, L. and Gulley, J.D. (2009) 'Surge propagation constrained by a persistent subglacial conduit, Bakaninbreen–Paulabreen, Svalbard', *Annals of Glaciology,* 50(52), pp. 81-86.

Berthier, E. and Brun, F. (2019) 'Karakoram geodetic glacier mass balances between 2008 and 2016: persistence of the anomaly and influence of a large rock avalanche on Siachen Glacier', *Journal of Glaciology*, 65(251), pp. 494-507.

Berthier, E., Vincent, C., Magnússon, E., Gunnlaugsson, Á.Þ., Pitte, P., Le Meur, E., Masiokas, M., Ruiz, L., Pálsson, F., Belart, J.M.C. and Wagnon, P. (2014) 'Glacier topography and elevation changes derived from Pléiades sub-meter stereo images', *The Cryosphere*, 8(6), pp. 2275-2291.

Bevington, A. and Copland, L. (2014) 'Characteristics of the last five surges of Lowell Glacier, Yukon, Canada, since 1948', *Journal of Glaciology*, 60(219), pp. 113-123.

Bhambri, R., Bolch, T. and Chaujar, R.K. (2011a) 'Mapping of debris-covered glaciers in the Garhwal Himalayas using ASTER DEMs and thermal data', *International Journal of Remote Sensing*, 32(23), pp. 8095-8119.

Bhambri, R., Bolch, T., Chaujar, R.K. and Kulshreshtha, S.C. (2011b) 'Glacier changes in the Garhwal Himalaya, India, from 1968 to 2006 based on remote sensing', *Journal of Glaciology*, 57(203), pp. 543-556.

Bhambri, R., Hewitt, K., Kawishwar, P. and Pratap, B. (2017) 'Surge-type and surge-modified glaciers in the Karakoram', *Scientific Reports*, 7(1), p. 15391.

Bhushan, S., Syed, T.H., Arendt, A.A., Kulkarni, A.V. and Sinha, D. (2018) 'Assessing controls on mass budget and surface velocity variations of glaciers in Western Himalaya', *Scientific Reports*, 8(1), p. 8885.

Bhutiyani, M.R., Kale, V.S. and Pawar, N.J. (2007) 'Long-term trends in maximum, minimum and mean annual air temperatures across the Northwestern Himalaya during the twentieth century', *Climatic Change,* 85(1-2), pp. 159-177.

Björnsson, H. (1998) 'Hydrological characteristics of the drainage system beneath a surgng glacier', *Nature*, 395, pp. 771-774.

Bolch, T., Buchroithner, M., Pieczonka, T. and Kunert, A. (2008) 'Planimetric and volumetric glacier changes in the Khumbu Himal, Nepal, since 1962 using Corona, Landsat TM and ASTER data', *Journal of Glaciology*, 54(187), pp. 592-600.

Bolch, T., Kulkarni, A., Kaab, A., Huggel, C., Paul, F., Cogley, J.G., Frey, H., Kargel, J.S., Fujita, K., Scheel, M., Bajracharya, S. and Stoffel, M. (2012) 'The state and fate of Himalayan glaciers', *Science*, 336(6079), pp. 310-4.

Bolch, T., Pieczonka, T. and Benn, D.I. (2011) 'Multi-decadal mass loss of glaciers in the Everest area (Nepal Himalaya) derived from stereo imagery', *The Cryosphere*, 5(2), pp. 349-358.

Bolch, T., Shea, J.M., Liu, S., Azam, F.M., Gao, Y., Gruber, S., Immerzeel, W.W., Kulkarni, A., Li, H., Tahir, A.A., Zhang, G. and Zhang, Y. (2019) 'Status and change of the cryosphere in the extended Hindu Kush Himalaya region', in *The Hindu Kush Himalaya Assessment*. pp. 209-255.

Bollasina, M., Bertolani, L. and Tartari, G. (2002) 'Meteorological observations at high altitude in the Khumbu Valley, Nepal Himalayas, 1994-1999 ', *Bulletin of Glaciological Research*, 19, pp. 1-11.

Bookhagen, B. (2016) 'Glaciers and monsoon systems', in *The Monsoons and Climate Change*. Springer, pp. 225-249.

Bookhagen, B. and Burbank, D.W. (2006) 'Topography, relief, and TRMM-derived rainfall variations along the Himalaya', *Geophysical Research Letters*, 33(L08405).

Bookhagen, B. and Burbank, D.W. (2010) 'Toward a complete Himalayan hydrological budget: Spatiotemporal distribution of snowmelt and rainfall and their impact on river discharge', *Journal of Geophysical Research*, 115(F03019).

Braithwaite, R.J. and Raper, S.C.B. (2009) 'Estimating equilibrium-line altitude (ELA) from glacier inventory data', *Annals of Glaciology*, 50(53), pp. 127-132.

Brock, B.W., Mihalcea, C., Kirkbride, M.P., Diolaiuti, G., Cutler, M.E.J. and Smiraglia, C. (2010) 'Meteorology and surface energy fluxes in the 2005–2007 ablation seasons at the Miage debris-covered glacier, Mont Blanc Massif, Italian Alps', *Journal of Geophysical Research*, 115(D9).

Brun, F., Berthier, E., Wagnon, P., Kaab, A. and Treichler, D. (2017) 'A spatially resolved estimate of High Mountain Asia glacier mass balances, 2000-2016', *Nature Geoscience*, 10(9), pp. 668-673.

Brun, F., Buri, P., Miles, E.S., Wagnon, P., Steiner, J., Berthier, E., Ragettli, S., Kraaijenbrink, P., Immerzeel, W.W. and Pellicciotti, F. (2016) 'Quantifying volume loss from ice cliffs on debris-covered glaciers using high-resolution terrestrial and aerial photogrammetry', *Journal of Glaciology*, pp. 1-12.

Brun, F., Wagnon, P., Berthier, E., Jomelli, V., Maharjan, S.B., Shrestha, F. and Kraaijenbrink, P.D.A. (2019) 'Heterogeneous Influence of Glacier Morphology on the Mass Balance Variability in High Mountain Asia', *Journal of Geophysical Research-Earth Surface*, 124(6), pp. 1331-1345.

Budd, W.F. and McInnis, B.J. (1974) 'Modelling periodically surging glaciers', *Science*, 186(4167), pp. 925-927.

Burke, M.J., Woodward, J., Russell, A.J., Fleisher, P.J. and Bailey, P.K. (2010) 'The sedimentary architecture of outburst flood eskers: A comparison of ground-penetrating radar data from Bering Glacier, Alaska and Skeithararjokull, Iceland', *Geological Society of America Bulletin*, 122(9-10), pp. 1637-1645.

Chand, M.B. and Kayastha, R.B. (2018) 'Study of thermal properties of supraglacial debris and degree-day factors on Lirung glacier, Nepal', *Sciences in Cold and Arid Regions*, 10(5), pp. 357-368.

Chudley, T.R. and Willis, I.C. (2018) 'Glacier surges in the north-west West Kunlun Shan inferred from 1972 to 2017 Landsat imagery', *Journal of Glaciology*, 65(249), pp. 1-12.

Clarke, G.K.C. (1987) 'Fast glacier flow: Ice streams, surging, and tidewater glaciers', *Journal of Geophysical Research*, 92(B9), p. 8835.

Clarke, G.K.C., Collins, S.G. and Thompson, D.E. (1984) 'Flow, thermal structure, and subglacial conditions of a surge-type glacier', *Canadian Journal of Earth Sciences*, 21(2), pp. 232-240.

Collier, E., Nicholson, L.I., Brock, B.W., Maussion, F., Essery, R. and Bush, A.B.G. (2014) 'Representing moisture fluxes and phase changes in glacier debris cover using a reservoir approach', *The Cryosphere*, 8(4), pp. 1429-1444.

Conway, H. and Rasmussen, L.A. (2000) 'Summer temperature profiles within supraglacial debris on Khumbu Glacier, Nepal', in Nakawo, M., Raymond, C.F. and Fountain, A. (eds.) *Debris-Covered Glaciers*. Wallingford: IAHS Press, pp. 89-97.

Cook, S.J. and Swift, D.A. (2012) 'Subglacial basins: Their origin and importance in glacial systems and landscapes', *Earth-Science Reviews*, 115(4), pp. 332-372.

Copland, L., Pope, S., Bishop, M.P., Shroder, J.F., Clendon, P., Bush, A., Kamp, U., Seong, Y.B. and Owen, L.A. (2009) 'Glacier velocities across the central Karakoram', *Annals of Glaciology*, 50(52), pp. 41-49.

Copland, L., Sylvestre, T., Bishop, M.P., Shroder, J.F., Seong, Y.B., Owen, L.A., Bush, A. and Kamp, U. (2011) 'Expanded and recently increased glacier surging in the Karakoram', *Arctic, Antarctic, and Alpine Research*, 43(4), pp. 503-516.

De Ferranti, J. (2012) 'Viewfinder Panorama DEMs [Online]'. Available online at: http://viewfinderpanoramas.org/ (accessed on 22/03/2019).

Dehecq, A., Gourmelen, N., Gardner, A.S., Brun, F., Goldberg, D., Nienow, P.W., Berthier, E., Vincent, C., Wagnon, P. and Trouvé, E. (2018) 'Twenty-first century glacier slowdown driven by mass loss in High Mountain Asia', *Nature Geoscience*, 12(1), pp. 22-27.

Deline, P. (2005) 'Change in surface debris cover on Mont Blanc massif glaciers after the'Little Ice Age' termination', *The Holocene*, 15(2), pp. 302-309.

Desio, A. (1954) 'An exceptional glacier advance in the Karakoram-Ladakh region', *Journal of Glaciology*, 2(16), pp. 383-385.

DHM (2017) *Monsoon Onset and Withdrawal date*. Available at: http://www.dhm.gov.np/uploads/climatic/115290543monsoon%20onset%20n%20withdrawal%202017.pdf (Accessed: 30/05/2018).

Dimri, A.P., Kumar, D., Choudhary, A. and Maharana, P. (2018) 'Future changes over the Himalayas: Mean temperature', *Global and Planetary Change*, 162, pp. 235-251.

Dobreva, I., Bishop, M. and Bush, A. (2017) 'Climate–Glacier Dynamics and Topographic Forcing in the Karakoram Himalaya: Concepts, Issues and Research Directions', *Water*, 9(6).

Dolgoushin, L.D. and Osipova, G.B. (1975) 'Glacier surges and the problem of their forecasting.', *IAHS Publication*, 104 (Symposium at Moscow 1971 - Snow and Ice), pp. 292-304.

Dowdeswell, J.A., Hamilton, G. and Hagen, J.O. (1991) 'The duration of the active phase on surge-type glaciers: contrasts between Svalbard and other regions. ', *Journal of Glaciology*, 37(127), pp. 388-400.

Eisen, O., Harrison, W.D., Raymond, C.F., Echelmeyer, K.A., Bender, G.A. and Gorda, J.L.D. (2005) 'Variegated Glacier, Alaska, USA: a century of surges', *Journal of Glaciology*, 51(174), pp. 399-406.

Evans, S.G. and Delaney, K.B. (2015) 'Catastrophic mass flows in the mountain glacial environment', in Haeberli, W., Whiteman, C. and Shroder Jr, J.F. (eds.) *Snow and Ice-Related Hazards, Risks, and Disasters.* Amsterdam: Elsevier, pp. 563-606.

Evatt, G.W., Abrahams, I.D., Heil, M., Mayer, C., Kingslake, J., Mitchell, S.L., Fowler, A.C. and Clark, C.D. (2015) 'Glacial melt under a porous debris layer', *Journal of Glaciology*, 61(229), pp. 825-836.

Falaschi, D., Bolch, T., Lenzano, M.G., Tadono, T., Lo Vecchio, A. and Lenzano, L. (2018) 'New evidence of glacier surges in the Central Andes of Argentina and Chile', *Progress in Physical Geography: Earth and Environment*, 42(6), pp. 792-825.

Farinotti, D., Huss, M., Fürst, J.J., Landmann, J., Machguth, H., Maussion, F. and Pandit, A. (2019) 'A consensus estimate for the ice thickness distribution of all glaciers on Earth', *Nature Geoscience*, 12(3), pp. 168-173.

Farr, T.G., Rosen, P.A., Caro, E., Crippen, R., Duren, R., Hensley, S., Kobrick, M., Paller, M., Rodriguez, E., Roth, L., Seal, D., Shaffer, S., Shimada, J., Umland, J., Werner, M., Oskin, M., Burbank, D. and Alsdorf, D. (2007) 'The Shuttle Radar Topography Mission', *Reviews of Geophysics*, 45(2).

Finlayson, A., Phillips, E., Benediktsson, Í.Ö., Zoet, L.K., Iverson, N.R. and Everest, J. (2019) 'Subglacial drumlins and englacial fractures at the surge-type glacier, Múlajökull, Iceland', *Earth Surface Processes and Landforms*, 44(1), pp. 367-380.

Fleisher, P.J., Cadwell, D.H. and Muller, E.H. (1998) 'Tsivat basin onduit system persists through two surges, Bering Piedmont Glacier, Alaska', *GSA Bulletin*, 110(7), pp. 877-887.

Flowers, G.E., Roux, N., Pimentel, S. and Schoof, C.G. (2011) 'Present dynamics and future prognosis of a slowly surging glacier', *The Cryosphere*, 5(1), pp. 299-313.

Fort, M. (1987) 'Sporadic morphogenesis in a continental subduction setting: an example from the Annapurna range, Nepal Himalaya', *Zeitschrift für Geomorphologie, Supplementary Issues*, pp. 9-36.

Frappé, T.-P. and Clarke, G.K.C. (2007) 'Slow surge of Trapridge Glacier, Yukon Territory, Canada', *Journal of Geophysical Research*, 112(F3).

Fujii, Y. (1977) 'Field experiment on glacier ablation under a layer of debris cover ', *Seppyo*, pp. 20-21.

Gardelle, J., Arnaud, Y. and Berthier, E. (2011) 'Contrasted evolution of glacial lakes along the Hindu Kush Himalaya mountain range between 1990 and 2009', *Global and Planetary Change*, 75(1-2), pp. 47-55.

Gardelle, J., Berthier, E. and Arnaud, Y. (2012) 'Slight mass gain of Karakoram glaciers in the early twenty-first century', *Nature Geoscience*, 5(5), pp. 322-325.

Gardelle, J., Berthier, E., Arnaud, Y. and Kääb, A. (2013) 'Region-wide glacier mass balances over the Pamir-Karakoram-Himalaya during 1999-2011', *The Cryosphere*, 7(4), pp. 1263-1286.

Gardner, J.S. and Hewitt, K. (1990) 'A surge of Bualtar Glacier, Karakoram range, Pakistan: a possible landslide trigger', *Journal of Glaciology*, 36(123), pp. 159-162.

Gerlitz, L., Conrad, O. and Böhner, J. (2015) 'Large-scale atmospheric forcing and topographic modification of precipitation rates over High Asia – a neural-network-based approach', *Earth System Dynamics*, 6(1), pp. 61-81.

Gibson, M.J., Glasser, N.F., Quincey, D.J., Mayer, C., Rowan, A.V. and Irvine-Fynn, T.D.L. (2017) 'Temporal variations in supraglacial debris distribution on Baltoro Glacier, Karakoram between 2001 and 2012', *Geomorphology*, 295, pp. 572-585.

Gibson, M.J., Irvine-Fynn, T.D.L., Wagnon, P., Rowan, A.V., Quincey, D.J., Homer, R. and Glasser, N.F. (2018) 'Variations in near-surface debris temperature through the summer monsoon on Khumbu Glacier, Nepal Himalaya', *Earth Surface Processes and Landforms*, 43(13), pp. 2698-2714.

Giesen, R.H. and Oerlemans, J. (2013) 'Climate-model induced differences in the 21st century global and regional glacier contributions to sea-level rise', *Climate Dynamics*, 41(11-12), pp. 3283-3300.

Grant, K.L., Stokes, C.R. and Evans, I.S. (2009) 'Identification and characteristics of surge-type glaciers on Novaya Zemlya, Russia Arctic', *Journal of Glaciology*, 55(194), pp. 960-971.

Gubler, S., Fiddes, J., Keller, M. and Gruber, S. (2011) 'Scale-dependent measurement and analysis of ground surface temperature variability in alpine terrain', *The Cryosphere*, 5(2), pp. 431-443.

Haeberli, W., Kääb, A., Paul, F., Chiarle, M., Mortara, G., Mazza, A., Deline, P. and Richardson, S. (2002) 'A surge-type movement at Ghiacciaio del Belvedere and a developing slope instability in the east face of Monte Rosa, Macugnaga, Italian Alps', *Norsk Geografisk Tidsskrift - Norwegian Journal of Geography*, 56(2), pp. 104-111.

Hambrey, M.J., Quincey, D.J., Glasser, N.F., Reynolds, J.M., Richardson, S.J. and Clemmens, S. (2008) 'Sedimentological, geomorphological and dynamic context of debris-mantled glaciers, Mount Everest (Sagarmatha) region, Nepal', *Quaternary Science Reviews*, 27(25-26), pp. 2361-2389.

Harrison, W.D., Echelmeyer, K.A., Chacho, E.F., Raymond, C.F. and Benedict, R.J. (1994) 'The 1987–88 surge of West Fork Glacier, Susitna Basin, Alaska, U.S.A', *Journal of Glaciology*, 40(135), pp. 241-254.

Herreid, S. and Pellicciotti, F. (2020) 'The state of rock debris covering Earth’s glaciers', *Nature Geoscience*, 13, pp. 621–627.

Hewitt, K. (2007) 'Tributary glacier surges: an exceptional concentration at Panmah Glacier, Karakoram Himalaya', *Journal of Glaciology*, 53(181), pp. 181-188.

Hughes, P. (2008) 'Response of a Montenegro glacier to extreme summer heatwaves in 2003 and 2007', *Geografiska Annaler: Series A, Physical Geography*, 90(4), pp. 259-267.

Humlum, O. (1997) 'Active layer thermal regime at three rock glaciers in Greenland', *Permafrost and Periglacial Processes*, 8, pp. 383-408.

Huss, M. (2012) 'Extrapolating glacier mass balance to the mountain-range scale: the European Alps 1900–2100', *The Cryosphere*, 6(4), pp. 713-727.

Huss, M. (2013) 'Density assumptions for converting geodetic glacier volume change to mass change', *The Cryosphere*, 7(3), pp. 877-887.

Huss, M. and Hock, R. (2015) 'A new model for global glacier change and sea-level rise', *Frontiers in Earth Science*, 3.

Immerzeel, W.W., Kraaijenbrink, P.D.A., Shea, J.M., Shrestha, A.B., Pellicciotti, F., Bierkens, M.F.P. and de Jong, S.M. (2014) 'High-resolution monitoring of Himalayan glacier dynamics using unmanned aerial vehicles', *Remote Sensing of Environment*, 150, pp. 93-103.

Immerzeel, W.W., van Beek, L.P. and Bierkens, M.F. (2010) 'Climate change will affect the Asian water towers', *Science*, 328(5984), pp. 1382-5.

Inoue, J. and Yoshida, M. (1980) 'Ablation and heat exchange over the Khumbu Glacier', *Seppyo*, pp. 26-33.

Jiang, S., Nie, Y., Liu, Q., Wang, J., Liu, L., Hassan, J., Liu, X. and Xu, X. (2018) 'Glacier change, supraglacial debris expansion and glacial lake evolution in the Gyirong River Basin, central Himalayas, between 1988 and 2015', *Remote Sensing*, 10(7).

Jiskoot, H., Boyle, P. and Murray, T. (1998) 'The incidence of glacier surging in Svalbard: evidence from multivariate statistics', *Computers & Geosciences*, 24(4), pp. 387-399.

Jiskoot, H., Curran, C.J., Tessler, D.L. and Shenton, L.R. (2009) 'Changes in Clemenceau Icefield and Chaba Group glaciers, Canada, related to hypsometry, tributary detachment, length–slope and area–aspect relations', *Annals of Glaciology*, 50(53), pp. 133-143.

Juen, M., Mayer, C., Lambrecht, A., Wirbel, A. and Kueppers, U. (2016) 'Thermal properties of a supraglacial debris layer with respect to lithology and grain size', *Geografiska Annaler: Series A, Physical Geography*, 95(3), pp. 197-209.

Kääb, A. (2005) 'Combination of SRTM3 and repeat ASTER data for deriving alpine glacier flow velocities in the Bhutan Himalaya', *Remote Sensing of Environment*, 94(4), pp. 463-474.

Kääb, A., Berthier, E., Nuth, C., Gardelle, J. and Arnaud, Y. (2012) 'Contrasting patterns of early twenty-first-century glacier mass change in the Himalayas', *Nature*, 488(7412), pp. 495-8.

Kääb, A., Reynolds, J.M. and Haeberli, W. (2005) 'Glacier and permafrost hazards in high mountains', 23, pp. 225-234.

Kamb, B. (1987) 'Glacier surge mechanism based on linked cavity configuration of the basal water conduit system', *Journal of Geophysical Research*, 92(B9), p. 9083.

Kamb, B., Raymond, C.F., Harrison, W.D., Engelhart, H., Echelmeyer, K.A., Humphrey, N., Brugman, M.M. and Pfeffer, T. (1985) 'Glacier surge mechanism: 1982-1983 surge of Variegated Glacier, Alaska', *Science*, 227(4686), pp. 469-479.

Kattel, D.B. and Yao, T. (2013) 'Recent temperature trends at mountain stations on the southern slope of the central Himalayas', *Journal of Earth System Science*, 122(1), pp. 215-227.

Kayastha, R.B., Takeuchi, Y., Nakawo, M. and Ageta, Y. (2000) 'Practical prediction of ice melting beneath various thickness of debris cover on Khumbu Glacier, Nepal, using a positive degree-day factor', *IAHS Publication*, pp. 71-82.

Khan, M.I. (1989) *Ablation on Barpu glacier, Karakoram Himalaya, Pakistan a study of melt processes on a faceted, debris-covered ice surface*. PhD Thesis thesis. Wilfred Laurier University.

King, O., Dehecq, A., Quincey, D. and Carrivick, J. (2018) 'Contrasting geometric and dynamic evolution of lake and land-terminating glaciers in the central Himalaya', *Global and Planetary Change*, 167, pp. 46-60.

King, O., Quincey, D.J., Carrivick, J.L. and Rowan, A.V. (2017) 'Spatial variability in mass loss of glaciers in the Everest region, central Himalayas, between 2000 and 2015', *The Cryosphere*, 11(1), pp. 407-426.

Kirkbride, M.P. and Deline, P. (2013) 'The formation of supraglacial debris covers by primary dispersal from transverse englacial debris bands', *Earth Surface Processes and Landforms*, 38(15), pp. 1779-1792.

Kochtitzky, W., Jiskoot, H., Copland, L., Enderlin, E., McNabb, R., Kreutz, K. and Main, B. (2019) 'Terminus advance, kinematics and mass redistribution during eight surges of Donjek Glacier, St. Elias Range, Canada, 1935 to 2016', *Journal of Glaciology*, pp. 1-15.

Kotlyakov, V.M., Osipova, G.B. and Tsvetkov, D.G. (2008) 'Monitoring glacier surges of the Pamirs, central Asia, from space', *Annals of Glaciology*, 48, pp. 125-134.

Kraaijenbrink, P.D.A., Bierkens, M.F.P., Lutz, A.F. and Immerzeel, W.W. (2017) 'Impact of a global temperature rise of 1.5 degrees Celsius on Asia's glaciers', *Nature*, 549(7671), pp. 257-260.

Krishnan, R., Shrestha, A.B., Ren, G., Rajbhandari, R., Saeed, S., Sanjay, J., Syed, M.A., Vellore, R., Xu, Y., You, Q. and Ren, Y. (2019) 'Unravelling climate change in the Hindu Kush Himalaya: rapid warming in the mountains and increasing extremes', in Wester, P., Mishra, A., Mukherji, A. and Shrestha, A.B. (eds.) *The Hindu Kush Himalaya Assessment: Mountains, Climate Change, Sustainability and People*. Cham: Springer International Publishing, pp. 57-97.

Kulkarni, A.V., Bahuguna, I., Rathore, B., Singh, S., Randhawa, S., Sood, R. and Dhar, S. (2007) 'Glacial retreat in Himalaya using Indian Remote Sensing satellite data', *Current science*, 92(1), pp. 69-74.

Laha, S., Kumari, R., Singh, S., Mishra, A., Sharma, T., Banerjee, A., Nainwal, H.C. and Shankar, R. (2017) 'Evaluating the contribution of avalanching to the mass balance of Himalayan glaciers', *Annals of Glaciology*, 58(75pt2), pp. 110-118.

Lea, J.M., Mair, D.W.F. and Rea, B.R. (2014) 'Evaluation of existing and new methods of tracking glacier terminus change', *Journal of Glaciology*, 60(220), pp. 323-332.

Leprince, S., Barbot, S., Ayoub, F. and Avouac, J.-P. (2007) 'Automatic and Precise Orthorectification, Coregistration, and Subpixel Correlation of Satellite Images, Application to Ground Deformation Measurements', *IEEE Transactions on Geoscience and Remote Sensing*, 45(6), pp. 1529-1558.

Lettau, H.H. (1969) 'Note on aerodynamic roughness parameter estimation on the basis of roughness element description', *Journal of Applied Meteorology*, 8, pp. 828-832.

Lovell, A.M., Carr, J.R., Rowan, A.V. and Stokes, C.R. (2018a) 'The spatial variation of supraglacial debris characteristics and their influence on glacier melt on Annapurna South Glacier, Nepal [abstract]', *20th EGU General Assembly, EGU2018, Proceedings from the conference held 4-13 April, 2018* Vienna, Austria. p. p.9622.

Lovell, A.M., Carr, J.R. and Stokes, C.R. (2018b) 'Topographic controls on the surging behaviour of Sabche Glacier, Nepal (1967 to 2017)', *Remote Sensing of Environment*, 210, pp. 434-443.

Lovell, A.M., Carr, J.R. and Stokes, C.R. (2019) 'Spatially variable glacier changes in the Annapurna Conservation Area, Nepal, 2000 to 2016', *Remote Sensing*, 11(12).

Manandhar, S., Pandey, V.P. and Kazama, F. (2012) 'Hydro-climatic trends and people's perceptions: case of Kali Gandaki River Basin, Nepal', *Climate Research*, 54(2), pp. 167-179.

Marzeion, B., Jarosch, A.H. and Hofer, M. (2012) 'Past and future sea-level change from the surface mass balance of glaciers', *The Cryosphere*, 6(6), pp. 1295-1322.

Mattson, L. (1993) 'Ablation on debris covered glaciers: an example from the Rakhiot Glacier, Panjab, Himalaya', *IAHS Publication*, 218, pp. 289-296.

Maurer, J. and Rupper, S. (2015) 'Tapping into the Hexagon spy imagery database: A new automated pipeline for geomorphic change detection', *ISPRS Journal of Photogrammetry and Remote Sensing*, 108, pp. 113-127.

Maurer, J.M., Schaefer, J.M., Rupper, S. and Corley, A. (2019) 'Acceleration of ice loss across the Himalayas over the past 40 years', *Science Advances*, 5(6), p. eaav7266.

Maussion, F., Scherer, D., Finkelnburg, R., Richters, J., Yang, W. and Yao, T. (2011) 'WRF simulation of a precipitation event over the Tibetan Plateau, China – an assessment using remote sensing and ground observations', *Hydrology and Earth System Sciences*, 15(6), pp. 1795-1817.

Maussion, F., Scherer, D., Mölg, T., Collier, E., Curio, J. and Finkelnburg, R. (2014) 'Precipitation seasonality and variability over the Tibetan Plateau as resolved by the High Asia Reanalysis', *Journal of Climate*, 27(5), pp. 1910-1927.

Meier, M.F. and Post, A. (1969) 'What are glacier surges?', *Canadian Journal of Earth Sciences*, 6(4), pp. 807-817.

Mihalcea, C., Mayer, C., Diolaiuti, G., D'Agata, C., Smiraglia, C., Lambrecht, A., Vuillermoz, E. and Tartari, G. (2008) 'Spatial distribution of debris thickness and melting from remote-sensing and meteorological data, at debris-covered Baltoro glacier, Karakoram, Pakistan', *Annals of Glaciology*, 48(1), pp. 49-57.

Mihalcea, C., Mayer, C., Diolaiuti, G., Lambrecht, A., Smiraglia, C. and Tartari, G. (2006) 'Ice ablation and meteorological conditions on the debris-covered area of Baltoro glacier, Karakoram, Pakistan', *Annals of Glaciology*, 43(1), pp. 292-300.

Miles, E.S., Willis, I., Buri, P., Steiner, J.F., Arnold, N.S. and Pellicciotti, F. (2018) 'Surface pond energy absorption across four Himalayan glaciers accounts for 1/8 of total catchment ice loss', *Geophys Res Lett*, 45(19), pp. 10464-10473.

Mishra, V. (2015) 'Climatic uncertainty in Himalayan water towers', *Journal of Geophysical Research: Atmospheres*, 120(7), pp. 2689-2705.

Molden, D.J., Shrestha, A.B., Nepal, S. and Immerzeel, W.W. (2016) 'Downstream implications of climate change in the Himalayas', in Biswas, A.K. and Tortajada, C. (eds.) *Water Security, Climate Change and Sustainable Development*. Singapore: Springer Singapore, pp. 65-82.

Mölg, N., Bolch, T., Rastner, P., Strozzi, T. and Paul, F. (2018) 'A consistent glacier inventory for Karakoram and Pamir derived from Landsat data: distribution of debris cover and mapping challenges', *Earth System Science Data*, 10(4), pp. 1807-1827.

Mölg, T., Maussion, F. and Scherer, D. (2013) 'Mid-latitude westerlies as a driver of glacier variability in monsoonal High Asia', *Nature Climate Change*, 4(1), pp. 68-73.

Moon, T. and Joughin, I. (2008) 'Changes in ice front position on Greenland's outlet glaciers from 1992 to 2007', *Journal of Geophysical Research*, 113(F2).

Murray, T., Dowdeswell, J.A., Drewry, D.J. and Frearson, I. (1998) 'Geometric evolution and ice dynamics during a surge of Bakaninbreen, Svalbard', *Journal of Glaciology*, 44(147), pp. 263-272.

Murray, T., Strozzi, T., Luckman, A., Jiskoot, H. and Christakos, P. (2003) 'Is there a single surge mechanism? Contrasts in dynamics between glacier surges in Svalbard and other regions', *Journal of Geophysical Research: Solid Earth*, 108(B5).

Murray, T., Stuart, G.W., Miller, P.J., Woodward, J., Smith, A.M., Porter, P.R. and Jiskoot, H. (2000) 'Glacier surge propagation by thermal evolution at the bed', *Journal of Geophysical Research: Solid Earth*, 105(B6), pp. 13491-13507.

Nakawo, M. and Rana, B. (1999) 'Estimate of ablation rate of glacier ice under a supraglacial debris layer', *Geografiska Annaler, Series A: Physical Geography*, 81(4), pp. 695-701.

Nakawo, M. and Young, G.J. (1981) 'Field experiments to determine the effect of a debris layer on ablation of glacier ice', *Annals of Glaciology*, 2(1), pp. 85-91.

Nakawo, M. and Young, G.J. (1982) *Estimate of glacier ablation under a debris layer from surface temperature and meteorological variables*.

Nicholson, L. and Benn, D.I. (2006) 'Calculating ice melt beneath a debris layer using meteorological data', *Journal of Glaciology*, 52(178), pp. 463-470.

Nicholson, L. and Benn, D.I. (2013) 'Properties of natural supraglacial debris in relation to modelling sub-debris ice ablation', *Earth Surface Processes and Landforms*, 38(5), pp. 490-501.

Nicholson, L.I., McCarthy, M., Pritchard, H.D. and Willis, I. (2018) 'Supraglacial debris thickness variability: impact on ablation and relation to terrain properties', *The Cryosphere*, 12(12), pp. 3719-3734.

Nie, Y., Sheng, Y., Liu, Q., Liu, L., Liu, S., Zhang, Y. and Song, C. (2017) 'A regional-scale assessment of Himalayan glacial lake changes using satellite observations from 1990 to 2015', *Remote Sensing of Environment*, 189, pp. 1-13.

Nolan, M. (2003) 'The “Galloping Glacier” trots: decadal-scale speed oscillations within the quiescent phase', *Annals of Glaciology*, 36, pp. 7-13.

Nuth, C. and Kääb, A. (2011) 'Co-registration and bias corrections of satellite elevation data sets for quantifying glacier thickness change', *The Cryosphere*, 5(1), pp. 271-290.

Oi, H., Higaki, D., Yagi, H., Usuki, N. and Yoshino, K. (2014) 'Report of the investigation of the flood disaster that occurred on May 5, 2012 along the Seti River in Nepal', *International Journal of Erosion Control Engineering*, 7(4), pp. 111-117.

Ojha, S., Fujita, K., Asahi, K., Sakai, A., Lamsal, D., Nuimura, T. and Nagai, H. (2016) 'Glacier area shrinkage in eastern Nepal Himalaya since 1992 using high-resolution inventories from aerial photographs and ALOS satellite images', *Journal of Glaciology*, 62(233), pp. 512-524.

Østrem, G. (1959) 'Ice melting under a thin layer of moraine, and the existence of ice cores in moraine ridges', *Geografiska Annaler*, 41(4), pp. 228-230.

Palazzi, E., von Hardenberg, J. and Provenzale, A. (2013) 'Precipitation in the Hindu-Kush Karakoram Himalaya: Observations and future scenarios', *Journal of Geophysical Research: Atmospheres*, 118(1), pp. 85-100.

Panthi, J., Dahal, P., Shrestha, M., Aryal, S., Krakauer, N., Pradhanang, S., Lakhankar, T., Jha, A., Sharma, M. and Karki, R. (2015) 'Spatial and temporal variability of rainfall in the Gandaki River Basin of Nepal Himalaya', *Climate*, 3(1), pp. 210-226.

Patel, L.K., Sharma, P., Thamban, M., Singh, A. and Ravindra, R. (2016) 'Debris control on glacier thinning—a case study of the Batal glacier, Chandra basin, Western Himalaya', *Arabian Journal of Geosciences*, 9(4).

Paul, F. (2015) 'Revealing glacier flow and surge dynamics from animated satellite image sequences: examples from the Karakoram', *The Cryosphere*, 9(6), pp. 2201-2214.

Paul, F., Barrand, N.E., Baumann, S., Berthier, E., Bolch, T., Casey, K., Frey, H., Joshi, S.P., Konovalov, V., Bris, R.L., Mölg, N., Nosenko, G., Nuth, C., Pope, A., Racoviteanu, A., Rastner, P., Raup, B., Scharrer, K., Steffen, S. and Winsvold, S. (2013) 'On the accuracy of glacier outlines derived from remote-sensing data', *Annals of Glaciology*, 54(63), pp. 171-182.

Paul, F., Bolch, T., Kääb, A., Nagler, T., Nuth, C., Scharrer, K., Shepherd, A., Strozzi, T., Ticconi, F., Bhambri, R., Berthier, E., Bevan, S., Gourmelen, N., Heid, T., Jeong, S., Kunz, M., Lauknes, T.R., Luckman, A., Merryman Boncori, J.P., Moholdt, G., Muir, A., Neelmeijer, J., Rankl, M., VanLooy, J. and Van Niel, T. (2015) 'The glaciers climate change initiative: Methods for creating glacier area, elevation change and velocity products', *Remote Sensing of Environment*, 162, pp. 408-426.

Pellicciotti, F., Stephan, C., Miles, E., Herreid, S., Immerzeel, W.W. and Bolch, T. (2015) 'Mass-balance changes of the debris-covered glaciers in the Langtang Himal, Nepal, from 1974 to 1999', *Journal of Glaciology*, 61(226), pp. 373-386.

Phan, V.H., Lindenbergh, R. and Menenti, M. (2017) 'Assessing orographic variability in glacial thickness changes at the Tibetan Plateau using ICESat laser altimetry', *Remote Sensing*, 9(160), pp. 1-19.

Pieczonka, T. and Bolch, T. (2015) 'Region-wide glacier mass budgets and area changes for the Central Tien Shan between ~1975 and 1999 using Hexagon KH-9 imagery', *Global and Planetary Change*, 128, pp. 1-13.

Pokharel, A.K. and Hallett, J. (2015) 'Distribution of rainfall intensity during the summer monsoon season over Kathmandu', *Weather*, 70(9), pp. 257-261.

Pratt-Sitaula, B., Burbank, D.W., Heimsath, A.M., Humphrey, N.F., Oskin, M. and Putkonen, J. (2011) 'Topographic control of asynchronous glacial advances: A case study from Annapurna, Nepal', *Geophysical Research Letters*, 38(24).

Pritchard, H.D. (2019) 'Asia's shrinking glaciers protect large populations from drought stress', *Nature*, 569(7758), pp. 649-654.

Quincey, D., Smith, M., Rounce, D., Ross, A., King, O. and Watson, C. (2017) 'Evaluating morphological estimates of the aerodynamic roughness of debris covered glacier ice', *Earth Surface Processes and Landforms*.

Quincey, D.J., Braun, M., Glasser, N.F., Bishop, M.P., Hewitt, K. and Luckman, A. (2011) 'Karakoram glacier surge dynamics', *Geophysical Research Letters*, 38(18), p. L18504.

Quincey, D.J., Luckman, A. and Benn, D. (2009) 'Quantification of Everest region glacier velocities between 1992 and 2002, using satellite radar interferometry and feature tracking', *Journal of Glaciology*, 55(192), pp. 596-606.

Quincey, D.J., Richardson, S.D., Luckman, A., Lucas, R.M., Reynolds, J.M., Hambrey, M.J. and Glasser, N.F. (2007) 'Early recognition of glacial lake hazards in the Himalaya using remote sensing datasets', *Global and Planetary Change*, 56(1-2), pp. 137-152.

Racoviteanu, A.E., Arnaud, Y., Williams, M.W. and Manley, W.F. (2015) 'Spatial patterns in glacier characteristics and area changes from 1962 to 2006 in the Kanchenjunga–Sikkim area, eastern Himalaya', *The Cryosphere*, 9(2), pp. 505-523.

Racoviteanu, A.E., Paul, F., Raup, B., Khalsa, S.J.S. and Armstrong, R. (2009) 'Challenges and recommendations in mapping of glacier parameters from space: results of the 2008 Global Land Ice Measurements from Space (GLIMS) workshop, Boulder, Colorado, USA', *Annals of Glaciology*, 50(53), pp. 53-69.

Radić, V., Bliss, A., Beedlow, A.C., Hock, R., Miles, E. and Cogley, J.G. (2013) 'Regional and global projections of twenty-first century glacier mass changes in response to climate scenarios from global climate models', *Climate Dynamics*, 42(1-2), pp. 37-58.

Ragettli, S., Bolch, T. and Pellicciotti, F. (2016) 'Heterogeneous glacier thinning patterns over the last 40 years in Langtang Himal, Nepal', *The Cryosphere*, 10, pp. 2075-2097.

Rana, B., Nakawo, M., Ageta, Y. and Seko, K. (1998) *'Glacier ablation under debris cover: field observations on Lirung glacier, Nepal Himalayas' International Conference on Ecohydrology of High Mountain Areas*. Kathmandu.

Rea, B.R., Whalley, W.B., Dixon, T.S. and Gordon, J.E. (1999) 'Plateau icefields as contributing areas to valley glaciers and the potential impact on reconstructed ELAs: a case study from the Lyngen Alps, North Norway', *Annals of Glaciology*, 28, pp. 97-102.

Reid, T.D. and Brock, B.W. (2010) 'An energy-balance model for debris-covered glaciers including heat conduction through the debris layer', *Journal of Glaciology*, 56(199), pp. 903-916.

Ren, Y.-Y., Ren, G.-Y., Sun, X.-B., Shrestha, A.B., You, Q.-L., Zhan, Y.-J., Rajbhandari, R., Zhang, P.-F. and Wen, K.-M. (2017) 'Observed changes in surface air temperature and precipitation in the Hindu Kush Himalayan region over the last 100-plus years', *Advances in Climate Change Research*, 8(3), pp. 148-156.

Reznichenko, N., Davies, T., Shulmeister, J. and McSaveney, M. (2010) 'Effects of debris on ice-surface melting rates: an experimental study', *Journal of Glaciology*, 56(197), pp. 384-394.

Richardson, S.D. and Reynolds, J.M. (2000) 'An overview of glacial hazards in the Himalayas', *Quaternary International*, 65-66, pp. 31-47.

Rignot, E., Echelmeyer, K. and Krabill, W. (2001) 'Penetration depth of interferometric synthetic-aperture radar signals in snow and ice', *Geophysical Research Letters*, 28(18), pp. 3501-3504.

Robson, B.A., Nuth, C., Nielsen, P.R., Girod, L., Hendrickx, M. and Dahl, S.O. (2018) 'Spatial variability in patterns of glacier change across the Manaslu Range, central Himalaya', *Frontiers in Earth Science*, 6.

Rounce, D., Watson, C. and McKinney, D. (2017) 'Identification of hazard and risk for glacial lakes in the Nepal Himalaya using satellite imagery from 2000–2015', *Remote Sensing*, 9(7), p. 654.

Rounce, D.R. and McKinney, D.C. (2014) 'Debris thickness of glaciers in the Everest area (Nepal Himalaya) derived from satellite imagery using a nonlinear energy balance model', *The Cryosphere*, 8(4), pp. 1317-1329.

Rounce, D.R., Quincey, D.J. and McKinney, D.C. (2015) 'Debris-covered glacier energy balance model for Imja–Lhotse Shar Glacier in the Everest region of Nepal', *The Cryosphere*, 9(6), pp. 2295-2310.

Rowan, A.V., Egholm, D.L., Quincey, D.J. and Glasser, N.F. (2015) 'Modelling the feedbacks between mass balance, ice flow and debris transport to predict the response to climate change of debris-covered glaciers in the Himalaya', *Earth and Planetary Science Letters*, 430, pp. 427-438.

Rowan, A.V., Quincey, D.J., Gibson, M.J., Glasser, N.F., Westoby, M.J., Irvine-Fynn, T.D.L., Porter, P.R. and Hambrey, M.J. (2018) 'The sustainability of water resources in High Mountain Asia in the context of recent and future glacier change', *Geological Society, London, Special Publications*, 462(1), pp. 189-204.

Roznik, E.A. and Alford, R.A. (2012) 'Does waterproofing Thermochron iButton dataloggers influence temperature readings?', *Journal of Thermal Biology*, 37(4), pp. 260-264.

Sakai, A., Nishimura, K., Kadota, T. and Takeuchi, N. (2009) 'Onset of calving at supraglacial lakes on debris-covered glaciers of the Nepal Himalaya', *Journal of Glaciology*, 55(193), pp. 909-917.

Sakai, A., Takeuchi, N., Fujita, K. and Nakawo, M. (2000) 'Role of supraglacial ponds in the ablation process of a debris-covered glacier in the Nepal Himalayas', *IAHS Publication*, pp. 119-132.

Salerno, F., Guyennon, N., Thakuri, S., Viviano, G., Romano, E., Vuillermoz, E., Cristofanelli, P., Stocchi, P., Agrillo, G., Ma, Y. and Tartari, G. (2015) 'Weak precipitation, warm winters and springs impact glaciers of south slopes of Mt. Everest (central Himalaya) in the last 2 decades (1994–2013)', *The Cryosphere*, 9(3), pp. 1229-1247.

Salerno, F., Thakuri, S., Tartari, G., Nuimura, T., Sunako, S., Sakai, A. and Fujita, K. (2017) 'Debris-covered glacier anomaly? Morphological factors controlling changes in the mass balance, surface area, terminus position, and snow line altitude of Himalayan glaciers', *Earth and Planetary Science Letters*, 471, pp. 19-31.

Sam, L., Bhardwaj, A., Singh, S. and Kumar, R. (2015) 'Remote sensing flow velocity of debris-covered glaciers using Landsat 8 data', *Progress in Physical Geography: Earth and Environment*, 40(2), pp. 305-321.

Scherler, D., Bookhagen, B. and Strecker, M.R. (2011a) 'Hillslope-glacier coupling: The interplay of topography and glacial dynamics in High Asia', *Journal of Geophysical Research*, 116(F2).

Scherler, D., Bookhagen, B. and Strecker, M.R. (2011b) 'Spatially variable response of Himalayan glaciers to climate change affected by debris cover', *Nature Geoscience*, 4(3), pp. 156-159.

Scherler, D., Leprince, S. and Strecker, M. (2008) 'Glacier-surface velocities in alpine terrain from optical satellite imagery—Accuracy improvement and quality assessment', *Remote Sensing of Environment*, 112(10), pp. 3806-3819.

Scherler, D., Wulf, H. and Gorelick, N. (2018) 'Global Assessment of Supraglacial Debris-Cover Extents', *Geophysical Research Letters*, 45(21), pp. 11,798-11,805.

Schwanghart, W., Bernhardt, A., Stolle, A., Hoelzmann, P., Adhikari, B.R., Andermann, C., Tofelde, S., Merchel, S., Rugel, G., Fort, M. and Korup, O. (2015) 'Repeated catastrophic valley infill following medieval earthquakes in the Nepal Himalaya', *Sciencexpress*, pp. 1-9.

Schwanghart, W., Worni, R., Huggel, C., Stoffel, M. and Korup, O. (2016) 'Uncertainty in the Himalayan energy–water nexus: estimating regional exposure to glacial lake outburst floods', *Environmental Research Letters*, 11(7).

Sevestre, H. and Benn, D.I. (2015) 'Climatic and geometric controls on the global distribution of surge-type glaciers: implications for a unifying model of surging', *Journal of Glaciology*, 61(228), pp. 646-662.

Sharma, P., Patel, L.K., Ravindra, R., Singh, A., K, M. and Thamban, M. (2016) 'Role of debris cover to control specific ablation of adjoining Batal and Sutri Dhaka glaciers in Chandra Basin (Himachal Pradesh) during peak ablation season', *Journal of Earth System Science*, 125(3), pp. 459-473.

Sharp, M.J. (1988) 'Surging glaciers: behaviour and mechanisms', *Progress in Physical Geography*, 12(3), pp. 349-370.

Shea, J.M., Immerzeel, W.W., Wagnon, P., Vincent, C. and Bajracharya, S. (2015a) 'Modelling glacier change in the Everest region, Nepal Himalaya', *The Cryosphere*, 9(3), pp. 1105-1128.

Shea, J.M., Wagnon, P., Immerzeel, W.W., Biron, R., Brun, F. and Pellicciotti, F. (2015b) 'A comparative high-altitude meteorological analysis from three catchments in the Nepalese Himalaya', *International Journal of Water Resources Development*, 31(2), pp. 174-200.

Shean, D.E., Alexandrov, O., Moratto, Z.M., Smith, B.E., Joughin, I.R., Porter, C. and Morin, P. (2016) 'An automated, open-source pipeline for mass production of digital elevation models (DEMs) from very-high-resolution commercial stereo satellite imagery', *ISPRS Journal of Photogrammetry and Remote Sensing*, 116, pp. 101-117.

Shekhar, M.S., Chand, H., Kumar, S., Srinivasan, K. and Ganju, A. (2010) 'Climate-change studies in the western Himalaya', *Annals of Glaciology*, 51(54), pp. 105-112.

Shrestha, A.B., Wake, C.P., Dibb, J.E. and Mayewski, P.A. (2000) 'Precipitation fluctuations in the Nepal Himalaya and its vicinity and relationship with some large scale climatological parameters', *International Journal of Climatology*, 20(3), pp. 317-327.

Shrestha, A.B., Wake, C.P., Mayewski, P.A. and Dibb, J.E. (1999) 'Maximum temperature trends in the Himalaya and its vicinity: an analysis based on temperature records from Nepal for the period 1971–94', *Journal of Climate*, 12(9), pp. 2775-2786.

Shukla, A. and Garg, P.K. (2019) 'Evolution of a debris-covered glacier in the western Himalaya during the last four decades (1971–2016): A multiparametric assessment using remote sensing and field observations', *Geomorphology*, 341, pp. 1-14.

Singh, P. and Kumar, N. (1997) 'Effect of orography on precipitation in the western Himalayan region', *Journal of Hydrology*, 199(1-2), pp. 183-206.

Smith, M.W., Quincey, D.J., Dixon, T., Bingham, R.G., Carrivick, J.L., Irvine-Fynn, T.D.L. and Rippin, D.M. (2016) 'Aerodynamic roughness of glacial ice surfaces derived from high-resolution topographic data', *Journal of Geophysical Research: Earth Surface*, 121(4), pp. 748-766.

Solomon, S., Qin, D., Manning, M., Chen, Z., Marquis, M., Averyt, K., Tignor, M. and Miller, H. (2007) 'Contribution of working group I to the fourth assessment report of the intergovernmental panel on climate change, 2007'. Cambridge University Press, Cambridge.

Soncini, A., Bocchiola, D., Confortola, G., Minora, U., Vuillermoz, E., Salerno, F., Viviano, G., Shrestha, D., Senese, A., Smiraglia, C. and Diolaiuti, G. (2016) 'Future hydrological regimes and glacier cover in the Everest region: The case study of the upper Dudh Koshi basin', *Sci Total Environ*, 565, pp. 1084-1101.

Steiner, J.F., Litt, M., Stigter, E.E., Shea, J., Bierkens, M.F.P. and Immerzeel, W.W. (2018) 'The importance of turbulent fluxes in the surface energy balance of a debris-covered glacier in the Himalayas', *Frontiers in Earth Science*, 6.

Steiner, J.F. and Pellicciotti, F. (2016) 'Variability of air temperature over a debris-covered glacier in the Nepalese Himalaya', *Annals of Glaciology*, 57(71), pp. 295-307.

Takeuchi, Y., Kayastha, R.B. and Nakawo, M. (2000) 'Characteristics of ablation and heat balance in debris-free and debis-covered areas of Khumbu Glacier, Nepal Himalayas, in the pre-monsoon', in Nakawo, M., Raymond, C.F. and Fountain, A. (eds.) *Debris-Covered Glaciers*. Wallingford: IAHS Press, pp. 53-61.

Thakuri, S., Salerno, F., Smiraglia, C., Bolch, T., D'Agata, C., Viviano, G. and Tartari, G. (2014) 'Tracing glacier changes since the 1960s on the south slope of Mt. Everest (central Southern Himalaya) using optical satellite imagery', *The Cryosphere*, 8(4), pp. 1297-1315.

Thompson, S., Benn, D.I., Mertes, J. and Luckman, A. (2016) 'Stagnation and mass loss on a Himalayan debris-covered glacier: processes, patterns and rates', *Journal of Glaciology*, pp. 1-19.

Thompson, S.S., Benn, D.I., Dennis, K. and Luckman, A. (2012) 'A rapidly growing moraine-dammed glacial lake on Ngozumpa Glacier, Nepal', *Geomorphology*, 145-146, pp. 1-11.

Toutin, T. (2002) 'Three-dimensional topographic mapping with ASTER stereo data in rugged topography', *IEEE Transactions on Geoscience and Remote Sensing*, 40(10), pp. 2241-2247.

Turrin, J.B., Forster, R.R., Sauber, J.M., Hall, D.K. and Bruhn, R.L. (2014) 'Effects of bedrock lithology and subglacial till on the motion of Ruth Glacier, Alaska, deduced from five pulses from 1973 to 2012', *Journal of Glaciology*, 60(222), pp. 771-781.

Veh, G., Korup, O., von Specht, S., Roessner, S. and Walz, A. (2019) 'Unchanged frequency of moraine-dammed glacial lake outburst floods in the Himalaya', *Nature Climate Change*, 9(5), pp. 379-383.

Vincent, C., Wagnon, P., Shea, J.M., Immerzeel, W.W., Kraaijenbrink, P., Shrestha, D., Soruco, A., Arnaud, Y., Brun, F., Berthier, E. and Sherpa, S.F. (2016) 'Reduced melt on debris-covered glaciers: investigations from Changri Nup Glacier, Nepal', *The Cryosphere*, 10(4), pp. 1845-1858.

Waltham, A.C. (1972) 'A contribution to the geology of the Annapurna and Nilgiri Himals, Nepal', *Geological Magazine*, 109(03), p. 205.

Watson, C.S., Quincey, D.J., Carrivick, J.L. and Smith, M.W. (2016) 'The dynamics of supraglacial ponds in the Everest region, central Himalaya', *Global and Planetary Change*, 142, pp. 14-27.

Westoby, M.J., Brasington, J., Glasser, N.F., Hambrey, M.J. and Reynolds, J.M. (2012) '‘Structure-from-Motion’ photogrammetry: A low-cost, effective tool for geoscience applications', *Geomorphology*, 179, pp. 300-314.

Wiltshire, A.J. (2014) 'Climate change implications for the glaciers of the Hindu Kush, Karakoram and Himalayan region', *The Cryosphere*, 8(3), pp. 941-958.

Wouters, B., Gardner, A.S. and Moholdt, G. (2019) 'Global Glacier Mass Loss During the GRACE Satellite Mission (2002-2016)', *Frontiers in Earth Science*, 7.

Yamada, T. and Sharma, C. (1993) 'Glacier lakes and outburst floods in the Nepal Himalaya', *IAHS Publications-Publications of the International Association of Hydrological Sciences*, 218, pp. 319-330.

Yamanaka, H. (1982) 'Radiocarbon ages of upper quaternary deposit in central Nepal and their geomorphological significance', *The Science Reports of Tohoku University, 7th series (Geography)*, 32(1), pp. 46-60.

Yao, T., Thompson, L., Yang, W., Yu, W., Gao, Y., Guo, X., Yang, X., Duan, K., Zhao, H., Xu, B., Pu, J., Lu, A., Xiang, Y., Kattel, D.B. and Joswiak, D. (2012) 'Different glacier status with atmospheric circulations in Tibetan Plateau and surroundings', *Nature Climate Change*, 2(9), pp. 663-667.

Ye, Q., Yao, T., Kang, S., Chen, F. and Wang, J. (2006) 'Glacier variations in the Naimona'nyi region, western Himalaya, in the last three decades', *Annals of Glaciology*, 43(1), pp. 385-389.

Zemp, M., Frey, H., Gärtner-Roer, I., Nussbaumer, S.U., Hoelzle, M., Paul, F., Haeberli, W., Denzinger, F., Ahlstrøm, A.P., Anderson, B., Bajracharya, S., Baroni, C., Braun, L.N., Cáceres, B.E., Casassa, G., Cobos, G., Dávila, L.R., Delgado Granados, H., Demuth, M.N., Espizua, L., Fischer, A., Fujita, K., Gadek, B., Ghazanfar, A., Ove Hagen, J., Holmlund, P., Karimi, N., Li, Z., Pelto, M., Pitte, P., Popovnin, V.V., Portocarrero, C.A., Prinz, R., Sangewar, C.V., Severskiy, I., Sigurđsson, O., Soruco, A., Usubaliev, R. and Vincent, C. (2015) 'Historically unprecedented global glacier decline in the early 21st century', *Journal of Glaciology*, 61(228), pp. 745-762.

Zemp, M., Huss, M., Thibert, E., Eckert, N., McNabb, R., Huber, J., Barandun, M., Machguth, H., Nussbaumer, S.U., Gartner-Roer, I., Thomson, L., Paul, F., Maussion, F., Kutuzov, S. and Cogley, J.G. (2019) 'Global glacier mass changes and their contributions to sea-level rise from 1961 to 2016', *Nature*, 568(7752), pp. 382-386.

Zhao, L., Ding, R. and Moore, J.C. (2014) 'Glacier volume and area change by 2050 in high mountain Asia', *Global and Planetary Change*, 122, pp. 197-207.

Appendix A: Summary of glacier characteristics and glacier changes in the Annapurna Conservation Area

Table 1: Spreadsheet summary of glacier characteristics, area change, surface elevation change and mass balance for 174 glaciers in the Annapurna Conservation Area. AH = Annapurna Himal, MH = Muktinath Himal and DH = Damodar Himal. Sabche glacier is highlighted in yellow.

GLIMS ID	Glacier name	Longitude	Latitude	Sub-region	Min elev (m asl) (2000 outlines)	Max elev (m asl) (2000 outlines)	Elevation range (m)	Median elev (m asl)	Gradient (°)	Accumulation zone gradient (°)	Ablation zone gradient (°)	HI (classification)	Avalanche likelihood ratio	Area (2000) (km^2)	Area (2015) (km^2)	Glacier area change per yr (% a^{-1})	DEM_1	Date	DEM_2	Date	Interval (yr)	Mean dh (m)	Mean dh pr yr (m a^{-1})	dh uncertainty pr yr (m a^{-1})	Mass balance (m w.e.)	Mass balance pr yr (m w.e. a^{-1})	Mass balance uncertainty pr yr (m w.e. a^{-1})
G083954E28576N	East Annapurna	83.959472	28.569036	AH	4721	7525	2804	5770	35.33	43.50	25.87	V bottom heavy	0.70	11.80	10.84	-0.54	NaN	NaN	NaN	NaN	NaN	NaN	NaN	NaN	NaN	NaN	NaN
G083996E28612N	Gangapurna	83.985303	28.627688	AH	NaN	NaN	NaN	NaN	NaN	NaN	NaN	NaN	NaN	NaN	NaN	NaN	NaN	NaN	NaN	NaN	NaN	NaN	NaN	NaN	NaN	NaN	NaN
G084117E28453N	Kawache	84.116768	28.450751	AH	2433	2844	411	2517	11.78	20.55	4.31	V bottom heavy	11.90	0.61	0.40	-2.31	NaN	NaN	NaN	NaN	NaN	NaN	NaN	NaN	NaN	NaN	NaN
G083815E28542N	KG001	83.811633	28.540168	AH	4984	7579	2595	6391	31.83	38.67	29.79	Equidimensional	0.40	10.05	**9.08**	-0.65	NaN	NaN	NaN	NaN	NaN	NaN	NaN	NaN	NaN	NaN	NaN
G083802E28672N	KG003	83.806437	28.675238	AH	5772	7103	1331	6489	33.84	28.45	40.45	Equidimensional	0.36	2.26	1.81	-1.32	NaN	NaN	NaN	NaN	NaN	NaN	NaN	NaN	NaN	NaN	NaN
G083779E28671N	KG004	83.779697	28.673596	AH	4537	6659	2122	5275	26.68	36.58	18.69	V bottom heavy	1.33	1.71	1.20	-1.99	NaN	NaN	NaN	NaN	NaN	NaN	NaN	NaN	NaN	NaN	NaN
G083728E28660N	KG005	83.766208	28.661611	AH	4678	6999	2321	5746	26.10	29.06	23.30	Equidimensional	0.72	8.49	7.68	-0.64	NaN	NaN	NaN	NaN	NaN	NaN	NaN	NaN	NaN	NaN	NaN
	KG037	83.74275	28.637671	AH	4983	5444	461	5218	24.50	20.05	29.30	Equidimensional	2.04	0.61	0.44	-1.83	NaN	NaN	NaN	NaN	NaN	NaN	NaN	NaN	NaN	NaN	NaN
G083716E28646N	KG038	83.721552	28.639193	AH	4633	5352	719	5014	26.39	25.70	26.97	Equidimensional	3.34	0.63	0.52	-1.18	NaN	NaN	NaN	NaN	NaN	NaN	NaN	NaN	NaN	NaN	NaN
G083913E28638N	M001	83.896488	28.644793	AH	4103	7243	3140	5656	21.09	41.71	14.17	Equidimensional	0.44	13.60	13.27	-0.16	NaN	NaN	NaN	NaN	NaN	NaN	NaN	NaN	NaN	NaN	NaN
G083803E28699N	M002	83.820511	28.712081	AH	4977	7083	2106	5303	20.24	37.67	5.49	V bottom heavy	0.63	4.57	4.31	-0.38	NaN	NaN	NaN	NaN	NaN	NaN	NaN	NaN	NaN	NaN	NaN
G083956E28626N	M003	83.943949	28.633625	AH	4734	7395	2661	5750	17.03	36.77	9.89	V bottom heavy	0.48	17.82	17.35	-0.18	NaN	NaN	NaN	NaN	NaN	NaN	NaN	NaN	NaN	NaN	NaN
G083930E28641N	M004	83.929794	28.641482	AH	5490	6111	621	5901	34.69	31.76	35.93	V top heavy	0.26	0.49	0.49	-0.07	NaN	NaN	NaN	NaN	NaN	NaN	NaN	NaN	NaN	NaN	NaN
G084244E28473N	M005	84.240892	28.471178	AH	4440	5337	897	5030	10.96	10.58	11.09	V top heavy	0.53	4.23	2.49	-2.74	NaN	NaN	NaN	NaN	NaN	NaN	NaN	NaN	NaN	NaN	NaN
G084260E28476N	M005_1	84.254986	28.461382	AH	NaN	NaN	NaN	NaN	NaN	NaN	NaN	NaN	NaN	NaN	1.38	NaN	NaN	NaN	NaN	NaN	NaN	NaN	NaN	NaN	NaN	NaN	NaN
G084260E28476N	M005_2	84.259631	28.475021	AH	NaN	NaN	NaN	NaN	NaN	NaN	NaN	NaN	NaN	NaN	0.30	NaN	NaN	NaN	NaN	NaN	NaN	NaN	NaN	NaN	NaN	NaN	NaN
G084277E28479N	M006	84.276401	28.477686	AH	4825	5474	649	5215	20.30	16.94	22.90	V top heavy	0.29	1.75	1.50	-0.95	NaN	NaN	NaN	NaN	NaN	NaN	NaN	NaN	NaN	NaN	NaN
G083872E28641N	M007	83.877475	28.649036	AH	4700	6239	1539	5202	25.18	34.84	17.55	V bottom heavy	1.03	3.91	3.50	-0.71	NaN	NaN	NaN	NaN	NaN	NaN	NaN	NaN	NaN	NaN	NaN
G084177E28528N	M008	84.174324	28.545318	AH	4158	6391	2233	4943	25.06	32.31	18.08	V bottom heavy	1.41	7.21	6.59	-0.57	NaN	NaN	NaN	NaN	NaN	NaN	NaN	NaN	NaN	NaN	NaN
G084086E28561N	M009	84.084697	28.574478	AH	4645	7417	2772	5656	24.91	40.92	14.66	V bottom heavy	0.47	9.32	9.24	-0.06	NaN	NaN	NaN	NaN	NaN	NaN	NaN	NaN	NaN	NaN	NaN
G084028E28586N	M010	84.02575	28.58551	AH	5049	6287	1238	5674	30.00	37.17	26.88	Equidimensional	0.87	2.23	1.85	-1.12	NaN	NaN	NaN	NaN	NaN	NaN	NaN	NaN	NaN	NaN	NaN
G084259E28493N	M094	84.250861	28.488531	AH	4922	5690	768	5281	17.37	19.48	15.42	Equidimensional	0.18	2.22	1.87	-1.05	NaN	NaN	NaN	NaN	NaN	NaN	NaN	NaN	NaN	NaN	NaN
G084243E28491N	M095	84.234587	28.500019	AH	4610	5649	1039	5133	16.30	15.60	16.75	Equidimensional	0.28	1.98	1.69	-0.99	NaN	NaN	NaN	NaN	NaN	NaN	NaN	NaN	NaN	NaN	NaN
G083871E28659N	M105	83.874198	28.66619	AH	4670	5636	966	5088	16.54	21.53	14.65	Bottom heavy	1.35	2.71	2.50	-0.53	SRTM	22/02/2000	SPOT7_lower_dem	25/02/2016	15	-6.30	-0.42	0.27	-5.37	-0.36	0.29
G083832E28688N	M107	83.844484	28.685783	AH	4919	6030	1111	5031	14.14	16.50	8.73	V bottom heavy	1.29	3.79	3.66	-0.24	SRTM	22/02/2000	SPOT7_lower_dem	25/02/2016	15	-4.96	-0.33	0.38	-4.23	-0.28	0.41
G083830E28695N	M108	83.835341	28.699147	AH	4922	6379	1457	5114	19.24	34.07	7.03	V bottom heavy	0.75	2.73	2.59	-0.34	SRTM	22/02/2000	SPOT7_lower_dem	25/02/2016	15	-2.69	-0.18	0.27	-2.30	-0.15	0.29
G083853E28525N	MSM001	83.853119	28.525197	AH	4237	7110	2873	5439	29.38	36.22	23.26	Bottom heavy	0.61	5.59	**4.49**	-1.32	NaN	NaN	NaN	NaN	NaN	NaN	NaN	NaN	NaN	NaN	NaN
G083846E28537N	MSM002	83.844714	28.53678	AH	4902	5611	709	5279	25.62	25.76	25.50	Equidimensional	1.36	0.93	0.83	-0.73	NaN	NaN	NaN	NaN	NaN	NaN	NaN	NaN	NaN	NaN	NaN
G083882E28561N	MSM003	83.882887	28.565856	AH	4888	5584	696	5320	23.58	23.68	23.53	V top heavy	0.21	1.39	1.10	-1.37	NaN	NaN	NaN	NaN	NaN	NaN	NaN	NaN	NaN	NaN	NaN
G083892E28572N	MSM004	83.892197	28.576183	AH	5168	6466	1298	5531	21.69	27.85	16.51	V bottom heavy	0.41	2.15	1.56	-1.83	NaN	NaN	NaN	NaN	NaN	NaN	NaN	NaN	NaN	NaN	NaN
G083912E28572N	MSM005	83.912369	28.569977	AH	4348	7157	2809	5803	24.23	34.92	19.42	Equidimensional	0.53	12.12	11.31	-0.44	NaN	NaN	NaN	NaN	NaN	NaN	NaN	NaN	NaN	NaN	NaN
G083936E28585N	MSM006	83.936915	28.573684	AH	4575	7120	2545	5514	31.93	40.13	23.38	V bottom heavy	0.58	3.95	3.21	-1.25	NaN	NaN	NaN	NaN	NaN	NaN	NaN	NaN	NaN	NaN	NaN
G083959E28546N	MSM007	83.959435	28.5477	AH	4824	6155	1331	5490	31.20	47.05	24.29	Equidimensional	0.52	1.97	**1.86**	-0.39	NaN	NaN	NaN	NaN	NaN	NaN	NaN	NaN	NaN	NaN	NaN
G083950E28520N	MSM008	83.949864	28.515586	AH	4820	6269	1449	5393	46.09	51.24	37.94	V bottom heavy	0.56	2.79	2.70	-0.23	NaN	NaN	NaN	NaN	NaN	NaN	NaN	NaN	NaN	NaN	NaN
G083968E28535N	MSM013	83.969026	28.533868	AH	4901	5565	664	5211	39.25	41.43	36.92	Equidimensional	5.03	0.18	0.18	-0.02	NaN	NaN	NaN	NaN	NaN	NaN	NaN	NaN	NaN	NaN	NaN
G084014E28561N	Sabche glacier	84.009552	28.552753	AH	4087	7489	3402	5065	28.2	NaN	NaN	V bottom heavy	NaN	9.05	**9.10**	NaN	NaN	NaN	NaN	NaN	NaN	NaN	NaN	NaN	NaN	NaN	NaN
G084059E28538N	MSM018	84.042361	28.539392	AH	3924	7488	3564	4860	27.17	41.63	14.85	V bottom heavy	0.72	13.97	13.95	-0.01	NaN	NaN	NaN	NaN	NaN	NaN	NaN	NaN	NaN	NaN	NaN
G084065E28515N	MSM019	84.063085	28.511635	AH	5153	5594	441	5329	23.89	23.76	24.08	V bottom heavy	2.53	0.32	0.32	0.05	NaN	NaN	NaN	NaN	NaN	NaN	NaN	NaN	NaN	NaN	NaN
G084074E28509N	MSM020	84.069594	28.50223	AH	4918	6105	1187	5306	22.57	26.82	16.51	V bottom heavy	1.26	2.37	**1.99**	-1.07	NaN	NaN	NaN	NaN	NaN	NaN	NaN	NaN	NaN	NaN	NaN
G084142E28500N	MSM021	84.106963	28.510787	AH	4620	7740	3120	6356	25.10	23.89	25.94	Top heavy	0.21	48.46	47.66	-0.11	NaN	NaN	NaN	NaN	NaN	NaN	NaN	NaN	NaN	NaN	NaN
G084142E28500N	MSM021_1	84.102773	28.480301	AH	3621	4653	1032	4194	20.75	16.63	25.35	Top heavy	0.00	1.11	1.00	-0.66	NaN	NaN	NaN	NaN	NaN	NaN	NaN	NaN	NaN	NaN	NaN
G084186E28467N	MSM023	84.189266	28.462773	AH	4212	6231	2019	4776	31.52	42.15	18.77	V bottom heavy	1.51	2.14	1.75	-1.22	NaN	NaN	NaN	NaN	NaN	NaN	NaN	NaN	NaN	NaN	NaN
G084197E28477N	MSM024	84.203153	28.466688	AH	4513	5730	1217	5028	28.69	32.48	25.36	Bottom heavy	1.42	1.12	0.96	-0.94	NaN	NaN	NaN	NaN	NaN	NaN	NaN	NaN	NaN	NaN	NaN
G084212E28476N	MSM025	84.21457	28.470073	AH	4681	5194	513	4956	20.67	21.13	20.28	Equidimensional	1.82	1.18	1.09	-0.53	NaN	NaN	NaN	NaN	NaN	NaN	NaN	NaN	NaN	NaN	NaN
G083876E28575N	MSM026	83.875174	28.571507	AH	5025	6101	1076	5375	31.41	37.55	22.39	V bottom heavy	0.62	1.08	0.74	-2.09	NaN	NaN	NaN	NaN	NaN	NaN	NaN	NaN	NaN	NaN	NaN
G083949E28532N	MSM030	83.950422	28.532875	AH	4957	5875	918	5366	29.11	33.29	23.70	Bottom heavy	1.06	0.86	0.77	-0.75	NaN	NaN	NaN	NaN	NaN	NaN	NaN	NaN	NaN	NaN	NaN
G083851E28629N	North Annapurna	83.807699	28.641585	AH	4060	8067	4007	6145	21.87	31.35	18.33	Equidimensional	0.42	22.96	**22.08**	-0.26	NaN	NaN	NaN	NaN	NaN	NaN	NaN	NaN	NaN	NaN	NaN
G083832E28563N	South Annapurna	83.871047	28.538114	AH	3780	8051	4271	5551	19.98	40.45	12.01	Bottom heavy	0.69	27.73	26.68	-0.25	NaN	NaN	NaN	NaN	NaN	NaN	NaN	NaN	NaN	NaN	NaN
G084081E28875N	KG014	84.080599	28.871374	DH	5364	6238	874	5875	15.64	38.07	11.88	Top heavy	0.35	2.40	2.22	-0.50	NaN	NaN	NaN	NaN	NaN	NaN	NaN	NaN	NaN	NaN	NaN
G084072E28859N	KG015	84.074343	28.859843	DH	5654	6057	403	5840	15.91	24.40	11.52	Equidimensional	0.68	0.41	0.21	-3.21	NaN	NaN	NaN	NaN	NaN	NaN	NaN	NaN	NaN	NaN	NaN
G084110E28893N	KG016	84.078424	28.899678	DH	5229	6709	1480	5979	8.68	12.27	8.04	Equidimensional	0.34	7.59	7.22	-0.32	SRTM	22/02/2000	HMA_DEM8m_AT_20140119	19/01/2014	13	3.13	0.24	0.91	2.67	0.21	0.97
G084098E28916N	KG018	84.107691	28.911217	DH	5423	6361	938	5960	15.08	22.35	12.44	Top heavy	0.33	3.35	2.65	-1.40	SRTM	22/02/2000	HMA_DEM8m_AT_20140119	19/01/2014	13	1.50	0.12	0.39	1.28	0.10	0.42
G084075E28939N	KG020	84.079354	28.935186	DH	5451	6030	579	5761	21.15	29.64	17.41	Equidimensional	0.36	0.58	0.49	-1.01	SRTM	22/02/2000	HMA_DEM8m_AT_20140119	19/01/2014	13	-3.52	-0.27	0.07	-3.00	-0.23	0.07
G084096E28927N	KG021	84.100625	28.926338	DH	5595	6280	685	5964	20.83	27.06	18.02	Equidimensional	0.25	0.60	0.57	-0.37	SRTM	22/02/2000	HMA_DEM8m_AT_20140119	19/01/2014	13	1.24	0.10	0.07	1.06	0.08	0.08
G084130E28928N	KG022	84.121602	28.918197	DH	5399	6407	1008	6117	16.23	23.21	14.77	V top heavy	0.23	3.57	3.09	-0.89	SRTM	22/02/2000	HMA_DEM8m_AT_20151001	01/10/2015	15	-1.22	-0.08	0.40	-1.04	-0.07	0.43
G084129E28944N	KG023	84.129422	28.944497	DH	5650	6381	731	6089	23.80	35.88	19.65	V top heavy	0.39	0.84	0.78	-0.44	SRTM	22/02/2000	HMA_DEM8m_AT_20131120	20/11/2013	13	2.27	0.17	0.10	1.94	0.15	0.11
G084124E28961N	KG024	84.120494	28.958267	DH	5448	6240	792	6018	21.57	15.52	26.96	V top heavy	0.14	1.54	**1.34**	-0.85	SRTM	22/02/2000	HMA_DEM8m_AT_20140119	19/01/2014	13	2.85	0.22	0.18	2.43	0.19	0.19
G084131E28956N	KG025	84.130564	28.952278	DH	5608	6258	650	5948	20.87	30.63	16.60	Equidimensional	0.39	0.74	0.66	-0.72	SRTM	22/02/2000	HMA_DEM8m_AT_20140119	19/01/2014	13	-1.92	-0.15	0.09	-1.63	-0.13	0.09
G084142E28952N	KG026	84.136958	28.946686	DH	5643	6371	728	5937	22.82	43.99	13.91	Bottom heavy	0.54	0.72	0.63	-0.89	NaN	NaN	NaN	NaN	NaN	NaN	NaN	NaN	NaN	NaN	NaN

Table 1 continued.

G084134E28934N	KG027	84.134909	28.932443	DH	5838	6412	574	6115	22.25	37.10	15.68	Equidimensional	0.39	0.63	0.58	-0.61	NaN	NaN	NaN	NaN	NaN	NaN	NaN	NaN	NaN	NaN	NaN
G084148E28934N	KG028	84.144763	28.924299	DH	5614	6414	800	6093	13.99	27.86	11.35	Top heavy	0.29	1.91	1.44	-1.64	SRTM	22/02/2000	HMA_DEM8m_AT_20131120	20/11/2013	13	-2.35	-0.18	0.24	-2.01	-0.15	0.26
G084148E28934N	KG028_1	84.136533	28.927332	DH	NaN	NaN	NaN	NaN	NaN	NaN	NaN	NaN	NaN	NaN	0.26	NaN	NaN	NaN	NaN	NaN	NaN	NaN	NaN	NaN	NaN	NaN	NaN
G084159E28942N	KG029	84.159449	28.939989	DH	5748	6124	376	5941	26.21	25.57	26.68	Equidimensional	0.06	0.23	0.17	-1.74	SRTM	22/02/2000	HMA_DEM8m_AT_20131120	20/11/2013	13	-3.65	-0.28	0.03	-3.11	-0.24	0.03
G084167E28936N	KG030	84.15448	28.926056	DH	5524	6410	886	6031	13.45	13.84	13.20	Top heavy	0.26	2.33	2.23	-0.28	SRTM	22/02/2000	HMA_DEM8m_AT_20151001	01/10/2015	15	-1.88	-0.13	0.26	-1.61	-0.11	0.28
G084177E28935N	KG031	84.177567	28.932209	DH	5616	6270	654	5956	18.94	19.67	18.40	Equidimensional	0.02	0.76	0.65	-0.91	SRTM	22/02/2000	HMA_DEM8m_AT_20131120	20/11/2013	13	-3.26	-0.25	0.09	-2.78	-0.21	0.10
G084132E28911N	KG033	84.170707	28.912914	DH	5364	6738	1374	6075	5.43	6.04	5.29	Equidimensional	0.19	22.43	**20.92**	-0.45	SRTM	22/02/2000	HMA_DEM8m_AT_20151001	01/10/2015	15	-2.40	-0.16	2.55	-2.05	-0.14	2.73
G084132E28911N	KG033_1	84.161097	28.920842	DH	NaN	NaN	NaN	NaN	NaN	NaN	NaN	NaN	NaN	NaN	0.16	NaN	NaN	NaN	NaN	NaN	NaN	NaN	NaN	NaN	NaN	NaN	NaN
G084195E28908N	KG034	84.192554	28.902393	DH	5527	6319	792	5821	12.25	31.71	7.18	V bottom heavy	0.40	1.92	1.58	-1.15	NaN	NaN	NaN	NaN	NaN	NaN	NaN	NaN	NaN	NaN	NaN
G084212E28905N	KG035	84.214811	28.901782	DH	5426	6339	913	5943	12.34	17.81	10.27	Top heavy	0.13	4.61	4.39	-0.32	SRTM	22/02/2000	HMA_DEM8m_AT_20151001	01/10/2015	15	-2.89	-0.19	0.50	-2.46	-0.16	0.54
G084221E28914N	KG036	84.222891	28.908989	DH	5770	6236	466	6001	10.08	7.69	13.87	Equidimensional	0.03	1.35	1.15	-1.00	SRTM	22/02/2000	HMA_DEM8m_AT_20131120	20/11/2013	13	-2.94	-0.23	0.16	-2.51	-0.19	0.18
G084077E28853N	KG041	84.08199	28.85798	DH	5388	6221	833	5747	9.46	10.35	9.06	Bottom heavy	0.23	2.85	2.60	-0.59	SRTM	22/02/2000	HMA_DEM8m_AT_20140119	19/01/2014	13	-2.86	-0.22	0.33	-2.44	-0.19	0.35
G084102E28932N	KG042	84.105838	28.930969	DH	5625	6272	647	5968	29.41	32.39	27.27	Equidimensional	0.29	1.31	1.17	-0.70	SRTM	22/02/2000	HMA_DEM8m_AT_20140119	19/01/2014	13	2.97	0.23	0.15	2.53	0.19	0.16
G084086E28936N	KG043	84.095206	28.932907	DH	5435	6169	734	5838	31.36	33.10	29.72	Top heavy	0.31	0.87	0.64	-1.76	NaN	NaN	NaN	NaN	NaN	NaN	NaN	NaN	NaN	NaN	NaN
G084089E28931N	KG044	84.088149	28.931494	DH	5632	6163	531	5980	24.36	23.58	24.71	V top heavy	0.05	0.51	0.44	-0.95	SRTM	22/02/2000	HMA_DEM8m_AT_20140119	19/01/2014	13	-3.06	-0.24	0.06	-2.61	-0.20	0.06
	KG045	84.113916	28.922309	DH	NaN	NaN	NaN	NaN	19.60	20.50	17.99	NaN	NaN	NaN	NaN	NaN	NaN	NaN	NaN	NaN	NaN	NaN	NaN	NaN	NaN	NaN	NaN
G084095E28858N	M040	84.089923	28.860782	DH	5490	6143	653	5809	25.44	35.02	20.95	Equidimensional	0.65	0.62	0.27	-3.77	SRTM	22/02/2000	HMA_DEM8m_AT_20140119	19/01/2014	13	-6.05	-0.47	0.07	-5.15	-0.40	0.08
G084108E28879N	M041	84.110742	28.879422	DH	5557	6197	640	5824	19.46	28.50	14.28	Bottom heavy	0.38	0.55	0.49	-0.76	SRTM	22/02/2000	HMA_DEM8m_AT_20140119	19/01/2014	13	-2.88	-0.22	0.06	-2.46	-0.19	0.07
G084121E28869N	M042	84.131067	28.879857	DH	5509	6351	842	5781	15.69	28.87	8.61	V bottom heavy	0.65	3.08	1.64	-3.11	NaN	NaN	NaN	NaN	NaN	NaN	NaN	NaN	NaN	NaN	NaN
G084121E28869N	M042_1	84.125262	28.860767	DH	NaN	NaN	NaN	NaN	NaN	NaN	NaN	NaN	NaN	NaN	0.93	NaN	NaN	NaN	NaN	NaN	NaN	NaN	NaN	NaN	NaN	NaN	NaN
G084167E28860N	M043	84.121494	28.843496	DH	5148	6405	1257	5892	10.38	17.81	8.20	Top heavy	0.34	5.19	4.76	-0.55	NaN	NaN	NaN	NaN	NaN	NaN	NaN	NaN	NaN	NaN	NaN
G084145E28866N	M044	84.149048	28.871766	DH	5501	6529	1028	5888	15.93	36.56	9.88	V bottom heavy	0.50	3.30	2.96	-0.69	NaN	NaN	NaN	NaN	NaN	NaN	NaN	NaN	NaN	NaN	NaN
G084187E28836N	M045	84.161023	28.84517	DH	5267	6347	1080	5896	10.87	20.40	8.38	Top heavy	0.28	3.19	2.85	-0.72	NaN	NaN	NaN	NaN	NaN	NaN	NaN	NaN	NaN	NaN	NaN
G084168E28852N	M045_1	84.187942	28.828954	DH	5390	6102	712	5811	17.81	19.64	16.93	Top heavy	0.30	1.14	0.98	-0.95	NaN	NaN	NaN	NaN	NaN	NaN	NaN	NaN	NaN	NaN	NaN
G084168E28852N	M045_2	84.16833	28.852402	DH	5736	6025	289	5851	14.04	15.47	13.31	V bottom heavy	1.51	0.29	0.10	-4.31	SRTM	22/02/2000	HMA_DEM8m_AT_20151001	01/10/2015	15	-10.99	-0.73	0.03	-9.37	-0.62	0.03
G084238E28813N	M046	84.240439	28.812889	DH	5501	6237	736	5905	32.50	33.60	31.73	Top heavy	0.50	0.51	0.43	-1.07	NaN	NaN	NaN	NaN	NaN	NaN	NaN	NaN	NaN	NaN	NaN
G084150E28835N	M047	84.15191	28.838261	DH	5434	6297	863	5980	27.57	39.16	24.38	V top heavy	0.41	0.73	0.62	-0.98	NaN	NaN	NaN	NaN	NaN	NaN	NaN	NaN	NaN	NaN	NaN
G084163E28829N	M049	84.156043	28.822989	DH	5295	6328	1033	5709	22.26	43.32	14.49	V bottom heavy	0.71	1.18	0.78	-2.27	NaN	NaN	NaN	NaN	NaN	NaN	NaN	NaN	NaN	NaN	NaN
G084174E28827N	M050	84.173766	28.830044	DH	5436	6102	666	5847	28.87	35.26	26.06	V top heavy	1.17	0.41	0.33	-1.43	NaN	NaN	NaN	NaN	NaN	NaN	NaN	NaN	NaN	NaN	NaN
G084183E28804N	M051	84.184007	28.801976	DH	5270	5800	530	5530	22.37	27.90	19.07	Equidimensional	0.51	0.56	0.44	-1.52	NaN	NaN	NaN	NaN	NaN	NaN	NaN	NaN	NaN	NaN	NaN
G084191E28819N	M052	84.189133	28.817955	DH	5363	6100	737	5780	20.87	35.87	17.75	Top heavy	0.41	1.39	1.15	-1.12	NaN	NaN	NaN	NaN	NaN	NaN	NaN	NaN	NaN	NaN	NaN
G084207E28847N	M053	84.2067	28.850181	DH	5540	5930	390	5695	10.86	11.84	10.41	V bottom heavy	1.06	0.86	0.72	-1.14	SRTM	22/02/2000	HMA_DEM8m_AT_20131120	20/11/2013	13	-5.05	-0.39	0.10	-4.31	-0.33	0.11
G084214E28850N	M054	84.215835	28.853234	DH	5405	5931	526	5627	10.81	11.05	10.76	Bottom heavy	1.18	0.61	0.39	-2.38	SRTM	22/02/2000	HMA_DEM8m_AT_20151001	01/10/2015	15	-10.20	-0.68	0.07	-8.70	-0.58	0.07
G084213E28836N	M055	84.218831	28.837425	DH	5609	5778	169	5693	18.90	17.93	19.96	Equidimensional	0.75	0.26	0.13	-3.27	SRTM	22/02/2000	HMA_DEM8m_AT_20131120	20/11/2013	13	-9.55	-0.73	0.03	-8.14	-0.63	0.03
G084228E28829N	M056	84.229964	28.832594	DH	5508	5964	456	5714	27.64	31.27	24.02	Bottom heavy	0.23	0.44	0.38	-0.93	NaN	NaN	NaN	NaN	NaN	NaN	NaN	NaN	NaN	NaN	NaN
G084236E28824N	M057	84.233729	28.822457	DH	5222	6347	1125	5804	19.66	25.19	16.34	Equidimensional	0.24	1.56	1.38	-0.76	NaN	NaN	NaN	NaN	NaN	NaN	NaN	NaN	NaN	NaN	NaN
G084243E28821N	M058	84.24645	28.823075	DH	5249	6161	912	5585	15.48	16.55	14.90	V bottom heavy	0.21	1.04	0.79	-1.61	NaN	NaN	NaN	NaN	NaN	NaN	NaN	NaN	NaN	NaN	NaN
G084223E28820N	M059	84.22337	28.819618	DH	5321	6312	991	5724	23.16	31.26	16.62	Bottom heavy	0.46	1.22	**1.16**	-0.34	NaN	NaN	NaN	NaN	NaN	NaN	NaN	NaN	NaN	NaN	NaN
G084237E28804N	M060	84.233789	28.804796	DH	5482	6332	850	5624	9.38	12.61	7.82	V bottom heavy	0.34	1.52	1.00	-2.28	NaN	NaN	NaN	NaN	NaN	NaN	NaN	NaN	NaN	NaN	NaN
G084237E28804N	M060_1	84.230794	28.810416	DH	NaN	NaN	NaN	NaN				NaN		NaN	0.33	NaN	NaN	NaN	NaN	NaN	NaN	NaN	NaN	NaN	NaN	NaN	NaN
G084185E28879N	M061	84.214298	28.871723	DH	5037	6444	1407	5724	9.01	24.94	5.79	Equidimensional	0.45	13.83	12.87	-0.47	NaN	NaN	NaN	NaN	NaN	NaN	NaN	NaN	NaN	NaN	NaN
G084264E28884N	M063	84.266934	28.879222	DH	5297	6877	1580	5602	22.99	40.00	8.02	V bottom heavy	1.10	2.78	2.35	-1.03	NaN	NaN	NaN	NaN	NaN	NaN	NaN	NaN	NaN	NaN	NaN
G084283E28881N	M063_1	84.28359	28.880424	DH	5526	6647	1121	6168	47.69	51.49	45.05	Top heavy	0.00	0.71	0.64	-0.68	NaN	NaN	NaN	NaN	NaN	NaN	NaN	NaN	NaN	NaN	NaN
G084183E28853N	M064	84.173156	28.857596	DH	5685	6342	657	5877	11.16	18.51	9.50	V bottom heavy	1.34	0.77	0.30	-4.11	NaN	NaN	NaN	NaN	NaN	NaN	NaN	NaN	NaN	NaN	NaN
G084183E28853N	M064_1	84.183565	28.854696	DH	NaN	NaN	NaN	NaN	NaN	NaN	NaN	NaN	NaN	NaN	0.20	NaN	NaN	NaN	NaN	NaN	NaN	NaN	NaN	NaN	NaN	NaN	NaN
G084242E28796N	M100	84.240916	28.793072	DH	5339	5832	493	5623	19.85	21.24	18.96	Top heavy	0.47	0.29	0.25	-0.86	NaN	NaN	NaN	NaN	NaN	NaN	NaN	NaN	NaN	NaN	NaN
G084245E28791N	M101	84.244448	28.789611	DH	5423	5837	414	5686	27.15	19.29	33.15	V top heavy	0.31	0.17	0.08	-3.48	NaN	NaN	NaN	NaN	NaN	NaN	NaN	NaN	NaN	NaN	NaN
G084175E28819N	M102	84.177307	28.82016	DH	5330	5940	610	5626	25.77	30.02	22.86	Equidimensional	0.47	0.39	0.30	-1.59	NaN	NaN	NaN	NaN	NaN	NaN	NaN	NaN	NaN	NaN	NaN
G084187E28808N	M103	84.186967	28.808596	DH	5405	5732	327	5569	14.47	11.36	15.71	Equidimensional	0.92	0.35	0.22	-2.43	NaN	NaN	NaN	NaN	NaN	NaN	NaN	NaN	NaN	NaN	NaN
G084131E28828N	M104	84.134424	28.835365	DH	5394	6042	648	5691	19.66	19.73	19.47	Equidimensional	0.20	1.87	1.25	-2.23	SRTM	22/02/2000	HMA_DEM8m_AT_20131120	20/11/2013	13	-3.79	-0.29	0.23	-3.23	-0.25	0.24
G084200E28807N	M115	84.199134	28.805474	DH	5438	5595	157	5500	18.72	19.54	17.74	V bottom heavy	0.33	0.11	0.05	-3.98	NaN	NaN	NaN	NaN	NaN	NaN	NaN	NaN	NaN	NaN	NaN
G084203E28800N	M116	84.201108	28.797519	DH	5388	5679	291	5534	23.59	22.90	24.13	Equidimensional	0.72	0.21	0.14	-2.26	NaN	NaN	NaN	NaN	NaN	NaN	NaN	NaN	NaN	NaN	NaN
G084097E28875N	M117	84.095338	28.878864	DH	5669	6200	531	5943	22.94	23.79	22.31	Equidimensional	0.36	0.84	0.68	-1.32	SRTM	22/02/2000	HMA_DEM8m_AT_20140119	19/01/2014	13	-0.86	-0.07	0.10	-0.74	-0.06	0.11
G084115E28878N	M119	84.116375	28.880035	DH	5827	6223	396	6108	35.23	33.77	35.80	V top heavy	0.45	0.14	0.07	-3.31	NaN	NaN	NaN	NaN	NaN	NaN	NaN	NaN	NaN	NaN	NaN
G084221E28890N	M120	84.226045	28.890781	DH	5468	6337	869	6133	35.22	21.65	38.89	V top heavy	0.27	1.62	1.32	-1.26	NaN	NaN	NaN	NaN	NaN	NaN	NaN	NaN	NaN	NaN	NaN
G084239E28917N	U001	84.233126	28.906575	DH	5475	6835	1360	5973	5.56	5.02	5.75	V bottom heavy	0.17	9.19	8.50	-0.50	SRTM	22/02/2000	HMA_DEM8m_AT_20131120	20/11/2013	13	-3.52	-0.27	1.19	-3.00	-0.23	1.27
G084254E28913N	U002	84.248623	28.915484	DH	5596	6871	1275	6073	14.82	30.78	7.94	V bottom heavy	0.22	5.33	4.92	-0.52	SRTM	22/02/2000	HMA_DEM8m_AT_20131120	20/11/2013	13	-2.26	-0.17	0.75	-1.93	-0.15	0.80
G084289E28902N	U003	84.289434	28.902728	DH	5439	6797	1358	5967	NaN	NaN	NaN	NaN	NaN	11.26	10.29	-0.57	NaN	NaN	NaN	NaN	NaN	NaN	NaN	NaN	NaN	NaN	NaN
G084273E28925N	U004	84.272259	28.924721	DH	6005	6295	290	6173	14.00	9.89	19.16	Top heavy	0.00	0.50	0.36	-1.93	SRTM	22/02/2000	HMA_DEM8m_AT_20131120	20/11/2013	13	-1.67	-0.13	0.06	-1.42	-0.11	0.07
G083947E28838N	KG006	83.948684	28.836612	MH	5657	6010	353	5849	13.69	10.77	15.77	Equidimensional	0.01	0.71	0.57	-1.24	SRTM	22/02/2000	SPOT7_upper_dem	20/10/2015	15	-9.20	-0.61	0.08	-7.84	-0.52	0.08
G083944E28835N	KG007	83.943475	28.836103	MH	5648	5939	291	5769	11.64	13.96	10.25	Bottom heavy	0.02	0.47	0.33	-1.93	SRTM	22/02/2000	SPOT7_upper_dem	20/10/2015	15	-13.89	-0.93	0.05	-11.85	-0.79	0.05
G083963E28839N	KG008	83.962071	28.838382	MH	5729	6012	283	5862	17.33	15.06	20.20	Equidimensional	0.21	0.30	0.17	-2.87	SRTM	22/02/2000	SPOT7_upper_dem	20/10/2015	15	-13.71	-0.91	0.03	-11.69	-0.78	0.04
	KG009	83.971149	28.832943	MH	5447	5977	530	5721	13.88	25.01	11.30	Equidimensional	0.21	0.93	0.81	-0.89	SRTM	22/02/2000	SPOT7_upper_dem	20/10/2015	15	-9.96	-0.66	0.10	-8.49	-0.57	0.11
G083981E28833N	KG010	83.981475	28.833175	MH	5590	6137	547	5866	15.47	21.16	12.54	Equidimensional	0.15	1.03	0.96	-0.49	SRTM	22/02/2000	HMA_DEM8m_AT_20140119	19/01/2014	13	-2.46	-0.19	0.12	-2.10	-0.16	0.13
G083988E28834N	KG011	83.98775	28.834523	MH	5704	6099	395	5892	17.63	14.95	19.66	Equidimensional	0.13	0.35	0.26	-1.76	SRTM	22/02/2000	HMA_DEM8m_AT_20140119	19/01/2014	13	-10.73	-0.83	0.04	-9.15	-0.70	0.04

Table 1 continued.

G084025E28828N	KG012	84.023936	28.82769	MH	5478	5757	279	5660	15.37	5.64	22.27	V top heavy	0.02	0.30	0.26	-0.94	SRTM	22/02/2000	HMA_DEM8m_AT_20140119_	19/01/2014	13	-3.85	-0.30	0.03	-3.28	-0.25	0.04
G084028E28814N	KG013	84.035374	28.827152	MH	5251	6458	1207	5568	16.46	27.67	7.92	V bottom heavy	0.34	3.00	2.57	-0.97	NaN	NaN	NaN	NaN	NaN	NaN	NaN	NaN	NaN	NaN	NaN
G083940E28806N	KG017	83.941921	28.807226	MH	6154	6473	319	6348	12.16	2.54	25.76	V top heavy	0.25	0.41	0.41	-0.15	NaN	NaN	NaN	NaN	NaN	NaN	NaN	NaN	NaN	NaN	NaN
G084014E28798N	KG039	84.002864	28.813815	MH	5313	6444	1131	5912	13.36	13.46	13.34	Equidimensional	0.25	3.73	3.49	-0.43	NaN	NaN	NaN	NaN	NaN	NaN	NaN	NaN	NaN	NaN	NaN
G084016E28823N	KG040	84.016451	28.824088	MH	5308	5898	590	5590	22.44	37.99	17.00	Equidimensional	0.35	0.62	**0.45**	-1.83	NaN	NaN	NaN	NaN	NaN	NaN	NaN	NaN	NaN	NaN	NaN
G083989E28819N	KG046	83.993676	28.821103	MH	5565	5831	266	5669	20.52	30.38	13.26	V bottom heavy	0.42	0.20	0.08	-4.12	SRTM	22/02/2000	SPOT7_upper_dem	20/10/2015	15	-2.30	-0.15	0.02	-1.96	-0.13	0.02
G083872E28715N	M011	83.871192	28.717188	MH	5251	5880	629	5540	12.70	17.01	9.90	Equidimensional	0.22	1.51	1.29	-0.99	SRTM	22/02/2000	SPOT7_lower_dem	25/02/2016	15	-11.89	-0.79	0.15	-10.14	-0.68	0.16
G083902E28762N	M012	83.905375	28.760542	MH	5307	6034	727	5537	12.62	23.43	6.53	Equidimensional	0.44	1.55	0.97	-2.49	SRTM	22/02/2000	SPOT7_lower_dem	25/02/2016	15	-10.72	-0.71	0.13	-9.14	-0.61	0.14
G083898E28771N	M012_1	83.897677	28.771578	MH	5629	5884	255	5788	15.07	13.36	16.06	V top heavy	0.03	0.24	0.23	-0.36	SRTM	22/02/2000	SPOT7_lower_dem	25/02/2016	15	-8.61	-0.57	0.02	-7.34	-0.49	0.03
G083906E28748N	M013	83.896793	28.749696	MH	5391	6018	627	5728	14.74	11.52	16.83	Equidimensional	0.18	1.65	1.54	-0.46	SRTM	22/02/2000	SPOT7_lower_dem	25/02/2016	15	1.19	0.08	0.17	1.01	0.07	0.18
G083929E28759N	M014	83.930143	28.766715	MH	5227	5885	658	5630	13.66	13.01	13.87	V top heavy	0.52	1.40	1.22	-0.84	SRTM	22/02/2000	SPOT7_lower_dem	25/02/2016	15	-4.14	-0.28	0.14	-3.53	-0.24	0.15
G083923E28774N	M015	83.907469	28.772163	MH	5428	6428	1000	5723	8.93	5.02	9.95	V bottom heavy	0.48	1.46	1.27	-0.86	SRTM	22/02/2000	SPOT7_lower_dem	25/02/2016	15	-7.57	-0.50	0.15	-6.46	-0.43	0.16
G083938E28774N	M016	83.954552	28.779498	MH	5048	5926	878	5527	15.53	29.36	11.64	Equidimensional	0.69	1.90	1.76	-0.47	SRTM	22/02/2000	SPOT7_upper_dem	20/10/2015	15	-3.54	-0.24	0.20	-3.02	-0.20	0.22
G084011E28748N	M017	83.99924	28.753449	MH	4859	6341	1482	5274	17.98	43.04	9.44	V bottom heavy	0.56	2.54	2.26	-0.75	NaN	NaN	NaN	NaN	NaN	NaN	NaN	NaN	NaN	NaN	NaN
G084036E28753N	M018	84.077016	28.756652	MH	5056	6540	1484	5729	8.11	16.66	5.04	Bottom heavy	0.26	15.77	15.27	-0.21	SRTM	22/02/2000	HMA_DEM8m_AT_20140119_	19/01/2014	13	-2.77	-0.21	1.87	-2.36	-0.18	2.00
G084075E28734N	M020	84.075332	28.732052	MH	5133	6035	902	5569	13.42	18.87	10.57	Equidimensional	0.45	2.05	1.65	-1.30	SRTM	22/02/2000	HMA_DEM8m_AT_20140119_	19/01/2014	13	-4.25	-0.33	0.24	-3.62	-0.28	0.25
G084099E28732N	M021	84.098073	28.729709	MH	5157	5788	631	5518	20.90	27.66	17.88	Top heavy	0.42	0.88	0.58	-2.28	SRTM	22/02/2000	HMA_DEM8m_AT_20140119_	19/01/2014	13	-6.93	-0.53	0.10	-5.91	-0.45	0.11
G084109E28727N	M022	84.109957	28.728323	MH	5305	5736	431	5475	24.97	36.22	17.92	V bottom heavy	0.65	0.49	**0.42**	-1.05	NaN	NaN	NaN	NaN	NaN	NaN	NaN	NaN	NaN	NaN	NaN
G084106E28720N	M023	84.107093	28.721698	MH	5396	5873	477	5642	15.32	11.27	20.01	Equidimensional	0.09	1.05	1.02	-0.19	SRTM	22/02/2000	HMA_DEM8m_AT_20140119_	19/01/2014	13	2.96	0.23	0.12	2.53	0.19	0.13
G084114E28710N	M024	84.117431	28.708793	MH	5122	5849	727	5412	20.25	23.44	16.90	V bottom heavy	0.22	2.09	1.78	-0.98	SRTM	22/02/2000	HMA_DEM8m_AT_20140119_	19/01/2014	13	-9.12	-0.70	0.24	-7.78	-0.60	0.26
G084072E28779N	M025	84.072717	28.77902	MH	5342	5792	450	5547	22.56	24.96	20.44	Equidimensional	0.37	0.40	0.30	-1.65	SRTM	22/02/2000	HMA_DEM8m_AT_20140119_	19/01/2014	13	0.22	0.02	0.05	0.19	0.01	0.05
G084089E28774N	M026	84.088344	28.773511	MH	5463	5712	249	5594	13.73	11.63	15.78	Equidimensional	0.20	0.25	0.18	-1.68	SRTM	22/02/2000	HMA_DEM8m_AT_20140119_	19/01/2014	13	-5.67	-0.44	0.03	-4.83	-0.37	0.03
G083973E28815N	M028	83.987173	28.817641	MH	5339	6103	764	5783	11.99	11.44	12.23	Top heavy	0.26	1.59	1.28	-1.29	SRTM	22/02/2000	SPOT7_upper_dem	20/10/2015	15	-5.89	-0.39	0.17	-5.02	-0.33	0.18
G084036E28800N	M031	84.036573	28.803731	MH	5163	5971	808	5485	17.22	28.13	10.83	V bottom heavy	0.43	2.61	2.51	-0.26	SRTM	22/02/2000	HMA_DEM8m_AT_20140119_	19/01/2014	13	-4.45	-0.34	0.30	-3.79	-0.29	0.32
G084005E28793N	M032	84.006473	28.794207	MH	5061	5864	803	5616	22.97	18.38	25.46	V top heavy	0.71	0.95	0.88	-0.47	NaN	NaN	NaN	NaN	NaN	NaN	NaN	NaN	NaN	NaN	NaN
G084029E28779N	M033	84.010897	28.780404	MH	5019	6350	1331	5559	12.28	17.45	10.32	Bottom heavy	0.31	4.58	4.40	-0.27	NaN	NaN	NaN	NaN	NaN	NaN	NaN	NaN	NaN	NaN	NaN
G083997E28815N	M034	83.996717	28.809651	MH	5295	6107	812	5673	11.43	10.09	12.34	Equidimensional	0.35	1.60	1.44	-0.69	SRTM	22/02/2000	HMA_DEM8m_AT_20140119_	19/01/2014	13	-1.86	-0.14	0.19	-1.59	-0.12	0.20
G083989E28799N	M035	83.998776	28.802836	MH	5256	6123	867	5530	18.57	28.18	10.77	V bottom heavy	0.47	1.64	1.30	-1.40	NaN	NaN	NaN	NaN	NaN	NaN	NaN	NaN	NaN	NaN	NaN
G083958E28802N	M036	83.959617	28.802032	MH	5389	5662	273	5499	10.83	14.06	7.50	Bottom heavy	0.57	0.89	0.83	-0.44	NaN	NaN	NaN	NaN	NaN	NaN	NaN	NaN	NaN	NaN	NaN
G083957E28819N	M037	83.957282	28.814733	MH	5437	6451	1014	5758	19.24	25.92	12.28	V bottom heavy	0.47	1.97	1.74	-0.79	SRTM	22/02/2000	SPOT7_upper_dem	20/10/2015	15	-9.54	-0.64	0.21	-8.14	-0.54	0.23
G083946E28825N	M038	83.945282	28.825498	MH	5610	6168	558	5866	14.23	11.36	16.53	Equidimensional	0.07	1.11	0.99	-0.71	SRTM	22/02/2000	SPOT7_upper_dem	20/10/2015	15	-4.95	-0.33	0.12	-4.22	-0.28	0.13
G083939E28757N	M039	83.937964	28.763439	MH	5372	5918	546	5560	19.39	22.80	14.08	V bottom heavy	0.18	0.61	0.13	-5.27	SRTM	22/02/2000	SPOT7_lower_dem	25/02/2016	15	-7.71	-0.51	0.06	-6.57	-0.44	0.07
G083939E28757N	M039_1	83.938798	28.759213	MH	NaN	NaN	NaN	NaN	NaN	NaN	NaN	NaN	NaN	NaN	0.35	NaN	NaN	NaN	NaN	NaN	NaN	NaN	NaN	NaN	NaN	NaN	NaN
G084153E28710N	M082	84.154351	28.71127	MH	5340	5821	481	5649	28.77	32.98	27.36	V top heavy	0.36	0.34	0.27	-1.25	SRTM	22/02/2000	HMA_DEM8m_AT_20131120_	20/11/2013	13	-6.88	-0.53	0.04	-5.87	-0.45	0.04
G083888E28741N	M097	83.887972	28.741747	MH	5331	6023	692	5816	24.48	5.16	34.89	V top heavy	0.23	0.59	0.50	-1.01	NaN	NaN	NaN	NaN	NaN	NaN	NaN	NaN	NaN	NaN	NaN
G083971E28824N	M098	83.972743	28.824798	MH	5539	5859	320	5725	11.43	9.73	12.62	Top heavy	0.29	0.62	0.52	-1.14	SRTM	22/02/2000	SPOT7_upper_dem	20/10/2015	15	-5.76	-0.38	0.07	-4.91	-0.33	0.07
G084048E28825N	M099	84.048992	28.824126	MH	5481	5689	208	5584	16.61	12.80	22.22	Equidimensional	0.11	0.26	0.14	-3.06	SRTM	22/02/2000	HMA_DEM8m_AT_20140119_	19/01/2014	13	-6.63	-0.51	0.03	-5.65	-0.43	0.03
G083933E28782N	M109	83.935764	28.784023	MH	5524	5999	475	5775	31.11	29.91	32.18	Equidimensional	0.28	0.26	0.18	-2.12	SRTM	22/02/2000	SPOT7_upper_dem	20/10/2015	15	2.32	0.15	0.03	1.98	0.13	0.03
	M110	84.099174	28.720874	MH	5185	5798	613	5603	26.04	24.37	26.94	V top heavy	0.26	0.50	0.38	-1.55	SRTM	22/02/2000	HMA_DEM8m_AT_20140119_	19/01/2014	13	-2.19	-0.17	0.06	-1.87	-0.14	0.06
G084129E28707N	M111	84.127721	28.706568	MH	5247	5692	445	5453	13.13	16.70	10.82	Equidimensional	0.21	0.98	0.81	-1.16	SRTM	22/02/2000	HMA_DEM8m_AT_20131120_	20/11/2013	13	-9.58	-0.74	0.12	-8.17	-0.63	0.13
G084039E28723N	M112	84.039731	28.721495	MH	5496	6369	873	5927	26.68	28.46	25.02	Equidimensional	0.38	1.21	1.17	-0.25	NaN	NaN	NaN	NaN	NaN	NaN	NaN	NaN	NaN	NaN	NaN
G084011E28767N	M113	84.01347	28.765025	MH	4961	6244	1283	5673	16.40	12.44	18.10	Top heavy	0.03	2.53	2.25	-0.72	SRTM	22/02/2000	HMA_DEM8m_AT_20140119_	19/01/2014	13	-0.96	-0.07	0.29	-0.82	-0.06	0.31
G083983E28810N	M114	83.982236	28.810198	MH	5431	5680	249	5572	15.57	15.48	15.61	Top heavy	1.23	0.22	0.09	-3.92	SRTM	22/02/2000	HMA_DEM8m_AT_20140119_	19/01/2014	13	-3.54	-0.27	0.03	-3.02	-0.23	0.03
G084162E28710N	M130	84.162879	28.708931	MH	5203	5748	545	5445	24.57	39.81	16.79	Bottom heavy	0.43	0.67	0.51	-1.60	NaN	NaN	NaN	NaN	NaN	NaN	NaN	NaN	NaN	NaN	NaN
G084142E28711N	M131	84.144039	28.710629	MH	5288	5799	511	5502	21.62	24.62	18.95	Bottom heavy	0.42	0.57	0.41	-1.83	SRTM	22/02/2000	HMA_DEM8m_AT_20131120_	20/11/2013	13	-6.05	-0.47	0.07	-5.16	-0.40	0.07
G084149E28719N	M132	84.149992	28.718433	MH	5169	5812	643	5549	27.33	36.12	23.45	Top heavy	0.45	0.59	0.52	-0.79	NaN	NaN	NaN	NaN	NaN	NaN	NaN	NaN	NaN	NaN	NaN
G083958E28832N	M134	83.956629	28.830949	MH	5779	6001	222	5856	12.78	11.31	13.07	V bottom heavy	0.59	0.13	0.04	-4.83	SRTM	22/02/2000	SPOT7_upper_dem	20/10/2015	15	-16.80	-1.12	0.01	-14.32	-0.95	0.02
G083958E28832N	M134_1	83.960236	28.832821	MH	NaN	NaN	NaN	NaN	NaN	NaN	NaN	NaN	NaN	NaN	0.04	NaN	NaN	NaN	NaN	NaN	NaN	NaN	NaN	NaN	NaN	NaN	NaN
G083907E28733N	M146	83.903518	28.735739	MH	5245	5795	550	5519	22.50	31.30	20.05	Equidimensional	0.20	0.84	0.50	-2.69	SRTM	22/02/2000	SPOT7_lower_dem	25/02/2016	15	-5.42	-0.36	0.08	-4.62	-0.31	0.09
G083960E28827N	M147	83.961117	28.826044	MH	5729	5851	122	5791	14.15	12.26	16.17	Equidimensional	0.18	0.11	0.09	-0.79	SRTM	22/02/2000	SPOT7_upper_dem	20/10/2015	15	-11.66	-0.78	0.01	-9.94	-0.66	0.01